ARMY RESEARCH LABORATORY

Volume I: Select Papers

ARL Summer Student Research Symposium

ARL-TM-2008 August 2008

Approved for public release; distribution unlimited.

NOTICES

Disclaimers

The findings in this report are not to be construed as an official Department of the Army position unless so designated by other authorized documents.

Citation of manufacturer's or trade names does not constitute an official endorsement or approval of the use thereof.

Destroy this report when it is no longer needed. Do not return it to the originator.

Army Research Laboratory
Adelphi, MD 20783-1197

ARL-TM-2008 **August 2008**

Volume I: Select Papers

ARL Summer Student Research Symposium

Approved for public release; distribution unlimited.

REPORT DOCUMENTATION PAGE

Form Approved
OMB No. 0704-0188

Public reporting burden for this collection of information is estimated to average 1 hour per response, including the time for reviewing instructions, searching existing data sources, gathering and maintaining the data needed, and completing and reviewing the collection information. Send comments regarding this burden estimate or any other aspect of this collection of information, including suggestions for reducing the burden, to Department of Defense, Washington Headquarters Services, Directorate for Information Operations and Reports (0704-0188), 1215 Jefferson Davis Highway, Suite 1204, Arlington, VA 22202-4302. Respondents should be aware that notwithstanding any other provision of law, no person shall be subject to any penalty for failing to comply with a collection of information if it does not display a currently valid OMB control number.
PLEASE DO NOT RETURN YOUR FORM TO THE ABOVE ADDRESS.

1. REPORT DATE *(DD-MM-YYYY)*
August 2008

2. REPORT TYPE
Final

3. DATES COVERED (From - To)

4. TITLE AND SUBTITLE
Volume I: Select Papers

5a. CONTRACT NUMBER

5b. GRANT NUMBER

5c. PROGRAM ELEMENT NUMBER

6. AUTHOR(S)
ARL Summer Student Research Symposium

5d. PROJECT NUMBER

5e. TASK NUMBER

5f. WORK UNIT NUMBER

7. PERFORMING ORGANIZATION NAME(S) AND ADDRESS(ES)
U.S. Army Research Laboratory
2800 Powder Mill Road
Adelphi, MD 20783-1197

8. PERFORMING ORGANIZATION REPORT NUMBER
ARL-TM-2008

9. SPONSORING/MONITORING AGENCY NAME(S) AND ADDRESS(ES)

10. SPONSOR/MONITOR'S ACRONYM(S)

11. SPONSOR/MONITOR'S REPORT NUMBER(S)

12. DISTRIBUTION/AVAILABILITY STATEMENT
Approved for public release; distribution unlimited.

13. SUPPLEMENTARY NOTES

14. ABSTRACT

The ARL Summer Student Research Symposium is an ARL Director's Award Program for all the students participating in various summer scholarship and contract activities across ARL. The goal of the program is to recognize and publicize exceptional achievements made by the students and their mentors in the support of Army science.

All college undergraduate and graduate students receiving research appointments and conducting summer studies at ARL are automatically enrolled in the symposium program. As an integral part of their summer study, all students are required to write a paper on their work which summarizes their major activity and its end product.

The program is conducted on two separate competitive levels: undergraduate and graduate. The format of the paper in both levels is the same. However, the evaluation will take into consideration the difference in the academic level of the students.

All students submitted their research paper for directorate review. Directorate judging panels selected one or two papers from each competition category for the laboratory-wide competition at the Summer Student Symposium on 7 August 2008.

Students selected by their directorate for competition participated in the one-day Summer Student Symposium on 7 August 2008. At the symposium the students presented their papers to the ARL Director and an ARL Fellows panel.

This volume of the Summer Student Symposium Proceedings contains the papers presented at the symposium.

15. SUBJECT TERMS

16. SECURITY CLASSIFICATION OF:			17. LIMITATION OF ABSTRACT	18. NUMBER OF PAGES	19a. NAME OF RESPONSIBLE PERSON
a. REPORT	b. ABSTRACT	c. THIS PAGE			Vallen Emery
U	U	U	UL	241	19b. TELEPHONE NUMBER (*Include area code*) (301) 394-3585

Standard Form 298 (Rev. 8/98)
Prescribed by ANSI Std. Z39.18

Contents

Director's Foreword **v**

Introduction **1**

Computational & Information Sciences Directorate (CISD) **3**

Experimental Laboratory Environments: Image and OCR Tool Kit (IOTK) Utility Exploration 5

STEP, APG Site – Building Molecular Crystals with Defects for Atomistic Simulations 55

Human Research & Engineering Directorate (HRED) **71**

Robotic Intelligent Control System with Human Inspired Plan Selection 73

Sensors and Electron Devices Directorate (SEDD) **89**

Development of a Miniaturized Photoacoustic Chemical Sensor 91

Demonstration of a Multiplexed Electrospray Micromachined in Silicon Substrates for Fuel Atomization 107

Survivability/Lethality Analysis Directorate (SLAD) **121**

Structural Response for Armor Panels Due to Blast: Generation of A Response Database for Use in Vulnerability Analysis Codes 123

Improvements of Techniques and Devices for Survivability, Lethality, and Vulnerabilities Analysis....137

Vehicle Technology Directorate (VTD) **161**

Design and Construction of a Low Reynolds Number Aerodynamic Performance Analysis Tank 163

Photogrammetry Technique for Deformation Measurement of Millimeter-Scale Wings....179

Weapons & Materials Research Directorate (WMRD) **193**

Novel Thin Film Materials for Tunable Device Applications....195

Dynamic Fracture in Glass 209

Distribution List **233**

INTENTIONALLY LEFT BLANK.

Director's Foreword

The Army Research Laboratory (ARL) mission is to "Provide innovative science, technology, and analyses to enable full spectrum operations." As the Army's corporate laboratory we provide the technological underpinnings critical to providing capabilities required by our current and future Soldiers.

Our nation is projected to experience a shortage of scientists and engineers. ARL recognizes the criticality of intellectual capital in generating capabilities for the Army. As the Army's corporate laboratory, addressing the projected shortfall is a key responsibility for us. We have therefore identified the nation's next generation of scientists and engineers as a key community of interest and have generated a robust educational outreach program to strengthen and support them. We have achieved many successes with this community, and believe that the breadth and depth of our outreach programs will have a significant positive effect on the participants, facilitating their journey toward becoming this Nation's next generation of scientists and engineers.

A fundamental component of our outreach program is to provide research experiences at ARL to students. During the summer of 2008, we supported research experiences at ARL for over 100 undergraduate and graduate students. Each of these students was required to write a paper describing the results of the work they performed while at ARL. While all of the students engaged in our summer research program had remarkable experiences and had excellent results, only a select number could be presented at our symposium. The papers contained herein were those presented at the symposium and they show that the nation truly does have high caliber people pursuing degrees in scientific and engineering disciplines.

We are very pleased to have hosted this outstanding group of students for the summer. It is our hope that they will continue their pursuit of technical degrees and will someday assist us in providing critical technologies for our Soldiers.

INTENTIONALLY LEFT BLANK.

Introduction

The ARL Summer Student Research Symposium is an ARL Director's Award Program for all the students participating in various summer scholarship and contract activities across ARL. The goal of the program is to recognize and publicize exceptional achievements made by the students and their mentors in the support of Army science.

All college undergraduate and graduate students receiving research appointments and conducting summer studies at ARL are automatically enrolled in the symposium program. As an integral part of their summer study, all students are required to write a paper on their work which summarizes their major activity and its end product.

The program is conducted on two separate competitive levels: undergraduate and graduate. The format of the paper in both levels is the same. However, the evaluation will take into consideration the difference in the academic level of the students.

All students submitted their research paper for directorate review. Directorate judging panels selected one or two papers from each competition category for the laboratory-wide competition at the Summer Student Symposium on 7 August 2008.

Students selected by their directorate for competition participated in the one-day Summer Student Symposium on 7 August 2008. At the symposium the students presented their papers to the ARL Director and an ARL Fellows panel.

This volume of the Summer Student Symposium Proceedings contains the papers presented at the symposium.

INTENTIONALLY LEFT BLANK.

Computational & Information Sciences Directorate (CISD)

INTENTIONALLY LEFT BLANK.

U.S. Army Research Laboratory

SUMMER RESEARCH TECHNICAL PAPER

Experimental Laboratory Environments: Image and OCR Tool Kit (IOTK) Utility Exploration

by Nicole Giffen, Luis Hernandez, and Douglas Briesch

Contents

List of Figures 7

List of Tables 7

Abstract 8

1. Introduction/Background 9

2. Purpose and Scope of the Report 11

3. Lab Environment 11

3.1 Infrastructure 11

3.2 Data 12

3.3 IOTK 13

4. Methodology 14

4.1 Scoring 14

4.2 Data Set Generation and Ground-truthing 15

4.3 Procedure 16

5. Results and Discussion 17

6. Summary, Conclusions, and Recommendations 22

7. References 24

Appendix A. Sample of grayscale TIF Collection Form 25

Appendix B. Sample of Black and White JPEG Collection Form 27

Appendix C. Sample Ground-Truth Form 29

Appendix D. Generated Data Sets 31

Appendix E. Sample Manual Accuracy Report 33

Appendix F. Sample IOTK Accuracy Report 39

List of Figures

Figure 1. Document image segmentation. 10
Figure 2. Sample grayscale TIF and black and white JPEG test document images 13
Figure 3. IOTK character accuracy data flow.....13
Figure 4. ISRI analytic tool kit representative character accuracy reports. 19
Figure 5. IOTK test run results display.....20
Figure 6. Vendor A error analysis for one image. 21
Figure 7. Vendor B error analysis for one image.....21

List of Tables

Table 1. Practice test run using manual method. 17
Table 2. Experiment test run using manual method and IOTK. 18
Table 3. Scoring character category comparison. 22

Abstract

The objective of this research effort was to explore a computer software application that acts as an environment for image processing and optical character recognition (OCR) investigations. Our intentions are that this application could become a novel tool for these investigations. This prototype tool kit, called the Image and OCR Tool Kit (IOTK), was explored using a database created from previously collected and scanned representative document pages. A series of automated and manual tests were performed using multiple OCR engines and the results were timed, scored, compared, and analyzed. In addition, the usability and effectiveness of the tool kit as a processing, experimentation, and testing environment was evaluated using methods described in this paper. The findings, conclusions, and recommendations are provided to further the refinement of this prototype environment.

1. Introduction/Background

Foreign language translation in support of military operations and operations other than war is an expensive proposition and a task the military wants to see automated. Because the Army deploys to locations around the world, the ability to process the content of paper documents written in a foreign language is crucial. The U.S. Army Research Laboratory (ARL) has been conducting research, development, and evaluation in document digital image processing, optical character recognition (OCR), and machine translation (MT) as a system with Department of Defense (DoD) organizations, industry, and academia partners for several years. These efforts have produced a number of embedded system containing OCR and MT capabilities, such as those found in references 1 and 2. These efforts aim to (1) enhance the Army translators' and analysts' ability to deal with large collections of foreign language printed documents, (2) define algorithms and procedures for dealing with noisy document data for OCR/MT, (3) identify OCR and image processing activities that boost MT and the effective use of existing software tool kits, and (4) validate workflow tools for choosing different OCR and MT computational approaches into Army environments with limited linguistic, translation, or infrastructure expertise.

Image processing is a form of information processing in which the input is an image such as a photograph, scanned machine printed, hand printed, or cursive handwriting document, or a still frame from video. The purpose of image processing is to assist the human viewer by improving the appearance of the images and preparing those images for measurement and feature analysis. Both of these areas are extremely important, as they form the basis for the exploitation of captured documents from the battlefield by military information systems.

Because document collection images are captured or obtained under less than ideal conditions, they contain a number of defects and imperfections. Document degradations that occur from capture processes like optical based scanning and camera capture are prevalent. Geometric distortions (such as skew, rotation, reduction), non-uniform illumination artifacts (brightness and contrast adjustments, color correction, focus), random fluctuations in the image pixels (such as noise in the form of speckles or "salt and pepper" in the document image), among others, are pervasive. Various algorithms can be applied to enhance the visibility of details and information in the image with the goal of producing an accurate representation of the original document (*3*). Once the image has been adjusted, it is necessary to apply layout analysis techniques (such as image segmentation, page segmentation, and region or zone classification) to identify and decompose the content of the document image for further automated processing (*3*).

Handwritten or printed text document collections are extensive. These documents need to be detected, localized, tracked, extracted, and recognized from a given image. Variations in text due to differences in size, style, orientation, and alignment coupled with low image fidelity and

complex backgrounds make the problem of automatic text extraction and recognition extremely challenging.

The study and application of algorithms and techniques that handle the cleaning of image artifacts and noise, the enhancement of features and details contained within the image, segmentation, and the performance of OCR using a representative collection is necessary to understand the issues associated with field generated imagery (see figure 1). This is a pre-requisite to discovering the most effective methods to process these images as well as to providing information and details critical for post processes. These post processes include retrieval, content extraction, data and document mining, image processing, data processing, document management, and other specialized processes targeting information distillation.

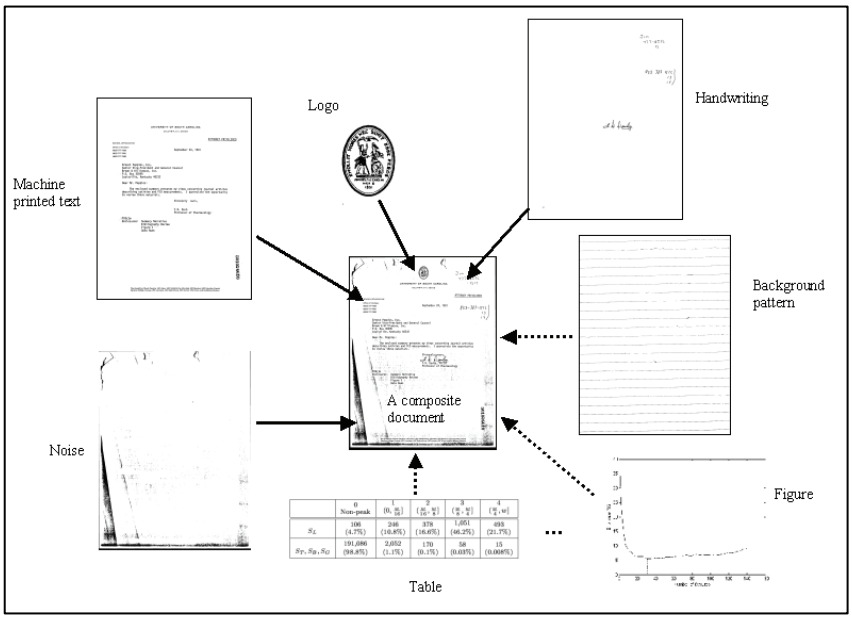

Figure 1. Document image segmentation.

The application of algorithms, such as those found in DocLib (*4*), or commercial image processing tool kits are either too generic or too specialized for handling the random combination of imperfections and degradations found in realistic collections. In addition, foreign language scripts poses challenges to algorithms and techniques mainly designed to handle Latin scripts (*5*). Experimentation and testing is required to determine what combinations of algorithms are best to process a particular set of document imagery.

Document image processing is a time intensive process, especially when dealing languages based on the Arabic script. The use of realistic data, available computing power, and an image and OCR tool kit that is extensible and adaptable provides the foundation needed for further research, testing, and evaluation within digital image processing and OCR, as well as other related domains. ARL initiated an effort to build such a tool kit, branded as the Image and OCR Tool Kit (IOTK), as an integrated environment in the summer of 2007. The use of IOTK will

provide several components, including, but not limited to, image triage capabilities, image cleanup, component disaggregation, and OCR, as well as techniques for obtaining quantitative information identifying which algorithms will be best for accomplishing the digital image processing and OCR requirements. We propose that such a tool kit will assist with all the phases in image processing, text recognition, and analysis tasks.

2. Purpose and Scope of the Report

This report has two purposes:

- Reporting the successful use of an IOTK as an environment to conduct evaluations of document image processing, analysis, and text recognition.
- Show the results of an experiment measuring and evaluating the performance of selected commercial OCR engines using the traditional OCR methodology and scoring methods to compare and contrast the utility of an IOTK environment.

The scope of this report covers Arabic script used by the Dari language. The intended readers of this report include practicing digital image processing and OCR researchers, engineers, and technical managers.

The next section presents a brief description of the overall infrastructure used to support the experimentation:

- Equipment and software infrastructure used.
- Short discussion on IOTK design, features, functionality, and capabilities
- Data sets generation and ground-truth discussion

Section 4 presents and discusses the procedures, data collection, analysis, and calculation aspects. In section 5, we discuss the experiment results of the use of IOTK as compared to older approaches. Section 6 provides a summary, conclusions, and recommendations.

3. Lab Environment

3.1 Infrastructure

The equipment used consisted of the following:

- Laptop – Dell Latitude D810

  OS Name: Microsoft Windows XP Professional

Version: 5.1.2600 Service Pack 2 Build 2600

System Type: X86-based PC

Processor: x86 Family 6 Model 13 Stepping 8 Genuine Intel ~2127 Mhz

BIOS Version/Date Dell Inc. A03, 7/4/2005

Memory: 2.00 GB

- Scanner – Fujitsu fi-4750C

  Scanner Type: ADF (Automatic Document Feeder) and FB (Flatbed)

  A3 Duplex Color Scanner

  Color Scanning Speed: 20 pppm/40 ipm

  Binary Scanning Speed: 50 ppm/90 ipm

  Double Feeding Detection

  SCSI-2 Interface

  Optical Resolution 400 dpi

  Output Resolution:

    Color 50 to 600 dpi (Addressable by 1 dpi)

    Grayscale 50 to 600 dpi (Addressable by 1 dpi)

    Binary 50 to 800 dpi (Addressable by 1 dpi)

The software load used consisted of the following:

- Desktop applications: Microsoft Office 2003
- Scanning application: Scansoft Paperport Pro v 9.0
- Software application prototype: Image and OCR Tool Kit v 0.6
- OCR software application: Vendor A, Vendor B

3.2 Data

Test data consisted of 166 pages that were collected from representative users of the Dari language. For each page in the document set, there was a 300 dpi image generated as a TIF and JPEG file. The images were produced under laboratory conditions similar to capture operations using typical capture devices found in tactical fixed facilities. The operator who performed the scanning had an introductory training session, but was not an “expert” user of the scanner hardware or supporting software. Samples of the scanned pages are shown in figure 2.

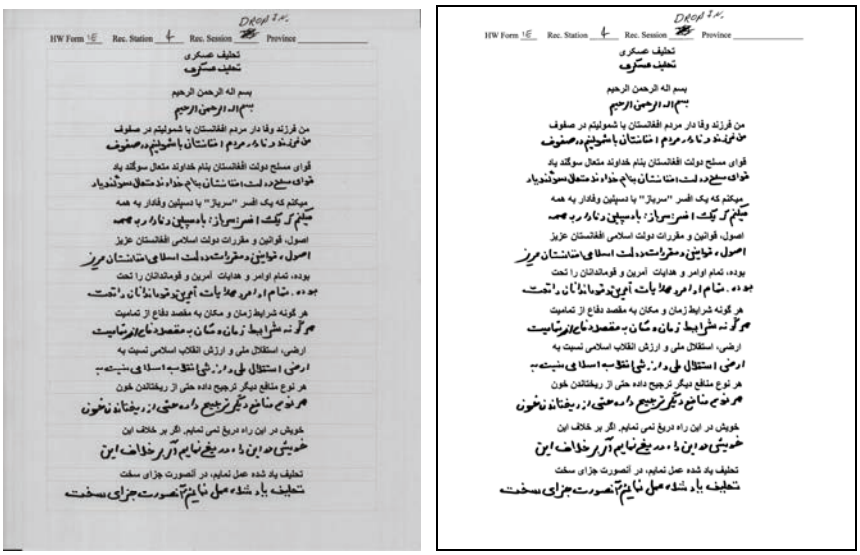

Figure 2. Sample grayscale TIF and black and white JPEG test document images.

3.3 IOTK

The approach that IOTK uses in exposing functionality and capabilities as an adaptable environment is one that integrates core technologies, such as OCR, using available Application Programming Interfaces (API) or Software Development Kits (SDK) and facilitating interactions with such.

Four modules have been prototyped in IOTK that provide the functionality described in figure 3.

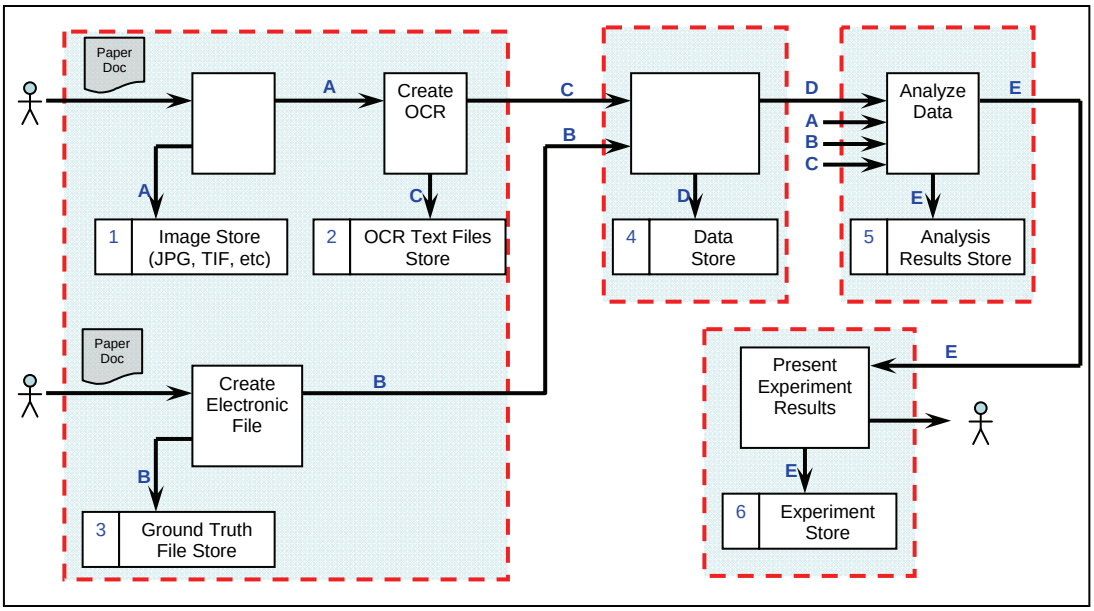

Figure 3. IOTK character accuracy data flow.

Image Document Management Module – provides the capability to organize collections of images into document sets. These document sets are maintained in a database. They consist of the document images, the ground-truth text files, and other related files.

Run OCR Engine Module – handles the OCR engine interface, allowing for selection of OCR engines, language, and adjustment of OCR options as needed. This provides the OCR output files.

Run Scoring Module – provides the functionality of comparing the OCR output text file with the respective ground-truth text file and generating an accuracy report output text file.

Analyze Test Runs Module – allows for viewing and analyzing the accuracy results of Test Runs, including detailed statistics. Test Run results can be stored in a database for ease of retrieval during subsequent uses of IOTK. The list of available features includes the following:

- Character Category Breakdown
- Total Document Character Analysis
- Word Analysis
- Error Analysis
- List of Past Test Runs
- Test Run Metrics
- Report Generation

To achieve an end-to-end process, the "Perform Test Run" functionality is provided. This function will take a user-specified document set, language, and OCR engine and execute all the processes required to obtain experiment metrics in one step.

4. Methodology

4.1 Scoring

The analytic tools provided by the Information Science Research Institute (ISRI) at the University of Nevada, Las Vegas (UNLV) provides the basis for measuring character and word accuracy for OCR systems (*6*). These tools are shell programs written in C that are suitable for use in batch scripting. The evaluation routines are console programs accepting a number of parameters and performing their task in a non-interactive manner. The users of these routines must provide the OCR generated files and correct ("ground-truth") text files. Given these files, the routines will compare them and produce measures of character recognition performance. A character or word accuracy report is produced providing information about the number of

characters in the ground-truth, the number of errors made by the OCR system under test, and overall accuracy scores. Also provided is a complete enumeration of the characters recognized and compared to the ground-truth characters.

These routines were integrated into IOTK as part of the Run Scoring Module and formed the basis for the experimentation conducted in this exploration.

4.2 Data Set Generation and Ground-truthing

The test data used consisted of a subset of a larger data corpora consisting of 166 original hardcopy pages that were obtained in Kabul, Afghanistan, from representative users of the Dari language in April 2008. A total of four master collection pages named Form 1E through 4E were prepared using Microsoft Office Word 2003 and saved as Word documents. Each page contained representative Arabic-scripted Dari sentences intended to capture handwritten equivalent sentences from the users. These pages were used to generate document images using Scansoft PaperPort Pro v 9.0 and a Fujitsu scanner. The resulting images were saved and stored as both TIF and JPEG images with varying resolutions and quality levels using a methodic scanning session approach.

Each scanning session was saved in a different file folder. The names of the folders were constructed to reflect the type of image format and their variation in resolution and image quality. For example, (1) a folder filled with handwritten Dari document images scanned in grayscale at 300 dpi and saved as a TIF image was named *HW_Dari_300_GS_TIF*, and (2) a folder of handwritten Dari document images scanned in black and white at 300 dpi, a quality level of 90, and saved as a JPEG image was called *HW_Dari_300_90ql_BW_JPG*. Stored in each folder were between 37 and 47 individual document images. The identifying factors of each page – form number (1E, 2E, 3E, and 4E), the recording station, and recording session – were combined to form the document images' file names. For example, a document form 3E, recorded at station 1, session 14 would be saved as *hwform3e0114*.

The resulting total number of document images accounting for 11 variations in image quality, resolution, and format was 1,826. They were organized into 44 data sets consisting of anywhere between 37 and 47 images. Additional information about the data sets can be found in appendix C.

Ground-truths, essentially the "answer key" that OCR outputs are compared to and scored against, were also generated for each document form. These files were required to be in Unicode (UTF-16) format. The approach used to generate Unicode (UTF-16) text was to open the original form document using Word and save it as a UTF-16 text file after doubling the existing sentences in the original form. For scoring accuracy purposes, doubling the existing sentences was required in order to account for the electronic text as well as the handwritten samples now present in the generated image.

Using a subset of the data set generated, we intend to use manual methods and the IOTK prototype to explore the benefits of IOTK's automated process over the manual process. In addition, we also hope to assess the added value of using an automated, user-friendly interface.

4.3 Procedure

This exercise represents a pilot test of our methodology. It will be done in two phases. In the first phase, all processes will be performed using IOTK's prototype functionality. In the second phase, the OCR evaluation process will be performed using manual methods typical of current practice. Commercial-Off-The-Shelf (COTS) OCR engine software from two vendors will be used to generate OCR output text files.

As part of IOTK's automated process, a document set and language is user specified and a test run performed for both vendors. The entire process, from when the document set is selected until the DoD scores are stored in the database, is timed and recorded in a Microsoft Excel worksheet. The OCR engine runtime is also recorded.

Phase two, the manual OCR evaluation process, is also timed from beginning to end. It is executed using the following steps:

1. Create a directory which will be the output working directory.
2. With Windows Explorer, navigate to the "*C:\Program Files\IOTK*" directory and copy the files "*Accuracy.exe*", "*Wordacc.exe*", and "*cygwin.dll*" to the output directory.
3. Navigate to the Document Set directory and copy all the ground truth files in the "*\Ground Truth*" subdirectory into the output directory. The Document Set directory will be under "*C:\Program Files\IOTK\Document Sets*".
4. Open OCR Engine (Vendor A, Vendor B, as applicable).
5. Ensure correct language is selected.
6. Load an image.
7. Recognize the image.
8. Save the results as a Unicode (UTF-16) text file into the output directory. Name the output file the same as the input image, except add "*_ocr*" to the end. For example, *Doc1.jpg* → *Doc1_ocr.txt*.
9. Repeat steps 6–8 for all images in the document set.
10. After all the images have been recognized, go out to the DOS command line. Click Start → Run. Enter "*cmd*" and click "*OK*".
11. Navigate to the output directory.

12. Run the DoD scoring software on each of the OCR output files, comparing each file to the corresponding ground-truth file. The command line is "*accuracy –u <Ground Truth file> <OCR Output file> <Score file>*". Name the score file the same as the OCR output file, except replace "*ocr.txt*" with "*_score.txt*" at the end.

13. After all the score files have been generated, bring up Microsoft Excel.

14. Open up each score file for each image and transfer the %Right numbers for each category into an Excel spreadsheet.

15. When all the %Right numbers have been transferred, save the Excel file with a name of "*<Document Set name>_Accuracy_Report.xls*".

Once the test runs are completed, the results are compared to one another in time to process the image, the OCR generation, and scoring. Then the user will explore and provide comments about the user interface and its ability to handle the outcomes of the accuracy scoring process.

5. Results and Discussion

Following the methodology discussed in section 4 we ran a selected number of test runs using the data set generated from the Dari representative user collection. To familiarize the person conducting the experiment with the methodology, we ran a practice test run using the *HW_Dari_300_GS_TIF_Form_1E* document set. This document set contained 37 document images representing a resolution of 300 dpi stored as a grayscale (8-bit) TIFF format. The raw time information was captured in table 1.

Table 1. Practice test run using manual method.

Manual Method			
Task	Vendor A		
	Time (h:min:s)		Cumulative Time (h:min:s)
Run OCR Engine	Start	9:48:00	0:25:00
	Stop	10:13:00	
Accuracy Scoring	Start	12:22:00	0:35:00
	Stop	12:57:00	
Generate Report	Start	1:05:00	0:47:00
	Stop	1:32:00	
	Start	1:40:00	
	Stop	2:00:00	
Total Time (h:min:s)			1:47:00

For the experiment, the document set *HW_Dari_300_90ql_BW_JPG_Form_1E* was used. This document set contained 37 document images representing a resolution of 300 dpi and stored as a bi-tonal (black and white) JPEG format at a 90% quality.

The test runs results are captured in table 2.

Table 2. Experiment test run using manual method and IOTK.

Task	Manual Method		IOTK	
	Vendor A Time (h:min:s)	Vendor B Time (h:min:s)	Vendor A Time (min)	Vendor B Time (min)
Run OCR Engine	0:20:00	0:04:00	0:08:00	0:01:00
Accuracy Scoring	0:22:00	0:37:00		
Generate Report	0:30:00	0:29:00		
Total Time	1:12:00	1:10:00	0:13:00	0:11:00

The gray regions in table 2 indicate that the difference in timing was negligible due to the process automation in IOTK.

From the results displayed in table 2, it is evident that a significant difference in time between the manual method and IOTK's method is present, as expected. In this particular process flow in digital image and OCR experimentation, it is clear that automation reduces the time required to evaluate technologies such as OCR.

Given the IOTK results shown in table 2, it was decided to run the entire generated Afghani Military data collection consisting of 44 document sets and tallying 1, 826 document images through IOTK using both OCR vendors. The total time it took to complete these OCR accuracy evaluations for Vendor A was 9 h and 44 min (9.733 h) and for Vendor B 9 h and 12 min (9.2 h). Using the results found in table 2, it can be estimated that the same process conducted manually using Vendor A would take approximately 52 h and 48 min, while Vendor B would take 51 h and 20 min. This would equate to a person working a non-stop 8-h day for 6.5 days and 6.375 days, respectively. These results reinforce our expectation that a test environment such as IOTK will significantly reduce the amount of time required to conduct experimentation and evaluation of OCR engines from multiple vendors.

One outcome of the test run is the character accuracy reports for the vendor OCR software. Using the manual method renders reports in a format that is not conducive to easy analysis and understanding. For example, because the reports (shown in figure 4) are created using the Unicode encoding values for each character being compared by the scoring algorithm, it is

difficult to analyze the obtained data. In a test run containing 37 individual accuracy reports, it is a time consuming task to use the Unicode standard to decode the resulting Unicode values. This would be required in order to determine trends such as a particular character being misrecognized consistently. Furthermore, because it is necessary to manipulate and assimilate these individual reports, i.e., manually transcribing raw data to a common tool such as Microsoft Excel, the risk of human error is greater.

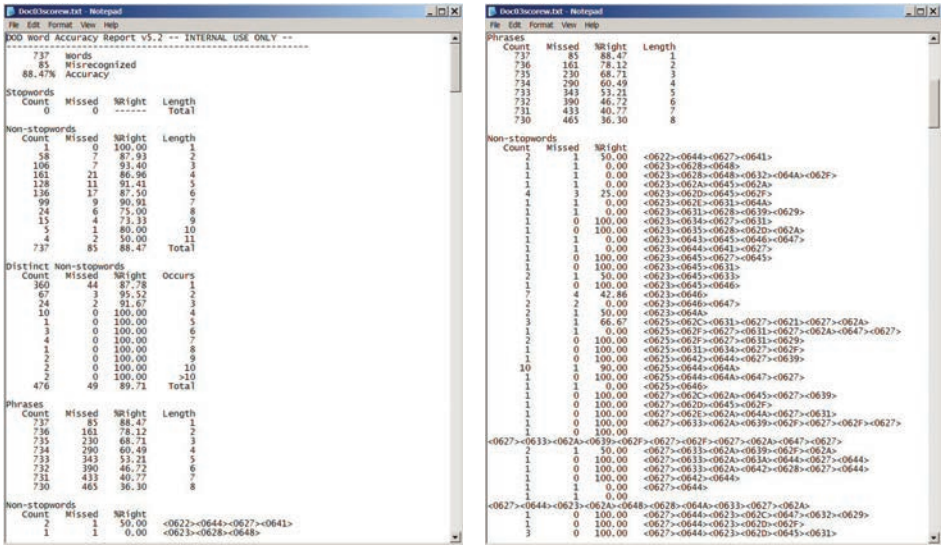

```
Doc03scorew.txt - Notepad
File  Edit  Format  View  Help
DOD Word Accuracy Report v5.2 -- INTERNAL USE ONLY --
=====================================================
   737   Words
    85   Misrecognized
 88.47%  Accuracy

Stopwords
  Count   Missed   %Right   Length
      0        0   ------    Total

Non-stopwords
  Count   Missed   %Right   Length
      1        0   100.00        1
     58        7    87.93        2
    106        7    93.40        3
    161       21    86.96        4
    128       11    91.41        5
    136       17    87.50        6
     99        9    90.91        7
     24        6    75.00        8
     15        4    73.33        9
      5        1    80.00       10
      4        2    50.00       11
    737       85    88.47    Total

Distinct Non-stopwords
  Count   Missed   %Right   Occurs
    360       44    87.78        1
     67        3    95.52        2
     24        2    91.67        3
     10        0   100.00        4
      1        0   100.00        5
      3        0   100.00        6
      4        0   100.00        7
      1        0   100.00        8
      2        0   100.00        9
      2        0   100.00       10
      2        0   100.00      >10
    476       49    89.71    Total

Phrases
  Count   Missed   %Right   Length
    737       85    88.47        1
    736      161    78.12        2
    735      230    68.71        3
    734      290    60.49        4
    733      343    53.21        5
    732      390    46.72        6
    731      433    40.77        7
    730      465    36.30        8

Non-stopwords
  Count   Missed   %Right
      2        1    50.00   <0622><0644><0627><0641>
      1        1     0.00   <0623><0628><0648>
```

```
Doc03scorew.txt - Notepad
File  Edit  Format  View  Help
Phrases
  Count   Missed   %Right   Length
    737       85    88.47        1
    736      161    78.12        2
    735      230    68.71        3
    734      290    60.49        4
    733      343    53.21        5
    732      390    46.72        6
    731      433    40.77        7
    730      465    36.30        8

Non-stopwords
  Count   Missed   %Right
      2        1    50.00   <0622><0644><0627><0641>
      1        1     0.00   <0623><0628><0648>
      1        1     0.00   <0623><0628><0648><0632><064A><062F>
      1        1     0.00   <0623><062A><0645><062A>
      4        3    25.00   <0623><062D><0645><062F>
      1        1     0.00   <0623><062E><0631><064A>
      1        1     0.00   <0623><0631><0628><0639><0629>
      1        0   100.00   <0623><0634><0627><0631>
      1        0   100.00   <0623><0635><0628><062D><062A>
      1        1     0.00   <0623><0643><0645><0646><0647>
      1        1     0.00   <0623><0644><0641><0627>
      1        0   100.00   <0623><0645><0627><0645>
      1        0   100.00   <0623><0645><0631>
      2        1    50.00   <0623><0645><0633>
      1        0   100.00   <0623><0645><0646>
      7        4    42.86   <0623><0646>
      2        2     0.00   <0623><0646><0647>
      2        1    50.00   <0623><064A>
      3        1    66.67   <0625><062C><0631><0627><0621><0627><062A>
      1        1     0.00   <0625><062F><0627><0631><0627><062A><0647><0627>
      2        0   100.00   <0625><062F><0627><0631><0629>
      1        0   100.00   <0625><0631><0634><0627><062F>
      1        0   100.00   <0625><0642><0644><0627><0639>
     10        1    90.00   <0625><0644><064A>
      1        0   100.00   <0625><0644><064A><0647><0627>
      1        1     0.00   <0625><0646>
      1        0   100.00   <0627><062C><062A><0645><0627><0639>
      1        0   100.00   <0627><062D><0645><062F>
      1        0   100.00   <0627><062E><062A><064A><0627><0631>
      1        0   100.00   <0627><0633><062A><0639><062F><0627><062F><0627>
      1        0   100.00
<0627><0633><062A><0639><062F><0627><062F><0627><062A><0647><0627>
      2        1    50.00   <0627><0633><062A><0639><062F><062A>
      1        0   100.00   <0627><0633><062A><063A><0644><0627><0644>
      1        0   100.00   <0627><0633><062A><0642><0628><0627><0644>
      1        0   100.00   <0627><0642><0644>
      1        1     0.00   <0627><0644>
      1        1     0.00
<0627><0644><0623><062A><0648><0628><064A><0633><0627><062A>
      1        0   100.00   <0627><0644><0623><062C><0647><0632><0629>
      1        0   100.00   <0627><0644><0623><062D><062F>
      3        0   100.00   <0627><0644><0623><062D><0645><0631>
```

Figure 4. ISRI analytic tool kit representative character accuracy reports.

Through the use of the interface in IOTK one can individually select each accuracy report and obtain individual image scores as well as aggregate information for the entire test run without any tabulation required by the user (see figure 5). IOTK's Character Analysis display facilitates the examination of the raw data, because it visualizes the glyphs representing the characters contained in the document image.

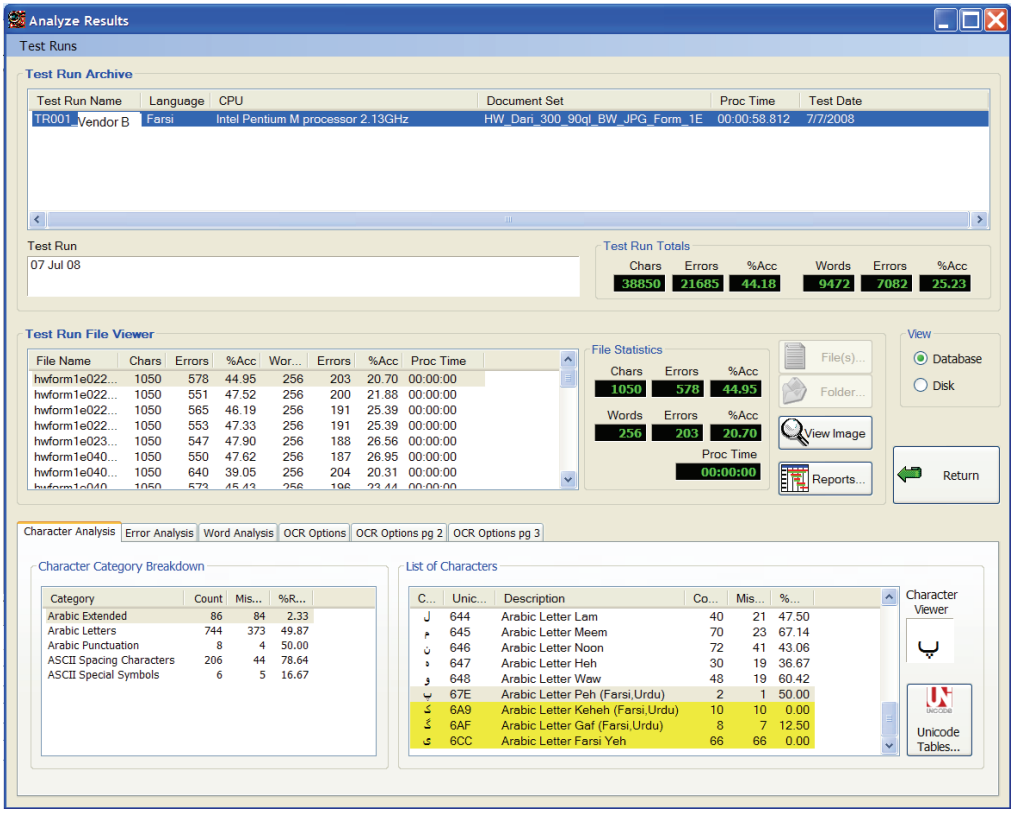

Figure 5. IOTK test run results display.

IOTK's Error Analysis display allows the user to find trends in characters that are misrecognized as other characters in an easy manner. As shown in figures 6 and 7, Vendor A misrecognized the Arabic letter آ (Alef with Madda above) as the letter ا (Alef) while Vendor B misrecognized the same character as the letter چ (Tchech).

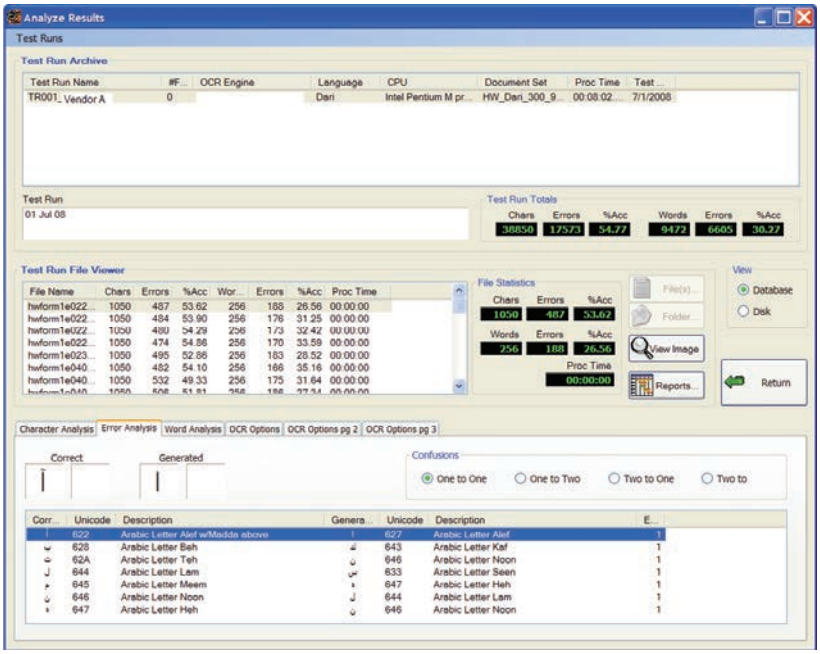

Figure 6. Vendor A error analysis for one image.

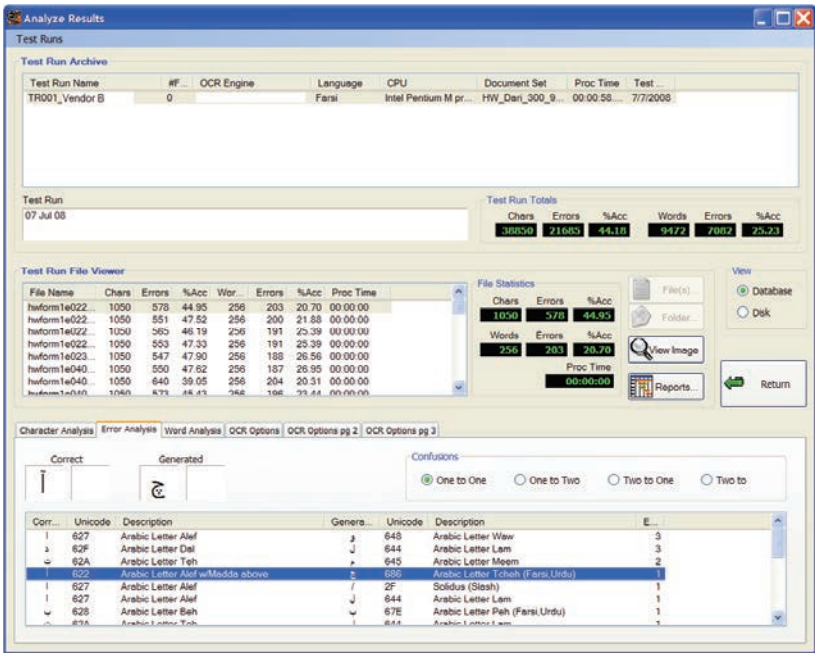

Figure 7. Vendor B error analysis for one image.

Through the use of the interfaces provided, IOTK eliminates the risk of human error when generating accuracy reports and comparisons between multiple OCR engines. It allows for quick retrieval of intermediary results in a visual, easy-to-use way.

Of the accuracy reports generated we noted minor discrepancies in the overall accuracy reported for the same document images. When using the same core method for scoring character accuracy, the manual method, which makes use of the vendor Graphical User Interface (GUI), shows small variances when compared to the vendor OCR technology embedded as an application in IOTK (as seen in table 3). These variances could be the result of small differences in the way the image was processed and recognized by the OCR software engines in their respective interfacing, i.e., page and zone segmentation, or the way the GUI manipulates the results from the technology.

Table 3. Scoring character category comparison.

File name: hwform1e022	Manual Method		IOTK	
Scoring Character Category	Vendor A	Vendor B	Vendor A	Vendor B
ASCII Spacing Characters	70.39%	81.07%	67.48%	78.64%
ASCII Special Symbols	16.67	16.67	16.67	16.67
Arabic Punctuation	50	50	50	50
Arabic Letters	59.68	49.46	59.01	49.87
Arabic Extended Letters	15.12	2.33	8.14	2.33
Total Accuracy	57.81	51.62	56.19	51.43

6. Summary, Conclusions, and Recommendations

The IOTK prototype system successfully provided a test environment for the evaluation and management OCR engine accuracy scoring that is fast and repeatable. This environment greatly reduces the amount of time required to conduct testing and experimentation in different areas of image processing. Through this exercise we have established the utility of having such an automated mechanism, and demonstrated its successful use. IOTK provides a suitable approach to providing new scientific insight through visual methods. It allowed us to develop a large collection of document images and store them in an organized, methodical manner. It also allowed us to retrieve, process, and analyze such a collection against multiple vendors expeditiously.

As experimental digital image processing and recognition algorithms are developed, the IOTK environment can be easily expanded to accommodate experimenting and testing with these algorithms in novel ways. With the use of available computing power, experimental methods, and alternate computational approaches such as those found in reference 7, we can quickly start processing document collections while determining the utility and implications of the approaches for categorization, segmentation, recognition, and retrieval of text information. Potential enhancements to make the system more robust and user friendly include the ability to provide a canvas-like area in which you can drag and drop these new functionalities and generate ad hoc workflows for further interaction studies.

Finally, the environment can benefit from added functionality in the way the raw data is analyzed and reported using common desktop applications such as spreadsheets.

7. References

1. Holland, M.; Schlesiger, C. High-Mobility Machine Translation for a Battlefield Environment. *In Proceedings of NATO/RTO Systems Concepts and Integration Symposium*, Monterey, CA. Hull, Canada: CCG, Inc., 1998, 15/1-3, ISBN 92-837-1006-1.

2. Hernandez, L.; Schlesiger, C. OCR for Collection, Management, and Retrieval of Documents: Development and Trial of a Document Exploitation Suite. *In Proceedings Symposium on Document Image Understanding Technology*, 2003.

3. Russ, J. C. *The Image Processing Handbook* Fourth Edition, 2002, ISBN 0-8493-1142-X.

4. Chen, K.; Jaeger, S.; Zhu, G.; Doermann, D. DOCLIB: A Document Processing Research Tool. *In Proceedings 2005 Symposium on Document Image Understanding Technology*, 2005.

5. Shafait, F.; Adnan-ul-Hasan; Keysers, D.; Breuel, T. M. Layout Analysis of Urdu Document Images. Multitopic Conference, 2006. INMIC '06. *IEEE* **23–24 Dec 2006**, 293–298.

6. Rice, S. V.; Nartker, T. A. *The ISRI Analytic Tools for OCR Evaluation*; ISRI Technical Report TR-96-02, August 1996.

7. Jung, K.; Kim, K. I.; Jain, A. K. Text Information Extraction in Images and Video: A Survey. *In Pattern Recognition Journal* **2004**, *37* (5), 977–997.

Appendix A. Sample of grayscale TIF Collection Form

DROP IN.

HW Form 1E Rec. Station 4 Rec. Session ~~23~~ Province _____

تحلیف عسکری

تحلیف عسکری

بسم اله الرحمن الرحیم

بسم اله الرحمن الرحیم

من فرزند وفا دار مردم افغانستان با شمولیتم در صفوف

من فرزند وفا دار مردم افغانستان با شمولیتم در صفوف

قوای مسلح دولت افغانستان بنام خداوند متعال سوگند یاد

قوای مسلح دولت افغانستان بنام خداوند متعال سوگند یاد

میکنم که یک افسر "سرباز" با دسپلین وفادار به همه

میکنم که یک افسر سرباز با دسپلین وفادار به همه

اصول، قوانین و مقررات دولت اسلامی افغانستان عزیز

اصول، قوانین و مقررات دولت اسلامی افغانستان عزیز

بوده، تمام اوامر و هدایات آمرین و قوماندانان را تحت

بوده، تمام اوامر و هدایات آمرین و قوماندانان را تحت

هر گونه شرایط زمان و مکان به مقصد دفاع از تمامیت

هر گونه شرایط زمان و مکان به مقصد دفاع از تمامیت

ارضی، استقلال ملی و ارزش انقلاب اسلامی نسبت به

ارضی استقلال ملی و ارزش انقلاب اسلامی نسبت به

هر نوع منافع دیگر ترجیح داده حتی از ریختاندن خون

هر نوع منافع دیگر ترجیح داده حتی از ریختاندن خون

خویش در این راه دریغ نمی نمایم. اگر بر خلاف این

خویش در این راه دریغ نمایم اگر بر خلاف این

تحلیف یاد شده عمل نمایم، در آنصورت جزای سخت

تحلیف یاد شده عمل نمایم در آنصورت جزای سخت

Appendix B. Sample of Black and White JPEG Collection Form

DROP IN.

HW Form 1E Rec. Station 4 Rec. Session ~~[illegible]~~ Province _____

تحلیف عسکری

تحلیف عسکری

بسم اله الرحمن الرحیم

بسم اله الرحمن الرحیم

من فرزند وفا دار مردم افغانستان با شمولیتم در صفوف

من فرزند وفا دار مردم افغانستان با شمولیتم در صفوف

قوای مسلح دولت افغانستان بنام خداوند متعال سوگند یاد

قوای مسلح دولت افغانستان بنام خداوند متعال سوگند یاد

میکنم که یک افسر "سرباز" با دسپلین وفادار به همه

میکنم که یک افسر سرباز با دسپلین وفادار به همه

اصول، قوانین و مقررات دولت اسلامی افغانستان عزیز

اصول، قوانین و مقررات دولت اسلامی افغانستان عزیز

بوده، تمام اوامر و هدایات آمرین و قوماندانان را تحت

بوده، تمام اوامر و هدایات آمرین و قوماندانان را تحت

هر گونه شرایط زمان و مکان به مقصد دفاع از تمامیت

هر گونه شرایط زمان و مکان به مقصد دفاع از تمامیت

ارضی، استقلال ملی و ارزش انقلاب اسلامی نسبت به

ارضی، استقلال ملی و ارزش انقلاب اسلامی نسبت به

هر نوع منافع دیگر ترجیح داده حتی از ریختاندن خون

هر نوع منافع دیگر ترجیح داده حتی از ریختاندن خون

خویش در این راه دریغ نمی نمایم. اگر بر خلاف این

خویش در این راه دریغ نمایم اگر بر خلاف این

تحلیف یاد شده عمل نمایم، در آنصورت جزای سخت

تحلیف یاد شده عمل نمایم در آنصورت جزای سخت

Appendix C. Sample Ground-Truth Form

HW Form ____ Rec. Station _____ Rec. Session _____ Province_____

تحلیف عسکری
تحلیف عسکری
بسم اله الرحمن الرحیم
بسم اله الرحمن الرحیم
من فرزند وفا دار مردم افغانستان با شمولیتم در صفوف
من فرزند وفا دار مردم افغانستان با شمولیتم در صفوف
قوای مسلح دولت افغانستان بنام خداوند متعال سوگند یاد
قوای مسلح دولت افغانستان بنام خداوند متعال سوگند یاد
میکنم که یک افسر "سرباز" با دسپلین وفادار به همه
میکنم که یک افسر "سرباز" با دسپلین وفادار به همه
اصول، قوانین و مقررات دولت اسلامی افغانستان عزیز
اصول، قوانین و مقررات دولت اسلامی افغانستان عزیز
بوده، تمام اوامر و هدایات آمرین و قوماندانان را تحت
بوده، تمام اوامر و هدایات آمرین و قوماندانان را تحت
هر گونه شرایط زمان و مکان به مقصد دفاع از تمامیت
هر گونه شرایط زمان و مکان به مقصد دفاع از تمامیت
ارضی، استقلال ملی و ارزش انقلاب اسلامی نسبت به
ارضی، استقلال ملی و ارزش انقلاب اسلامی نسبت به
هر نوع منافع دیگر ترجیح داده حتی از ریختاندن خون
هر نوع منافع دیگر ترجیح داده حتی از ریختاندن خون
خویش در این راه دریغ نمی نمایم. اگر بر خلاف این
خویش در این راه دریغ نمی نمایم. اگر بر خلاف این
تحلیف یاد شده عمل نمایم، در آنصورت جزای سخت
تحلیف یاد شده عمل نمایم، در آنصورت جزای سخت

INTENTIONALLY LEFT BLANK.

Appendix D. Generated Data Sets

Format	Image Type	Resolution	Quality Level	Document Type	Image Count	Test Run Number
Grayscale	TIF	100	N/A	Form 1E	37	1
Grayscale	TIF	100	N/A	Form 2E	39	2
Grayscale	TIF	100	N/A	Form 3E	43	3
Grayscale	TIF	100	N/A	Form 4E	47	4
Black & White	TIF	100	N/A	Form 1E	37	5
Black & White	TIF	100	N/A	Form 2E	39	6
Black & White	TIF	100	N/A	Form 3E	43	7
Black & White	TIF	100	N/A	Form 4E	47	8
Grayscale	TIF	200	N/A	Form 1E	37	9
Grayscale	TIF	200	N/A	Form 2E	39	10
Grayscale	TIF	200	N/A	Form 3E	43	11
Grayscale	TIF	200	N/A	Form 4E	47	12
Black & White	TIF	200	N/A	Form 1E	37	13
Black & White	TIF	200	N/A	Form 2E	39	14
Black & White	TIF	200	N/A	Form 3E	43	15
Black & White	TIF	200	N/A	Form 4E	47	16
Grayscale	TIF	300	N/A	Form 1E	37	17
Grayscale	TIF	300	N/A	Form 2E	39	18
Grayscale	TIF	300	N/A	Form 3E	43	19
Grayscale	TIF	300	N/A	Form 4E	47	20
Black & White	TIF	300	N/A	Form 1E	37	21
Black & White	TIF	300	N/A	Form 2E	39	22
Black & White	TIF	300	N/A	Form 3E	43	23
Black & White	TIF	300	N/A	Form 4E	47	24
Black & White	JPG	400	100	Form 1E	37	25
Black & White	JPG	400	100	Form 2E	39	26
Black & White	JPG	400	100	Form 3E	43	27
Black & White	JPG	400	100	Form 4E	47	28
Black & White	JPG	300	90	Form 1E	37	29
Black & White	JPG	300	90	Form 2E	39	30
Black & White	JPG	300	90	Form 3E	43	31
Black & White	JPG	300	90	Form 4E	47	32
Black & White	JPG	300	80	Form 1E	37	33
Black & White	JPG	300	80	Form 2E	39	34
Black & White	JPG	300	80	Form 3E	43	35
Black & White	JPG	300	80	Form 4E	47	36
Black & White	JPG	300	70	Form 1E	37	37
Black & White	JPG	300	70	Form 2E	39	38
Black & White	JPG	300	70	Form 3E	43	39
Black & White	JPG	300	70	Form 4E	47	40
Black & White	JPG	300	60	Form 1E	37	41
Black & White	JPG	300	60	Form 2E	39	42
Black & White	JPG	300	60	Form 3E	43	43
Black & White	JPG	300	60	Form 4E	47	44
Totals					1826	44

INTENTIONALLY LEFT BLANK.

Appendix E. Sample Manual Accuracy Report

```
DOD Accuracy Report v5.3 -- INTERNAL USE ONLY --
--------------------------------------------------
    1050   Characters
     524   Errors
   50.10%  Accuracy

       0   Reject Characters
       0   Suspect Markers
       0   False Marks
    0.00%  Characters Marked
   50.10%  Accuracy After Correction

     Ins    Subst      Del   Errors
       0        0        0        0   Marked
      51      329      144      524   Unmarked
      51      329      144      524   Total

   Count   Missed   %Right
     206       28    86.41   ASCII Spacing Characters
       6        5    16.67   ASCII Special Symbols
       8        3    62.50   Arabic Punctuation
     744      260    65.05   Arabic Letters
      86       84     2.33   Arabic Extended
    1050      380    63.81   Total

  Errors   Marked   Correct-Generated : ALL Confusions
      37        0   {}-{ <062D> <062B>!574 ...}
      23        0   {<06CC>}-{<064A>}
      20        0   {}-{<0648><0644> <0647> ...}
      16        0   {<0633><06A9><0631>...}-{<0649> <0623> <0648>...}
      15        0   {<0633><0648><06AF>...}-{<0644><0647><0645>!...}
      11        0   {<062A>}-{<064A>&lt;0631&gt;! !<0621>...}
      10        0   {<06CC>}-{<0649>}
       9        0   {}-{<0642>!<0644><064A>...}
       9        0   {<0628><0627> <062F>...}-{<0645><0625><0631>...}
       9        0   {<0645><0642><0635>...}-{<0639><0641><0645>...}
       9        0   {<06CC><06A9>}-{<0644><0643><0644>...}
       8        0   {<0648><0631><062A> ...}-{<0647> <0635>!<0625>...}
       7        0   {<0627><06CC><0646> ...}-{<0647><064A><0623>!.}
       7        0   {<062E><0648><06CC>...}-{<0635><0649> <062B>...}
       7        0   {<0644><0627><0641> ...}-{! <0623><062C><0645>...}
       7        0   {<0646><062F><0646> ...}-{<062B><0648><062A>...}
       6        0   { <062A><0631><062C>...}-{<06AF><062C><0649>...}
       6        0   {<0627><0648>}-{<0623> <0641><0649> ...}
       6        0   {<0642><0648><0627>...}-{<0645><0637> <0633>...}
       5        0   { <06AF><0648><0646>...}-{<0641><0645>}
       5        0   {}-{ }
```

```
5        0   {<0627><0631><0632>...}-{" <0641><0626>!}
5        0   {<0627><0646><0642>...}-{<0641><062A>! }
5        0   {<062F><0627><062F>...}-{<0647><0647> <0633>...}
5        0   {<062F><0631> <0622>...}-{<0646><0635><0648>! }
5        0   {<0639><0632><06CC>...}-{<0645><0645>!<064A>...}
5        0   {<0641><0631><0632>...}-{!<0646><0645><0644>...}
5        0   {<0645><0631><062F>}-{<0633> !<0698> }

4        0   { <0628><0631> }-{<062E>!<061F>}
4        0   {. <0627><06AF>}-{<0633><0648><0628>}
4        0   {<0627><0632> <062A>}-{<0621><0644><0623>...}
4        0   {<0627><0641><0633>...}-{<0623> <0636><0698>}
4        0   {<0628><0627><0632>"}-{<060C> <0631>:}
4        0   {<062A><062D><0644>...}-{<0646><0641><0628>...}
4        0   {<062F><0631><06CC>...}-{!<0633>}
4        0   {<062F><0648>}-{<0631><0641><0649> }
4        0   {<062F><06CC><06AF>}-{<0631><0648><0626>...}
4        0   {<0631><06CC><0646> }-{<0648><062A>}
4        0   {<0644><0627>}-{<062D>}
4        0   {<0645><0644><06CC>}-{<0641><0649> !}
4        0   {<0645><06CC> <0627>}-{ <0648><0648>}
4        0   {<0646><0645><06CC> }-{<0641><064A>}
4        0   {<0647><062F><0627>...}-{<0645><0624> <064A>}
4        0   {<0647><0631> }-{<0635> <0644><0648>}
4        0   {<0648>}-{ <0627><060C> }
3        0   { <0642><0648>}-{<0631>}
3        0   { <0648> }-{<0627><0621><062A>}
3        0   {"}-{<0627> <0627>}
3        0   {<0627><0644><0647>}-{<0623><062F>}
3        0   {<062A><062D><062A>}-{<062E><0643>}
3        0   {<062A><0639><0627>}-{<062B><0646><0645>}
3        0   {<062D><062A><06CC>}-{<0644><0645>}
3        0   {<062D><06CC><0645>}-{<062C><0645>!}
3        0   {<062F><0627>}-{<0644><0623><0625>}
3        0   {<062F><0627><0631>}-{<0631><0631><0635>}
3        0   {<062F><0631> }-{<0621><0647>}
3        0   {<0631><0627><062A>}-{!<060C><060C>}
3        0   {<0631><0627><06CC>}-{!!}
3        0   {<0634>}-{!<062A><0646>}
3        0   {<0636><06CC><060C>}-{<0635><0642>}
3        0   {<063A><0627>}-{<0638> <0645>}
3        0   {<0642><0644><0627>}-{<0638>! }
3        0   {<0642><0648>}-{<0626>! }
3        0   {<0645> }-{<062D><0644><0627>}
3        0   {<0645><06CC> }-{<0649> <0647>}
3        0   {<0647>}-{}
3        0   {<0648><0641><0627>}-{!}
3        0   {<06A9>}-{<0643>}
3        0   {<06CC><0627><062F>}-{<0628><0625><060C>}
3        0   {<06CC><062A><0645>}-{<064A><0646><0646>}
2        0   { <0648>}-{!}
2        0   {}-{<\n><0628>}
```

```
2        0   {}-{<0627> }
2        0   {}-{<0645>}
2        0   {<0622>}-{<0623>!}
2        0   {<0627><0632>}-{<0647><0621>}
2        0   {<0627><0644>}-{<0623>}
2        0   {<0627><0646>}-{<0623><0642>}
2        0   {<0628><0633>}-{<067E><0645>}
2        0   {<0628><0647>}-{<0645><0649>}
2        0   {<062A>}-{<062B>}

2        0   {<062A><0645>}-{<0647><0626>}
2        0   {<062F>}-{<060C> }
2        0   {<062F>}-{<0644><0649>}
2        0   {<062F><0648>}-{}
2        0   {<0631><0627>}-{!<0647>}
2        0   {<0632>}-{<0698> }
2        0   {<0633>}-{<0645><062D>}
2        0   {<0633><0628>}-{!<064A>}
2        0   {<0633><062A>}-{<0635>}
2        0   {<0633><062A>}-{<0646>}
2        0   {<0633><062E>}-{<0644><0647>}
2        0   {<0633><0644>}-{<0639><0645>}
2        0   {<0635><0648>}-{<0639>!}
2        0   {<0639><0645>}-{<0643>}
2        0   {<0644><0627>}-{<0643>}
2        0   {<0645>}-{<0647>}
2        0   {<0645><0646>}-{<0633>}
2        0   {<0645><0646>}-{<0642>}
2        0   {<0646>}-{<062B>}
2        0   {<0646><0645>}-{<0626>}
2        0   {<0647>}-{<0635><062A>}
2        0   {<0648><0641>}-{<0631><0646>}
2        0   {<06A9><0627>}-{<0623>}
2        0   {<06A9><0647>}-{<0630>}
2        0   {<06AF><0646>}-{<0643><0644>}
2        0   {<06CC>}-{ <064A>}
2        0   {<06CC>}-{<0627><064A>}
2        0   {<06CC><0641>}-{ <0637>}
2        0   {<06CC><06A9>}-{<0644><062A>}
2        0   {<06CC><06A9>}-{<064A><0643>}
1        0   { }-{}
1        0   {"}-{<0627>}
1        0   {"}-{<064A>}
1        0   {}-{-}
1        0   {}-{<062B>}
1        0   {}-{<0639>}
1        0   {}-{<0646>}
1        0   {}-{<0649>}
1        0   {<060C>}-{!}
1        0   {<060C>}-{<0621>}
1        0   {<0628>}-{<067E>}
1        0   {<062F>}-{<0644>}
```

```
     1        0   {<062F>}-{<0646>}
     1        0   {<0631>}-{<061D>}
     1        0   {<0632>}-{<0630>}
     1        0   {<0633>}-{}
     1        0   {<063A>}-{<0641>}
     1        0   {<063A>}-{<0646>}
     1        0   {<0642>}-{}
     1        0   {<0644>}-{}
     1        0   {<0645>}-{!}
     1        0   {<0645>}-{}
     1        0   {<0645>}-{<0639>}

     1        0   {<0646>}-{<0642>}
     1        0   {<0647>}-{<060C>}
     1        0   {<0647>}-{<0649>}
     1        0   {<0648>}-{ }
     1        0   {<0648>}-{!}
     1        0   {<0648>}-{"}
     1        0   {<067E>}-{<0644>}
     1        0   {<06AF>}-{<0643>}
     1        0   {<06CC>}-{<0644>}

Errors   Marked   Correct-Generated : ONE to one confusions
     2        0   {<062A>}-{<062B>}
     2        0   {<0645>}-{<0647>}
     2        0   {<0646>}-{<062B>}
     1        0   {<0628>}-{<067E>}
     1        0   {<062F>}-{<0644>}
     1        0   {<062F>}-{<0646>}
     1        0   {<0631>}-{<061D>}
     1        0   {<0632>}-{<0630>}
     1        0   {<063A>}-{<0641>}
     1        0   {<063A>}-{<0646>}
     1        0   {<0645>}-{!}
     1        0   {<0645>}-{<0639>}
     1        0   {<0646>}-{<0642>}
     1        0   {<0647>}-{<060C>}
     1        0   {<0647>}-{<0649>}
     1        0   {<0648>}-{ }
     1        0   {<0648>}-{!}
     1        0   {<0648>}-{"}

Errors   Marked   Correct-Generated : ONE to two confusions
     2        0   {<0622>}-{<0623>!}
     2        0   {<062F>}-{<060C> }
     2        0   {<062F>}-{<0644><0649>}
     2        0   {<0632>}-{<0698> }
     2        0   {<0633>}-{<0645><062D>}
     2        0   {<0647>}-{<0635><062A>}
```

```
Errors   Marked   Correct-Generated : TWO to one confusions
     4        0   {<0644><0627>}-{<062D>}
     2        0   {<0627><0644>}-{<0623>}
     2        0   {<0633><062A>}-{<0635>}
     2        0   {<0633><062A>}-{<0646>}
     2        0   {<0639><0645>}-{<0643>}
     2        0   {<0644><0627>}-{<0643>}
     2        0   {<0645><0646>}-{<0633>}
     2        0   {<0645><0646>}-{<0642>}
     2        0   {<0646><0645>}-{<0626>}

Errors   Marked   Correct-Generated : TWO to two confusions
     2        0   {<0627><0632>}-{<0647><0621>}
     2        0   {<0627><0646>}-{<0623><0642>}
     2        0   {<0628><0633>}-{<067E><0645>}

     2        0   {<0628><0647>}-{<0645><0649>}
     2        0   {<062A><0645>}-{<0647><0626>}
     2        0   {<0631><0627>}-{!<0647>}
     2        0   {<0633><0628>}-{!<064A>}
     2        0   {<0633><062E>}-{<0644><0647>}
     2        0   {<0633><0644>}-{<0639><0645>}
     2        0   {<0635><0648>}-{<0639>!}
     2        0   {<0648><0641>}-{<0631><0646>}

Errors   Marked   Correct-Generated : SINGLE Confusions
     4        0   {<0645>}-{<0647> | ! | <0639>}
     3        0   {<0646>}-{<062B> | <0642>}
     3        0   {<0648>}-{  | ! | "}
     2        0   {<062A>}-{<062B>}
     2        0   {<062F>}-{<0644> | <0646>}
     2        0   {<063A>}-{<0641> | <0646>}
     2        0   {<0647>}-{<060C> | <0649>}
     1        0   {<0628>}-{<067E>}
     1        0   {<0631>}-{<061D>}
     1        0   {<0632>}-{<0630>}

 Count   Missed   %Right
    24        1    95.83   {<\n>}
   182       27    85.16   { }
     4        4     0.00   {"}
     2        1    50.00   {.}
     8        3    62.50   {<060C>}
     4        2    50.00   {<0622>}
   132       38    71.21   {<0627>}
    24        7    70.83   {<0628>}
    46       16    65.22   {<062A>}
     4        2    50.00   {<062C>}
    16        5    68.75   {<062D>}
    12        3    75.00   {<062E>}
    52       25    51.92   {<062F>}
    60       20    66.67   {<0631>}
```

```
18       10    44.44   {<0632>}
30       12    60.00   {<0633>}
10        3    70.00   {<0634>}
 8        2    75.00   {<0635>}
 2        1    50.00   {<0636>}
 2        0   100.00   {<0637>}
14        4    71.43   {<0639>}
 8        4    50.00   {<063A>}
28        7    75.00   {<0641>}
14        7    50.00   {<0642>}
40       13    67.50   {<0644>}
70       21    70.00   {<0645>}
72       24    66.67   {<0646>}
30       14    53.33   {<0647>}
48       20    58.33   {<0648>}
 2        2     0.00   {<067E>}
10       10     0.00   {<06A9>}

8        6     25.00   {<06AF>}
66       66     0.00   {<06CC>}
```

Appendix F. Sample IOTK Accuracy Report

IOTK Accuracy Report (7/8/2008 2:13 PM)

Test Run Name: TR001_Vendor A
OCR Engine: Vendor A

Language:	Dari
CPU:	Intel Pentium M processor 2.13GHz
Document Set:	HW_Dari_300_90ql_BW_JPG_Form_1E
Process Time:	08:02.8
Test Date:	7/1/2008
Remarks:	1-Jul-08

Files Processed: 37 files

hwform1e0222score.txt	hwform1e0429score.txt
hwform1e0223score.txt	hwform1e0430score.txt
hwform1e0225score.txt	hwform1e0431score.txt
hwform1e0226score.txt	hwform1e0432score.txt
hwform1e0233score.txt	hwform1e0433score.txt
hwform1e0401score.txt	hwform1e0434score.txt
hwform1e0402score.txt	hwform1e0435score.txt
hwform1e0403score.txt	hwform1e0436score.txt
hwform1e0404score.txt	hwform1e0437score.txt
hwform1e0405score.txt	hwform1e0438score.txt
hwform1e0406score.txt	hwform1e0445score.txt
hwform1e0407score.txt	hwform1e0446score.txt
hwform1e0408score.txt	hwform1e0447score.txt
hwform1e0409score.txt	hwform1e0448score.txt
hwform1e0410score.txt	hwform1e0449score.txt
hwform1e0411score.txt	hwform1e04dropinscore.txt
hwform1e0412score.txt	hwform1e04extrascore.txt
hwform1e0413score.txt	hwform1e04rescheduledscore.txt
hwform1e0414score.txt	

Cumulative Accuracy

Characters:	38850
Errors:	17573
Accuracy:	54.77
Words:	9472
Errors:	6605
Accuracy:	30.27
Process Time:	0:00:00

Character Category Breakdown

Category	Count	Missed	%Right
ASCII Spacing Characters	7622	2001	73.75
ASCII Special Symbols	222	177	20.27
Arabic Punctuation	296	135	54.39
Arabic Letters	27528	10927	60.31
Arabic Extended	3182	2866	9.93

Total List of Characters

Character	Unicode	Count	Missed	%Right	Description
	D	888	126	85.81	Carriage Return
	20	6734	1875	72.16	Space
"	22	148	146	1.35	Quotation Mark
.	2E	74	31	58.11	Full Stop (Period)
،	60C	296	135	54.39	Arabic Comma
آ	622	148	72	51.35	Arabic Letter Alef w/Madda above
ا	627	4884	1418	70.97	Arabic Letter Alef
ب	628	888	413	53.49	Arabic Letter Beh
ت	62A	1702	704	58.64	Arabic Letter Teh
ج	62C	148	71	52.03	Arabic Letter Jeem
ح	62D	592	310	47.64	Arabic Letter Hah
خ	62E	444	213	52.03	Arabic Letter Khah
د	62F	1924	770	59.98	Arabic Letter Dal
ر	631	2220	678	69.46	Arabic Letter Reh
ز	632	666	289	56.61	Arabic Letter Zain
س	633	1110	526	52.61	Arabic Letter Seen
ش	634	370	181	51.08	Arabic Letter Sheen
ص	635	296	142	52.03	Arabic Letter Sad
ض	636	74	37	50.00	Arabic Letter Dad
ط	637	74	37	50.00	Arabic Letter Tah
ع	639	518	259	50.00	Arabic Letter Ain
غ	63A	296	147	50.34	Arabic Letter Ghain
ف	641	1036	519	49.90	Arabic Letter Feh
ق	642	518	240	53.67	Arabic Letter Qaf
ل	644	1480	620	58.11	Arabic Letter Lam
م	645	2590	1044	59.69	Arabic Letter Meem
ن	646	2664	1044	60.81	Arabic Letter Noon
ه	647	1110	512	53.87	Arabic Letter Heh
و	648	1776	681	61.66	Arabic Letter Waw
پ	67E	74	39	47.30	Arabic Letter Peh (Farsi,Urdu)
ک	6A9	370	370	0.00	Arabic Letter Keheh (Farsi,Urdu)
گ	6AF	296	142	52.03	Arabic Letter Gaf (Farsi,Urdu)
ی	6CC	2442	2315	5.20	Arabic Letter Farsi Yeh

One to One & One to Two Confusions

Correct	Unicode	Generated	Unicode	Errors
آ	622	ا	627	3
آ	622	ب , ا	628 , 627	2
آ	622	ا , '	627 , 27	2
ا	627		20	5
ا	627	ل	644	5
ا	627	و	648	3
ا	627	د	62F	2
ا	627	م	645	2
ا	627	(	28	2
ا	627	س	633	1
ا	627	ر	631	1
ا	627	ي	64A	1
ا	627	ت	62A	1
ا	627	١	6F1	1
ا	627	ص	635	1
ا	627	ك	643	1
ا	627		27	1
ا	627	آ	622	1
ا	627	ث , ح	62A , 62D	6
ا	627	١ ,	6F1 , 20	4
ا	627	. ,	2E , 20	2
ا	627	(,	28 , 20	2
ا	627	ه ,	647 , 20	2
ا	627	ل , و	644 , 648	2
ا	627	و , م	648 , 645	2
ب	628	م	645	5
ب	628	ن	646	4
ب	628	ي	64A	4
ب	628	پ	67E	4
ب	628	ل	644	2
ب	628	ك	643	1
ب	628	ف	641	1
ب	628	‘	2018	1
ب	628	ج	62C	1
ب	628	ى	649	1
ب	628	ا	627	1
ب	628	ه	647	1
ب	628	خ	62E	1
ب	628	ر	631	1
ب	628	ت	62A	1
ب	628	.	2E	1
ب	628	ز , ا	632 , 627	2
ب	628	, -	6D4 , 20	2
ب	628	. , ل	2E , 644	2

ر	631	ل	644	4
ر	631	(	28	2
ر	631	ب	628	2
ر	631	د	62F	1
ر	631	م	645	1
ر	631	.	2E	1
ر	631	ن	646	1
ر	631	گ	6AF	1
ر	631	,	2C	1
ر	631	ي	64A	1
ر	631	د ,	20 , 62F	2
ز	632	ر	631	3
ز	632	(	28	1
ز	632	ا , .	627 , 2E	2
س	633	م	645	3
س	633	ح	62D	1
س	633	د	62F	1
س	633	خ	62E	1
س	633	ن	646	1
س	633	ي	64A	1
س	633	ئ	626	1
س	633		20	1
س	633	ش	634	1
س	633	ن , ق	646 , 642	2
س	633	م , ح	645 , 62D	2
س	633	م , ه	645 , 647	2
ش	634	ا	627	2
ش	634	/	2F	1
ش	634	(	28	1
ش	634	ت	62A	1
ش	634	ق	642	1
ش	634	ن	646	1
ش	634	م , ك	645 , 643	2
ش	634	, ٠	20 , 6F0	2
ص	635	م	645	2
ص	635	ل	644	1
ص	635	گ	6AF	1
ص	635	غ	63A	1
ص	635	ه	647	1
ص	635	م , ن	645 , 646	2
ص	635	۶ ,	6F6 , 20	2
ص	635	, ت	20 , 62A	2
ص	635	, ل	20 , 644	2
ض	636	ن	646	1
ع	639	ر	631	2
ع	639	ج	62C	1
ع	639	ك	643	1
ع	639	، , ر	631 , 60C	2
ف	641	ق	642	6

ف	641	ن	646	6
ف	641	ر	631	3
ف	641	ك	643	2
ف	641	)	29	1
ف	641	ت	62A	1
ف	641	د	62F	1
ف	641	ل	644	1
ف	641	ب	628	1
ف	641	ع , ك	639 , 643	2
ف	641	خ , و	62E , 648	2
ف	641	ع , ن	639 , 646	2
ف	641	ض , ى	636 , 649	2
ف	641	ن , ى	646 , 649	2
ق	642	ت	62A	5
ق	642	ز	632	2
ق	642	ف	641	2
ق	642	ا	627	2
ق	642	ط	637	1
ق	642	م	645	1
ق	642	ه	647	1
ق	642	ز , ا	632 , 627	2
ل	644	ن	646	5
ل	644	س	633	1
ل	644		20	1
ل	644	(	28	1
ل	644	ر	631	1
ل	644	م , ك	645 , 643	2
ل	644	ز , ،	632 , 60C	2
ل	644	م ,	645 , 20	2
م	645	)	29	8
م	645	ي	64A	5
م	645	ه	647	3
م	645	ع	639	3
م	645	ل	644	3
م	645	ت	62A	3
م	645	د	62F	2
م	645	ك	643	2
م	645	ا	627	1
م	645	ر	631	1
م	645	ه	665	1
م	645	ح	62D	1
م	645	ئ	626	1
م	645	ق	642	1
م	645	ش	634	1
م	645	ن	646	1
م	645	ف	641	1
م	645	ا , ل	627 , 644	6
م	645	ت , ر	62A , 631	2
م	645	س , ر	633 , 631	2

م	645	د ,	62F , D	2
م	645	ا , ا	627 , 627	2
م	645	ل , س	644 , 633	2
م	645	/ ,	2F , 20	2
ن	646	ت	62A	17
ن	646		20	5
ن	646	ر	631	5
ن	646	م	645	4
ن	646	ل	644	2
ن	646	د	62F	2
ن	646	ا	627	2
ن	646	ں	6BA	2
ن	646	ه	665	1
ن	646	ى	649	1
ن	646	ش	634	1
ن	646	ي	64A	1
ن	646	o	6F	1
ن	646	ه	647	1
ن	646		D	1
ن	646	ل , ا	644 , 627	4
ن	646	ي ,	27 , 64A	4
ن	646	ل , ت	644 , 62A	2
ن	646	.ب ,	2E , 628	2
ن	646	ي , ز	64A , 632	2
ه	647	م	645	4
ه	647	ر	631	4
ه	647	ن	646	3
ه	647	ك	643	3
ه	647	ت	62A	2
ه	647	س	633	2
ه	647	ح	62D	1
ه	647	د	62F	1
ه	647	(	28	1
ه	647	ي	6D0	1
ه	647	ب	628	1
ه	647	ا	627	1
ه	647	ج	62C	1
ه	647	ه	6C1	1
ه	647	.	2E	1
ه	647	ي , ف	64A , 641	10
ه	647	م ,	20 , 645	2
و	648	ر	631	17
و	648	د	62F	13
و	648	(	28	2
و	648	ك	643	2
و	648	ن	646	2
و	648	ا	627	2
و	648	ح	62D	1
و	648	ه	647	1

و	648	«	AB	1
و	648		D	1
و	648	،	60C	1
و	648		20	1
و	648	ع	639	1
و	648	آ	622	1
و	648	ب	628	1
و	648	_	5F	1
و	648	د ,	62F , 20	4
و	648	, ،	60C , 20	2
و	648	ل , ت	644 , 62A	2
و	648	ر , ا	631 , 627	2
ت	62A	ن	646	6
ت	62A	ا	627	3
ت	62A	ر	631	2
ت	62A	ي	64A	2
ت	62A	د	62F	1
ت	62A	ث	62B	1
ت	62A	ك	643	1
ت	62A	)	29	1
ت	62A	م	645	1
ت	62A	ب , ن	628 , 646	2
ت	62A	ن , ن	646 , 646	2
ج	62C	گ	6AF	1
ح	62D	خ	62E	1
ح	62D	ك	643	1
ح	62D	ر	631	1
ح	62D	ا	627	1
ح	62D	س	633	1
ح	62D	ن	646	1
خ	62E	ف	641	3
خ	62E	ا	627	2
خ	62E	غ	63A	1
خ	62E	ت	62A	1
خ	62E	ح	62D	1
د	62F	ر	631	20
د	62F	ن	646	4
د	62F	ل	644	3
د	62F	ح	62D	3
د	62F	(	28	3
د	62F		20	2
د	62F	م	645	2
د	62F	ذ	630	2
د	62F	خ	62E	1
د	62F	ا	627	1
د	62F	گ	6AF	1
د	62F	ز	632	1
د	62F	ں	6BA	1
د	62F	ا , م	627 , 645	2

د	62F	ى ,	649 , 20	2
د	62F	ت ,	20 , 62A	2
د	62F	‘ ,	20 , 2018	2
د	62F	ر ,	20 , 631	2
غ	63A	ن	646	2
غ	63A	ع	639	1

Two to One & Two to Two Confusions

Correct	Unicode	Generated	Unicode	Errors
آ , م	622 , 645	ح	62D	2
ا , ب	627 , 628	(, و	648 , 29	2
ا , ر	627 , 631	م	645	2
ا , ر	627 , 631	م ,	D , 645	2
ا , ز	627 , 632	-	2D	2
ا , ز	627 , 632	م , م	645 , 645	2
ا , ز	627 , 632	s , i	73 , 69	2
ا , ز	627 , 632	ر , و	648 , 631	2
ا , ز	627 , 632	/ , ر	631 , 2F	2
ا , س	627 , 633	م	645	2
ا , س	627 , 633	ي , د	62F , 64A	2
ا , س	627 , 633	م , ك	643 , 645	2
ا , ف	627 , 641	ق	642	2
ا , ل	627 , 644	, ر	631 , 20	2
ا , ل	627 , 644	١ ,	6F1 , 20	2
ا , م	627 , 645	ر	631	4
ا , م	627 , 645	.	2E	2
ا , م	627 , 645	ى , ر	631 , 649	2
ا , ن	627 , 646	ر	631	4
ا , ه	627 , 647	ت , ر	631 , 62A	2
ا , و	627 , 648	) ,	29 , 20	2
ا , و	627 , 648	ر , ل	644 , 631	2
ب , ا	628 , 627	د	62F	4
ب , ا	628 , 627	.	2E	2
ب , ا	628 , 627	،	60C	2
ب , ت	628 , 62A	ه	647	2
ب , ر	628 , 631	- , و	2D , 648	2
ب , س	628 , 633	ج	62C	2
ب , س	628 , 633	م	645	2
ب , س	628 , 633	ر , س	633 , 631	2
ب , س	628 , 633	, ه	647 , 20	2
ب , ن	628 , 646	م	645	2
ب , ن	628 , 646	ي	64A	2
ب , ن	628 , 646	ع	639	2
ب , ن	628 , 646	(	28	2
ب , ن	628 , 646	ش	634	2
ب , ن	628 , 646	ي , ن	646 , 64A	4
ب , ن	628 , 646	م , ت	62A , 645	2

ه , ب	628 , 647	م	645	4
ه , ب	628 , 647	ر	631	4
ه , ب	628 , 647	ا	627	4
ه , ب	628 , 647	»	BB	2
ه , ب	628 , 647		27	2
ه , ب	628 , 647	ن	646	2
ه , ب	628 , 647	t	74	2
ه , ب	628 , 647	د	62F	2
ه , ب	628 , 647	٠	6F0	2
ه , ب	628 , 647	م , س	633 , 645	2
ه , ب	628 , 647	ا , ن	646 , 627	2
ه , ب	628 , 647	ى , ر	631 , 649	2

ب , ه	628 , 647	(, ے	28 , 6D2	2
ب , ه	628 , 647	ا , ي	64A , 627	2
ب , و	628 , 648	ك , ر	643 , 631	4
ب , و	628 , 648	د , ر	62F , 631	2
ب , و	628 , 648	ا , د	627 , 62F	2
ت , ح	62A , 62D	ش	634	2
ت , ح	62A , 62D	و	648	2
ت , ح	62A , 62D	ك	643	2
ت , ح	62A , 62D	گ	6AF	2
ت , ح	62A , 62D	ز	632	2
ت , ا	62A , 627	و , ي	648 , 64A	2
ت , ع	62A , 639	ك	643	2
ت , ق	62A , 642	ا , ا	627 , 627	2
ت , م	62A , 645	ع	639	4
ت , م	62A , 645	ك	643	4
ت , م	62A , 645	ل	644	2
ت , م	62A , 645	و	648	2
ت , م	62A , 645	ا , د	627 , 62F	2
ت , م	62A , 645	ا , ر	627 , 631	2
ت , م	62A , 645	ك , ا	643 , 627	2
ت , م	62A , 645	ل , و	644 , 648	2
ج , ز	62C , 632	ر	631	2
ج , ز	62C , 632	د	62F	2
ج , ز	62C , 632	ك , ل	643 , 644	2
ج , ز	62C , 632	ع , ر	639 , 631	2
ح , ت	62D , 62A	ا	627	2
ح , م	62D , 645	ش	634	2
ح , م	62D , 645	د	62F	2
ح , م	62D , 645	ه	647	2
خ , د	62E , 62F	ع	639	2
خ , د	62E , 62F	ن	646	2
خ , د	62E , 62F	ف , ر	641 , 631	2
خ , د	62E , 62F	م , ر	645 , 631	2
خ , د	62E , 62F	ه , ر	647 , 631	2
خ , ل	62E , 644	ك	643	2
خ , و	62E , 648	ا , د	627 , 62F	2
د , ا	62F , 627	ك	643	2
د , ا	62F , 627	ت	62A	2

د , ا	62F , 627	ا , ل	627 , 644	2
د , ر	62F , 631	ا	627	2
د , ر	62F , 631	c	63	2
د , ر	62F , 631	و	648	2
د , ر	62F , 631	ر , م	631 , 645	2
د , ر	62F , 631	H , w	48 , 77	2
د , ف	62F , 641	ت	62A	2
د , ف	62F , 641	ا	627	2
د , ف	62F , 641	ل	644	2
د , ف	62F , 641	ن	646	2
د , ف	62F , 641	١ ,	6F1 , 20	2
د , م	62F , 645	(, ر	631 , 29	2
د , ه	62F , 647	ا	627	2
د , ه	62F , 647	- , ر	631 , 2D	2
د , ه	62F , 647	. , ر	631 , 2E	2
د , و	62F , 648	, ر	631 , 20	2
د , و	62F , 648	ر , س	631 , 633	2
د , و	62F , 648	ا , س	627 , 633	2
ز , ش	632 , 634	)	29	2
ز , ش	632 , 634	م	645	2
ز , ش	632 , 634	/	2F	2
ز , ش	632 , 634	١	6F1	2
ز , ش	632 , 634	ن , ه	646 , 647	2
ز , ش	632 , 634	و , ر	648 , 631	2
ز , ش	632 , 634	, .	D , 2E	2
ز , ش	632 , 634	ي , د	64A , 62F	2
ز , م	632 , 645	ش	634	2
ز , م	632 , 645	«	AB	2
ز , م	632 , 645	ج	62C	2
ز , م	632 , 645	ن	646	2
ز , م	632 , 645	ب , ي	628 , 64A	2
س , ت	633 , 62A	ر	631	2
س , ت	633 , 62A	ش	634	2
س , ت	633 , 62A	م	645	2
س , ت	633 , 62A	ي	64A	2
س , ل	633 , 644	م	645	4
س , ل	633 , 644	غ	63A	2
س , ل	633 , 644	ر	631	2
س , ل	633 , 644		20	2
س , ل	633 , 644	د	62F	2
س , ل	633 , 644	م , ت	645 , 62A	2
س , ل	633 , 644	, ت	27 , 62A	2

س , م	633 , 645	م , !	645 , 21	2
ش , ر	634 , 631	م	645	2
ش , ر	634 , 631	د	62F	2
ش , ر	634 , 631	ر , س	631 , 633	2
ش , ر	634 , 631	ح , د	62D , 62F	2
ش , م	634 , 645	خ	62E	2
ش , م	634 , 645	م , ت	645 , 62A	2
ص , ف	635 , 641	گ	6AF	2
ص , ف	635 , 641	ا	627	2
ص , ف	635 , 641	ع , ي	639 , 64A	2
ص , ف	635 , 641	ك , ن	643 , 646	2
ص , و	635 , 648	م	645	2
ص , و	635 , 648	, ۶	20 , 6F6	2
ع , ا	639 , 627	)	29	2
ع , ا	639 , 627		20	2
ع , م	639 , 645	ر	631	2
ع , م	639 , 645	ك	643	2
ع , م	639 , 645	ب	628	2
ع , م	639 , 645	و , ر	648 , 631	2
ع , م	639 , 645	ك , ه	643 , 647	2
غ , ا	63A , 627	, ا	627 , 20	2
ف , ا	641 , 627	, s	20 , 73	2
ف , ر	641 , 631	ن , ي	646 , 64A	2
ف , س	641 , 633	ش	634	2
ف , س	641 , 633	ن	646	2
ف , س	641 , 633	خ , ي	62E , 64A	2
ف , ع	641 , 639	س , ب	633 , 628	2
ف , ع	641 , 639	غ , ن	63A , 646	2
ف , غ	641 , 63A	ه	647	2
ف , غ	641 , 63A	ن	646	2
ف , غ	641 , 63A		20	2
ف , غ	641 , 63A	ر	631	2
ف , غ	641 , 63A	خ , .	2E , 62E	2
ف , غ	641 , 63A	و , ح	648 , 62D	2
ف , غ	641 , 63A	ت ,	20 , 62A	2
ف , غ	641 , 63A	ر , ه	631 , 647	2
ف , غ	641 , 63A	ك , ي	643 , 64A	2
ف , غ	641 , 63A	ن , ع	646 , 639	2
ف , غ	641 , 63A	م , ق	645 , 642	2
ف , غ	641 , 63A	و , ل	648 , 644	2
ف , غ	641 , 63A	غ , ن	63A , 646	2
ف , غ	641 , 63A	م , ن	645 , 646	2

ق , ر	642 , 631	ا ,	627 , 20	2
ف , و	641 , 648	ر	631	2
ق , ل	642 , 644	و	648	2
ق , ل	642 , 644		20	2
ق , و	642 , 648	ز	632	4
ق , و	642 , 648	ح	62D	2
ق , و	642 , 648	چ	686	2
ق , و	642 , 648	ل	644	2
ق , و	642 , 648	ك	643	2
ق , و	642 , 648	ب	628	2
ق , و	642 , 648	خ	62E	2
ق , و	642 , 648	ت , ر	62A , 631	4
ق , و	642 , 648	ا , س	627 , 633	2
ق , و	642 , 648	د , ر	62F , 631	2
ق , و	642 , 648	ر , ه	631 , 647	2
ق , و	642 , 648	ت , ي	62A , 64A	2
ق , و	642 , 648	ك , ن	643 , 646	2
ق , و	642 , 648	د ,	62F , 20	2
ق , و	642 , 648	ل , ت	644 , 62A	2
ق , و	642 , 648	ف , ر	641 , 631	2
ق , و	642 , 648	ن , د	646 , 62F	2
ق , و	642 , 648	ا , ر	627 , 631	2
ل , ت	644 , 62A	م	645	2
ل , ت	644 , 62A	)	29	2
ل , ت	644 , 62A	ا , ى	627 , 6CC	2
ل , ح	644 , 62D	(, ا	627 , 29	2
ل , ح	644 , 62D	م	645	2
ل , ح	644 , 62D	(, ا	627 , 29	2
ل , ه	644 , 647	, /	20 , 2F	2
ل , ه	644 , 647	, -	20 , 2D	2
ل , ه	644 , 647	, H	20 , 48	2
م , ر	645 , 631	ر , /	631 , 2F	2
م , س	645 , 633	ا	627	2
م , س	645 , 633	ك	643	2
م , س	645 , 633	ك , د	643 , 62F	2
م , س	645 , 633	ا	627	2
م , س	645 , 633	ك	643	2
م , ق	645 , 642	س	633	2
م , ق	645 , 642	ت	62A	2
م , ن	645 , 646	.	2E	2
م , ن	645 , 646	ك	643	2
م , ن	645 , 646	خ	62E	2

م , ن	645 , 646	س	633	2
م , ن	645 , 646	ص	635	2
م , ن	645 , 646	H , W	48 , 57	4
م , ن	645 , 646	ت , ا	62A , 627	4
م , ن	645 , 646	٠ ,	6F0 , D	2
م , ن	645 , 646	ل , ا	644 , 627	2
م , ن	645 , 646	ل , ف	644 , 641	2
م , ن	645 , 646	س , ا	633 , 627	2
م , ن	645 , 646	ف , ۴	6F4 , 641	2
م , ن	645 , 646	ك , ا	643 , 627	2
م , ن	645 , 646	ل , ب	644 , 628	2
ن , ا	646 , 627	ر , \	631 , 5C	2
ن , ا	646 , 627	, ا	627 , 20	2
ن , د	646 , 62F	ز	632	4
ن , د	646 , 62F	ر	631	2
ن , د	646 , 62F	ر , ب	631 , 628	2
ن , س	646 , 633	خ	62E	4
ن , س	646 , 633	م	645	2
ن , س	646 , 633	ه , ش	647 , 634	2
ن , ق	646 , 642	ل , ت	644 , 62A	2
ن , م	646 , 645	ر	631	2
ن , م	646 , 645	4	34	2
ن , م	646 , 645	و	648	2
ن , م	646 , 645	د	62F	2
ن , م	646 , 645	خ , ا	62E , 627	2
ن , م	646 , 645	ب , ي	628 , 64A	2
ن , ه	646 , 647	د	62F	2
ن , ه	646 , 647	ا	627	2
ن , ه	646 , 647	ك , ر	643 , 631	2
ه , د	647 , 62F	ي	64A	2
ه , د	647 , 62F	پ	67E	2
ه , د	647 , 62F	م , ر	645 , 631	2
ه , د	647 , 62F	ص , ل	635 , 644	2
ه , ر	647 , 631	ا	627	4
ه , ر	647 , 631	١	6F1	4
ه , ر	647 , 631	غ	63A	2
ه , ر	647 , 631	<	3C	2
ه , ر	647 , 631	.	2E	2
ه , ر	647 , 631	) , ى	649 , 29	2
ه , ر	647 , 631	ل , ى	644 , 649	2
ه , ر	647 , 631	ن , ا	646 , 627	2
ه , ر	647 , 631	ا , ا	627 , 627	2
ه , ر	647 , 631	د , ى	62F , 649	2
ه , ر	647 , 631	ل , ل	644 , 644	2
ه , م	647 , 645	ك	643	2
و , ر	648 , 631	ر , /	631 , 2F	2
و , ف	648 , 641	ر , ن	631 , 646	4
و , ف	648 , 641	ا , ن	627 , 646	2

2	62A , 631	ت , ر	648 , 641	و , ف
2	627 , 62A	ا , ت	648 , 641	و , ف
2	645 , 62A	م , ت	648 , 641	و , ف
2	62F , 646	د , ن	648 , 641	و , ف
2	645 , 645	م , م	648 , 641	و , ف
2	634	ش	648 , 644	و , ل

INTENTIONALLY LEFT BLANK.

U.S. Army Research Laboratory

SUMMER RESEARCH TECHNICAL PAPER

STEP, APG Site – Building Molecular Crystals with Defects for Atomistic Simulations

by Lynn Munday

Contents

List of Figures 57

List of Tables 57

Abstract 58

1. Introduction/Background 59

2. Experiment/Calculations 61

3. Results and Discussions 66

4. Summary and Conclusions 68

5. References 70

List of Figures

Figure 1. Molecular structure of a) RDX, and b) HMX (Wikipedia, http://en.wikipedia.org/wiki/RDX or /HMX). 59

Figure 2. RDX molecular structure given by Choi (2) where a) is the ball and stick representation from Choi (*2*), and b) only shows the bonds. 61

Figure 3. RDX unit cells viewed on the a) (100) plane b) (010) plane and c) (001) plane. 63

Figure 4. 3x3 crystal lattice of RDX when viewed on the a) (100) plane and b) (010) plane and c) (001) plane. The 3-dimension view of the block is shown d) where the atoms are represented by space filling spheres. 64

Figure 5. Screw dislocation with [001] Burger's Vector and (010) glide plane viewed on the (001) plane. 66

Figure 6. Screw dislocation with [001] Burger's Vector, and (010) glide plane viewed on the (010) plane. 67

Figure 7. Two RDX grains with Σ = 5 large angle tilt grain boundary viewed on the (001) plane. 68

List of Tables

Table 1. Atomic positions of RDX given by Choi (2) where a = 13.182 Å, b = 11.574 Å, and c = 10.709 Å and the number in parentheses is the standard deviation. Atomic numbering is shown in figure 2. 62

Abstract

This report outlines the initial development of an atomistic model of the condensed phase energetic material hexahydro-1,3,5-trinitro-1,3,5-s-triazine (RDX) crystal to be used in studying its response to shock loading in the vicinity of crystal defects. In this work the atomistic model of the RDX molecular crystal is built and embedded with various point, line, and surface defects using the Multiscale Simulation Application Suite (MSAS) (*1*). MSAS is used to build the RDX crystals from RDX structural data given by Choi (*2*), and then an elastic solution is used to embed vacancies, dislocations, or grain boundaries. Once the geometry of the grain, crystal structure, and defects are input into MSAS, a data file is created and converted to a format used by other programs such as the classical molecular dynamics code LAMMPS. These models will be used in simulations to study molecular vibrations and phonons in the vicinity of defects and their coupling to intramolecular vibrations, and dislocation motion in the vicinity of defects. The work fits into a larger program investigating processes that effect hot spot formation and shock induced detonation.

1. Introduction/Background

Chemical energetic materials contain a metastable mixture of fuel and oxidizers which are triggered to decompose releasing energy as heat and pressure. The fuel and oxidizers are either separate solids mixed together producing a composite, or are contained in a single molecule. Composite energetic, like black powder, have a higher energy density than molecular energetic, but a slower energy release rate and thus contain less power. The decomposition rate of an energetic material is also dependent on the triggering stimulus and results in either detonation or deflagration. Detonation occurs when the decomposition is driven by an explosive shockwave and deflagration is a much slower process where the reaction is driven by a flame front. The amount of stimulus needed to trigger an energetic in the form of shock, friction, or heat gives a measure of its sensitivity. The process of converting an externally applied stimulus to chemical decomposition describes the triggering mechanism and is important to predicting an energetic's response. Understanding the trigger mechanism is useful in predicting the sensitivity and safety of handling, the stability and long term effects of storage, and reliability in producing the desired energy release.

Molecular energetic materials contain molecules arranged in a crystalline structure held together by hydrogen bonds. Nitramines are a common group of energetic molecules and contain the explosives RDX and HMX shown in figure 1. The molecular structure of nitramines contains nitro groups arranged about a carbon ring shown by the chemical structure in figure 1. Nitramines are common military high explosives because of their shock insensitivity and stability in storage. The bigger molecules in nitramines arrange themselves into a crystal structure giving them a large energy density and increased power and detonation velocities over composite energetics.

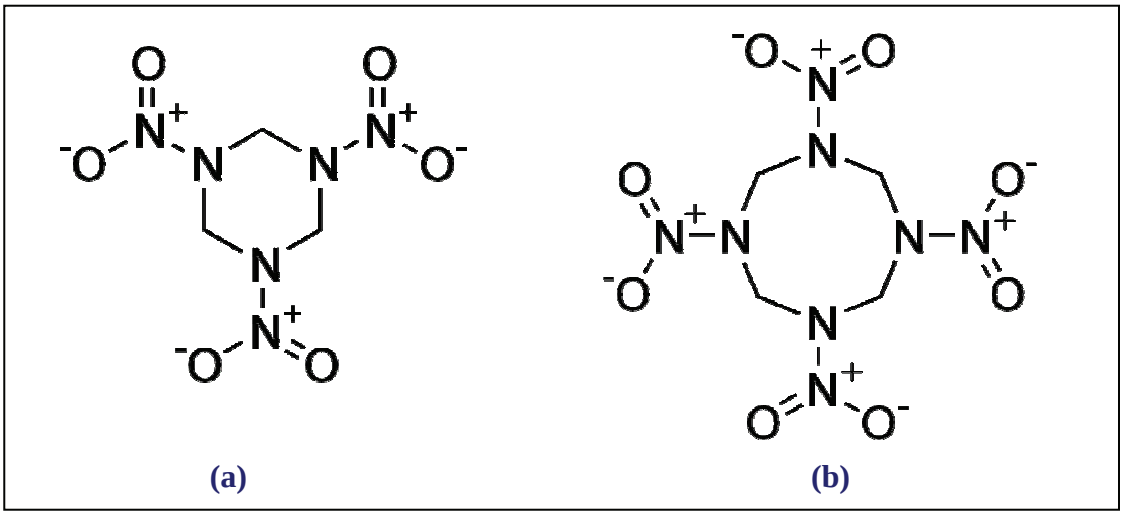

Figure 1. Molecular structure of a) RDX, and b) HMX (Wikipedia, http://en.wikipedia.org/wiki/RDX or /HMX).

Pressure and heat are used to initiate decomposition in energetic materials. A minimum amount of energy is required to be input into the metastable system to overcome the energy barrier of the fuel and oxidizers and cause them to react exothermically. In a detonation, pressure in the form of a shockwave leads to thermal heating of the bulk material, which decomposes and drives the shockwave producing a self sustaining reaction. The initial triggering mechanism that transfers the energy of the shock to the energetic producing the decomposition is of great interest, because it determines the later time energetic release and is used to predict the sensitivity of an energetic material.

Tarver (*3*) gives four main regions to the reaction zone of a shock loaded molecular energetic material. The first region is in the shock front where the energy of the shockwave is transferred to phonon modes in less than a picosecond. The second region is phonon up-pumping described by Dlott (*4*) where phonon modes anharmonically couple exciting the intramolecular vibrations of the molecule, which occurs on the order of tens of picoseconds. The third region is the chemical reconstitution region where the intramolecular vibrations cause the molecular bonds to break forming highly excited species and lasts a nanosecond. In the fourth region the excited molecular species go through deexcitation and form solid species in thermal and chemical equilibrium, which lasts on the order of microseconds.

The first two regions of the reaction zone are of main interest to this work where the energetic molecule is initially excited and can be studied using non-reactive molecular simulations. The simulations will first be used to study a perfect energetic molecular crystal to obtain phonon dispersion curves and other material properties related to inter and intramolecular vibrations including heat capacity and heat transfer, which may provide information on the formation of hot spots in isolated regions in the crystal. This analysis will then be extended to crystals containing defects such as voids, dislocations, and grain boundaries. The main goal is to determine the dispersion properties of phonons, their effects on the molecular crystal, and their ability to dissipate energy.

Continuum level material properties will also be derived for use in larger scale simulations. These properties will be used in studying non-shock induced decomposition, which usually leads to deflagration of the energetic material. Non-shock induced decomposition has been attributed to dissipation mechanisms in the crystal structure such as plastic deformation that may be related to this same phonon up-pumping triggering mechanism. Non-shock induced decomposition is almost always accidental, and is a safety concern when handling energetics and predicting their sensitivity.

Once a capability in this area has been developed for known energetic materials and is shown to match available experimental data, the process can then be extended to more complex and theoretical materials using quantum derived data. This will play an important role in the initial development of new materials where computational experiments can be used to predict the success of various chemical formulations. This capability will not only be applicable to

decomposition of energetic materials, but will also be useful in studying all types of failures in molecular crystals such as those used in molecular electronics and the pharmaceutical industry.

2. Experiment/Calculations

This section outlines building the atomistic model using the Multiscale Simulation Application Suite (MSAS) (*1*). The structural data for the RDX molecular crystal is given by Choi (*2*) and common atomistic defects embedded in the model are taken from examples used by Cawkwell (*5*).

Solid RDX is known to exist in two phases, α and β phases (*6*). The β-phase is unstable and short lived at ambient conditions. The α-phase exists under ambient conditions and its structure was found by Choi (*2*) using neutron-diffraction. In this work, only the α-phase of RDX will be considered. The α-phase RDX crystal possesses orthorhombic symmetry with eight molecules per unit cell, and belongs to the Pbca space group with unit cell sides a = 13.182 Å, b = 11.574 Å, and c = 10.709 Å. The atomic position of each atom shown in figure 2 is given in table 1.

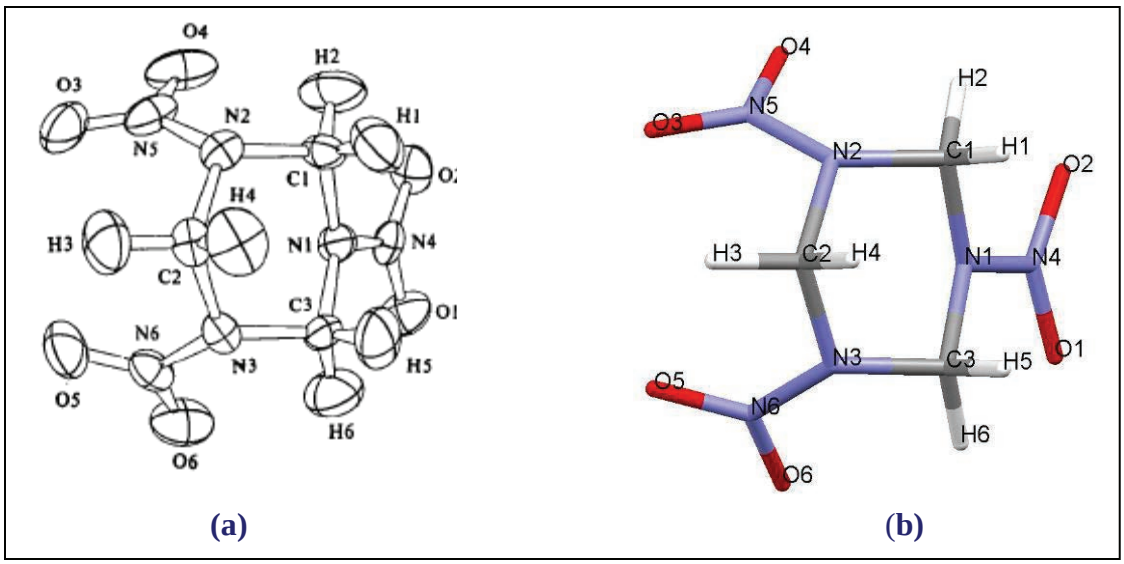

Figure 2. RDX molecular structure given by Choi (2) where a) is the ball and stick representation from Choi (*2*), and b) only shows the bonds.

Table 1. Atomic positions of RDX given by Choi (2) where a = 13.182 Å, b = 11.574 Å, and c = 10.709 Å and the number in parentheses is the standard deviation. Atomic numbering is shown in figure 2.

	x/a ($\times 10^4$)	y/b ($\times 10^4$)	z/c ($\times 10^4$)
C(1)	1839 (3)	3578 (3)	4400 (3)
C(2)	503 (2)	2440 (2)	3395 (3)
C(3)	1487 (2)	3813 (3)	2159 (3)
N(1)	1761 (2)	4360 (2)	3330 (2)
N(2)	877 (2)	2996 (2)	4537 (2)
N(3)	536 (1)	3222 (2)	2329 (2)
N(4)	2260 (2)	5379 (2)	3346 (2)
N(5)	155 (2)	3525 (2)	5294 (2)
N(6)	−333 (2)	3875 (2)	2078 (2)
O(1)	2270 (3)	5932 (3)	2388 (4)
O(2)	2649 (3)	5687 (3)	4338 (4)
O(3)	−693 (3)	3142 (4)	5262 (4)
O(4)	454 (4)	4271 (3)	5990 (3)
O(5)	−1121 (3)	3534 (4)	2504 (4)
O(6)	−236 (4)	4691 (4)	1390 (4)
H(1)	2401 (6)	2944 (7)	4226 (7)
H(2)	2013 (6)	4068 (6)	5244 (6)
H(3)	−261 (5)	2117 (6)	3540 (6)
H(4)	1015 (5)	1728 (5)	3192 (7)
H(5)	2052 (5)	3166 (6)	1917 (6)
H(6)	1440 (6)	4432 (7)	1413 (7)

The symmetry operations for the Pbca space group are used to construct the unit cell that is placed at each lattice site by providing the molecules position within the unit cell. All of the molecular positions and orientations are found by translating and applying symmetry operators to the molecule given in table 1. The symmetry operations and translations for each of the eight molecules in the Pbca space group are:

1) $$\{x, y, z\} = \begin{bmatrix} 1 & 0 & 0 \\ 0 & 1 & 0 \\ 0 & 0 & 1 \end{bmatrix} \begin{Bmatrix} x \\ y \\ z \end{Bmatrix} + \begin{Bmatrix} 0 \\ 0 \\ 0 \end{Bmatrix}$$

2) $$\{1/2 - x, -y, 1/2 + z\} = \begin{bmatrix} -1 & 0 & 0 \\ 0 & -1 & 0 \\ 0 & 0 & 1 \end{bmatrix} \begin{Bmatrix} x \\ y \\ z \end{Bmatrix} + \begin{Bmatrix} a/2 \\ b \\ c/2 \end{Bmatrix}$$

3) $$\{-x, 1/2 + y, 1/2 - z\} = \begin{bmatrix} -1 & 0 & 0 \\ 0 & 1 & 0 \\ 0 & 0 & -1 \end{bmatrix} \begin{Bmatrix} x \\ y \\ z \end{Bmatrix} + \begin{Bmatrix} a \\ b/2 \\ c/2 \end{Bmatrix}$$ **Equation 1**

4) $$\{1/2 + x, 1/2 - y, -z\} = \begin{bmatrix} 1 & 0 & 0 \\ 0 & -1 & 0 \\ 0 & 0 & -1 \end{bmatrix} \begin{Bmatrix} x \\ y \\ z \end{Bmatrix} + \begin{Bmatrix} a/2 \\ b/2 \\ c \end{Bmatrix}$$

5) $$\{-x,-y,-z\} = \begin{bmatrix} -1 & 0 & 0 \\ 0 & -1 & 0 \\ 0 & 0 & -1 \end{bmatrix} \begin{Bmatrix} x \\ y \\ z \end{Bmatrix} + \begin{Bmatrix} a \\ b \\ c \end{Bmatrix}$$

6) $$\{1/2 + x, y, 1/2 - z\} = \begin{bmatrix} 1 & 0 & 0 \\ 0 & 1 & 0 \\ 0 & 0 & -1 \end{bmatrix} \begin{Bmatrix} x \\ y \\ z \end{Bmatrix} + \begin{Bmatrix} a/2 \\ 0 \\ c/2 \end{Bmatrix}$$

7) $$\{x, 1/2 - y, 1/2 + z\} = \begin{bmatrix} 1 & 0 & 0 \\ 0 & -1 & 0 \\ 0 & 0 & 1 \end{bmatrix} \begin{Bmatrix} x \\ y \\ z \end{Bmatrix} + \begin{Bmatrix} 0 \\ b/2 \\ c/2 \end{Bmatrix}$$

8) $$\{1/2 - x, 1/2 + y, z\} = \begin{bmatrix} -1 & 0 & 0 \\ 0 & 1 & 0 \\ 0 & 0 & 1 \end{bmatrix} \begin{Bmatrix} x \\ y \\ z \end{Bmatrix} + \begin{Bmatrix} a/2 \\ b/2 \\ 0 \end{Bmatrix}$$

where x, y, z are atom positions of the basis molecule given in table 1 and a, b, c are the lengths of the sides of the orthorhombic unit cell. Molecule 1 is the base molecule and therefore does not under go any translations or symmetry operations. Molecules 2–4 are translations and rotations of the base molecule. Molecule five is an inversion of molecule 1 and is considered to be a left handed molecule. Molecules 6–8 are translations and rotations of the inversion, molecule 5. MSAS only includes rotation operations for transforming molecules; therefore, this basis is input by defining two separate molecules, the basis molecule 1 and the inversion molecule 5, and then rotating them to get the proper orientation. Then in MSAS, the crystal lattice is built by inputting the translations of each of the eight transformed molecules into the basis. Figure 3 shows projections of the eight RDX molecules in the basis structure along the different axis of the unit cell.

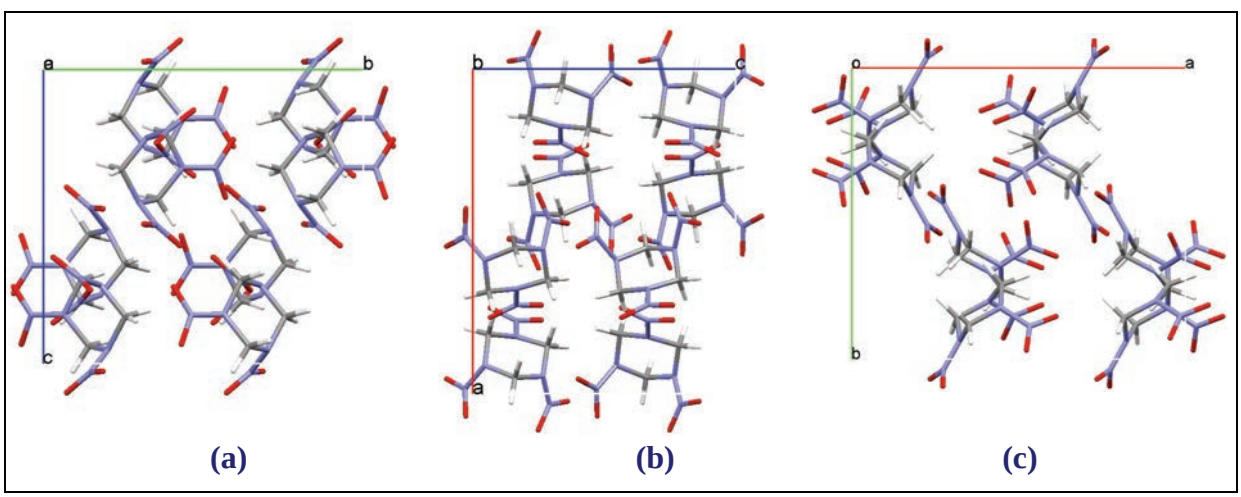

Figure 3. RDX unit cells viewed on the a) (100) plane b) (010) plane and c) (001) plane.

MSAS constructs the lattice from the defined basis by filling in the grain defined by a volume. The position vector, **r**, of all lattice points in the grain are given by

$$\mathbf{r} = u\mathbf{a} + v\mathbf{b} + w\mathbf{c}$$

where u, v, and w are integers and **a**, **b**, and **c** are the three lattice vectors along the crystal axis. The lattice is completely specified by defining the lengths of **a**, **b**, **c** and the three angles between them. For orthorhombic symmetry a≠b≠c and the lattice vectors are orthogonal. A grain containing 3 unit cells in the **a**, **b**, and **c** directions is shown in figure 4 for each plane, a) (100), b) (010), and c) (001).

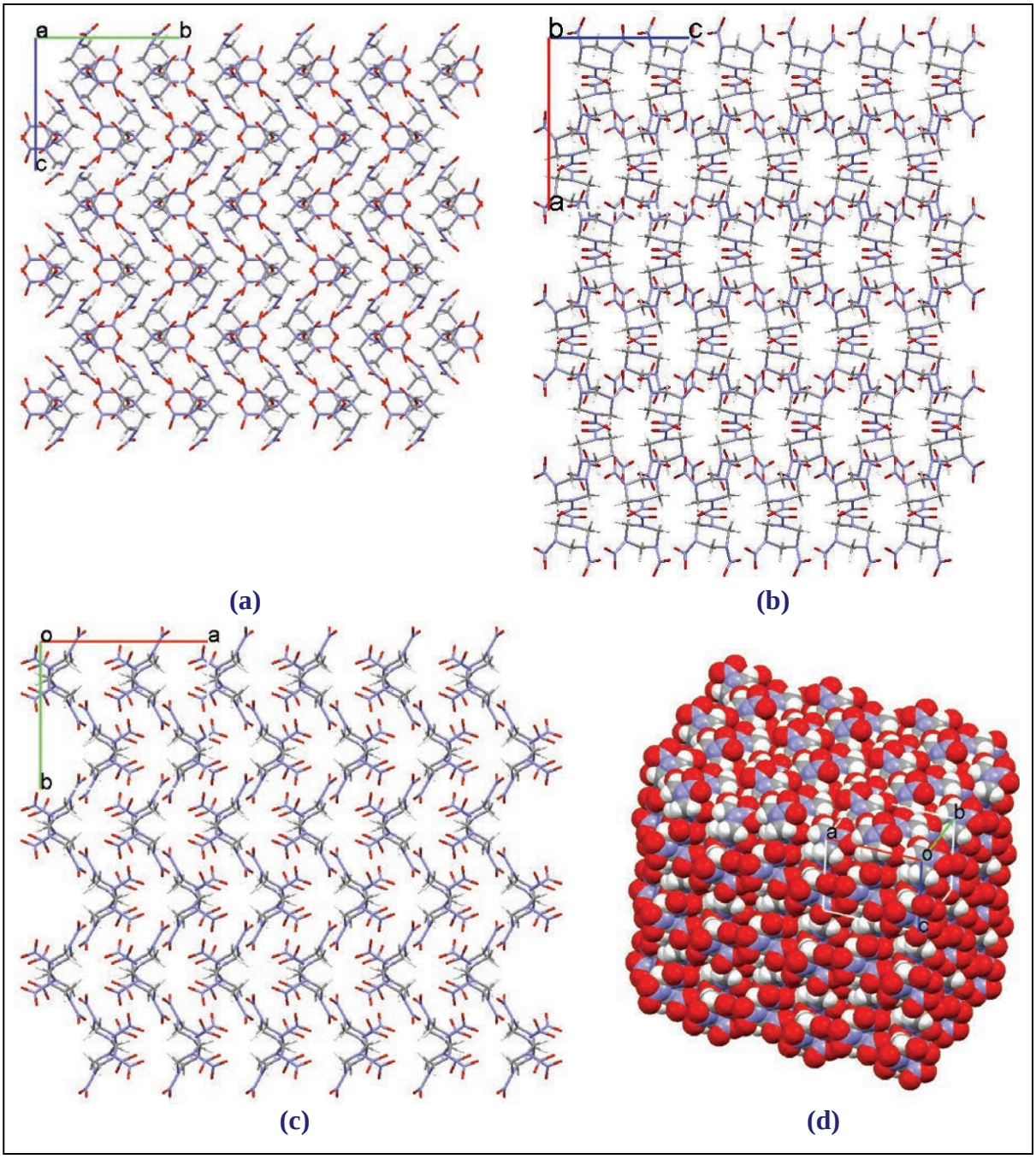

Figure 4. 3x3 crystal lattice of RDX when viewed on the a) (100) plane and b) (010) plane and c) (001) plane. The 3-dimension view of the block is shown d) where the atoms are represented by space filling spheres.

Once the lattice is defined a grain is constructed and defects are then embedded into the grain. In MSAS, point defects are substitutional and are placed randomly with in the grain based on a defined volume percentage. The substitutional defect can be a molecule, vacancy, or atom, and are substituted in at a molecules site within the basis. Interstitials can not be randomly placed in MSAS, but can be input into the structure periodically by overlaying them as a new lattice in the grain.

Line defects or dislocations are included by first specifying the Miller indices of the glide plane. Next the Burgers vector is input and the angle that it makes with the dislocation line. A pure screw dislocation is defined by a Burger's vector in the direction of the dislocation. Pure edge dislocations are defined by a Burger's vector perpendicular to the dislocation and mixed dislocations are mixed dislocations are given for angles $0 \leq \theta \leq 90$. The displacement of the lattice sites due to the dislocation are calculated by MSAS using isotropic elastic solutions for dislocations.

A summary of the steps taken to construct a grain of RDX in MSAS (*1*) and embed in it defects are as follows:

1. Define the right and left handed molecules for molecules 1 and 5 given in equation 1.
2. Create transformed molecules 2–4 by rotating molecule 1 about the proper axis given in equation 1. Create transformed molecules 6–8 by rotating molecule 5 about the proper axis given in equation 1.
3. Create the grains geometry by first defining the vertices of the grain corners, then connecting the vertices with edges, and finally grouping the edges together into faces. Once the faces enclose a volume a grain region is created.
4. Select a grain region and define a lattice in the region by first specifying the lattice orientation with respect to the global orthogonal coordinate system, then specifying the lattice vectors, a, b, and c, and finally applying the translations given in equation 1 to each of the eight molecules.
5. Select a grain region with a defined lattice and embed in it defect.
    i. For a point defect, specify whether it is a substitutional, vacancy, or interstitial and volume fraction of defects
    ii. For a line defect specify the Miller indices for the glide plane, the Burgers vector and the location, the angle the Burger's vector makes with the dislocation line and a point on the dislocation.

3. Results and Discussions

The procedure outlined in the previous section was used to build a 100 by 100 by 50 Å RDX crystal in MSAS and embed in it different defects. A screw dislocation and a Coincident Site Lattice or high angle Σ tilt grain boundary are reported here.

The screw dislocation is the same to that used by Cawkwell (5) for studies of plastic deformation in RDX where indentation results are cited that indicate the primary slip system having [001] Burger's Vectors gliding on the (010) plane. The isotropic elastic solution to a screw dislocation with Burgers Vector [001] will only cause displacements in the [001] direction. Figure 5 shows the (001) plane with the screw dislocation core area circled where small variations in the molecule locations are observed. There is very little difference in the molecular positions between figure 5 and figure 4c for the perfect lattice.

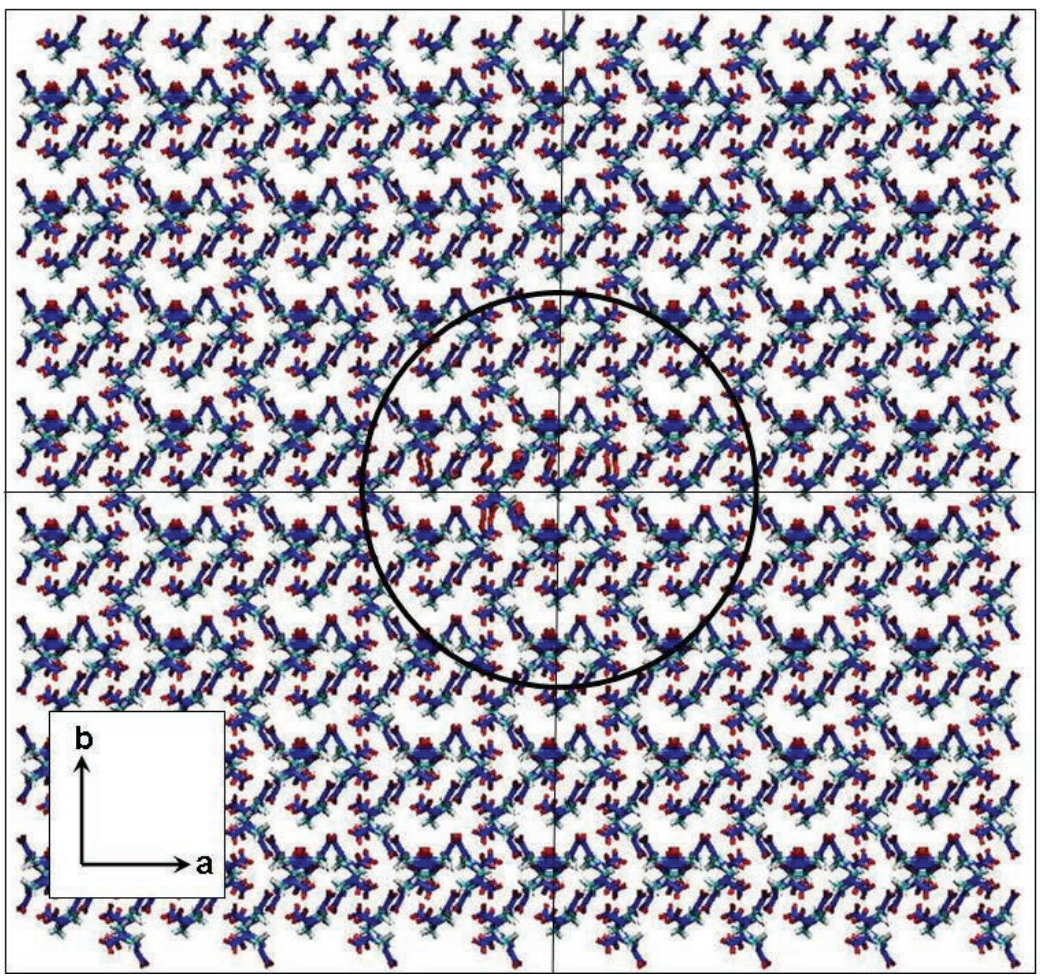

Figure 5. Screw dislocation with [001] Burger's Vector and (010) glide plane viewed on the (001) plane.

Figure 6 shows the screw dislocation viewed on the (010) plane which is also the glide plane. Molecules in this view are displaced in the ±[001] direction. The [001] Burger's vector is represented by the black arrow, and the handedness of the screw dislocation is shown by the curved arrow circling the Burger's Vector. The handedness of the screw dislocation can be observed by looking at how the molecules normal to the paper line up. For a right handed screw dislocation the molecules to the left of the screw dislocation are slightly displaced in the $[00\bar{1}]$ direction and the molecules to the right are displaced in the [001] direction. The screw dislocation is able to glide along the (010) plane, normal to the page, until it reaches a grain boundary at which point it becomes an edge dislocation.

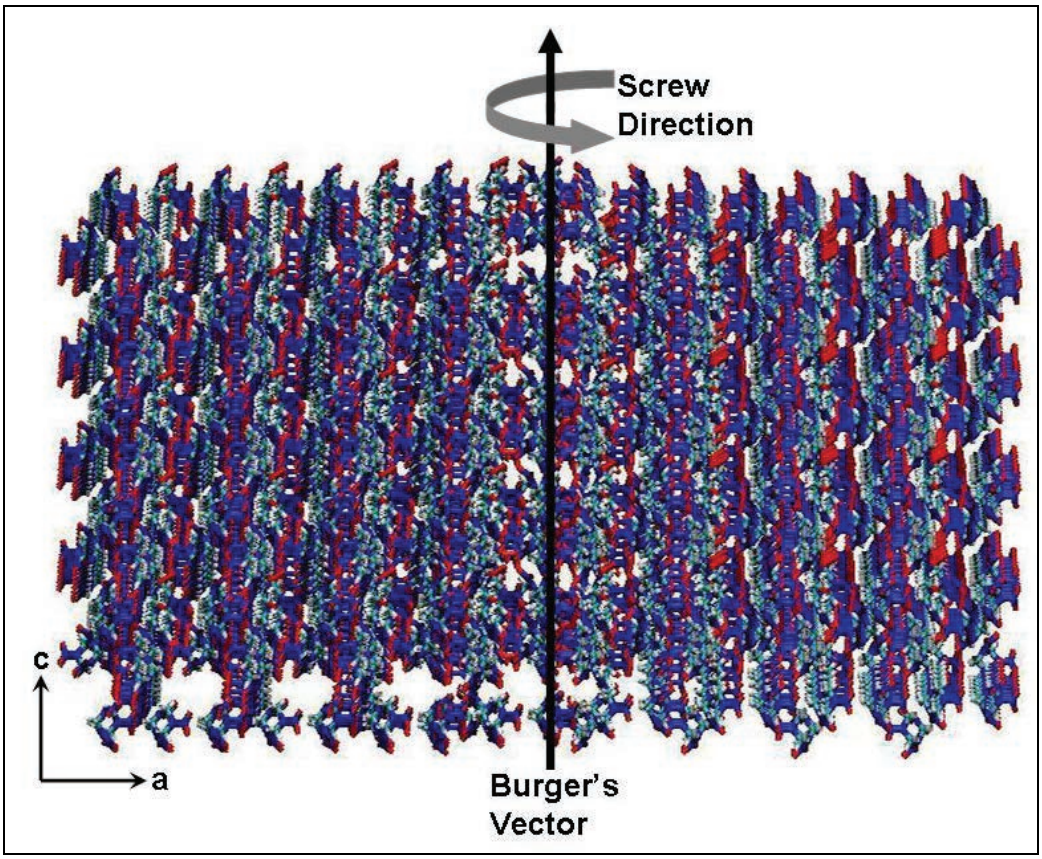

Figure 6. Screw dislocation with [001] Burger's Vector, and (010) glide plane viewed on the (010) plane.

A CSL or Σ high angle tilt grain boundary surface defect is the next RDX lattice constructed as shown in figure 7. This is a Σ = 5 tilt boundary, meaning that equivalent site lattices will line up at the grain boundary after every 5 lattice sites. This grain boundary is created by rotating each grain by ± θ/2 around the [001] axis. Figure 7 shows the grain structures for the two rotated grains viewed on the (001) plane where the grain where the hypotenuse of the right triangle is placed along the grain boundary. The rotation angle is found by requiring every 5 lattice sites along the [001] direction to coincide and is given by the equation

$$\frac{\theta}{2} = \sin^{-1}\left(\frac{b}{5a}\right)$$

where a and b are the lattice constants and are shown by the shaded right triangle in figure 7. The two grains should be mirror images of each other when reflected at the (010) grain boundary, but this is not the case as figure 7 indicates. This may be a result of how MSAS handles the molecule rotations when the lattice orientation changes, or it may be a result of improperly post processing the output.

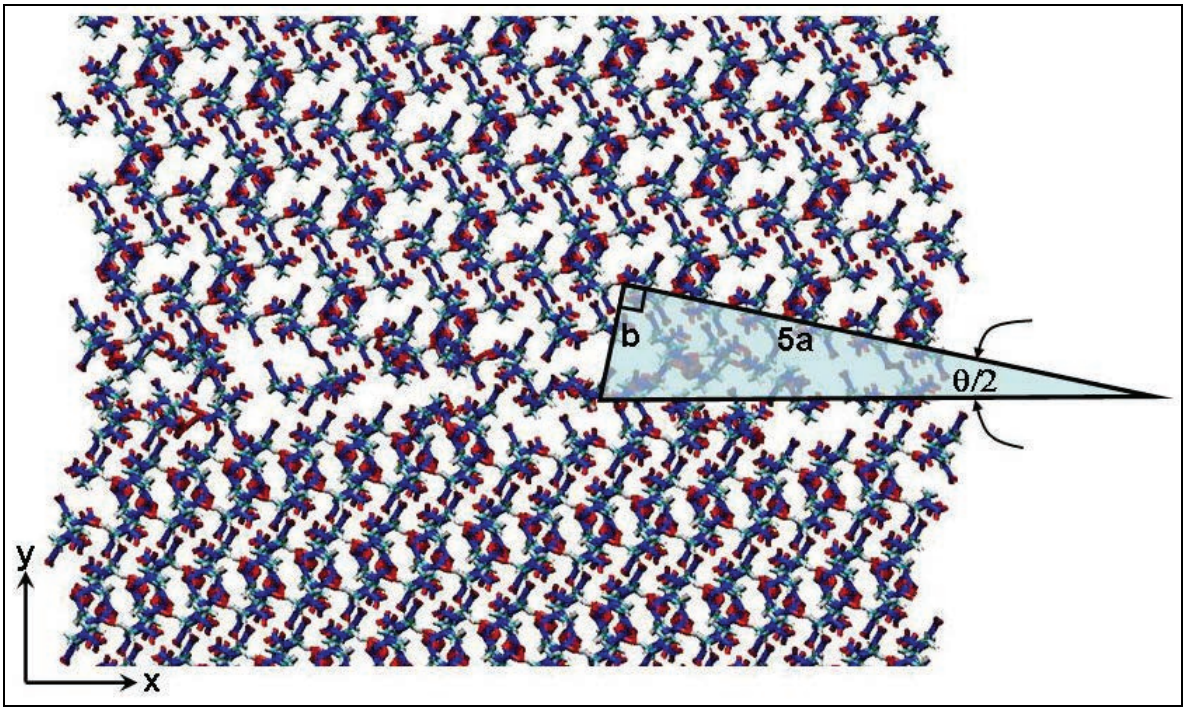

Figure 7. Two RDX grains with Σ = 5 large angle tilt grain boundary viewed on the (001) plane.

4. Summary and Conclusions

Three different RDX grain structures were produced using MSAS (*1*). The first grain constructed from Section I was for a perfect RDX lattice with crystallographic structural information obtained from Choi (*2*). This grain was then embedded with a screw dislocation in Section II whose dislocation system was given by Cawkwell (5). The third structure developed was for an RDX polycrystal consisting of two RDX grains with a Σ = 5 tilt boundary. The RDX polycrystal atomic structure in figure 7 was shown to contain some symmetry discrepancies along the (010) tilt boundary and the cause to these errors is to be determined in future work. The MSAS data was post processed with a C++ program into a format to be visualized in Visual Molecular Dynamics (VMD), and a format used to provide the atomic positions, bonds, bond angle, and bond twists connectivity for molecular simulations in LAMMPS.

The next step in this work will be running the molecular simulations on the developed crystals using the U.S. Army Research Laboratory (ARL) Major Shared Resource Center. The molecular simulations still need to be setup by researching proper boundary and initial conditions, intermolecular and intramolecular potentials, and numerical methods. These simulations will provide insight to the extremely small space and time region at and immediately following a shock front to determine the triggering mechanism of decomposition and the formation of hot spots.

5. References

1. Klass, O. *Multiscale Simulation Application Suite Example Problems*; ARL Contract W911QX-06-C-0048, 2007.
2. Choi, C. S.; Prince, E. The Crystal Structure of Cyclotrimethylene-trinitramine. *Acta Crystallographica* **1972**, *B 28*, 2857–2862.
3. Tarver, C. M.; Fried, L. E.; Ruggiero, A. J.; Calef, D. F. Energy Transfer in Solid Explosives. *Tenth Internation Detonation Symposium*, UCRL-JC-111343, 1993.
4. Dlott, D. D.; Fayer, M. D. Shocked Molecular Solids: Vibrational Up Pumping, Defect Hot Spot Formation, and the Onset of Chemistry. *Journal of Chemical Physics* **1990**, *92*, 3798-3812.
5. Cawkwell, M. J.; Sewell, T. D. *The Core Structure of the [001] Screw Dislocation in α-RDX*, Nuclear Weapons Highlights, LALP-07-041 (2007).
6. McCrone, W. C. 32. RDX (Cyclotrimethylenetrinitramine). *Analytical Chemistry* **1950**, *22*, 954.

Human Research & Engineering Directorate (HRED)

INTENTIONALLY LEFT BLANK.

U.S. Army Research Laboratory

SUMMER RESEARCH TECHNICAL PAPER

Robotic Intelligent Control System with Human Inspired Plan Selection

by Eric Dimperio

Contents

List of Figures **75**

Abstract **76**

Acknowledgment **77**

1. Introduction **78**

2. Dynamic Decision Making with Temporal Discounting **79**

2.1 Equations 80

2.2 Behavioral Effects 81

3. Re-planning in a Simulated Environment **82**

3.1 Simulator Description 83

3.2 Test Environment 84

3.3 Observations 84

4. Summary and Conclusions **85**

5. References **87**

List of Figures

Figure 1. Example of temporal discounting.....80
Figure 2. Approach avoidance theory.....81
Figure 3. Testing simulator.....83

Abstract

Recent psychological models of decision making go beyond stating how rational agents should act. They offer an explanation of why people make decisions that seem irrational. One such model is the decision field theory (DFT). This model describes decisions as a diffusion process where preferences for each alternative change. Unfortunately, DFT has only been used to explain specific data sets in highly controlled environments. Certain aspects of the theory have not even been tested together. This paper describes an implementation of DFT within a robot simulator as a test environment for transition to a physical robot. Results show that in a more complex environment with repeated decisions, DFT needs to be augmented to allow for more naturalistic behaviors.

Acknowledgment

The author wishes to acknowledge the mentorship of Troy Kelley.

1. Introduction

Early work in the field of robotics was primarily done by engineers. Electrical engineers developed and miniaturized sensors and effectors. Mechanical engineers built small, flexible, efficient chassis to carry the equipment. Computer engineers assembled computational systems that could either fit within the robot itself or that could control it remotely. Robots have seen great successes when needed to do simple repetitive tasks in a controlled environment.

Although there are still many advances to be made in robot engineering, the successes so far have allowed researchers to explore more complex control systems for robots operating in more complex environments. This involved attempting to get robots to show behaviors that have previously only been observed in animals and humans. Roboticists are specializing in areas like object recognition, language learning, gesture recognition, and path planning. All of these represent sub-problems necessary for interacting with people in a dynamic world.

The U.S. Army has a need for small robots that can autonomously interact in a complex environment. The use of manually controlled robots has grown dramatically in recent years and has been useful in several ways. Unmanned vehicles are being used in many situations where it is unsafe for Solders to operate. However, current robots still have their limitations. Current cave-exploring robots cannot use radio communications deep inside a cave. Without remote operation or global positioning system (GPS) controlled navigation, a robot needs to have the ability to explore on its own and know when to come out to provide updates and get guidance from its operators.

Robots used in military contexts must operate in conjunction with human experts to complete their tasks. The growing application of robots has expanded the academic fields applicable to robotics to include the social sciences. Human-robot teams impose a new level of interaction. Recent studies suggest that human-robot teams are more effective when robots communicate more like other humans (*1*). Recently, psychologists have turned to using robots as an effective tool for studying cognition. Growing interest in embodied and situated cognition has led many cognitive scientists to argue that human cognition can no longer be treated as a black box, but is instead a product of interactions among the brain, the body, and the environment (*2*). A robot allows one to experiment with brain models using a particular body in a physical environment.

This paper describes several efforts made toward implementing models of human psychological processes on a robot. Such a capability has several benefits to the scientific community. For over 40 years, artificial intelligence (AI) researchers have focused on improving the algorithms for making an artificial agent think rationally. This has led to software and robot agents that can do things such as sort large amounts of data in a manner far superior to people. However, there are still many basic capabilities that humans have that robots struggle with. For example,

recognizing a never before seen animal as a type of reptile or knowing how to retrieve an object hidden under a blanket, or even how to recognize a melody; these are all relatively easy decisions for people. There exists growing support among cognitive scientists that these capabilities will come from trying to mimic what is known about animal and human cognition. The goal of this particular effort is to provide a robot with a sophisticated plan selection algorithm that is modeled after human decision making.

For the purposes of this paper, a plan can be thought of as a sequence of intended actions producing some expected change in state. Research of preferential decision making tends to focus on choices where any consequences depend on a single action. These single action plans represent a special case of general plan selection. Although little research exists on the selection of multi-action plans, one can expect behaviors observed in the special case to apply in the general case. Of particular interest are behaviors that appear to be irrational.

Rational models of decision making are those derived from the normative expected value theory, which allows one to calculate maximum expected gains from alternatives. Expected value theory was expanded to expected utility theory to recognize that people have some sort of subjective value called a "utility." It is expected that people make selections so as to try to maximize the utility gained from the choice. This assumption has been the cornerstone of many decades of decision making models (*3*, *4*). Unfortunately, this assumption predicts very specific behaviors that are regularly violated by people (*5*). For this reason, many modern models of decision making have been focusing on the behaviors observed rather than on the behaviors expected.

In order to endow a robotic platform with humanlike, non-scripted decision making, I utilized a sophisticated computational process model of preferential decision making. In the psychology literature, two such models have been used to explain a series of effects seen in behavioral experiments. These effects demonstrate that humans regularly violate the axiomatic principles (fundamental mathematical assumptions) of expected utility theory. Both decision field theory (DFT) and the leaky competitive accumulator (LCA) model have been shown to accurately reproduce many of these "irrational" behaviors (6, *7*, *8*, *9*). DFT was implemented in this case because of a better ability to scale up for decisions among many actions.

2. Dynamic Decision Making with Temporal Discounting

DFT is a framework for applying decisions to an evidence accumulation model. It is defined as a continuous time dynamic process whereby at every point in time, a stochastic attention mechanism focuses on one of the features/outcomes of the choice situation. All choice alternatives are compared against each other along this particular feature dimension and a preference state for each alternative is incrementally adjusted. This process continues until a

preference value crosses some threshold, at which point the alternative with the maximum preference is selected.

Figure 1 demonstrates how preferences change over time in a decision between three given options. The topmost option is the first to hit the threshold, which ends the decision process. At that point, an action is taken to indicate that darkest line is selected.

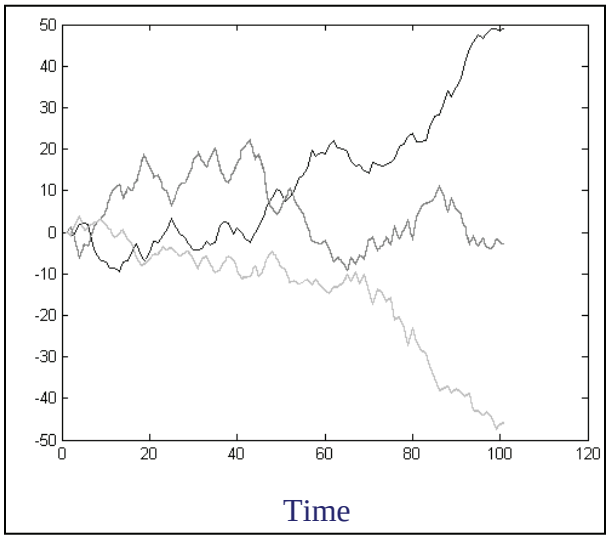

Figure 1. Example of temporal discounting.

2.1 Equations

The process of updating the preferences for each of J alternatives is simulated using the traditional equation for DFT:

$$P_i(t+h) = \sum_{j=1}^{J} S_{i_j} \cdot P_i(t) + \sum_{k=1}^{K} M_{i_k} \cdot W_k(t+h) + \varepsilon \tag{1}$$

There are some unique aspects of this framework to consider. The “S” parameters serve two functions. When Sij is i=j, the parameter controls a decay function, but when i!=j, it represents lateral inhibition from the other preference values. This lateral inhibition is distance dependent when distance is inversely proportional to the similarity of choice alternatives. The dynamic attention vector W(k) is 1 on the dimension being attended to and 0 elsewhere. The probability of attending to a particular dimension is determined by relative importance weights for those feature values. The term being subtracted merely normalizes these temporal evaluations to sum to zero. In this way, evidence for one alternative represents evidence against the other alternatives. The matrix M stores the expected values of choice alternatives along each of the feature dimensions. The specific mathematical properties of DFT and its operation as an Ornstein-Uhlenbeck process are out of the scope of this paper. See references 16 and 6 for derivations.

This value implementation differs from past implementations allowing multiple features by incorporating aspects of approach avoidance theory. The actual valuations in the M matrix are calculated based on its distance *d* from the present:

$$M_{i_k} = \sum_{d=1}^{H} V_{i_k d} \tag{2}$$

$$V_{i_k d} = \begin{cases} \dfrac{U_{i_k}}{d} & : U_{i_k} \geq 0 \\ .1 \cdot U_{i_k} + \dfrac{U_{i_k}}{d + .6} & : U_{i_k} < 0 \end{cases} \tag{3}$$

2.2 Behavioral Effects

Although the DFT framework has been used to explain specific context effects, temporal discounting, and speed/accuracy tradeoffs, these effects have not been demonstrated in a single implementation.

Approach/Avoidance: One pattern of behaviors observed in people has led to the creation of the approach avoidance theory. People tend to demonstrate temporal discounting of payoffs when making decisions (*11*). Earning $100 a year from now has less utility than earning $100 now. This phenomenon is very robust. In addition, it has been observed in multistage decision making (*12*). Multistage decision making requires the formation of more complex plans than those utilized in most decision studies. This suggests that payoffs expected from actions later in a plan should have a smaller weight than those expected early on. Approach avoidance theory (*13*) states that negative values (punishments/repulsive forces) fall off at a faster rate than positive values (figure 2).

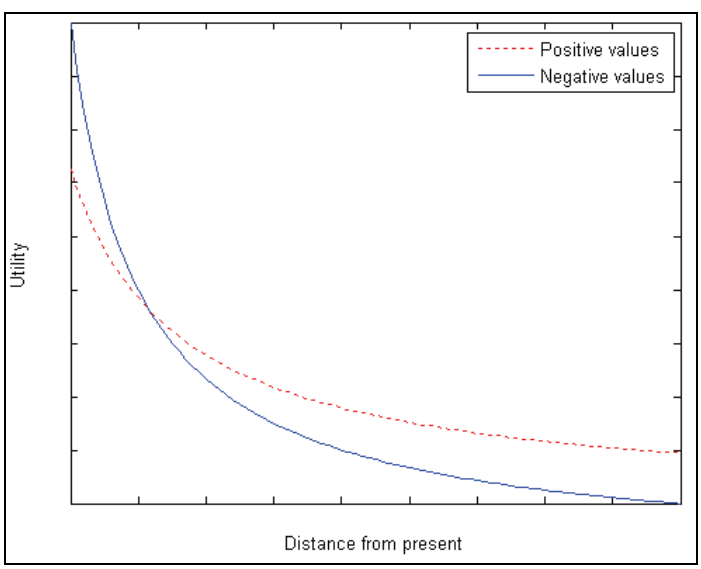

Figure 2. Approach avoidance theory.

This type of valuation mechanism has been previously incorporated into the DFT framework for consideration of risky, binary choices (*6*, *12*). Approach avoidance curves will be used to calculate the value of specific plans in the more recent multi-attribute, multi-alternative formulations of DFT.

Context Effects: In general, context effects describe violations of axiomatic principles of expected utility theory when choices are made in an alternative context. Three commonly described context effects are the similarity effect, the attraction effect, and the compromise effect. They occur when the relative choice probabilities of items change when presented with a third alternative as opposed to when presented with a binary choice.

The similarity effect occurs when a decoy alternative is added to the choice set such that it is similar to an existing option, but not significantly better or significantly worse. When people are presented with such a situation, the decoy action causes a drop in the probability of selecting the similar action while having little effect on the other action. The attraction effect occurs when the decoy added is similar to and dominated by (worse than) an existing alternative. As it is obviously a poor choice, the decoy is rarely selected, but it actually leads to an increase in the choice probability of the similar alternative. In the compromise effect, people prefer choosing a compromise between extreme alternatives even though there might not be any preference for that alternative when presented in a binary choice with an extreme alternative. See references 7 and 9 for more on the effects and how they represent violations of expected utility theory.

Speed/Accuracy Tradeoffs: The time one takes to make a decision influences the distribution of choices actually made (*14*). Taking more time to consider important decisions can lead to a better outcome. Unimportant decisions can be made fast, because bad choices are less severe. Experimentally, people can be made to make fast decisions, where they must rely more on initial biases rather than on actually considering the information at hand (*15*).

3. Re-planning in a Simulated Environment

Although the past implementations of DFT allow for large scale simulations to measure choice probabilities, they hinder the exploration of how planning operates in realistic conditions. To aid in that exploration, a simple two-dimensional robot simulator was implemented. The simulator consists of simplified models of both a robot and its environment. Within this basic architecture, the robot has knowledge of its environment utilizing the same knowledge structure as an existing robotic architecture called SS-RICS (*10*). The simulated robot also has basic plan generation capabilities. Plans correspond to paths though the environment. The focus of this simulator is the implementation of DFT as the path selection mechanism.

This simulator functions as a controlled environment in which one can test the strengths and weaknesses of DFT in a dynamic environment. The DFT framework was created to model static

single-stage decisions in a static environment. This tool was created primarily as a test bed for exploratory research. By altering the maps and the knowledge of the robot, we can see if this plan selection algorithm is sufficient for successfully navigating dynamic environments. It also allows us to observe any non-obvious behaviors predicted by the model. It also provides a fast development environment for testing the necessary capabilities of a path selection mechanism for intelligently controlling robot movement.

3.1 Simulator Description

The robot model has a simple two-wheel differential drive system defined by a body radius and velocities for each of the wheels. The robot senses its environment using an array of range finding sensors equally spaced around the front of the body, covering a 180° field of view. No frictional forces were modeled and lasers always returned a reading. The value returned was the true distance plus some normally distributed noise.

The simulator places the robot within a map containing multiple rooms. Figure 3 includes a screenshot of the simulator. Two main displays are given. The display on the left shows the true map, the placement of the robot, and a representation of the robot's range finding sensors. The display on the right is a representation of the knowledge/beliefs of the robot. This includes borders of rooms, transition points between rooms, planned paths, and the location of "enemies." The robot must plan paths to a specified goal. In this environment, it is trying to examine the tradeoffs of three different path features. The first feature is the estimated length of the path. The robot wants to keep overall path length to a minimum. The second feature is the estimated distance traveled through unknown space. Large values of this "unknown distance" indicate a greater chance of encountering unknown obstacles so it is ideal to select a path with a small unknown distance. Finally, the path has a danger level influenced by the existence of enemies in a particular room. The robot reconsiders available paths every time its knowledge of the world changes.

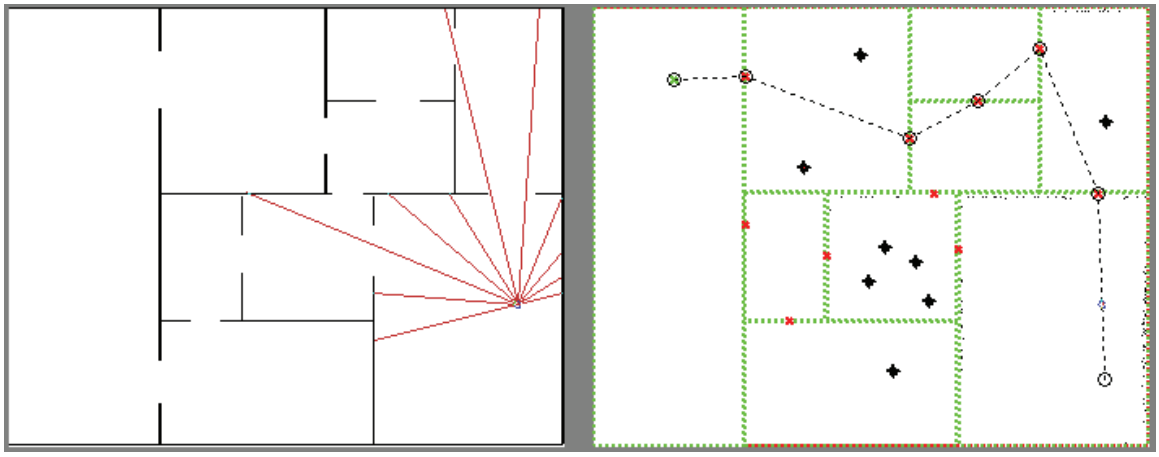

Figure 3. Testing simulator.

3.2 Test Environment

The first step in testing the simulator is to see the consequences of replanning in conditions mimicking the experiments conducted with the abstract implementation. Since the context effects can only be investigated by examining distributions of choice selections, I tried to replicate conditions demonstrating temporal discounting and speed/accuracy tradeoffs.

A map was generated as seen in figure 3. The robot's starting position is also shown. Although the robot plans and navigates on its own, the user is responsible for adding knowledge about the environment. For example, to simulate exploration of unknown spaces, the robot initially has sparse information. When it enters a room and records enough raw data about the room, the user must pause the system and indicate the location of any new rooms, doors, or enemies observed. The robot will then replan and the system can be started again.

3.3 Observations

One of the first unexpected behaviors observed was repetitive actions due to the temporal discounting. If we image two similar paths to a goal, both containing an enemy near the end of the path, the robot may select the path on its left. However, if it regularly reevaluates its plans, the negative influence of the approaching enemy makes the path less desirable as the robot approaches the goal. The robot can then act as if it becomes afraid and decides to go the other direction (to the right). It will continue along this direction until it comes close to the new enemy. It will then get scared and choose to go to the left given that the enemy it first encountered is far away and therefore seems less dangerous. The robot can get stuck, going back and forth in its decisions.

Several solutions exist to solving this problem. It was not the scope of this project to experimentally test any of these solutions under conditions of actual human path planning; however, some make more sense than others. One solution is to increase the importance of path length relative to the importance of avoiding enemies. In this case, the benefits of a shorter path outweigh the fears of the impending encounter with the enemy. Unfortunately, this does not provide a decent general solution. Parameters can be adjusted to stop the behavior in a particular situation, but there are other cases that still lead to repetition. A second solution is to incorporate learning to limit the temporal discounting. In this case, the robot would remember how bad the enemy appeared even when it moves away. At first, this seems like a decent solution, but it ultimately disregards the conclusions of studies of human discounting. People who discount the value of money given at a later time have presumably received money before and this memory does not stop the discounting. A third solution considered is the addition of dynamically changing importance of specific features. A growing importance of short paths might reflect a sense of urgency that grows as time passes. One of the benefits of this solution is that it has previously been incorporated into the DFT framework (*17*). A weakness to this solution is that it then requires a model of how each particular feature may change over time. A final solution considered is to include a bias for actions contained within a plan that was previously selected.

This solution supports observations of the “sunk costs” effect, where people will continue with a plan they have invested a lot into even when new information devalues the original plan. The final two suggested solutions will likely play a role in a fully cognitive autonomous robot; however, it is the last one that provides the most immediate solution for obtaining robust non-scripted behaviors on a physical robotic platform.

At some point while developing scenarios to look at speed/accuracy tradeoffs, it was realized that such tradeoffs might have two different forms. The studies discussed earlier with human participants involve an externally imposed time restriction. However, several changes to parameters could be used to force a faster decision when a decision agent knows time is a priority. This distinction is blurred in a path planning situation. If a user tells a robot it must get to its goal now, it cannot. It must still spend the time traversing a path and has the option to replan along the way. In this situation an external mandate for a quick decision may lead to an internal manipulation to speed up planning.

Within the DFT framework, one could lower the decision threshold to speed up decisions. This would lead to an increase on the reliance on biases as seen when forced to make quick decisions. Currently, the time needed to consider each step of a plan is not modeled. However, it does make sense that under time pressure, one could lower his/her planning horizon to limit the amount of branches in the search tree to explore. This however, requires some heuristic for measuring how close an abbreviated plan gets the agent to the intended goal. This would cause an agent to focus on immediate payoffs. This solution predicts that temporal discounting is a function of the time pressure felt by the agent.

4. Summary and Conclusions

By implementing DFT within a robot simulator, we can begin to see some of the challenges of taking a psychological model out of the laboratory and into the real world. Some mathematical models merely claim to describe patterns of behavior. Models such as DFT make bolder claims about the cognitive processes underlying the behavior. These processes should remain even under different conditions. For that reason, robotic implementations serve as alternative tests of such sophisticated cognitive models.

Recognizing that the jump from abstract mathematical evaluation to real-world interactions might be too drastic, a robot simulator in a simulated environment serves as a useful testing platform. In this particular case, we have recognized necessary changes and additions to DFT that need to exist before getting the types of semi-autonomous capabilities we hope for.

The lessons learned from this exercise are currently being incorporated into an implementation of DFT on an existing robotic architecture. The cognitive robotics team within the Human Research and Engineering Directorate (HRED) is working toward the development of a robotic

control system that is inspired more by models of human cognition than traditional AI approaches to robotics (*10*). Having DFT implemented within the architecture itself should allow for fast decisions. Initial tests on simple decisions show that they can be made in about .1 of a second. This will allow the robot to make decisions on-the-fly during real-time operation. This will permit us to observe how DFT style decisions function in complex environments. In addition, we hope to alter parameters to see how behaviors change. This is analogous to altering the "personality" of the robot. A robot with a high threshold parameter will make slow but accurate decisions. A robot with a fast discounting rate will be focused on the present and will make fast decisions.

5. References

1. Scheutz, M.; Schermerhorn, P.; Kramer, J.; Middendorff, C. *1st ACM International Conference on Human-Robot Interaction*, Salt Lake City, UT, 2006, 226–233.
2. Beer, R. "The Dynamics of Brain-Body-Environment Systems: A Status Report" in *The Elsevier Handbook of Embodied Cognitive Science*, Calvo, P. and Gomila, A., eds., Elsevier Press, In Press.
3. Savage, L. J. *The Foundations of Statistics*. New York: John Wiley and Sons, 1954.
4. von Neumann, J.; Morgenstern, O. *Theory of Games and Economic Behavior*. Princeton University Press: Princeton, NJ, 1947.
5. Tversky, A. *Psychological Review* **1972**, *79* (4), 281–299.
6. Busemeyer, J. R.; Townsend, J. T. *Psychological Review* **1993**, *100*, 432–459.
7. Busemeyer, J. R.; Johnson, J. G. "Micro-process models of decision-making" in *Cambridge Handbook of Computational Cognitive Modeling*, Sun, R., ed., Cambridge University Press, 2006.
8. Usher, M.; McClelland, J. L. *Psychological Review* **2001**, *102* (3), 550–592.
9. Usher, M.; McClelland, J. L. *Psychological Review* **2004**, *111*, 757–769.
10. Kelley, T. D. *International Journal of Advanced Robotic Systems* **2006**, *3* (3), 219–222.
11. Critchfield T. S.; Kollins, S. H. *Journal of Applied Behavior Analysis* **2001**, *34* (1), 101–122.
12. Johnson, J. G.; Busemeyer, J. R. *Theory and Decision* **2001**, *51*, 217–246.
13. Miller, N. E. "Experimental studies of conflict" in *Personality and the Behavior Disorders*, J. McV. Hunt., ed., The Ronald Press: New York, 1944, pp 431–465.
14. Vickers, D.; Burt, J.; Smith, P.; Brown, M. *Acta Psychologica* **1985**, *59* (2), 129–161.
15. Diederich, A. *Psychonomic Bulletin and Review* **2003**, *10* (1), 157–166.
16. Diederich, A.; Busemeyer, J. R. *Journal of Mathematical Psychology* **2003**, *47*, 304–322.
17. Busemeyer, J. R.; Dimperio, E.; Jessup, R. K. "Integrating Emotional Processes Into Decision-Making Models" in *Integrated Models of Cognitive Systems*, Gray, W., ed., Oxford University Press, 2007.

INTENTIONALLY LEFT BLANK.

Sensors and Electron Devices Directorate (SEDD)

INTENTIONALLY LEFT BLANK.

U.S. Army Research Laboratory

SUMMER RESEARCH TECHNICAL PAPER

Development of a Miniaturized Photoacoustic Chemical Sensor

by John S. Bender

Contents

List of Figures **93**

Abstract **94**

Acknowledgment **95**

1. Introduction/Background **96**

2. Experiment/Calculations **98**

2.1 MEMS-scale PA Cell 99

2.2 Quantum Cascade (QC) Laser 99

2.3 Sample Generation 100

2.4 Data Acquisition 100

3. Results and Discussion **101**

3.1 PA Signal Maximization 101

3.2 PAS Sensor Limit of Detection for DMMP and PA Cell Comparison 102

4. Summary and Conclusions **103**

5. References **104**

List of Figures

Figure 1. Schematic diagram outlining transduction techniques based on physical changes associated with the Photothermal effect. 97

Figure 2. Schematic diagram of photoacoustic cell. 98

Figure 3. Block diagram of photoacoustic (PA) setup. 99

Figure 4. Assembled MEMS-scale PA cells. 99

Figure 5. Modulation Frequency scans for (a) PA cell D3-002 and (b) PA cell D4-002. The maximum quadrature (*Y*) signal occurred when the in-phase (*X*) signal was at zero. 101

Figure 6. Comparison of photoacoustic spectrum of DMMP with FTIR spectrum of DMMP using PA cells (a) D3-002 and (b) D4-002. 102

Figure 7. Replicate measurements of detection limit for DMMP using PA cell D3-002. 102

Figure 8. Replicate measurements of detection limit of system using PA cell D4-002. 103

Abstract

The detection and identification of chemical warfare agents and hazardous industrial chemicals has become a priority for military and homeland defense applications. Therefore, there is an urgent need for a portable chemical sensing platform to increase battlefield survivability and decrease collateral damages. Current work focuses on the development of a miniaturized photoacoustic chemical sensor using a quantum cascade (QC) laser in combination with microelectromechanical systems (MEMS)-scale photoacoustic cell designs. Two photoacoustic cells were investigated, each producing detection limits for dimethyl methylphosphonate (DMMP), a standard nerve agent simulant, below 15 parts-per-billion (ppb), and the minimum detection limit for the system is 7(±2) ppb. Results suggest that sensitivity can be increased by incorporating an acoustic filter design into the sample delivery pathway of the cell and that continued development of a miniaturized photoacoustic sensor is viable.

Acknowledgment

The author wishes to acknowledge the mentorship of Dr. Ellen L. Holthoff.

1. Introduction/Background

Chemical Warfare Agents (CWAs) and other industrial chemicals continue to be a real and increasing threat to the warfighter as the enemy continues to rely on extremist and terroristic ideals. The relative ease with which terrorist groups can obtain these hazardous substances perpetuates the risk involved. For example, the use of Sarin gas by the Aum Shinrikyo terrorist group in 1995 (*1*) and the use of Chlorine gas in Iraq in 2007 (*2*) demonstrate the availability of these chemicals and the need for a ubiquitous sensor package that is portable, robust, adaptable, and energy efficient. A possible solution to satisfy these development parameters is a sensor based on photoacoustic spectroscopy (PAS).

PAS is a transduction technique in which the photothermal (PT) and photoacoustic (PA) effects are exploited. The PT effect is observed when incident radiation encounters an absorbing medium and promotes a component of that medium into an electronically excited state. This excitation is normally followed by a majority of the energy being released through a rapid, non-radiative relaxation, which produces heat followed by a change in temperature, density, and/or pressure. The PA effect is closely related to the PT effect and is observed when modulated radiation is incident upon the absorbing medium. When a gaseous sample is considered, the absorption of the modulated radiation produces a correspondingly modulated, longitudinally polarized pressure wave in response to the PT effect (*3*). This pressure wave can then be measured using a suitable transducer (e.g., acoustic microphone, piezoelectric transducer). PAS is considered to be an indirect method of detecting optical absorbance since the transmission of the radiation from the incident source is not measured to produce a signal. Recent, as well as past work, has confirmed the potential for the production of detection limits as low as the parts-per-trillion (ppt) range (*4*-*6*). Although these studies demonstrate the particular sensitivity of PAS, current work focuses on the scaling of the platform to reduce the logistics problems associated with traditional laboratory systems.

Limited research has been conducted in the area of photoacoustic sensor miniaturization (*5*-10). The initial investigation regarding characteristics of PAS when its components are scaled to a micro-design revealed that such a system will retain the sensitivity of a macro-design and may even surpass it (*5*-*8*). Recently, detection limits in the parts-per-billion (ppb) range have been shown for dimethyl methylphosphonate (DMMP) using a CO_2 laser in combination with a microelectromechanical systems (MEMS)-scale PA cell[5-8]. These results are promising, however, the CO_2 source is bulky and consumes a significant amount of power. In order to overcome these obstacles, MEMS-scale PA cells and quantum cascade (QC) lasers are currently being investigated for integration into a PAS sensor platform.

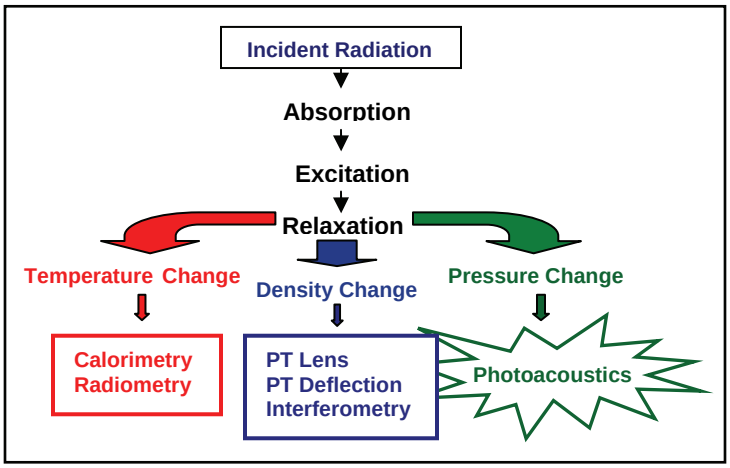

Figure 1. Schematic diagram outlining transduction techniques based on physical changes associated with the Photothermal effect.

For trace gas monitoring, mid-infrared (IR) QC laser sources are virtually ideal since the fundamental vibrations of molecules have the largest absorption coefficients in this region of the spectrum. These semiconductor sources are micro-fabricated to operate anywhere between ~3 µm and ~25 µm and are able to emit several milliwatts of power while operating at or near room temperature(*11-13*). Also, within the range of the spectrum for which they are fabricated, QC lasers are continuously tunable. This fact is of major importance to compound selectivity for detection. QC lasers are extremely advantageous to the development of miniaturized sensors for several reasons: compact packaging, reasonable spectral emission, and information rich mid-IR operation without cryogenic cooling (*14, 15*).

In order to achieve a miniature PA sensor, the traditional PA cell must be scaled down. This is convenient because unlike other absorption spectroscopy techniques, PAS signal generation is not solely dependent upon path length but is more volumetric in nature. In effect, signal generation may be increased with the miniaturization of the cell due to the inverse relationship of resonant chamber volume to the temperature/pressure coupling of the sample gas. The theoretical design of an acoustic cell is beyond the scope of this work. However, it has been described in great detail elsewhere (*4, 9, 10*). Generally, an acoustically resonant PA cell consists of a resonant chamber, buffer volumes, a gas inlet/outlet, windows, and a transducer. The buffer volumes are designed to act as acoustic filters to reduce noise from optical absorption at the windows and to allow the decay of pressure waves with minimal signal interference (*4*). A generic design criterion for these noise suppression structures suggests that the length and diameter of the buffer volumes should be half and 3 times that of the resonant chamber, respectively. These parameters dictate the efficacy of the acoustic filtration and stem directly from standard acoustical modeling practices (*4*). The PA cell (resonant chamber) itself has a resonant frequency associated with it, which can be described by (*9*)

$$f = \frac{c}{2l} \tag{1}$$

where f is the resonant frequency, c is the speed of sound at a given temperature, and l is the length of the resonant chamber. At this frequency of modulation, the PA signal is amplified due to the energy storage associated with the acoustic oscillation. Additionally, the PA cell is designed to minimize superfluous optical absorption. The optimal radius of the resonator can be found by focusing the incident beam so that the Rayleigh range coincides with half of the chamber length. Then, the beam waist radius can be found using[16]

$$l = \frac{2\pi r_0^2}{\lambda} \tag{2}$$

where l is the length of the resonator, r_0 is the laser beam radius at the beam waist, and λ is the wavelength of light being used. To ensure a clear aperture for the beam, the resonator radius should be 3 times that of r_0. This will minimize optical vignetting at a wide range of wavelengths and focal lengths.

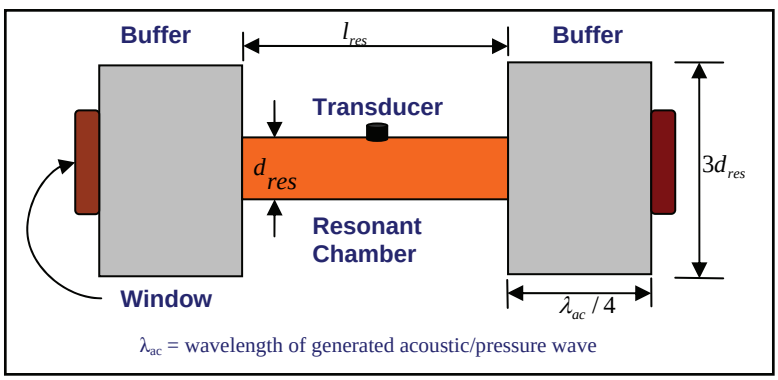

Figure 2. Schematic diagram of photoacoustic cell.

The work discussed within this paper focuses on the use of a continuously tunable QC laser in combination with two different MEMS-scale photoacoustic cell designs for the development of a portable PA sensor.

2. Experiment/Calculations

A schematic diagram illustrating the complete photoacoustic experimental setup used in this work is shown in figure 3. The system consisted of a quantum cascade laser with function generator for controlled excitation, permeation oven for sample introduction, MEMS-scale photoacoustic cell with microphone for detection, focusing optics, and lock-in amplifier for data acquisition.

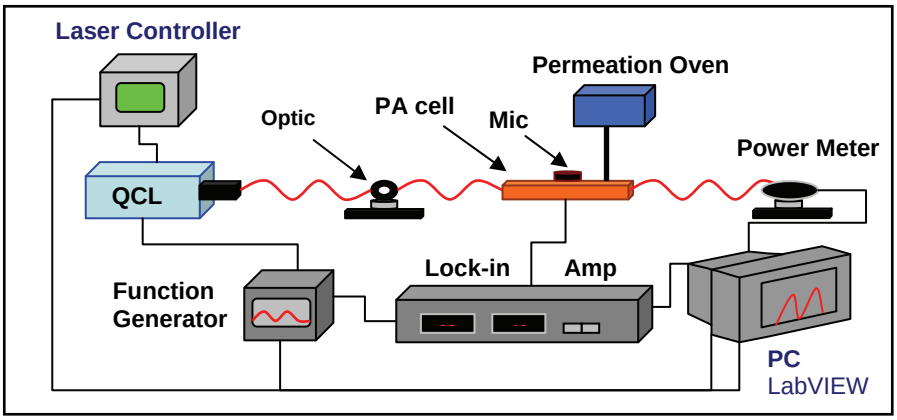

Figure 3. Block diagram of photoacoustic (PA) setup.

2.1 MEMS-scale PA Cell

Two PA cells were designed within Army Research Laboratory (ARL) and fabricated by Infotonics Technology Center, Inc. for investigation. The MEMS-scale PA cells used in this work have been scaled down from traditional PA cell size by roughly an order of magnitude, from the centimeter range to the millimeter range. Both cells had a resonant chamber that measured 10 mm long with a diameter measuring 0.864 mm. The buffer volumes measured half the length and 3 times the diameter of the resonator tube with a gas inlet located at one buffer and an outlet located at the other. Germanium windows (Edmund Optics, model: NT47-685) were fixed at each buffer with epoxy. I used an acoustic microphone (Knowles, model: FG-23629) as the transducer in both of the cells, which were mounted between circuit boards in order to create connections for the microphone power supply (AA battery) and output to a lock-in amplifier. Cell D3-002 had a convoluted inlet/outlet design, whereas, Cell D4-002 had a T-design for the gas inlet/outlet (figure 4).

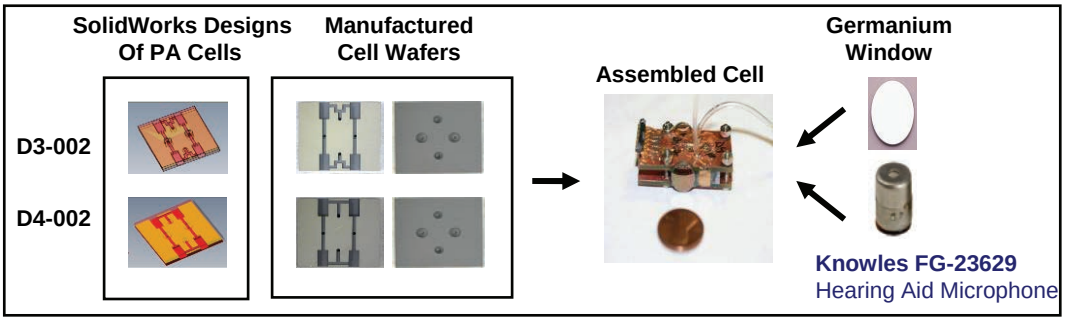

Figure 4. Assembled MEMS-scale PA cells.

2.2 Quantum Cascade (QC) Laser

A continuous wave (cw), external grating cavity QC laser (Daylight Solutions, Inc., model: 21096) with an external controller (Daylight Solutions, Inc.) was used as the incident source. The laser had a wavelength tuning range from 1005 cm^{-1} to 1070 cm^{-1} (9.34 µm to 9.95 µm) with its center wavelength at about 1042 cm^{-1} (9.6 µm). This range corresponds with a major

absorption feature of DMMP. I measured the spectral output of the laser at 16.22 mW. Modulation was achieved by employing a function generator (Stanford Research Systems, model: DS340) to pump the laser with a 6.00 V sine wave. A power meter (Ophir Optronics, model: Nova II) equipped with a thermal head (Ophir Optronics, model: 3A) was used to measure optical transmission from the laser, and I used a compact thermo-electric water chiller (Solid State Cooling Systems, model: Oasis 150 Chiller) to keep the laser temperature at 20 °C. Beam focusing was achieved with a plano-convex, CaF_2 focusing optic (ISP Optics, model: custom).

2.3 Sample Generation

The analyte, DMMP, was delivered to the PA cell by a calibration gas generator (VICI Metronics, model: Dynacalibrator 190). A certified DMMP permeation tube (VICI Metronics, model: Dynacal 107-150-7845-C100), which had a release rate of 1180(±2) ng/min, was placed in the oven and held at a constant temperature of 100 °C. Varying flow rates of the N_2 carrier gas from 200 mL/min. to 600 mL/min. governed the concentration of DMMP. Higher flow rates were avoided as the noise associated with the flow dramatically increased beyond the aforementioned range.

2.4 Data Acquisition

I used a lock-in amplifier (Stanford Research Systems, model: SR830 DSP) to capture the signal from the microphone of the PA cell and was operated with a 3 sec time constant at the modulation frequency of the QC laser. A PC with the program LabVIEW (National Instruments, version 8.2) was used to simultaneously control the laser, collect measurements from the power meter, and collect voltage measurements from the lock-in amplifier. The in-phase (X), quadrature (Y), amplitude (R), and phase angle (θ) elements of the PA signal were collected from the amplifier.

I obtained the photoacoustic spectrum of DMMP by holding the modulation frequency constant while a laser wavelength scan was performed with 1.07 ppm of DMMP used as the absorbing substrate. This allowed the determination of the major peak of interest and a comparison with Fourier transform infrared (FTIR) spectroscopy data. To collect the PA data, the source was tuned from 1032 cm^{-1} to 1070 cm^{-1} (9.3 µm to 9.7 µm), which is a range that corresponds with a major absorption feature of DMMP, in 0.5 cm^{-1} increments 50 measurements were made at each increment, and a mean value was calculated and recorded for the subsequent construction of the spectrum.

To find the modulation frequency at which the PA signal was maximized, I held the wavelength of the laser constant while a modulation frequency scan was performed with 1.07 ppm of DMMP used as the absorbing substrate. The scans were performed from 10 kHz to 40 kHz with each cell. I used the quadrature (Y) component of the PA signal for detection limit determinations,

and the maximum signal could be observed when the in-phase component did not produce a voltage.

To determine the limit of detection (LOD) of the system for DMMP, the modulation frequency and wavelength of the source were held constant as the concentration of DMMP was varied. Mean values and standard deviations of 200 signal measurements were calculated at each concentration. I used these values to prepare linear regressions with which the LOD could be calculated by taking 3 times the standard deviation of the background and dividing it by the slope of the linear function. Replicate LOD measurements were made, averaged, and analyzed statistically.

3. Results and Discussion

By obtaining the photoacoustic spectrum of DMMP, maximizing the photoacoustic signal of the system as a function of frequency, and measuring the PA signal as a function of concentration, the LOD of a PAS sensor platform using a modulated cw QC laser and a MEMS-scale PA cell was determined. Two PA cells were used and compared as an initial examination of design refinement. The thought behind these designs involved gas delivery/exhaust noise suppression.

3.1 PA Signal Maximization

The calculated resonant frequency of the PA cells corresponding to equation (1) was ~17.2 kHz. After an attempt to confirm this fundamental resonance frequency, it was found that the maximum signal did not correspond to the calculated value but was obtained at a 23.58 kHz modulation. This may be due to characteristics of the microphone, cell construction, and/or the miniaturization of the cell as it relates to the acoustic theory that determines this resonance. The subsequent portions of this work were performed using a 23.58 kHz modulation of the incident source in order to take full advantage of the signal strength. Note that the broad nature of acoustic resonance could easily result in slightly offset modulation frequencies at several different laser wavelengths.

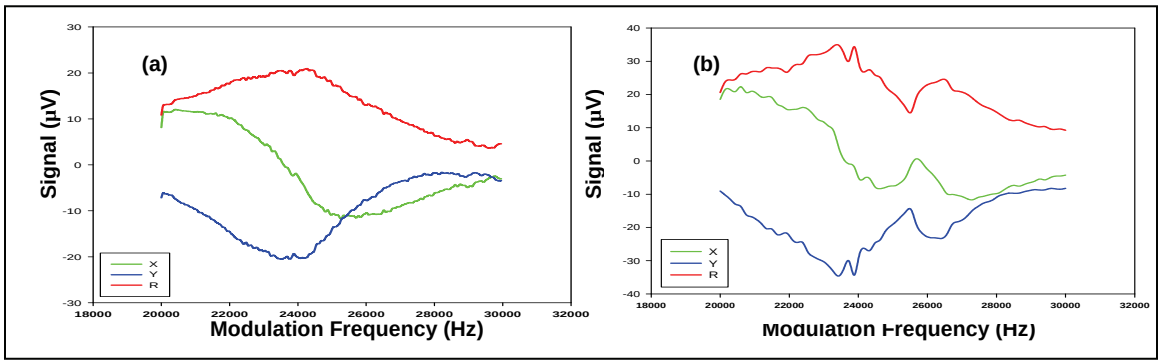

Figure 5. Modulation Frequency scans for (a) PA cell D3-002 and (b) PA cell D4-002. The maximum quadrature (*Y*) signal occurred when the in-phase (*X*) signal was at zero.

In order to find the wavelength at which to measure the PA signal, a PA spectrum of DMMP was obtained using both PA cells. These spectra were compared to FTIR data for DMMP. Although the mode hopping of the QC laser caused signal fluctuations, the spectra were found to be in agreement. In future applications, the laser may be operated in a single mode by simultaneous control of laser current, grating angle, and cavity length *(17)*. Based on the data collected, it was found that the major absorption peak occurred at 1050.90 cm^{-1} (9.5 µm).

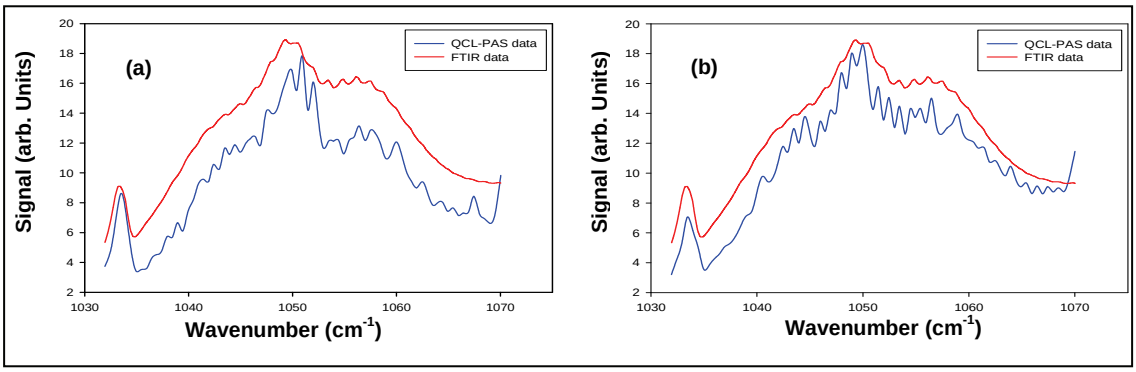

Figure 6. Comparison of photoacoustic spectrum of DMMP with FTIR spectrum of DMMP using PA cells (a) D3-002 and (b) D4-002.

3.2 PAS Sensor Limit of Detection for DMMP and PA Cell Comparison

The MEMS-scale PAS sensor 3σ limit of detection was determined at the 95% confidence interval to be 7(±2) ppb for DMMP (PA Cell D3-002). The linear regressions of signal vs. concentration showed excellent linearity with correlation coefficients ranging from 0.997 to 0.999.

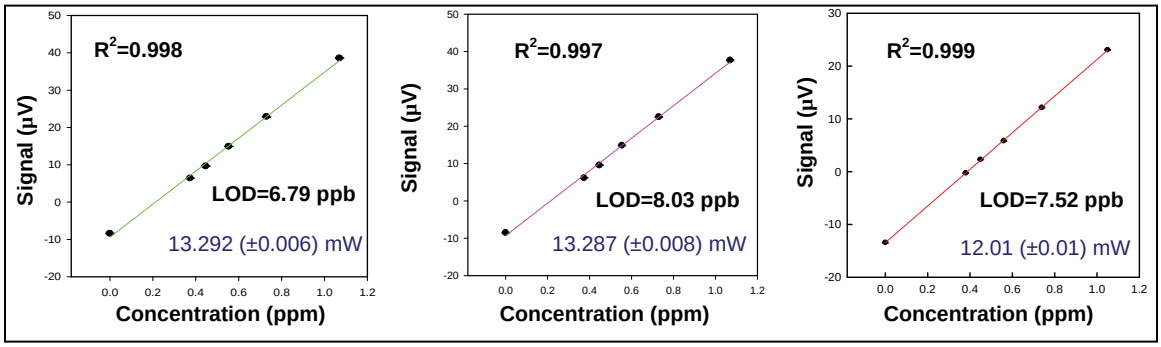

Figure 7. Replicate measurements of detection limit for DMMP using PA cell D3-002.

For cell D4-002, the 3σ limit of detection was estimated at the 95% confidence interval to be 13.7(±0.9) ppb for DMMP. Again, the linear regressions showed excellent linearity with correlation coefficients measuring 0.999.

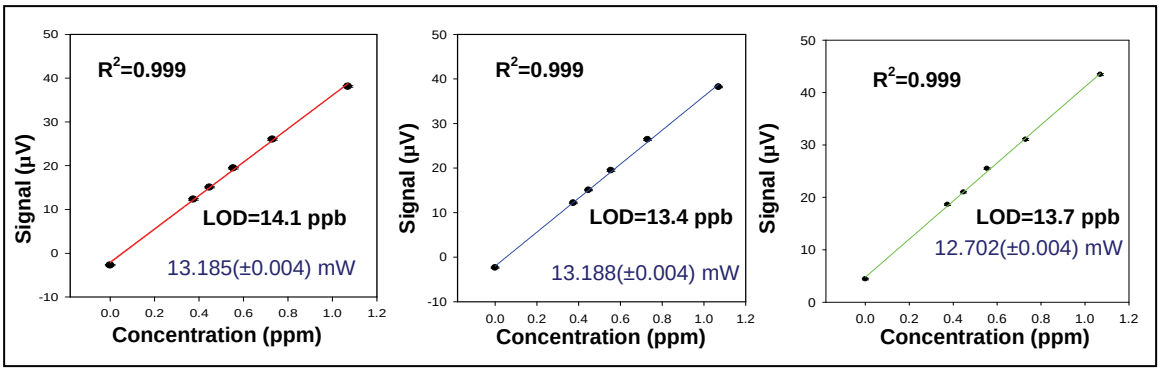

Figure 8. Replicate measurements of detection limit of system using PA cell D4-002.

I determined that the PA cells were statistically different at the 99.9% confidence interval. The difference is attributed to the pattern of the gas inlet/outlet design. The convoluted pathway of cell D3-002 may dampen gas flow noise before it passes through the resonator tube, whereas, the T-design of cell D4-002 does not act to the same degree, which effectively increases flow noise. Further reduction of delivery/exhaust noise may be possible with the addition of acoustic notches to the design of the pathway. These adjustments are made to increase overall sensitivity of the system.

4. Summary and Conclusions

It has been demonstrated that a MEMS-scale PAS sensing platform using a modulated cw QC laser as the incident source is capable of producing detection limits in the single digit ppb range for DMMP, a standard nerve agent simulant. The 30 min. pulmonary exposure limits for relative nerve agents have been reported at approximately 575 ppb and 5.8 ppb with regard to lethality and initial health effects, respectively (*18*). Although the necessary detection limit has not yet been realized, the results reported here show great promise toward this goal. With further optimization, this sensor platform should yield the desired results. Also, it has been determined that alternative designs for the PA cell may suppress noise and in effect, increase sensitivity. Current work focuses on PA cell design refinement, which will further suppress delivery/exhaust noise, and optics optimization, which will effectively increase spectral output available for absorption by the sample. Future work will involve testing of board level peripheral electronics and new laser sources.

5. References

1. Olson, K. B. *Emerging Infectious Diseases* **1999**, *5*, 513–516.
2. Semple, K. *New York Times*, March 18, 2007.
3. Petryk, M.W.P. *Applied Spectroscopy Reviews* **2007**, *42*, 287–343.
4. Bijnen, F.G.C.; Reuss, J.; Harren, F.J.M. *Review of Scientific Instruments* **1996**, *67*, 2914–2923.
5. Pellegrino, P.; Polcawich, R. *SPIE Chemical and Biological Sensing IV* **2003**, *5085*, 52–63.
6. Pellegrino P.; Polcawich, R.; Firebaugh, S. *SPIE Chemical and Biological Sensing V* **2004**, *5416*, 42–53.
7. Heaps, D.; Pellegrino, P. *SPIE Chemical and Biological Sensing VII* **2006**, *6218*, 621805-(1–9).
8. Heaps, D.; Pellegrino, P. *SPIE Chemical and Biological Sensing VIII* **2007**, *6554*, 65540F-(1–9).
9. Firebaugh, S. L.; Jensen, K. F.; Schmidt, M. A. *Journal of Microelctromechanical Systems* **2001**, *10*, 232–237.
10. Firebaugh, S. L.; Jensen, K. F.; Schmidt, M. A. *Journal of Applied Physics* **2002**, *92*, 1555–1563.
11. Paldus, B. A.; Spence, T. G.; Zare, R. N.; Oomens, J.; Harren, F.J.M.; Parker, D. H.; Gmachl, C.; Cappasso, F.; Sivco, D. L.; Baillargeon, J. N.; Hutchinson, A. L.; Cho, A. Y. *Optics Letters* **1999**, *24*, 178–180.
12. Kosterev, A.; Wysocki, G.; Bakhirkin, Y.; So, S.; Lewicki, R.; Fraser, M.; Tittel, F.; Curl, R. F. *Applied Physics B* **2008**, *90*, 165–176.
13. Kosterev, A. A.; Tittel, F. K. *IEEE Journal of Quantum Electronics* **2002**, *38*, 582–591.
14. Hvozdara, L.; Pennington, N.; Kraft, M.; Karlowatz, M.; Mizaikoff, B. *Vibrational Spectroscopy* **2002**, *30*, 53–58, 2002
15. Sigrist, M. W.; Bartlome, R.; Marinov, D.; Rey, J. M.; Vogler, D. E.; Wächter, H. *Applied Physics B* **2008**, *90*, 289–300.
16. Milonni, P. W.; Eberly, J. H. *Lasers*, John Wiley and Sons, Inc., 1988

17. Pushkarsky, M.; Tsekoun, A.; Dunayevskiy, I. G.; Go, R.; Patel, C. K. *PNAS* **2006**, *103*, 10846–10849.

18. *Federal Registry* **2003**, *68*, 58348–58350.

INTENTIONALLY LEFT BLANK.

U.S. Army Research Laboratory

SUMMER RESEARCH TECHNICAL PAPER

Demonstration of a Multiplexed Electrospray Micromachined in Silicon Substrates for Fuel Atomization

by Israel Boniche

Contents

List of Figures **109**

Abstract **110**

Acknowledgment **111**

1. Introduction/Background **112**

2. Fabrication **113**

2.1 Extractor Layer 113

2.2 Nozzle Array Layer 114

2.3 Assembly of Nozzle and Extractor Layers 115

3. Results and Discussion **117**

4. Summary and Conclusions **118**

5. References **119**

List of Figures

Figure 1. Electrospray device (12.5 mm x 12.5 mm x 1 mm) showing cone-jet and spray regions. A cut filter is attached to the ESpray device to create a reservoir for the fuel.....113

Figure 2. Process flow for the fabrication of the extractor layer. 114

Figure 3. Process flow for the fabrication of the nozzle array layer.....115

Figure 4. SEM image of a 75 µm outer diameter (O.D.) nozzle array layer with sharp sidewalls.....115

Figure 5. Assembled extractor and nozzle layers are epoxied to filter and to conducting stainless-steel tubes with inner wire. 116

Figure 6. Design guidelines and geometrical properties of various fabricated ESpray devices.....116

Figure 7. Electrospray test setup using pure Ethanol. High voltages (HV1 = 8 kV > HV2 = 7 kV) are applied to the nozzle and extractor layers; respectively, and grounded mesh collects the charged fluid. 117

Figure 8. Illuminated spray with laser diode. (a) Mist of droplets during electrospraying, and (b) appearance of side-spray that may flood extractor layer due to space-charge effects. 118

Abstract

This paper reports the design, fabrication, and testing of multiplexed electrospray (ESpray) devices micromachined in silicon substrates for portable power systems. Additionally, an experimental test-stand was developed to facilitate testing. Through the atomization or breaking down of fuel into finer droplets, this design aims to increase the efficiency for liquid hydrocarbons and enable the use of JP-8 diesel in miniaturized combustion systems such as gas heat engines and microcombustors. The microfabrication of ESpray prototypes requires standard photolithography and deep-reactive ion etching (DRIE) of silicon. Precise alignment and assembly of silicon nozzle and extractor layers is accomplished with optical fibers embedded between the surfaces of each layer. To demonstrate electrospraying, devices were first tested using Ethanol over a range of applied voltage and flow rates. Although limited by space-charge effects, 19-nozzle devices (12.5 mm by 12.5 mm by 1 mm) demonstrated flow rates of 0.50 ml/hr/nozzle and 0.35 ml/hr/nozzle for 90 µm and 75 µm outer diameter (O.D.) nozzles; respectively, with a 1 kV potential difference (and a $7x10^5$ V/m removal electric field) between the layers.

Acknowledgment

The author wishes to acknowledge the mentorships of Brian Morgan and Mike Waits.

1. Introduction/Background

In recent years, the U.S. Army has increased efforts to develop compact, portable power systems that can convert logistic, high-energy liquid fuels such as JP-8 into electrical energy (*1-3*). These power converters effectively used electrospray (ESpray) systems for breaking up fuel into fine droplets for meso-scale combustion applications. However, if smaller droplet sizes could be obtained, then it would be possible reduce fuel evaporation time and improve mixing with the ambient or oxidizer. As a result, a smaller volume would be necessary for combustion; and as a result, increase the combustion efficiency. Moreover, a previous work demonstrated that smaller droplet sizes are possible at the expense of a lower flow rate per nozzle (*2*). Thus, to maintain or increase flow rate requires increasing the number of jets or nozzles operating in parallel (multiplexing), as opposed to dispersing the liquid fuel from a single nozzle. This paper expands on previous work (*4*) and presents the microfabrication of ESpray devices in silicon substrates, as well as a technology demonstration using Ethanol as fuel. Consequently, this research work will be relevant to the microelectromechanical-systems (MEMS)-based power components efforts that are currently being developed in the Sensors & Electrons Devices Directorate (SEDD) under the power for the dismounted Soldier Army Technology Objective (ATO).

The ESpray phenomenon effectively disperses or breaks up a liquid into smaller droplets of uniform size (figure 1). A liquid such as JP-8 or Ethanol flows through a capillary tube and emerges at the tip. This liquid forms a Taylor cone at the tip of the nozzle through the balance of capillary forces, and the applied potential difference between the nozzle and extractor layers. When a critical electric field is reached and exceeded (due to applied voltages HV1-HV2), a thin jet of charged droplets emerges from the cone. Fluctuations at the tip of the jet disperse the charged particles past the extractor layer. Coulombic repulsive forces between the charged droplets cause them to spread into a mist and form the electrospray. Additionally, shielding from the droplets upstream (space-charge effects) can cause satellite droplets, near the edge of the spray, to fly back to the extractor; which may lead to flooding and disrupt the electrospray (*5*). To counteract this effect, an additional electrically grounded collector mesh is placed upstream (figure 1), so that a sufficient large driving field (HV2 – gnd) pulls away the mist from the extractor layer.

This paper presents the fabrication and the development of a test procedure to determine the maximum flow rates, limited by space-charge, for various device designs. This will enable the development of an empirical design space model to determine the optimum geometry for maximizing liquid flux (flow rate/area).

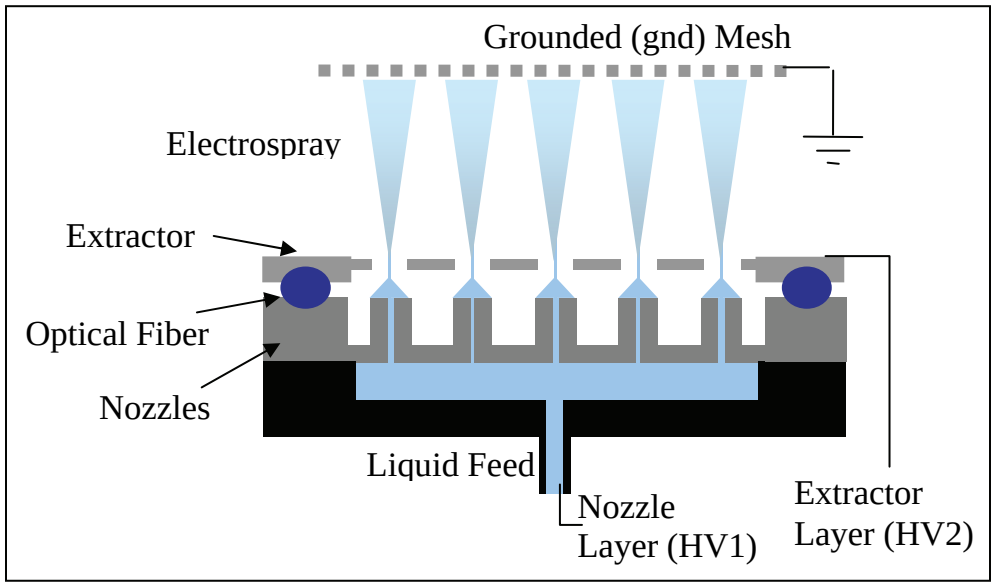

Figure 1. Electrospray device (12.5 mm x 12.5 mm x 1 mm) showing cone-jet and spray regions. A cut filter is attached to the ESpray device to create a reservoir for the fuel.

2. Fabrication

The multiplexed electrospray (ESpray) consists of three main components: (1) extractor layer, (2) nozzle array layer, and (3) optical fiber as a spacer (*4*) (figure 1). The main function of the fiber optic cable (with diameter of 250 ± 5 µm) is to provide electrical insulation and set the gap between the two silicon layers. Additionally, the optical fiber segment is embedded within etched regions on the surface, and after using an epoxy to keep in place, the nozzle arrays can be precisely centered below the extractor holes to within 2 µm. The assembled ESpray is then attached to a cut filter that serves as the fluid reservoir and feeds in the fluid to the device. Micromachining in silicon allows for batch fabrication of ESpray devices with a high density of nozzles of varying nozzle diameter, and nozzle separation or pitch. Using design rules previously developed (*4*, *5*), devices with outer nozzle diameters (O.D.) of 90 µm and 75 µm were fabricated to accommodate for applications where different flow rates, droplet diameters, and geometries are required. As a first step to demonstrate and facilitate testing at the Army Research Laboratory (ARL), devices with 19 nozzles arranged in a hexagonal pattern were fabricated at 1310 nozzles/cm^2 and 1890 nozzles/cm^2 for the 90 µm and 75 µm O.D.; respectively.

2.1 Extractor Layer

The fabrication of the extractor layer consists of a two-mask process using a 100 mm diameter silicon substrate (~205 µm in thickness) with a 1 µm thermally-grown SiO_2 (figure 2). First, the topside oxide layer is patterned to define a cavity or active area for the extractor holes. Next, using a front-to-back alignment camera system, the bottom-side oxide is patterned to define the

extractor holes and alignment trenches for the optical fibers. Then, a deep reactive ion etching (DRIE) of silicon partially etches the extractor holes and trenches. After that, the substrate is reversed to etch the cavity on the topside, thereby completing the extractor membrane. To make electrical contact to the extractor layer, the remaining oxide is completely removed using a 6:1 buffer oxide wet-etch (BOE) solution. Lastly, the different size extractor layer dies on the silicon substrate are then separated using a dicing saw.

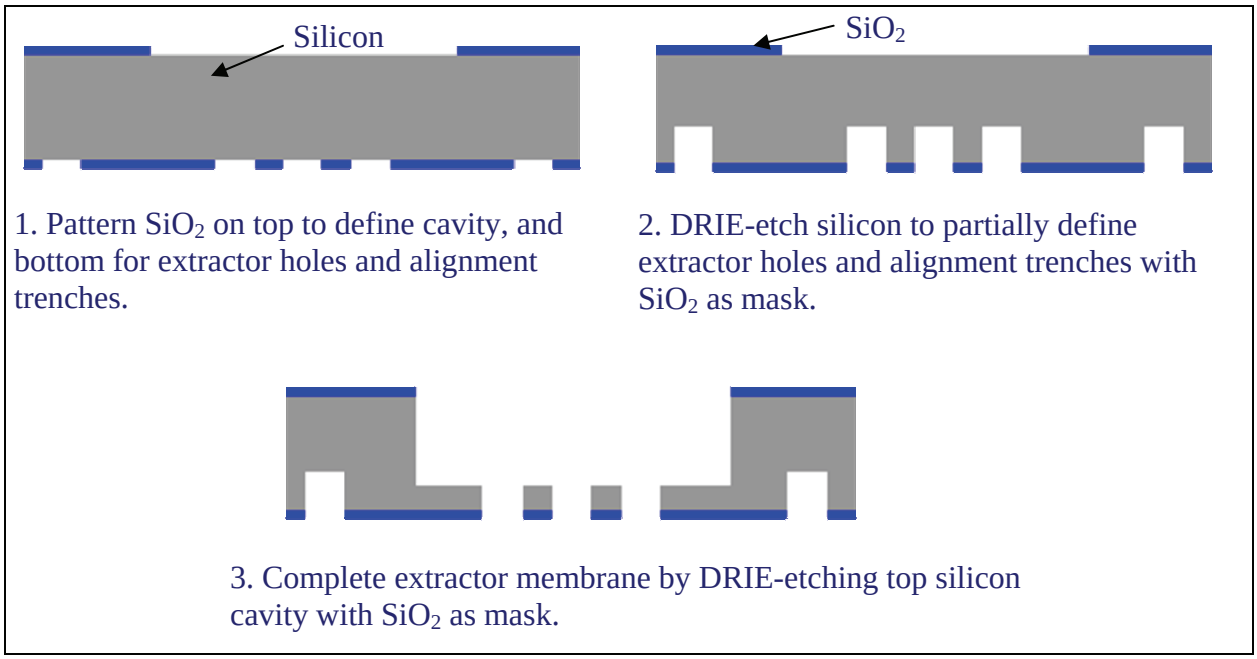

Figure 2. Process flow for the fabrication of the extractor layer.

2.2 Nozzle Array Layer

The nozzle array requires a three-mask process using a 100 mm diameter silicon substrate (~445 µm in thickness) with 1.1 µm thick thermally-grown oxide (figure 3). A positive-tone photoresist (AZ 5214) layer is used to pattern a top-side 2 µm oxide (thermal plus PECVD) to define nozzle holes and alignment trenches. After removing the first resist layer, a 6 µm photoresist (AZ 9245) layer covers the surrounding area, and the nozzle holes are pre-etched using DRIE. This pre-etch is done to take into account the difference in etch rate (RIE-lag) between the inner diameter of the holes and the surrounding open areas. Next, the bottom side 3 µm oxide layer is patterned using a back-to-front alignment method (as was done with the extractor layer), and RIE etched. To define the nozzle height and optical fiber trench depth, the topside silicon is etched using a DRIE process. By tailoring the deposition and etching times of the DRIE cycles for each device design, sharp sidewall profiles were achieved. Sharp sidewalls throughout the nozzle array are required for mechanical stability for each nozzle. The SEM image of a 75 µm O.D. device shows the sharp sidewalls obtained for 200 µm tall nozzles (figure 4).

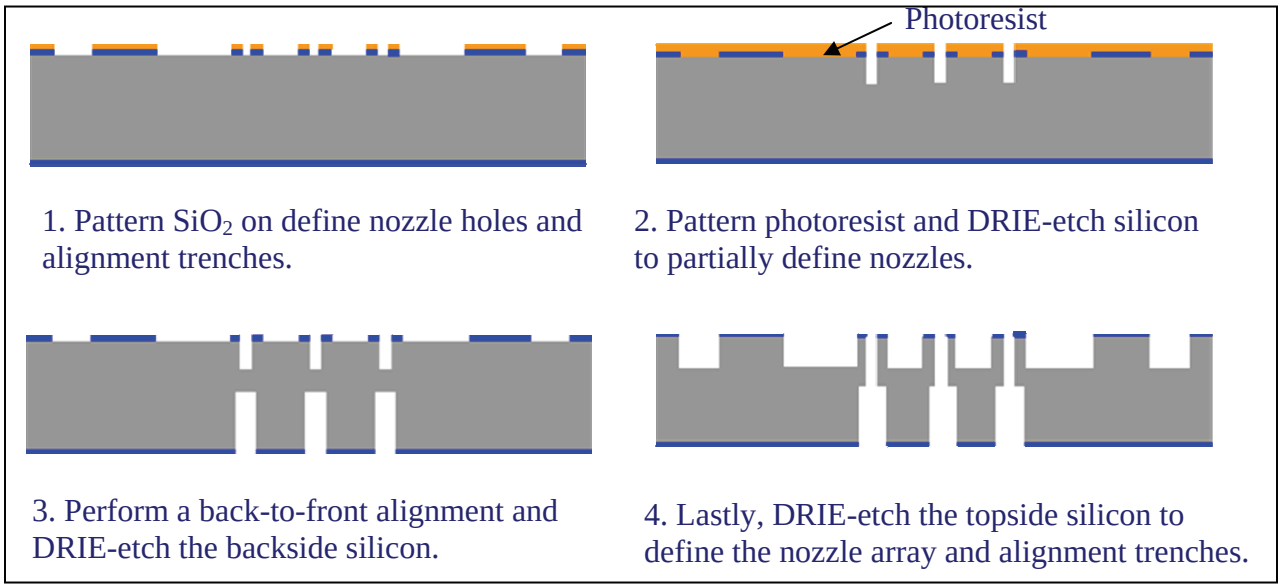

Figure 3. Process flow for the fabrication of the nozzle array layer.

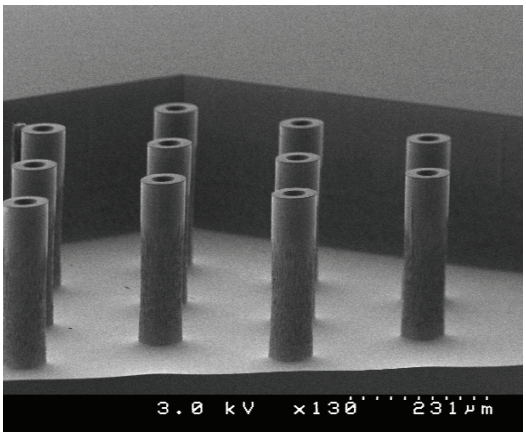

Figure 4. SEM image of a 75 µm outer diameter (O.D.) nozzle array layer with sharp sidewalls.

2.3 Assembly of Nozzle and Extractor Layers

Once the fabrication of the individual layers is complete, optical fiber segments (with diameter of 250 ± 5 µm) are fixed in the trenches around the nozzle layer with an epoxy (figure 5). Similarly, epoxy is applied in the trenches of the extractor layer, and is carefully placed (with trenches facing down) on the optical fibers. The two layers slide into place with a small applied force on the top extractor layer. As a result, the nozzle center can be aligned within 2 µm of the center of the extractor opening (RD). The dimensions of the assembled device are then measured using an optical system, and are summarized in figure 6. Furthermore, a cut plastic filter is attached with a soft silicone to the back of the nozzle layer; thus, forming a reservoir for the supplied fluid (figure 6). A stainless-steel tube is attached to the cut filter to provide a feed into the reservoir. Additionally, a stainless-steel wire is wound on the surface of the cut filter and extended down through the tube to enhance electrification of the fluid and block large air bubbles from reaching the nozzles by reducing the cross-sectional area of the tube.

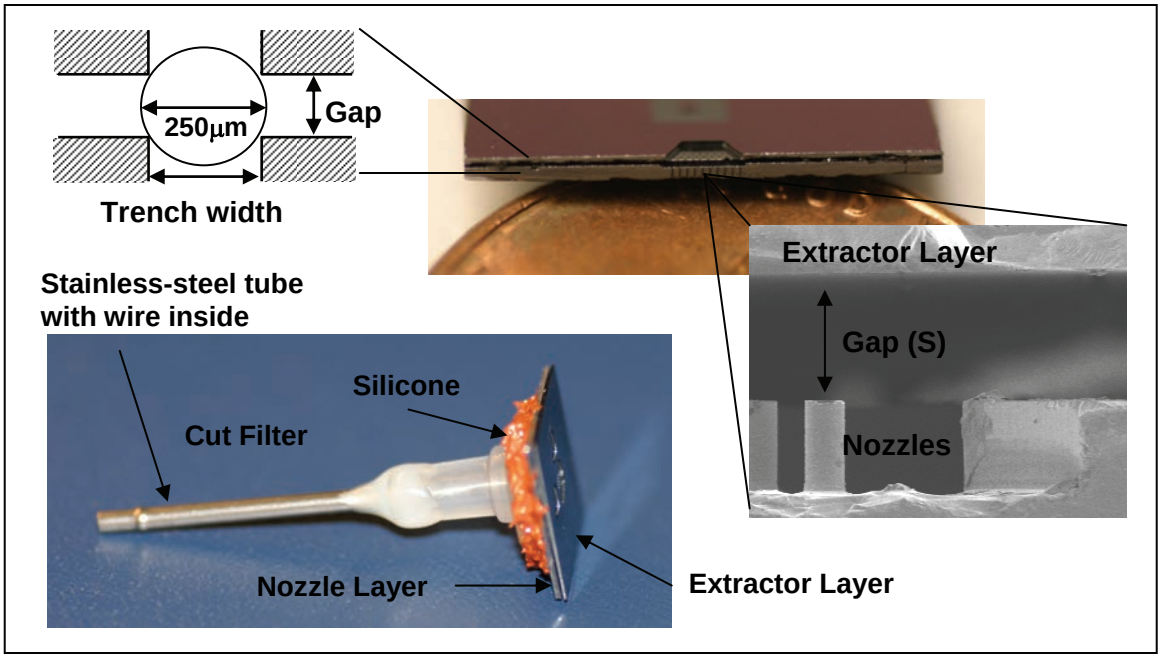

Figure 5. Assembled extractor and nozzle layers are epoxied to filter and to conducting stainless-steel tubes with inner wire.

O.D. (μm)	I.D. (μm)	Nozzle height, H (μm)	Membrane, T (μm)	Gap, S (μm)	Pitch, P (μm)	Extractor RD (μm)
90	45	237	48	213	300	180
90	45	244	49	190	300	180
90	45	248	53	197	300	180
75	37	206	56	200	250	150
75	37	197	46	167	250	150

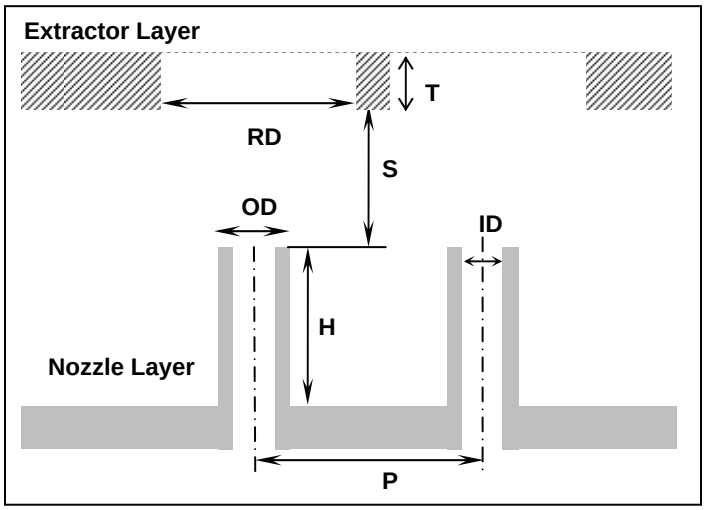

Figure 6. Design guidelines and geometrical properties of various fabricated ESpray devices.

3. Results and Discussion

The assembled ESpray device is fixed on a horizontal Teflon rod and electrical contacts are made to the device. Specifically, a high voltage (HV1) of 8 kV is applied to the stainless-steel feeding tube that is in direct contact with the Ethanol; while a lower voltage (HV2) of 7 kV is applied on the surface of the extractor via a bent wire (figure 7). As a result, a 1 kV potential difference is maintained between the nozzle array and extractor layers. A grounded stainless-steel mesh 10 mm downstream, collects and neutralizes the charged particles within the spray. After the voltages are set, the desired flow rate is set syringe pump, and the fuel is fed into the stainless-steel tube. A laser diode module allows visualization of the fluid spray dispersing away from the extractor layer, while a camera system records the spray (figure 8a).

Preliminary tests indicate that flow rates in excess of 0.5 ml/hr/nozzle and 0.35 ml/hr/nozzle can be achieved for devices with nozzle outer diameters (O.D.) of 90 µm and 75 µm; respectively. Device performance seems to be limited by space-charge effects where downstream droplets shield above droplets from the grounded collector, which previous work showed these effects depend on array size, pitch, electric (E) field, and flow rate (5).

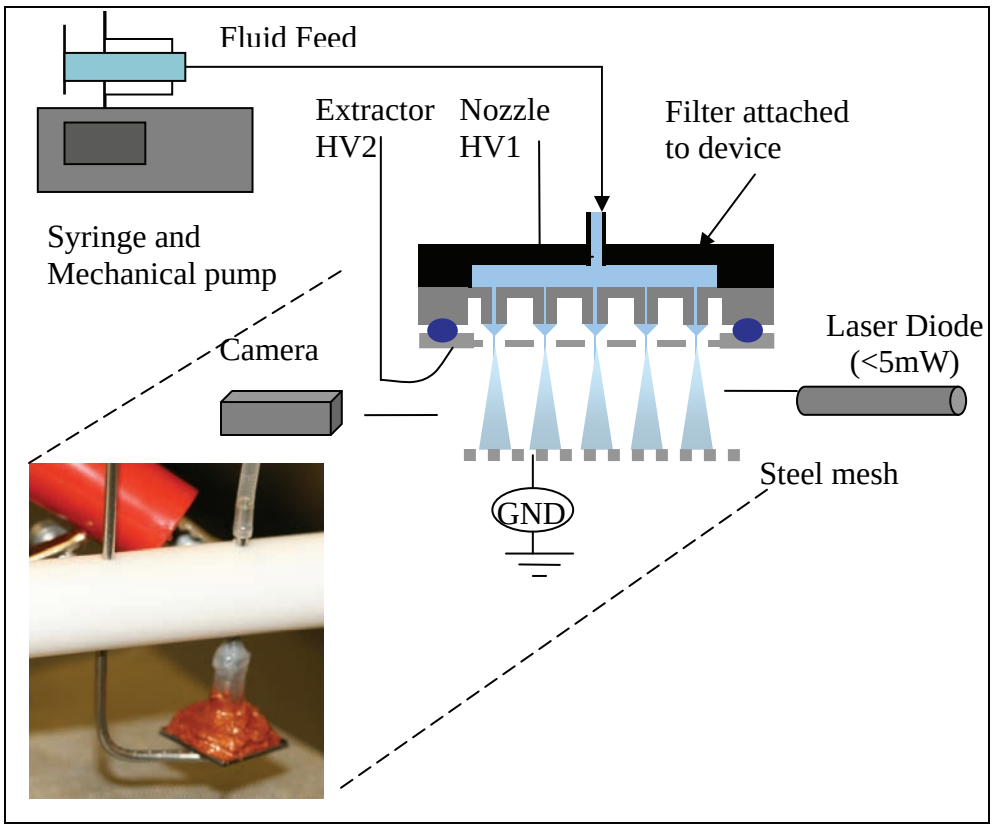

Figure 7. Electrospray test setup using pure Ethanol. High voltages (HV1 = 8 kV > HV2 = 7 kV) are applied to the nozzle and extractor layers; respectively, and grounded mesh collects the charged fluid.

For a fixed geometry and E-field, the space charge effect limits the maximum flow rate through the device. Above this flow rate, droplets are observed to fly back to the extractor, and eventually lead to flooding; therefore, this sets the maximum flow rate for the given device design (figure 8b). Using this experimental procedure, future work will focus on developing a more complete understanding of space-charge effects and use a phase doppler system to determine droplet diameters and velocity.

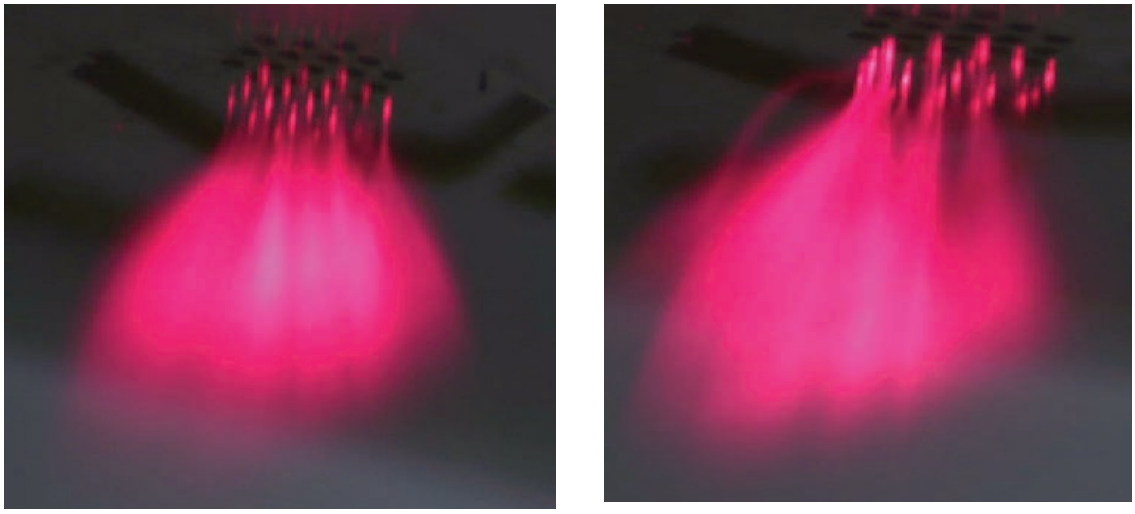

(a) (b)

Figure 8. Illuminated spray with laser diode**.** (a) Mist of droplets during electrospraying, and (b) appearance of side-spray that may flood extractor layer due to space-charge effects.

4. Summary and Conclusions

This work has shown the microfabrication and preliminary performance of multiplexed electrospraying (ESpray) devices. Furthermore, an experimental procedure was developed to determine maximum liquid flux for a given design limited by space charge effects. Micromachining in silicon substrates allows for compact, small-scale fuel atomization devices for portable power applications. ESpray devices with 90 and 75 µm outer diameter (O.D.) nozzles were fabricated in silicon substrates. These devices were assembled and then tested using pure Ethanol to determine the voltages and flow rates required for operation. Preliminary tests indicated that flow rates >0.5 ml/hr/nozzle and 0.35 ml/hr/nozzle (space-charge limited) can be achieved for devices with 90 µm and 75 µm O.D.; respectively. Future work will further investigate space-charge and extend the operation regions (required voltages, air flow rates in combustors, and fuel flow rates) of these devices by using Ethanol and the logistics fuel JP-8. Furthermore, the integration of this MEMS-based fuel atomizer with a JP-8 catalytic combustion system will also be investigated. Lastly, it may be possible to also integrate a MEMS-based thermoelectric generator, the focus of my graduate work at the University of Florida, to further generate power from the hot exhaust gasses (due to JP-8 combustion) for sensor/control systems.

5. References

1. Huth, J.; Ezekiel, H.; Buffalino, A.; Gomez, A.; Roychoudhury, S. *SunPower, Inc.*, http://www.precision-combustion.com/HP-08.pdf, 1–5, 2006.
2. Deng, W.; Klemic, J. F.; Li, X.; Reed, M. A.; Gomez, A. *Proceedings of the Combustion Institute* **2007,** *31*, 239–2246.
3. Deng, W.; Klemic, J. F.; Li, X.; Reed, M. A.; Gomez, A. *Journal of Aerosol Science* **2006**, *37*, 696–714.
4. Waits, C. M.; Morgan, B.; Deng, W.; Jankowski, N. R.; Gomez, A.; Geil, B. *Solid-State Sensors, Actuators, and Microsystems Workshop (Hilton Head Conference)*, 220–223, 2008.
5. Deng, W., Ph.D. Dissertation, Yale University, Ch. 3, 57–87, 2008.

INTENTIONALLY LEFT BLANK.

Survivability/Lethality Analysis Directorate (SLAD)

INTENTIONALLY LEFT BLANK.

U.S. Army Research Laboratory

SUMMER RESEARCH TECHNICAL PAPER

Structural Response for Armor Panels Due to Blast: Generation of A Response Database for Use in Vulnerability Analysis Codes

by Raquel Ciappi

Contents

List of Figures 125

List of Tables 125

Abstract 126

1. Introduction 127

2. Background 128

3. Calculations 128

4. Results and Discussion 130

5. Summary and Conclusions 133

6. Educational Benefits 134

7. References 135

List of Figures

Figure 1. The wedge panel as part of the larger panel configurations for inclusion into the parameterized response archive. 127

Figure 2. The unitary pressure-impulse wave form used for generating the blast loading. 129

Figure 3. The 3x3 ft^2 and 5x1 ft^2 wedge panels as modeled for stress analysis. 129

Figure 4. The computed reflected blast pressure impulse needed to fracture the 3x3 ft^2 wedge panels. 130

Figure 5. The computed reflected blast pressure impulse needed to fracture the 5x1 ft^2 wedge panels. 131

Figure 6. Variation of the (blast impulse/panel thickness) with panel thickness for 3x3 ft^2 panels. 131

Figure 7. Variation of the (blast impulse/panel thickness) with panel thickness for 5x1 ft^2 panels. 132

Figure 8. Variation of the (maximum deflection/panel thickness) for the 3x3 ft^2 wedge panels. 132

Figure 9. Variation of the (maximum deflection/panel thickness) for the 5x1 ft^2 wedge panels. 133

List of Tables

Table 1. RHA material properties. 130

Abstract

Blast effects on armor panels of Army ground vehicles are modeled and compiled to create an archive of structural responses for SLAD's vulnerability analysis codes. The archive is mainly concerned with values of blast pressure impulse and the corresponding panel deflection. This effort is part of a larger SLAD effort for flat, wedge, and curved panels of different angles, panel size, and materials. The effort presented here is concerned only with Rolled Homogeneous Armor (RHA) wedge panels, while the larger effort encompasses curved panels. For each panel size, seven wedge angles each with eight wall thicknesses were computed. The finite-element stress analysis code ALGOR was used. The structural response for the panels is computed with emphasis on determining both the blast pressure impulse that will cause the panels to structurally fail (fracture), and the maximum deflection of the panel. Effort for the other panels and parameters is continued currently by SLAD's personnel toward the goal of continuously populating the blast response archive.

1. Introduction

The U.S Army Research Laboratory Survivability Lethality Analysis Directorate (ARL/SLAD) generates blast damage estimates for both ground and air systems in support of Army and tri-service efforts. In particular, blast damage estimates, as discussed in this report, are for external blast events from conventional explosives rather than detonations that occur within a structure. The estimates may follow the form of a lethal miss distance (LMD) referenced off the front, sides, rear and top of a target, or they may consist of higher-fidelity lethal blast contours surrounding a target. The Parameterized Response Archive (PRA) was created in order to improve the consistency and efficiency of the methods used to create blast damage estimates in SLAD's vulnerability / lethality analysis codes. Essentially, the PRA is a collection of target response data consisting of maximum deflection and acceleration for each target material and configuration for a given blast load.

The present effort is a small part of the larger effort and was tailored to match the 6-week effort duration (June 3rd to July 17). This report examines 3x3 ft^2 and 5x1 ft^2 RHA wedge panels. SLADS's larger effort will continue for additional panel shapes (curved) and sizes (3x5 and 5x5 ft^2), as shown in figure 1, for the remaining of FY08.

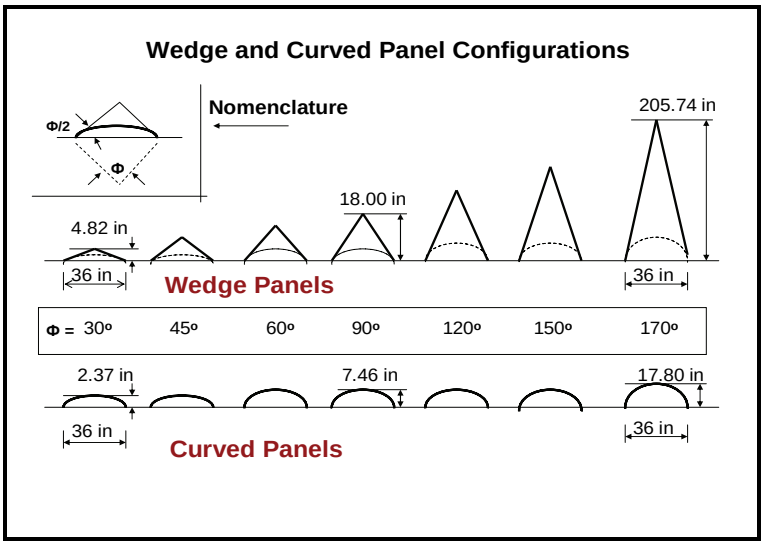

Figure 1. The wedge panel as part of the larger panel configurations for inclusion into the parameterized response archive.

2. Background

This paper documents the PRA data generated for RHA armor for various wedge and curved panel configurations. A prior effort (*1*) examined four aluminum flat panel sizes. The PRA is an essential part of the blast analysis tool being integrated within ARL's primary vulnerability/lethality code, MUVES-S2.

For the PRA development, the Professional Mechanical Event Simulation (MES) package from the computerized finite element code ALGOR (*2*, *3*) was used. MES allows the use of non-linear material models and the application of a time varying impulsive pressure to the target plate. The dynamic response of the plate can be visualized during the simulations and results options such as stress, strain, and displacement are available to the user.

3. Calculations

I made computations on two RHA panel sizes of 3x3 ft^2 and 5x1 ft^2. Each of the panels was shaped into 7 wedge angles of 30-, 45-, 60-, 90-, 120-, 150- and 170-degree wedges. Each wedge angle case, was varied in thicknesses; 0, 1/16, 3/16, 1/4, 3/8, 1/2 , 5/8, 3/4, and 1-in (1.5875-, 4.7625-, 6.35-, 9.525-, 12.7-, 15.875-, 19.05-, and 25.4-mm). I computed a total of 112 cases, and imposed fixed-fixed boundary conditions on the four panel sides.

The ALGOR finite element code was used (*2*), with its Mechanical Event Simulation (MES) module (*3*). The reflected-pressure blast impulse wave shown in figure 2 is multiplied by a peak reflected pressure value, for consistency with reference 1.

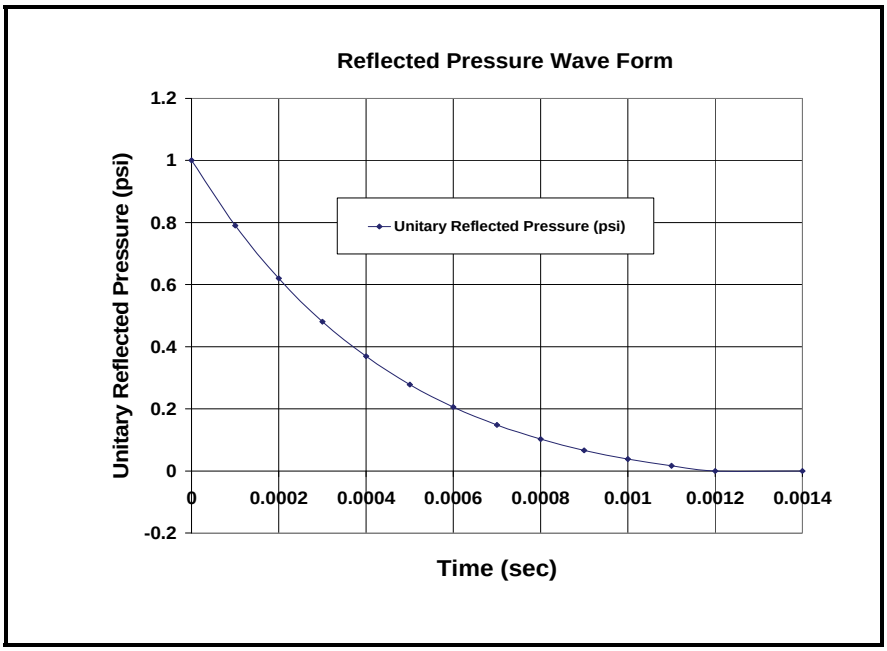

Figure 2. The unitary pressure-impulse wave form used for generating the blast loading.

Fourteen solid geometry files were constructed for the wedge configurations (seven angles for two panel sizes), and the thicknesses were then varied. The wedges were overlaid with a grid/mesh such that the element sizes were kept nearly constant. Figure 3 depicts the solid models produced.

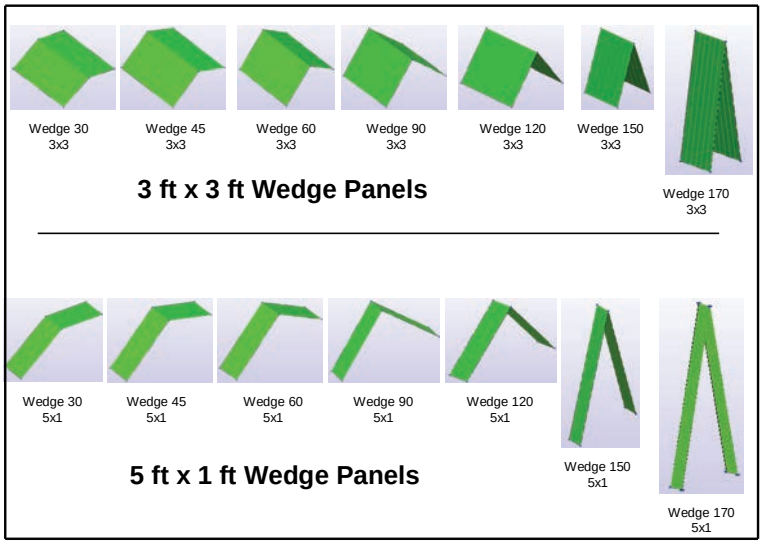

Figure 3. The 3x3 ft^2 and 5x1 ft^2 wedge panels as modeled for stress analysis.

The material properties used for the RHA are listed in table 1. I selected the von Mises material failure model with isotropic hardening for plasticity. The ultimate (fracture) stress is 170,000 lb/in^2.

Table 1. RHA material properties.

RHA Armor Material Properties	
Mass Density	.0007347 lb-sec^2/in^4
Modulus of Elasticity	29,000,000 lb/in^2
Poisson's Ratio	0.30
Yield Strength	160,000 lb/in^2
Strain Hardening	51,418.4 lb/in^2
Ultimate Strength	170,000 lb/in^2

I based the computation process on providing a peak pressure multiplier for the blast pressure wave form given in figure 2. Computations were typically made up to 0.006 sec (6 ms) to calculate the stress and deflection response.

4. Results and Discussion

For the 112 cases computed, about 4 -5 iterations were required per case to properly estimate the pressure values needed to cause failure to each of the panels. To avoid making a large number of iterative calculations, a variance of 10 psi over-pressure was allowed to identify panel failure from no-failure case, e.g., if the iteration of 500 psi indicated panel failure and another iteration at 480 psi indicated no failure, it was assumed that the panel failed at approximately 490 psi. Run times varied between 8 to 50 minutes.

The computed reflected pressure impulse to cause panel failure is shown in figures 4 and 5 for the 3x3 and 5x1, respectively.

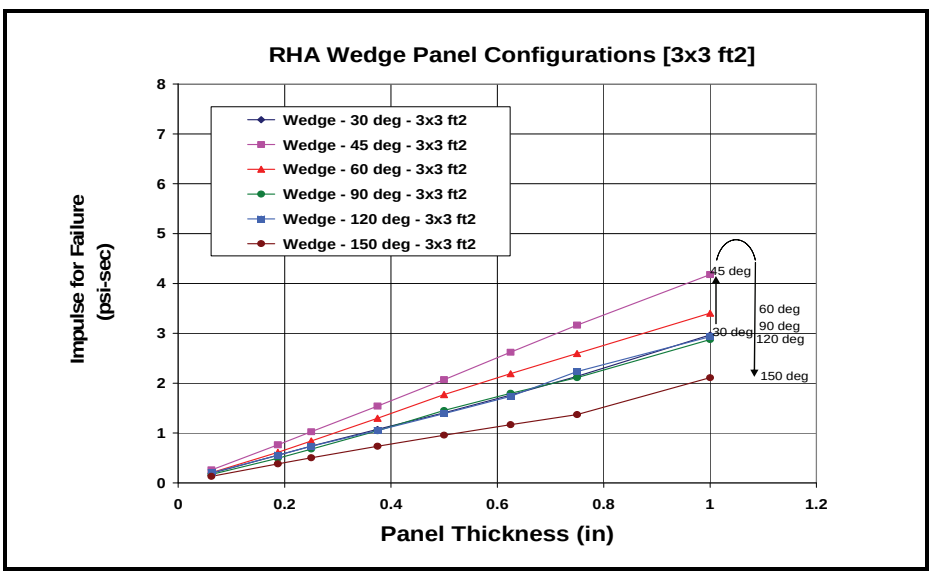

Figure 4. The computed reflected blast pressure impulse needed to fracture the 3x3 ft^2 wedge panels.

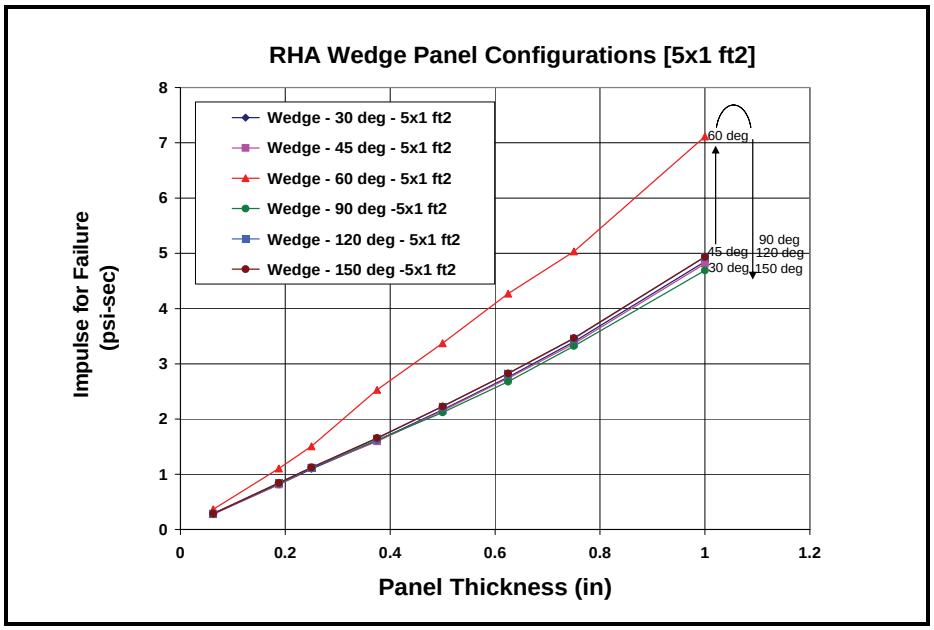

Figure 5. The computed reflected blast pressure impulse needed to fracture the 5x1 ft^2 wedge panels.

The impulse increases almost linearly with panel thickness, for all wedge angles. The case of the 170-deg wedge was not included due to difficulty in the ALGOR code to properly apply the surface pressure. Figures 6 and 7 present the same results except with the impulse value being normalized by the panel thickness itself.

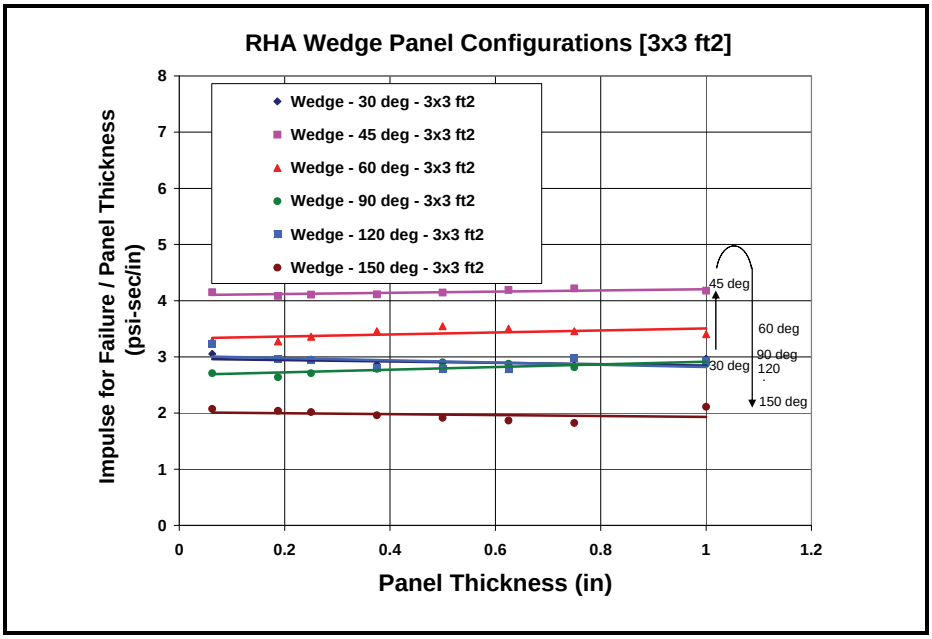

Figure 6. Variation of the (blast impulse/panel thickness) with panel thickness for 3x3 ft^2 panels.

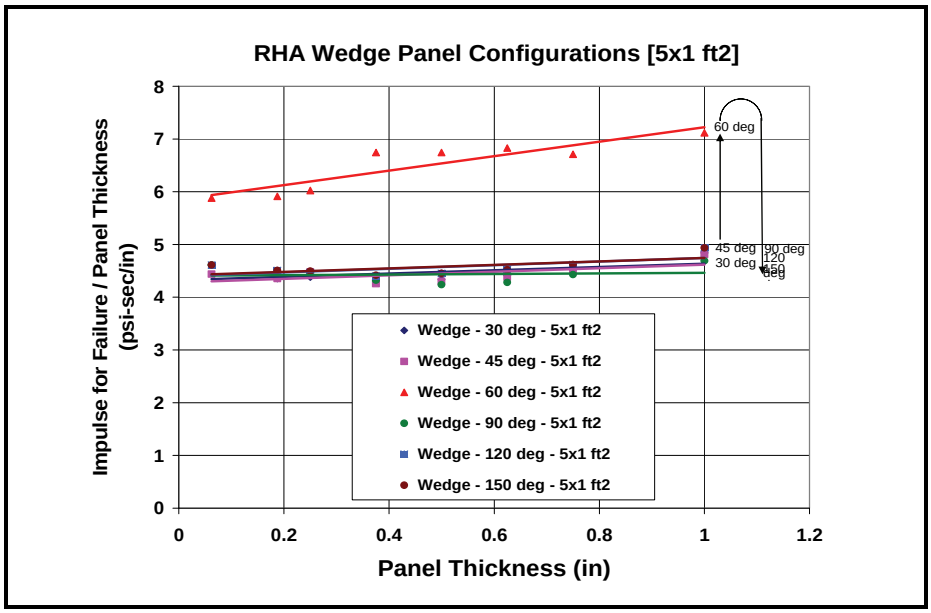

Figure 7. Variation of the (blast impulse/panel thickness) with panel thickness for 5x1 ft^2 panels.

For most configurations computed, this impulse-to-thickness ratio seems to be almost constant, except for the 60-deg, 5x1 panel which showed increasing values. Figures 8 and 9 display the variation of the panel maximum deflection (normalized by the panel thickness) with the panel thickness itself for the 3x3 and 5x1 panels, respectively. Note that the maximum deflection of the panel which, unlike the flat panel, is no longer at the center of the panel.

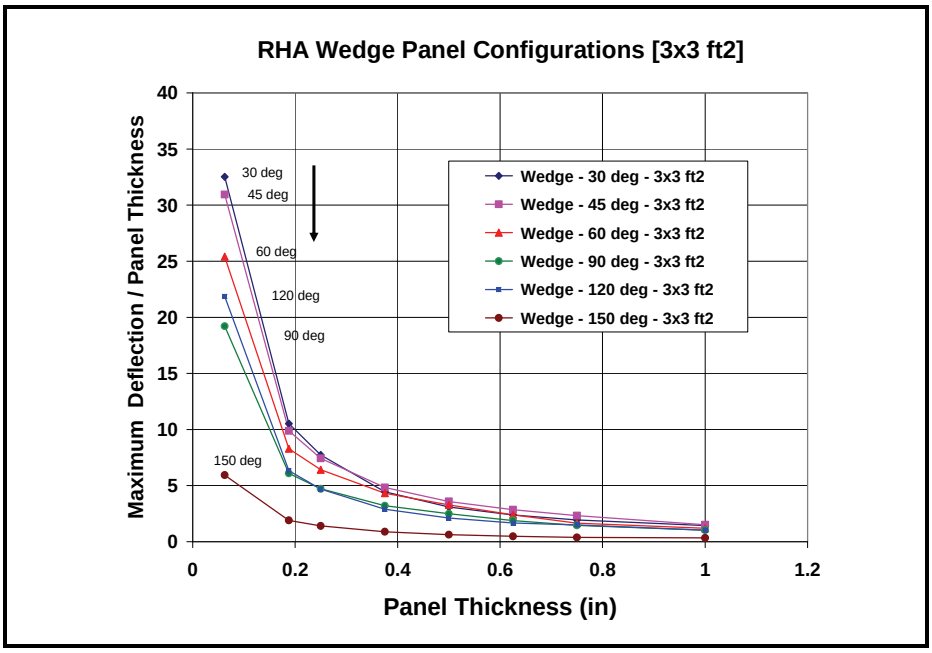

Figure 8. Variation of the (maximum deflection/panel thickness) for the 3x3 ft^2 wedge panels.

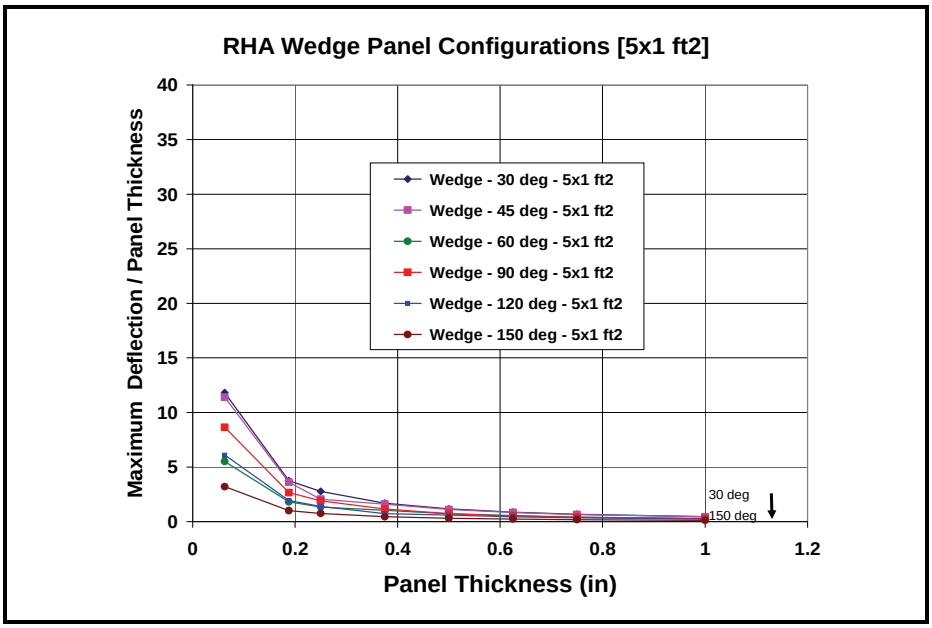

Figure 9. Variation of the (maximum deflection/panel thickness) for the 5x1 ft^2 wedge panels.

It was observed that most failures occurred earlier than the end of the loading impulse (1.2 ms). Most failures occurred between 0.8 to 1.2 ms. Panel failure was noted to happen in some panels, either along the side edges, or near the mid point of both members of the inverted V shape sides. The same computations made on the 5x1 ft^2 panels showed, as expected, larger pressure impulses needed to cause failure due to the larger rigidity (stiffness) of the panel due to its sides' aspect ratio.

5. Summary and Conclusions

The response of the various RHA panel configurations described previously were computed as part of SLAD's continuing effort to populate a larger archive for armor panel structural responses to an explosive blast. A total of 112 wedge panel geometries were generated and computed, requiring about 450-550 computer runs. Computer run time for each case ranged between 8 and 50 minutes.

Results indicated that the blast impulse needed to cause failure (fracture) to the panel increases almost linearly with the panel thickness up to about 0.8- to 0.9-in. This was observed for the two panel area sizes computed in this effort (3x3 and 5x1 ft^2).

The smaller panel 5x1ft^2 seemed to be more structurally rigid. It yielded less deflection under the same pressure/impulse, and seemed to require more impulse to fail than the larger 3x3 ft^2 panel of the same wedge angle. However, after closer inspection they yielded at about the same force.

For example:

5 x 1 ft^2 panel: Failed at ≈ 6 psi-s/in for a 0.25 in thick panel or ≈ 1.5 psi-s

Area * Impulse = Force

720 in^2 * 1.5 psi-s ≈ 1080 lbs-s

3 x 3 ft^2 panel: Failed at ≈ 3.4 psi-s/in for a 0.25 in thick panel or ≈ 0.85 psi-s

Area * Impulse = Force

1296 in^2 * 0.85 psi-s ≈ 1102 lbs-s

The ratio of (panel maximum deflection)/(panel thickness) decreases with the panel thickness. The thick panels deflects less than the thinner ones at failure, as might be expected. This was observed for both the 3x3 and 5x1 panels.

The yield stress of the material is usually reached (in most runs) very quickly (0.2 ms), and the material behaves plastically during the short blast duration of 1.2 ms. The failing material strength was reached for most cases between 0.7 to 1.3 ms, indicating the panel failed while the blast loading was still being applied. It was found that many of the panels failed at the side edges almost simultaneously (within 0.1 ms) or shortly before/after failing at other locations. The reverse order of the failure location was also observed for some panels of different angles.

6. Educational Benefits

During this six-week duration, I learned about the application of stress analysis tools and finite element methods to calculate stresses in a structure. I learned more about the commercial code ALGOR and its capabilities and limitations, over what I knew before. I learned about fast dynamic loading, material failure models, von Mises material failure criterion, material plastic response, and determining structural failure (fracture). As a junior mechanical engineering student, this exposure has served widening my technical scope and it exposed me to the mechanical engineering analysis field in this directorate of ARL.

7. References

1. Ciappi, R.; Lynch, D. "PRA Data Generation for Aluminum Armor Using ALGOR MES (Non linear Analysis) for Various Geometric Configurations", ARL Summer Student Research Report, August 2007.
2. "ALGOR Professional" (no authors listed), Training Manual, ALGOR Inc., Pittsburg, PA, 2007.
3. "ALGOR Mechanical Event Simulation" (no authors listed), Training Manual, ALGOR Inc., Pittsburg, PA, 2007.

INTENTIONALLY LEFT BLANK.

U.S. Army Research Laboratory

SUMMER RESEARCH TECHNICAL PAPER

Improvements of Techniques and Devices for Survivability, Lethality, and Vulnerability Analysis

by Nathan Meraz

Contents

List of Figures **139**

List of Tables **140**

Abstract **141**

Acknowledgment **142**

1. Introduction **143**

2. Systems for Spectral Analysis **144**

2.1 Background 144

2.2 Fiber Input Collection System....144

2.3 Two Color Analysis Instrument 145

2.4 High Resolution Etalon-Based Instrument....145

2.5 Calculations and Simulations 145

2.5.1 Magnifications and Focal Lengths 145

2.5.2 Lens Diameters....146

2.5.3 Field Lenses....147

2.5.4 ZEMAX Simulations....147

3. Transmission Experiment **150**

3.1 Background 150

3.2 Data Processing 152

3.2.1 Test Details....152

3.2.2 From Irradiance to Transmission 156

4. Conclusion **157**

5. References **159**

List of Figures

Figure 1. ARL spectrometer. 143

Figure 2. Schematic of the ARL spectrograph with fiber input; light is separated at the diffraction grating. 145

Figure 3. Diagram of an afocal system utilizing a field lens; the field lens increases the FOV by bending light into the next aperture. 147

Figure 4. Layout for the fiber input collection system.....147

Figure 5. Layouts for the two-color analysis instrument and etalon-based instrument. 148

Figure 6. Layout for the boresight camera.....148

Figure 7. Spot diagram for fiber input collection system; horizontal: wavelength and vertical: field. 149

Figure 8. Spot diagram for two-color analysis instrument and etalon-based instrument; horizontal: wavelength and vertical: field.....150

Figure 9. Spot diagram for boresight; horizontal: wavelength and vertical: field. 150

Figure 10. Obscurants on the battlefield: a) one-way path: tracking missile energy, b) two-way path: laser sends energy through obscurant; it scatters at the target and must return to the detector, and c) sensors with different paths using different spectral regions must all validate the target (*1*). 151

Figure 11. Mass extinction coefficients of standard screening smokes (*1*). 152

Figure 12. Light paths of a daytime transmission experiment. This example test setup shows many possible light paths into the spectrometer; only the attenuated signal should be used to measure transmission. 153

Figure 13. Initial data from transmission test (uncalibrated). The dark blue line is raw data. The thicker red line is the result of a smoothing function to remove noise due to optical turbulence. The obscurant was released near frame 1800. As it forms, the reflected/scattered solar energy causes an increase in irradiance. 154

Figure 14. Calculated transmission varying with weighted symmetric moving average. 155

Figure 15. Data reduction plots of transmission test. From top to bottom: 1) Initial data after being smoothed with running average; vertical line indicates user-determined frame at which the obscurant was released. 2) Maximum and minimum values for each chopper period. 3) The difference in max and min values removes background and solar energy. 4) Transmission plot. Values that are much larger than 100% occur when the obscurant is released. They cannot be avoided but do not affect the transmission data. 156

Figure 16. User check of modulation frequency during transmission test. 157

List of Tables

Table 1. System parameters for imaging. 146
Table 2. Optical designs.....149
Table 3. Effect of particle size to wavelength ratio on scattering direction (*1*).....155

Abstract

The Survivability/Lethality Analysis Directorate (SLAD) recently built a spectrometer that was able to capture sensor irradiance at 500 fps with 5 nm intervals over a 600 nm bandwidth range. This spectrometer was used to characterize the physical and optical properties of obscurants; a computer processing tool was developed for this system to determine the transmittance of an obscurant with respect to wavelength and time. Three optical systems have been designed to function alongside the current spectrometer to assist in the development of narrow bandwidth technologies as part of the ongoing SLAD effort to characterize signatures and study obscurant effects on sensor performance.

Acknowledgment

The author wishes to acknowledge the mentorship of Joseph Montoya.

1. Introduction

One function of the U.S. Army Research Laboratory's Survivability/Lethality Analysis Directorate (SLAD) is to develop tools, techniques, and methodologies for improving survivability, lethality, and vulnerability (SLV) analysis. The time spent during June 20 and July 7, 2008, was focused on this purpose. Three analysis tools were taken from sketches to complete preliminary designs and an essential data processing technique was developed for an ARL spectrometer.

Many spectral devices generate data on the physical and optical properties of battlefield equipment. These properties vary with wavelength, so tests need to examine a wide variety of wavelength bands. Recently a hyperspectral radiometer (spectrometer) (figure 1) was built that separates the visible and near-infrared (NIR) spectrum across a detector array, which records irradiance values at a maximum of 500 fps.

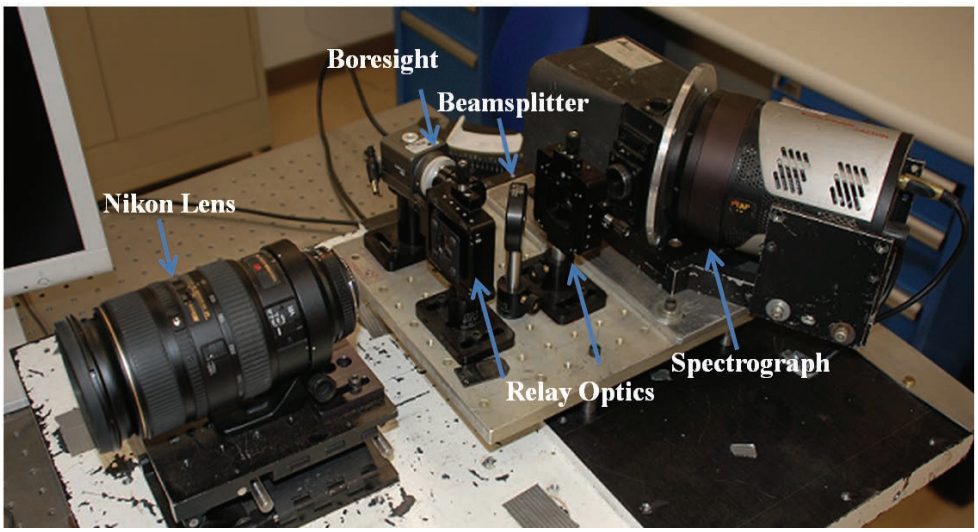

Figure 1. ARL spectrometer.

Typically, a radiometer is responsive to a very wide spectrum unless a filter is used. Generating data across the entire visible spectrum would require tremendous effort in organizing tests and equipment for these filtered devices. The time, cost, and uncertainty between measurements associated with this have been alleviated with the new spectrometer; however, the lack of a proper processing program has stifled its use. The creation of this program now allows for the full use of the data it generates.

The design of three spectral devices has been done to continue the efforts of the current spectrometer in characterizing and exploiting increasingly narrow bandwidth signatures. The following sections of this paper give an overview of these designs and demonstrate the recently

developed process of generating spectral transmission plots from the new spectrometer. The overall purpose of this work has been to develop techniques and tools for ARL engineers and scientists to characterize physical and optical properties of relevant systems.

2. Systems for Spectral Analysis

2.1 Background

The success of the ARL spectrometer influenced the designs of three more spectral instruments. A two-color analysis instrument and a high spectral resolution etalon-based instrument are to be used as tools for developing narrow spectral bandwidth technologies. A modular fiber input collection system was also developed to be used with other devices, namely spectrographs, which utilize fiber inputs. Every component in these three systems is off-the-shelf.

The design for the fiber system was completed first. Finishing this system first was necessary due to the complexity of imaging onto a 0.6 mm fiber. The other systems were relatively straightforward in creating the optical prescription. The work that went into developing the prescription for the fiber system carried over directly to the other systems since the same cameras and afocal layouts were used.

2.2 Fiber Input Collection System

This system is to be used with two currently owned spectrographs. Using them on their own is difficult due to the lack of adequate collection optics and boresighting capabilities. Adding these components greatly increases the functionality of the spectrographs. Collection optics allow for more light from the region of interest to enter the fiber, and the boresight ensures proper aim of the device (figure 2). Without these upgrades, the spectrographs are unusable for field measurements.

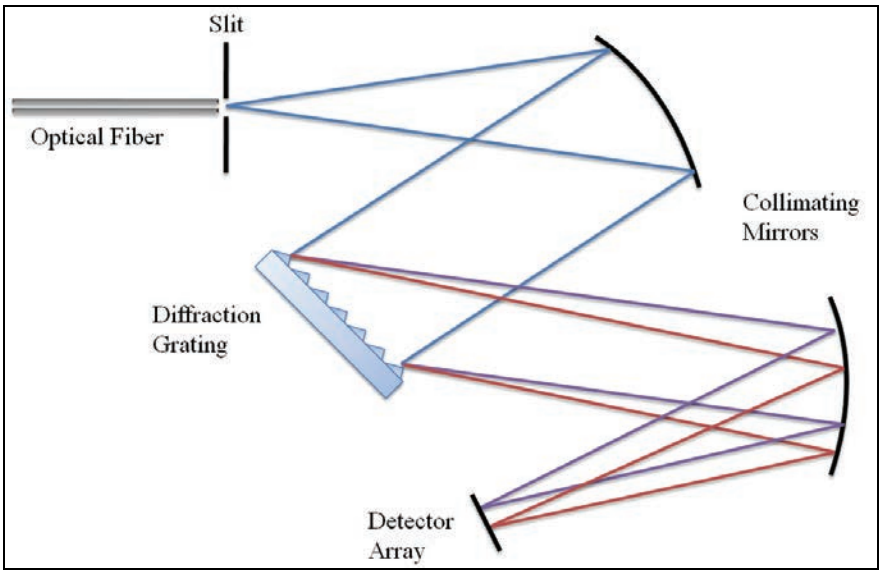

Figure 2. Schematic of the ARL spectrograph with fiber input; light is separated at the diffraction grating.

2.3 Two Color Analysis Instrument

The two images from this device will have two different bandpass wavelengths. A 50/50 beamsplitter sends two collimated beam through different interference filters before being imaged onto identical high-speed sensors with digital outputs. The purpose of this instrument is for signature collection at specific spectral bands. Future updates to this design will use one sensor for both images, allowing space for a boresighting camera.

2.4 High Resolution Etalon-Based Instrument

This instrument is also for signature collection. An etalon is an optical device with two flat, parallel, highly reflective surfaces separated some distance. Incident light interferes within the cavity of the etalon such that only certain wavelengths have nearly 100% transmission. Centering the wavelength is done by rotating the etalon. The light reflected from the etalon is used for boresighting.

2.5 Calculations and Simulations

2.5.1 Magnifications and Focal Lengths

Each of these designs uses a currently owned variable focal length Nikon camera lens, which produces an intermediate image 46.5 mm beyond its mating flange. The usable diameter of the image is roughly 35 mm. Relaying this image with the correct magnification to either a detector array or fiber was the goal for each design. The equation for magnification is given as

$$m \equiv \frac{h'}{h} \tag{1}$$

which is the ratio of the final image height *h'* to the initial height *h*. Each design has some form of beamsplitter that is placed in a collimated beam, meaning some optics are afocal. For afocal systems with two lenses,

$$m = \frac{f_2}{f_1} \tag{2}$$

with f_1 and f_2 being the focal lengths of the first and second lenses. This equation was the basis for transferring images as it defined the necessary focal lengths for each imaging path. The fiber optic path needed two sets of de-magnifiers to image onto the 600 µm fiber. The overall *m* is the multiplication of the two magnifications. Table 1 lists the focal lengths selected to achieve the necessary magnifications. For practical applications of the fiber system, it is only necessary to examine about one third of the full field of view from the Nikon lens (*7*). This translates to a magnification of about 1/16.67 at the fiber.

Table 1. System parameters for imaging.

	Fiber Input Collection System		Two-color Analysis Instrument		High Resolution Etalon-based System	
Image	***Fiber***	***Boresight***	***Color 1***	***Color 2***	***High-speed***	***Boresight***
h	10 mm	35 mm	35 mm	35 mm	35 mm	35 mm
h'	0.6 mm	8.46 mm	6.35 mm	6.35 mm	6.35 mm	8.46 mm
1/*m*	16.667	4.137	5.512	5.512	5.512	4.137
f1	75 mm	75 mm	150 mm	150 mm	150 mm	150 mm
f2	19 mm	35 mm	30 mm	30 mm	30 mm	35 mm
f3	75 mm	-	-	-	-	-
f4	18 mm	-	-	-	-	-

2.5.2 Lens Diameters

The spectrograph has an input fiber with a 600 µm core diameter and 0.20 Numerical Aperture (NA).

$$NA = n \sin\theta \cong \frac{D}{2f} \tag{3}$$

The NA describes the maximum angle θ for which light can enter the fiber optic. Matching it means the maximum amount of light enters the fiber and spectrograph. With 0.20 as the NA of the aperture and 18 mm selected for the focal length *f*, the diameter *D* of last lens must be at least 7.2 mm in air (n=1). The standard lens size of 12.7 mm (1/2 in.) was selected for this lens.

Lens diameters control how much light can enter the fiber. The NA of the fiber determines the maximum ray angle, which can be back-propagated to determine the necessary lens diameters. The ray-tracing program ZEMAX was used to ensure that the lenses with small diameters would not have any limiting apertures.

This geometrical ray-tracing methodology was also used for the other systems to determine the necessary clear apertures. There was no problem finding appropriate lenses from vendors.

2.5.3 Field Lenses

A problem for each system was discovered when creating ZEMAX ray-trace models: the optical prescription of the Nikon camera lens is unknown. Since it is unclear how light is exiting the Nikon lens, it becomes unclear how light will be relayed into the fiber. A solution is to add a field lens at the intermediate image behind the camera lens to redirect the light as needed (figure 3). The field lens bends ray bundles into the aperture of the next lens without changing the magnification. Several lenses of various powers were selected for purchase to allow the system operator to try for maximum collection.

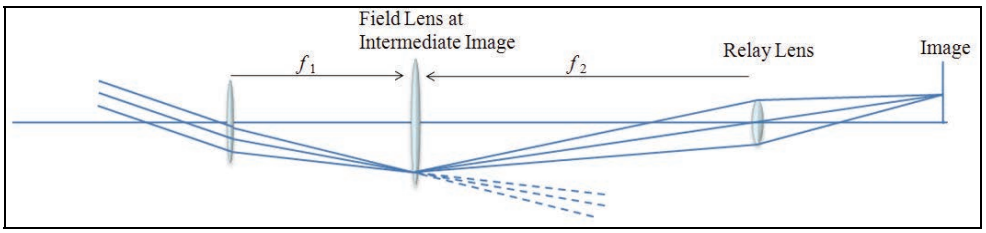

Figure 3. Diagram of an afocal system utilizing a field lens; the field lens increases the FOV by bending light into the next aperture.

2.5.4 ZEMAX Simulations

A ray-tracing program like ZEMAX is useful to model optical layouts (figures 4–6). Table 2 lists the optics and basic properties of each element in the systems. Spot diagrams (figure 7–9) show the impulse responses of the optical system as a function of field location and wavelength. An optical system that is limited by the detector array will have spots that fit within the individual detector pixels. These diagrams were used for checking image quality; however, there were no specified requirements for image quality.

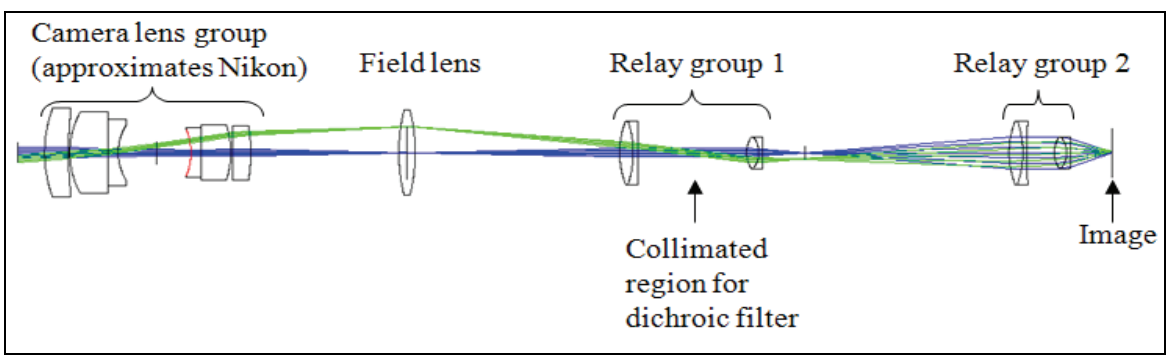

Figure 4. Layout for the fiber input collection system.

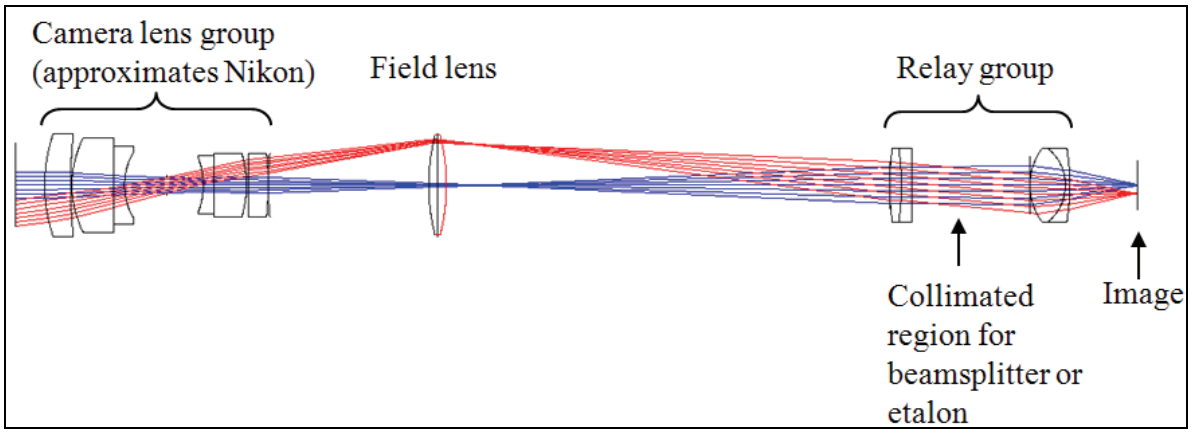

Figure 5. Layouts for the two-color analysis instrument and etalon-based instrument.

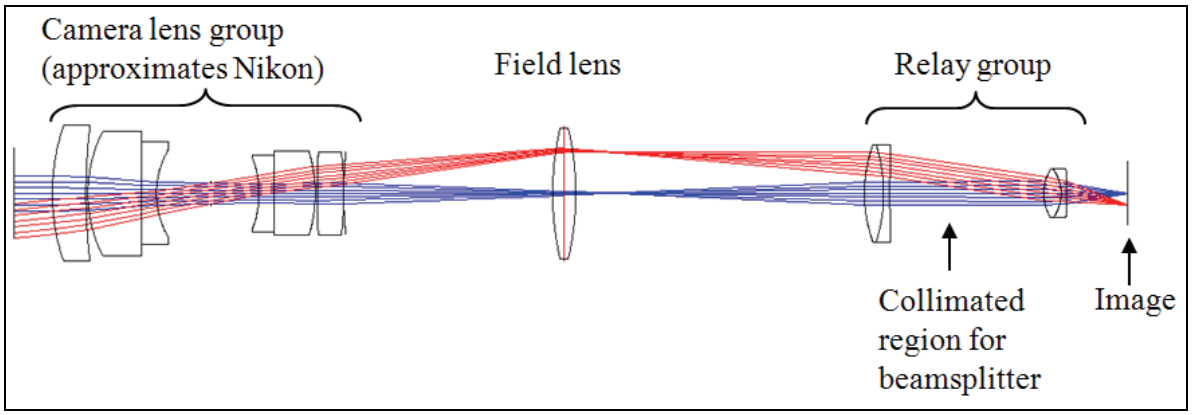

Figure 6. Layout for the boresight camera.

Table 2. Optical designs.

Fiber Input Collection System	Two-color Analysis Instrument	High Resolution Etalon-based System	Boresight
• Collection Optics o Nikon Lens o 80-400 mm focal length o *h'* = 10 mm • Field Lens o At intermediate image o Increases FOV • Relay Lens 1 o Long focal length • Dichroic Filter o > 633 nm transmitted o < 633 nm reflected o Collimated beam • Relay Lens 2 o Short focal length o *h'*= 8.87 mm • Relay Lens 3 o Long focal length • Relay Lens 4 o Images onto fiber o Short focal length o *h'* = 0.60 mm	• Collection Optics o Nikon Lens o 80-400 mm focal length o *h'* = 35 mm • Field Lens o At intermediate image o Increases FOV • Relay Lens 1 o Long focal length • 50/50 Beamsplitter o 50% Transmitted o Collimated beam • Relay Lens 2 o Images onto sensor o Short focal length o *h'* = 7 mm	• Collection Optics o Nikon Lens o 80-400 mm focal length o *h'* = 35 mm • Field Lens o At intermediate image o Increases FOV • Relay Lens 1 o Long focal length • Etalon o Wavelength of interest transmitted. All others reflected or filtered o Collimated beam • Relay Lens 2 o Images onto sensor o Short focal length o *h'* = 7 mm	• Collection Optics o Nikon Lens o 80-400 mm focal length o *h'* = 35 mm • Field Lens o At intermediate image o Increases FOV • Relay Lens 1 o Long focal length • Etalon or Dichroic Filter o Reflected light is used o Collimated beam • Relay Lens 2 o Images onto sensor o Short focal length o *h'* = 8.16 mm

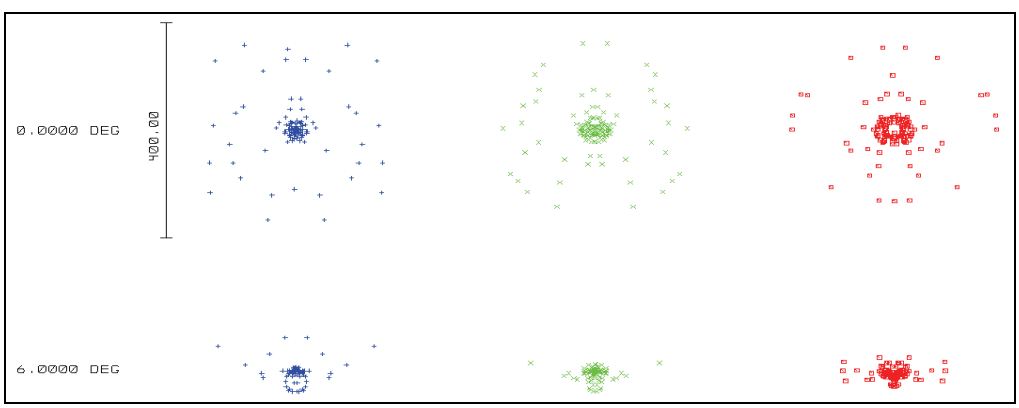

Figure 7. Spot diagram for fiber input collection system; horizontal: wavelength and vertical: field.

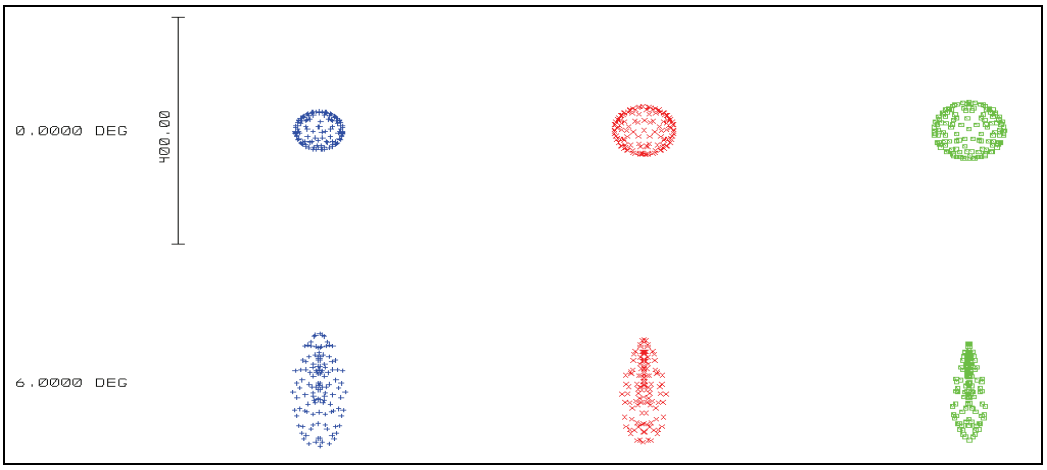

Figure 8. Spot diagram for two-color analysis instrument and etalon-based instrument; horizontal: wavelength and vertical: field.

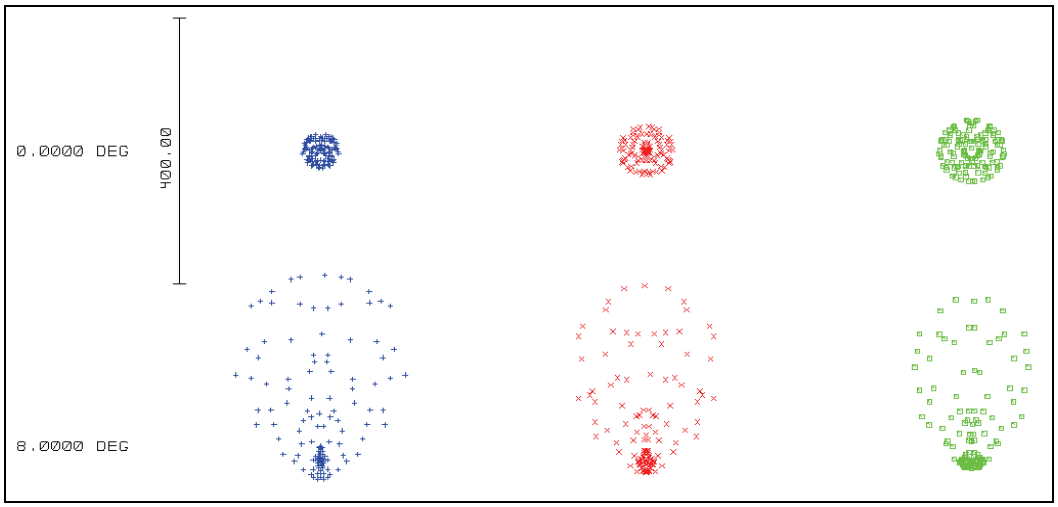

Figure 9. Spot diagram for boresight; horizontal: wavelength and vertical: field.

3. Transmission Experiment

3.1 Background

Radiometry characterizes the propagation of radiant energy through any media or optical system. Radiometric devices (radiometers) measure light and provide the means of describing such media or systems. A specific reason for exploring radiometry has been to characterize the physical properties of battlefield-induced contaminants to allow Army design engineers to assess the effects on electro-optical (EO) systems. As described in DOD-HDBK-178(ER), atmospheric obscurants reduce the performance of EO sensors by (1) attenuating signal radiation, (2) increasing noise, (3) introducing false signals, and (4) reducing image quality through wavefront

degradation. The devices and techniques within this experiment quantify the first of these effects: the attenuation of signal radiation (figure 10).

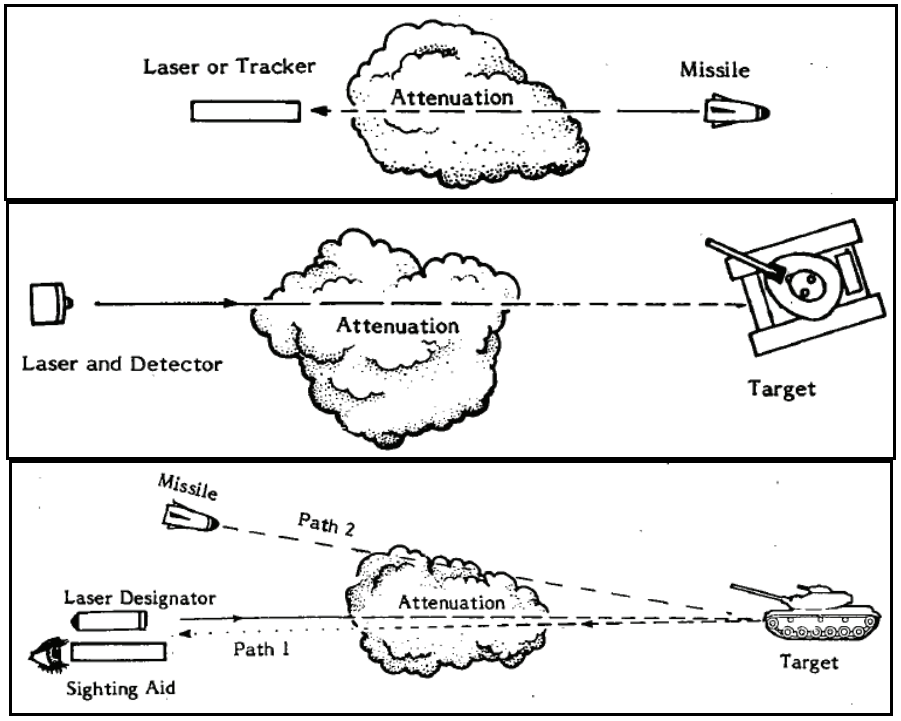

Figure 10. Obscurants on the battlefield: a) one-way path: tracking missile energy, b) two-way path: laser sends energy through obscurant; it scatters at the target and must return to the detector, and c) sensors with different paths using different spectral regions must all validate the target (*1*).

Attenuation (extinction) is comprised of two processes: absorption of energy and scattering of energy into different directions. The testing process that is detailed in this experiment does not distinguish between the effects of either process but quantifies their combined effect by measuring transmission. A spectrometer can measure the irradiance (W/m^2) exiting an obscurant and such data can be processed to generate a time and wavelength dependent transmission plot. Measuring transmitted energy is a step towards quantifying the physical property known as the mass extinction coefficient, which is used to compare obscurants and calculate their effects on sensor performance.

Transmission $T(\lambda)$ is the ratio of received sensor irradiance E_λ and the output irradiance from the source $E_{\lambda o}$. Light is incident upon the obscurant at some angle ϕ and travels a distance through layers of smoke with varying density ρ (*3*) such that

$$T(\lambda) \equiv \frac{E_\lambda}{E_{\lambda o}} = e^{-\sigma_\lambda} = e^{-k_\lambda \mu}$$

$$\sigma_k = \sec\phi \int k_\lambda \rho \, dz \tag{4}$$

$$u = \sec\phi \int \rho \, dz$$

This states that the sensor irradiance E_λ decreases with increasing path length through the smoke. By measuring the received irradiance and knowing the source output irradiance $E_{\lambda o}$, the optical depth σ_λ can be calculated. If the mass extinction coefficient is already known, the u[1] (g/m^2) values can be calculated and related to such things as temperature and wind speed. Nephelometers can measure ρ and a camera can track path lengths so that the mass extinction coefficient k_λ (m^2/g) can be calculated (figure 11).

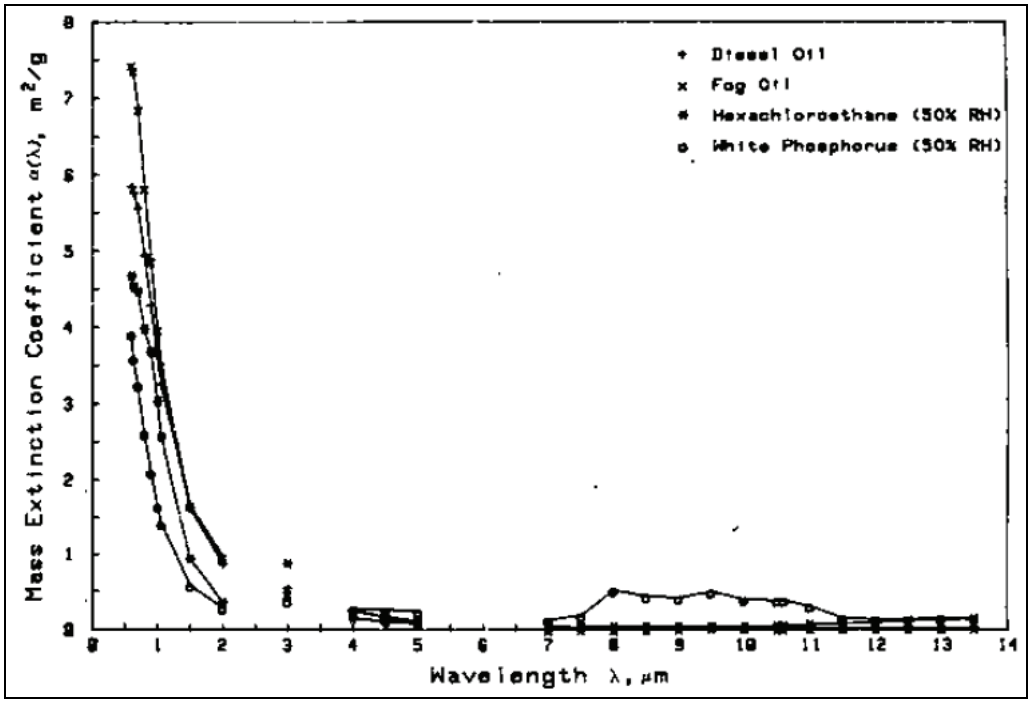

Figure 11. Mass extinction coefficients of standard screening smokes (*1*).

3.2 Data Processing

3.2.1 Test Details

Many transmission experiments utilize the above equations and processes. The goal of such tests is to generate a transmission plot for any wavelength of interest or for any wideband region, such as the entire visible spectrum.

If tests are performed in daylight, they are similar to the setup shown in figure 12. This attributes to extra light entering the spectrometer. Night tests would avoid the excess light, but are often unable to be arranged. There is often a large amount of light energy present as the obscurant is initially released. This adds irradiance that is neither a part of the obscurant or background, and the overall effect is often ignored in the both the processing and results.

[1] Also referred to as concentration path length (*CL*).

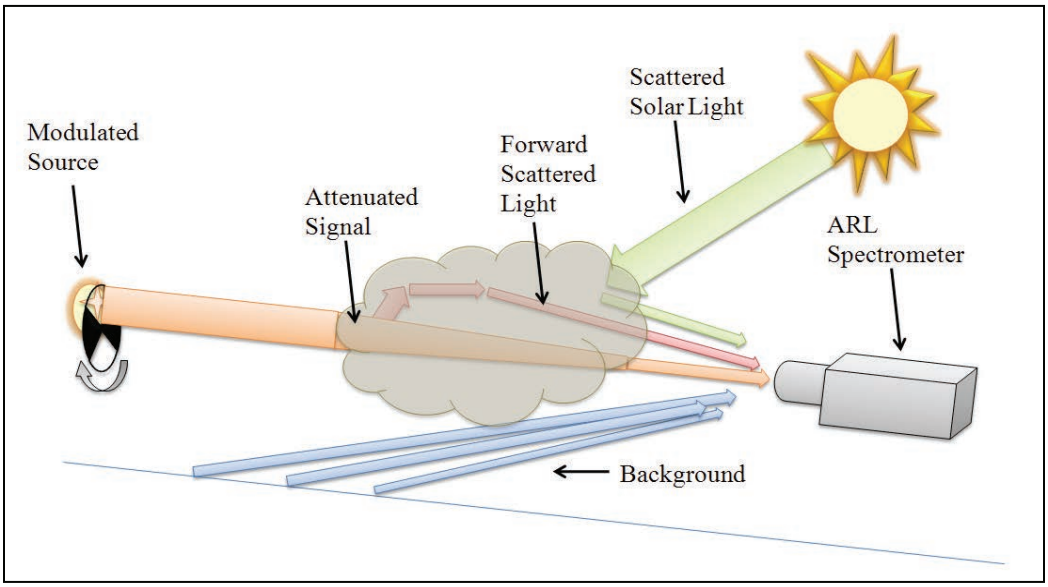

Figure 12. Light paths of a daytime transmission experiment. This example test setup shows many possible light paths into the spectrometer; only the attenuated signal should be used to measure transmission.

As shown in figure 12, there is a large amount of unwanted light entering the spectrometer. The wide field of view of the spectrometer allows background energy to enter the system. This light causes an offset in the sensor irradiance that changes little during the tests. The reflected solar light increases as the obscurant grows and this raises the received irradiance. The resulting output can be seen in figure 13. These two effects can be removed through the testing procedures and data processing.

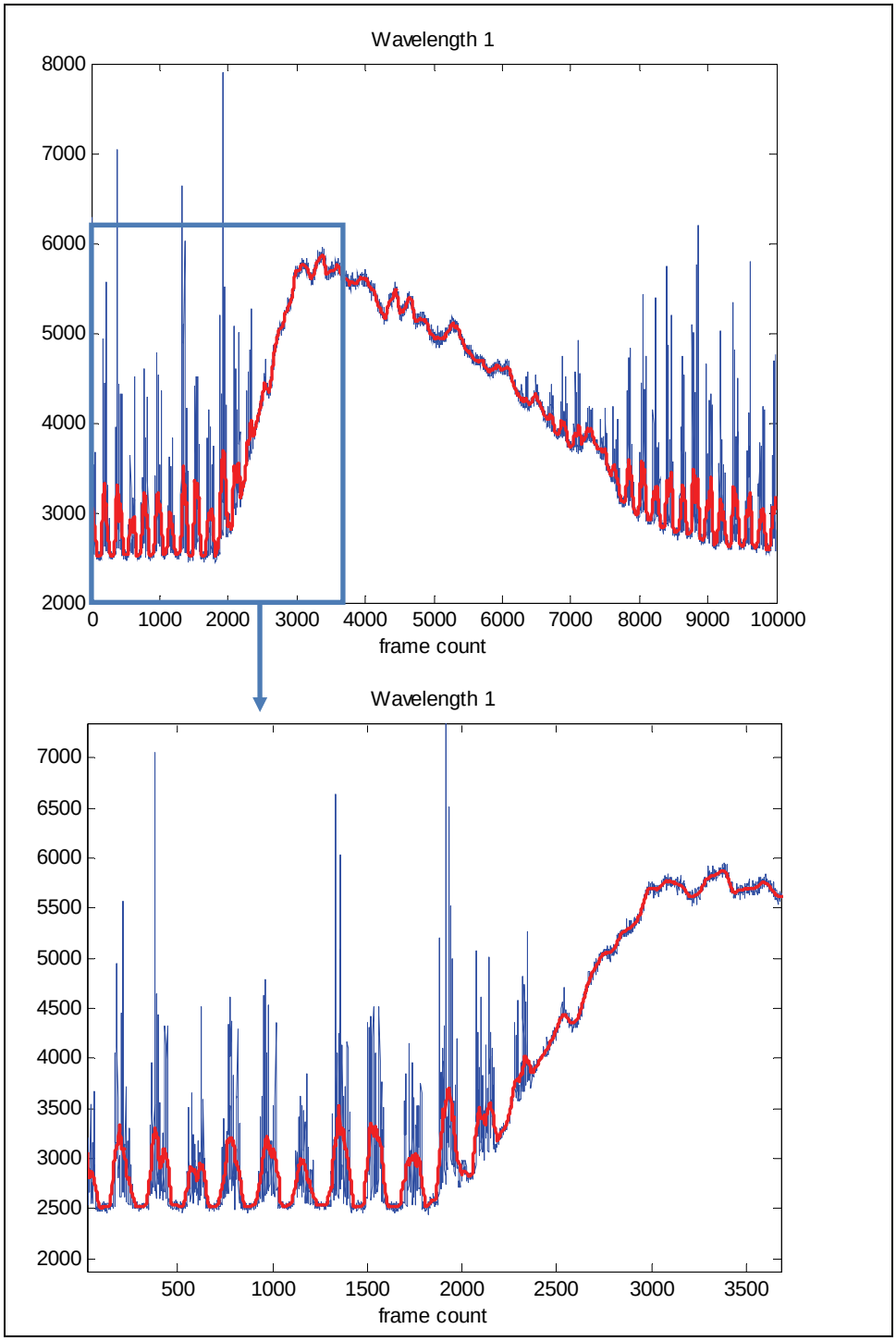

Figure 13. Initial data from transmission test (uncalibrated). The dark blue line is raw data. The thicker red line is the result of a smoothing function to remove noise due to optical turbulence. The obscurant was released near frame 1800. As it forms, the reflected/scattered solar energy causes an increase in irradiance.

Non-uniformity was noticed in the data for times when there was no obscurant due to optical turbulence in the atmosphere between the source and spectrometer. A running average operation was implemented to smooth the raw data and remove the high spatial noise. This symmetric moving average filter is weighted to allow the user to select a proper averaging of the data. The effects of varying the weights are shown in figure 14. The metric for choosing the weight was the increased uniformity of the data for times when no obscurant was present, as seen in frames 1–2000 of figure 13. These particular tests were chosen to use weight 20.

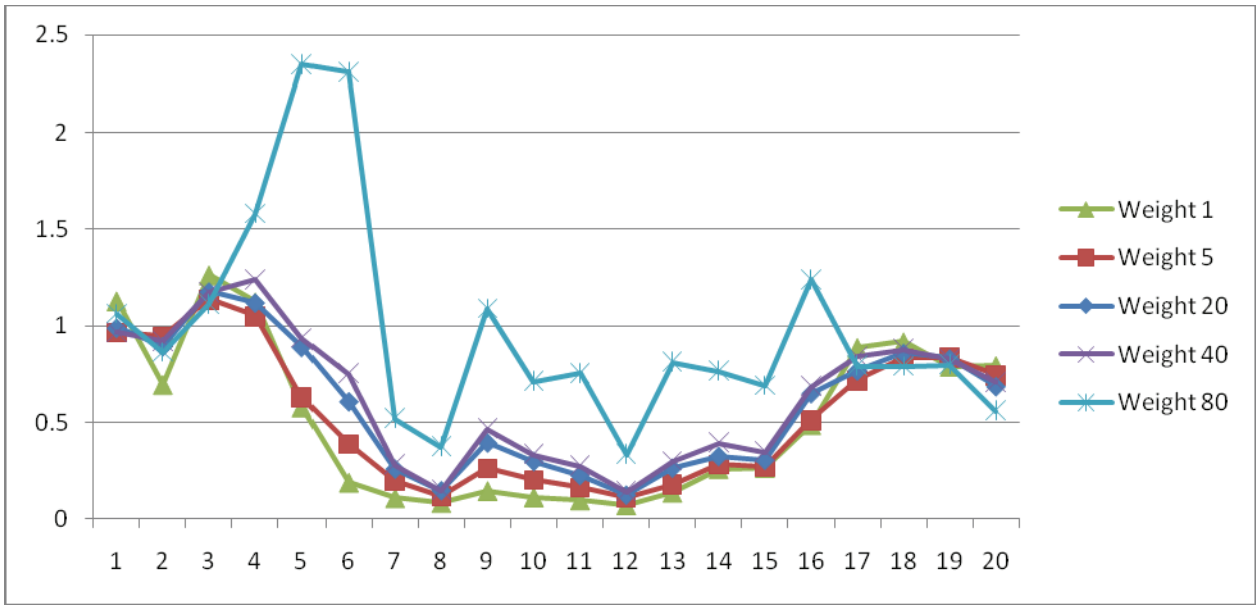

Figure 14. Calculated transmission varying with weighted symmetric moving average.

The scattered light that makes its way back into the spectrometer cannot be distinguished from the attenuated signal unless it is measured. The error this causes depends on the particle size of the obscurant, which statistically determines the amount of scattering in the forward direction (see table 3). This extra light created a bias in the data that was not removed. Updating the experiment procedures to measure scattered energy will increase accuracy by being able to remove this bias.

Table 3. Effect of particle size to wavelength ratio on scattering direction (*1*).

Particle Radius	Scattering Theory Used	Effect
Less than λ/10	Rayleigh scattering	Symmetric scattering; varies as (particle volume)^2 λ^{-4}
Greater than λ/10	Mie scattering	Maximum scattering
About λ/4	Mie scattering	Scattering mostly in forward direction; some spread
Greater than λ	Mie scattering	Almost entirely forward scattering
Greater than 10 λ	Geometric optics	Refraction, reflection, or diffraction

3.2.2 From Irradiance to Transmission

To remove the background and scattered solar energy from the transmission data, it was determined that tests should be done with a modulated source. When the source is off, the only light entering the system is from the background and scattered solar light. Subtracting the low irradiance value from the high irradiance value for each period leaves only the light from the source. The subtraction process reduces the data to one value for every period of the source modulation. An average source output value is taken from the data before the obscurant was released, and it is used to normalize the data and obtain transmission (figure 15).

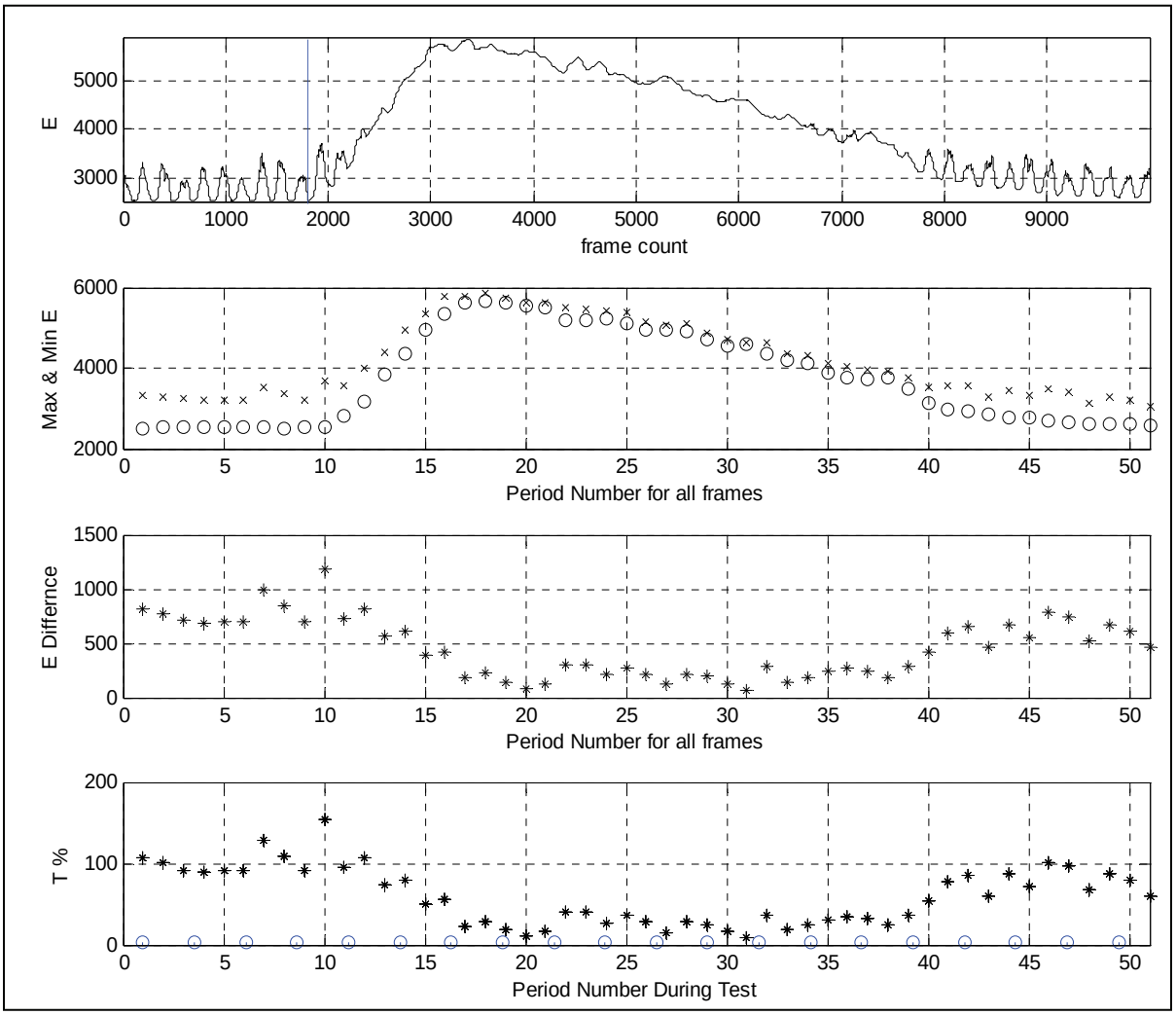

Figure 15. Data reduction plots of transmission test. From top to bottom: 1) Initial data after being smoothed with running average; vertical line indicates user-determined frame at which the obscurant was released. 2) Maximum and minimum values for each chopper period. 3) The difference in max and min values removes background and solar energy. 4) Transmission plot. Values that are much larger than 100% occur when the obscurant is released. They cannot be avoided but do not affect the transmission data.

The frequency of the chopper used to modulate the source may not be known during the test, or it may vary with the changing environment. One of the steps of the processing technique is to let the user see that the specified frequency matches the data. A plot of the frequencies within the data (figure 16) shows there is a peak at the frequency at which the source was being modulated and ensures calculation accuracy.

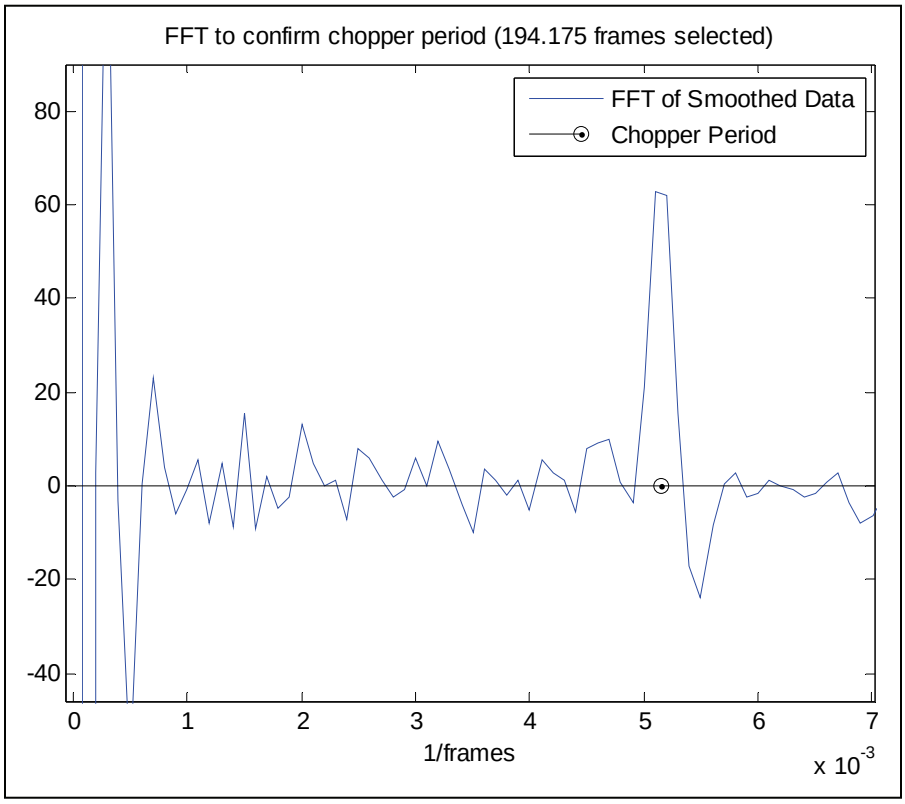

Figure 16. User check of modulation frequency during transmission test.

Since the transmission plots can be generated for any wavelength or wavelength range of interest, the final output is a matrix text file that lists transmission with respect to time and user-selected wavelength regions.

4. Conclusion

The development of tools, techniques, and methodologies determines SLAD's effectiveness in providing SLV analysis and evaluation support of Army and foreign weapon systems (*9*). This has been the intent of the work done as part of a summer internship for ARL. Improvements and suggestions have been made to testing methodologies, three preliminary spectral devices have been submitted for order, and an essential data processing technique was developed for SLV analysis.

Since target acquisition in combat is the most critical element affected by obscurants (such as dust), we have a compulsory task of investigating and assessing the effects of obscurants on target acquisition sensors. This is done by describing their physical/optical properties and by giving an assessment as to the expected obscurant concentrations. The result of this is to provide characterization that can answer the basic question of whether the target can be seen or acquired with a specific sensor.

This paper suggests improvements for measuring transmission, such as performing tests at night to remove unwanted light and measuring scattering and/or forward scattering to remove a bias from sensor irradiance. New reduction software was cultivated to process data for transmission experiments involving wide and narrow bandwidth outputs. This has been essential to the functionality of a recently built ARL spectrometer, and its output is now readily adapted for calculating mass extinction coefficients or other properties of obscurants. The preliminary designs for three new spectral instruments have been developed. The modular fiber input collection system will greatly increase the functionality of two currently owned spectrographs, and the two-color and etalon-based systems are necessary tools for developing narrow bandwidth technology. These efforts have increased ARL/SLAD's ability to characterize obscurants as part of our continuing mission to evaluate sensor performance.

5. References

1. *Military Handbook: Quantitative Description of Obscuration Factors For Electro-Optical and Millimeter Wave Systems*, DOD-HDBK-178(ER), U.S. Department of Defense, 1986.
2. Greivenkamp, J. E. *Field Guide to Geometrical Optics*, SPIE **2004**.
3. Wallace, J. M.; Hobbs, P. V. *Atmospheric Science: an introductory survey*, Academic Press, 1977.
4. Bruce, C. *Measuring Aerosol Density Using Nephelometry and Dosimetry*, New Mexico State University: Center for Atmospheric Sciences, 1987.
5. Hecht, E. *Optics*, Addison Wesley, 2002
6. Montoya, J. Personal communication, U.S. Army Research Laboratory: White Sands Missile Range, NM. July 2008.
7. Giles, M. Personal communication, ARL/SLAD, White Sands Missile Range, NM. July 2008.
8. Holtsberry, B. Personal communication, ARL/SLAD, White Sands Missle Range, NM. July 2008.
9. U.S. Army Research Laboratory Web site, SLAD. (2007 November 19), *Survivability/Lethality Analysis*. http://www.arl.army.mil/ (accessed July 18, 2008).

INTENTIONALLY LEFT BLANK.

Vehicle Technology Directorate (VTD)

INTENTIONALLY LEFT BLANK.

U.S. Army Research Laboratory

SUMMER RESEARCH TECHNICAL PAPER

Design and Construction of a Low Reynolds Number Aerodynamic Performance Analysis Tank

by John Gerdes

Contents

List of Figures **165**

Abstract **166**

1. Introduction/Background **167**

2. Experiment/Calculations **169**

2.1 Summary of Primary Functionality 169

2.2 Component Descriptions 170

2.2.1 Tank and Oil 170

2.2.2 Wing 171

2.2.3 Electronics 172

2.2.4 Actuation 173

2.2.5 Transmission 174

2.2.6 Supporting Structure 174

3. Results and Discussion **175**

4. Summary and Conclusions **176**

5. References **177**

List of Figures

Figure 1. Hand launching a UAV. 167
Figure 2. Flow field plots. 168
Figure 3. DRI micro wing. 169
Figure 4. Solidworks model of test apparatus. 170
Figure 5. The 75 gal tank. 170
Figure 6. Wing-in-ground effect on lift. 171
Figure 7. Miter gears. 171
Figure 8. Tethered fly. 172
Figure 9. Strain gage. 172
Figure 10. Optical encoder. 173
Figure 11. DAQ and signal generator. 173
Figure 12. Stepper motor and driver. 174
Figure 13. Coaxial drive shafts. 174
Figure 14. Effect of varying boundary distance on coefficient of lift. 175
Figure 15. Time history of wing beat. 176

Abstract

As part of the U.S. Army's mission to improve situational awareness of the Soldier in the battlefield, unmanned aerial vehicle (UAV) technology has emerged as a major research topic. The purpose of this study is to create a force analysis testing environment to facilitate the development and optimization of a micro-scale flapping wing. Additionally, other devices exposed to low Reynolds number flows, including fixed wing technology, can also be analyzed using this apparatus. With the resulting optimized wing designs obtained from this testing apparatus, UAVs will be lighter, more efficient, and have greater endurance, thus directly benefiting the Soldier through improved situational awareness.

1. Introduction/Background

In today's battlefield, the modern Soldier is faced with a new and rapidly evolving threat that is not always clearly defined. However, if the Soldier has a high level of situational awareness, threats are reduced and the Soldier becomes more agile and responsive to threats. In recent years, unmanned aerial vehicles (UAVs) have emerged as a highly successful mode of surveillance technology because of their versatility and effectiveness in improving situational awareness.

Development and successful deployment of an Army UAV (figure 1) requires a balance between several aerodynamic and practical capabilities including stealth, endurance, speed and altitude, and maneuverability. Based on the desired mission of the UAV, a good design will maximize those features deemed useful; however, this process requires extensive testing and optimization. The traditional approach to aircraft design makes use of classical aerodynamic theory, and perhaps, computational fluid dynamics simulations, complimented by experimental validation of the analytical design. Typically wind tunnel testing of aircraft components would provide these experimental data, but emerging technology is rapidly shrinking in size, which introduces some problems. A wind tunnel cannot always satisfy the desire to increase the length scale of the model for reasons of handling, instrumenting, and visualizing, while also maintaining the Reynolds number necessary for accurate test results. Dynamic pressures become too small to measure at small scale and low speeds, and therefore, a testing method more suited to small components is needed. Additionally, flapping-wing UAVs use non-traditional methods of lift generation that are difficult to accurately study in the wind tunnel environment.

Figure 1. Hand launching a UAV.

Difficulty in testing arises from the fundamental difference between fixed-wing and flapping-wing flight modes. Flapping-wing flight is inherently a more complex process and requires much more careful attention to geometric and dynamic parameters to ensure the validity of results. For a small flapping wing UAV, it is desirable to scale the wings up in size and reduce

flapping frequency. By properly scaling the aerodynamic properties, it is possible to produce meaningful test results in a slow, controlled, easily observable, and customizable environment. The design of this test apparatus was driven with these ideals in mind.

The fundamental benefit of this tank is that its working fluid is highly viscous compared to air. By increasing the working fluid viscosity, the wing can be scaled up and the flapping frequency can be reduced, while still allowing forces to be measured. The clarity of the working fluid and the walls of the tank permit easy visualization of the wing as it is tested, and the variable mounting points for hardware allow for easy reconfiguration of parts to suit different test parameters.

While this tank is primarily designed for usage with a flapping wing, it could easily be adapted to fixed-wing and rotary-wing testing. As long as the motion of the wing is accurately reproduced, there are a variety of ways to scale the Reynolds number to accurately represent the aerodynamic properties of the wing as it moves through the fluid. The wing size, fluid viscosity, and wing velocity all directly impact Reynolds number (figure 2) and can be altered to suit the requirements of the test being performed.

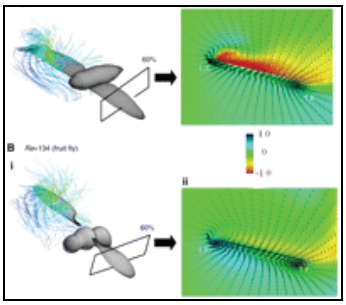

Figure 2. Flow field plots.

A great candidate for testing in this tank would be the millimeter-scale wings (figure 3) currently under development by the U.S. Army Research Laboratory (ARL). These wings are about 3 mm in length and are designed to flap at true biological speed, or about 120 Hz. By scaling up these wings and testing them in this tank, a variety of effects related to lift production, including geometry, timing, and dynamics, could be studied and optimized. For example, the relative phase of the two primary planes of motion (translation and twist) required for flight are highly interactive, but also very difficult to study. However, if the wings were flapping 100 times slower, force measurement and investigation of timing effects would be greatly facilitated, and therefore, the design of the wings would be improved.

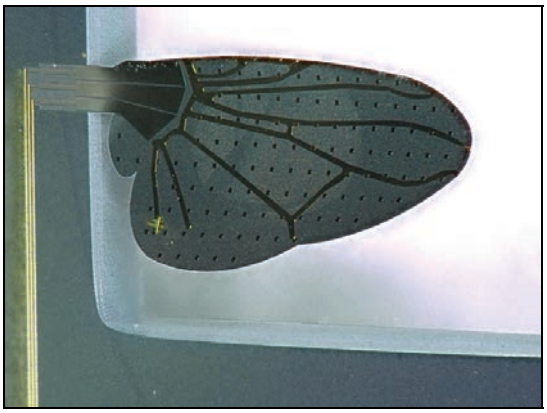

Figure 3. DRI micro wing.

The benefits of effectively optimizing UAV structures are very important and directly useful to the Soldier. Once the UAV is deployed in the battlefield, its optimal wing structure and/or flapping motion will increase flight times, resulting in less downtime, and therefore, less time where the Soldier has a reduction in situational awareness. Since UAVs will be made more efficient, less battery power or fuel will be required for the same flight time. Conversely, in the same flight time, higher altitudes, faster speeds, and longer range can be attained. An added benefit will be the ability to study insect-scale vehicles in detail that would possess a level of camouflage by virtue of small size and biomimicry. This tank would be an optimal setting to study and refine the control of highly miniaturized UAVs, a major achievement that is at present undemonstrated for insect-scale flight. To summarize, UAVs currently in service or under development can be made into more effective and useful tools for the Soldier through testing and optimization with this equipment.

2. Experiment/Calculations

2.1 Summary of Primary Functionality

The test apparatus (figure 4) consists primarily of three physical parts. First, there is the hexagonal tank that contains the working fluid and is mounted on a sheet of plywood. Second, the power transmission system is mounted across the top of the tank. Third, the test wing is mounted to the end of the drive shaft and submerged in the oil. Actuation is accomplished with two stepper motors equipped with optical encoders for position feedback. The steppers are driven by standard stepper motor drives, and the signals are generated in software. The two planes of motion that will be generated are focused on insect flight. When the primary drive shaft is rotated, the translational motion of the wing beat is accomplished. The secondary inner drive shaft will engage a set of miter gears resulting in wing twist (angle of attack) adjustments. Sensing is accomplished with at least two strain gages mounted on the wing root.

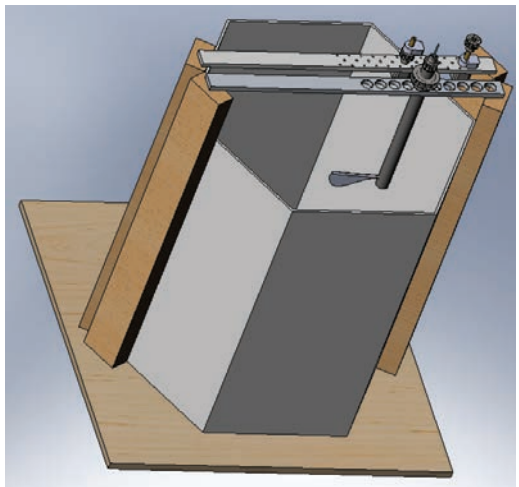

Figure 4. Solidworks model of test apparatus.

2.2 Component Descriptions

2.2.1 Tank and Oil

The primary component of this testing apparatus is an acrylic 75 gal hexagonal tank (figure 5). This tank is constructed of ¼ in. thickness acrylic and is rated to hold over 600 lb of fluid. This tank contains high viscosity (118cSt) mineral oil. Despite its higher viscosity, the oil is less dense than water, and therefore, the tank will have no problem containing the significant weight of 75 gal of fluid. This particular oil has several desirable properties for the testing environment. Most importantly, the high level of clarity allows for easy observation of the test in progress as well as facilitating the eventual application of optical measurements of both the flow field and model. Additionally, the large kinematic viscosity creates favorable Reynolds number conditions. Since the fluid is so viscous, the airfoil can be flapped much more slowly than in air while matching Reynolds number. This translates to higher resolution in the data collection process as well as improved controllability.

Figure 5. The 75 gal tank.

An important concern in the sizing of the tank was the influence of ground effect (figure 6) on the downwash. This effect is caused by downwash hitting a solid bottom surface (i.e., ground,

bottom of tank, any lower boundary), circulating upwards and creating a false cushion of lift that would not normally be present in free flight. When a wing is operated at very low altitude, this effect appears and causes significant error in forces measured. Ensuring the accuracy of force measurement results required that the tank be sized such that free air flight characteristics were accurately produced during testing. Based on the results of Dickinson (*1*), the coefficient of lift reaches an asymptotic value at a certain distance from each of the side, bottom, and top boundaries of the tank respectively.

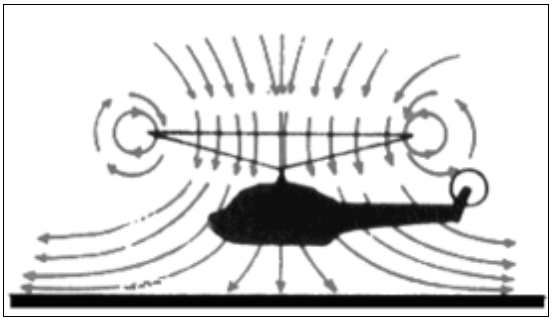

Figure 6. Wing-in-ground effect on lift.

Using this information, the required tank size was determined based on the desired wing span. The hexagonal tank measures about 25 in. x 25 in. x 30 in., which is more than enough space cushion for a wing of up to 6 in. to be within 99% of the asymptotic values.

2.2.2 Wing

The wing currently employed is inspired by the *Drosophila Melanogaster* (fruit fly). Its structure is biologically derived, as it uses a combination of structural ribs and a thin membrane. The ribs are constructed of thin carbon fiber strips, with a thin aluminum outer border for shape-holding and structural rigidity. The membrane is Top Flite Monokote, a heat shrink wrap commonly employed in the construction of model airplanes. The wing has a steel spar for attachment to the transmission. The spar has two strain gages mounted orthogonally for force measurement, and the end of the spar engages one of the two miter gears (figure 7) used for power transmission.

Figure 7. Miter gears.

The sizing of the wing was a very important consideration, since geometric properties including wing span, thickness, and chord all contribute to the Reynolds number experienced during the wing beat. In so much as is possible, the wings are scaled isometrically compared to an actual

fruit fly wing, although thickness of the membrane and spars are larger than scaling would allow. The size constraint was determined by using this equation for Reynolds number:

$$Re = (c * R * \vartheta * f)/\gamma \tag{1}$$

Where c is wing chord, R is wing span, θ is flapping range, f is flapping rate, and γ is kinematic viscosity of the working fluid.

Based on studies of tethered flies (figure 8) by Gotz and Wandel (*2*), a typical fruit fly exhibits a chord Reynolds number of 136 in flight. Using 136 as the target Reynolds number, and a desired flapping rate of 1–2 Hz, the acceptable size of the wing was determined to be approximately 6 cm. It should be noted that this wing size will cause forces measured to fall well within the asymptotic values for free air flight as shown in the tank sizing analysis.

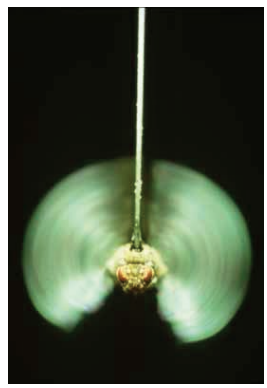

Figure 8. Tethered fly.

2.2.3 Electronics

Data is collected using a pair of orthogonally mounted pre-wired strain gages (figure 9) on the wing spar connecting the wing to the power transmission system. These strain gages were chosen for their small size, 1.0 mm x 0.7 mm and have stress relief pads to mitigate the effect of the wires placing stress on the strain gage. Since the wing is highly dynamic, this is an important error source to account for, especially when the measured values will be on the order of tenths of Newtons.

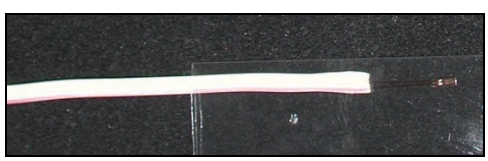

Figure 9. Strain gage.

Optical encoders (figure 10) mounted axially on the drive shafts allow force and position to be fully recorded throughout the wing beat. The encoders used measure 500 pulses per revolution, resulting in a resolution of 0.72 degrees. By trigonometrically resolving forces measured and

pairing this data with angular position from the encoders, lift and drag can be determined at each data point measured, and overall flight characteristics can be mapped.

Figure 10. Optical encoder.

All data inputs are analog voltages and are handled using a computer-driven data acquisition and signal generator (figure 11) interfaced for subsequent filtering and processing. Arbitrarily defined wave forms can be used as the input signal that drives the wing, allowing for customizable flapping motion. This implies that almost any flapping wing beat that can be observed in nature can be accurately reproduced in software and then realized in the physical test environment.

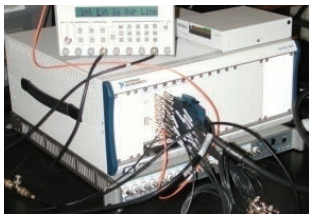

Figure 11. DAQ and signal generator.

2.2.4 Actuation

Actuation of the wing will be performed by a pair of stepper motors and drivers (figure 12). Stepper motors were chosen for this application because of their high degree of precision, as well as their versatility. Stepper motors can be moved in increments of less than a single degree in either direction, and can also be moved at multiple revolutions per second. Additionally, stepper motors have a fairly strong holding torque when not moving and will be resistant to float errors. The steppers are actuated with a simple stepper driver that generates the necessary voltages. The driver receives square waves at a desired frequency as well as a direction bit. The driver then automatically generates the required high voltage pulses to energize the coils of the stepper and create the rotary motion.

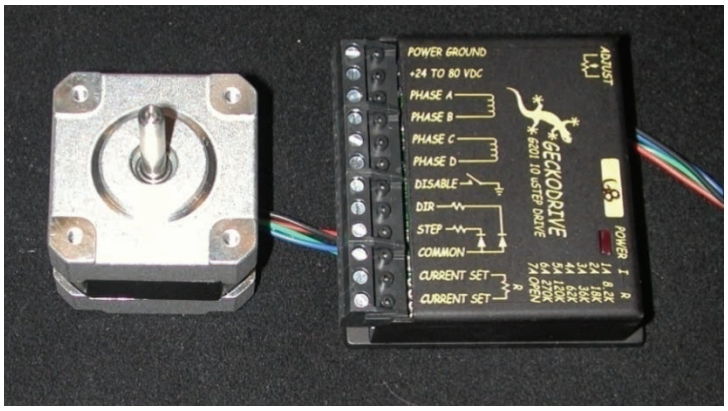

Figure 12. Stepper motor and driver.

2.2.5 Transmission

In order to transmit the rotary motion of the stepper motors into a flapping wing motion, a coaxial drive shaft system (figure 13) is employed. The stepper motors each have a timing pulley installed on their output shafts. These timing pulleys then each connect to a drive belt, which transmits power to the two coaxial drive shafts. The two drive shafts are spaced using delrin bushings to provide smooth operation. The outer drive shaft controls the translational plane of motion, and when rotated, directly flaps the wing. The inner drive shaft controls the twist (angle of attack) of the wing. The rotary motion of the shaft is transmitted to a pair of miter gears arranged orthogonally, inside the bottom of the primary drive shaft. The result is that when the inner shaft is rotated, the gears engage, the rotation is transmitted axially along the wing, and the wing is pitched. Independent control of the two drive shafts is made possible by the two separate timing pulley and belt drive assemblies, allowing complex wing beats to be reproduced, simply by generating the appropriate signals in the software.

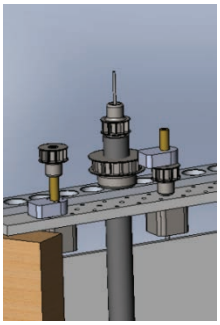

Figure 13. Coaxial drive shafts.

2.2.6 Supporting Structure

The weight of the transmission system, stepper motors, drive shafts, timing pulleys, and other hardware is too great to be safely supported by the walls of the acrylic tank. To mitigate the risk of tank cracks and possible leakage, beams of wood are used as columns to support the weight of the transmission assembly over the tank. By varying the mounting location of the transmission

assembly relative to the support columns, a variety of positions within the tank are possible for the wing beat, depending on individual geometry of the flapping motion being tested. Additionally, multiple mounting locations are available for the stepper motors and drive shafts, allowing for different hardware configurations to suit the needs of the individual test being performed.

3. Results and Discussion

The sizing of the tank was an important consideration in this design. By locating the wing far enough from the sides, the top (fluid-air interface), and the bottom, free flight characteristics can accurately be reproduced to within 1% of true values. Based on results from Dickinson (*1*), the threshold for accurate data (defined as less than 1% error) is a distance of 1.44 wingspans from the bottom of the tank, 0.46 wingspans from the side of the tank, and 0.72 wingspans from the top of the tank (figure 14). The tank employed in this apparatus measures 25 in. x 25 in. x 30 in. and the wing measures about 3 in., placing the results well within the acceptable size constraint.

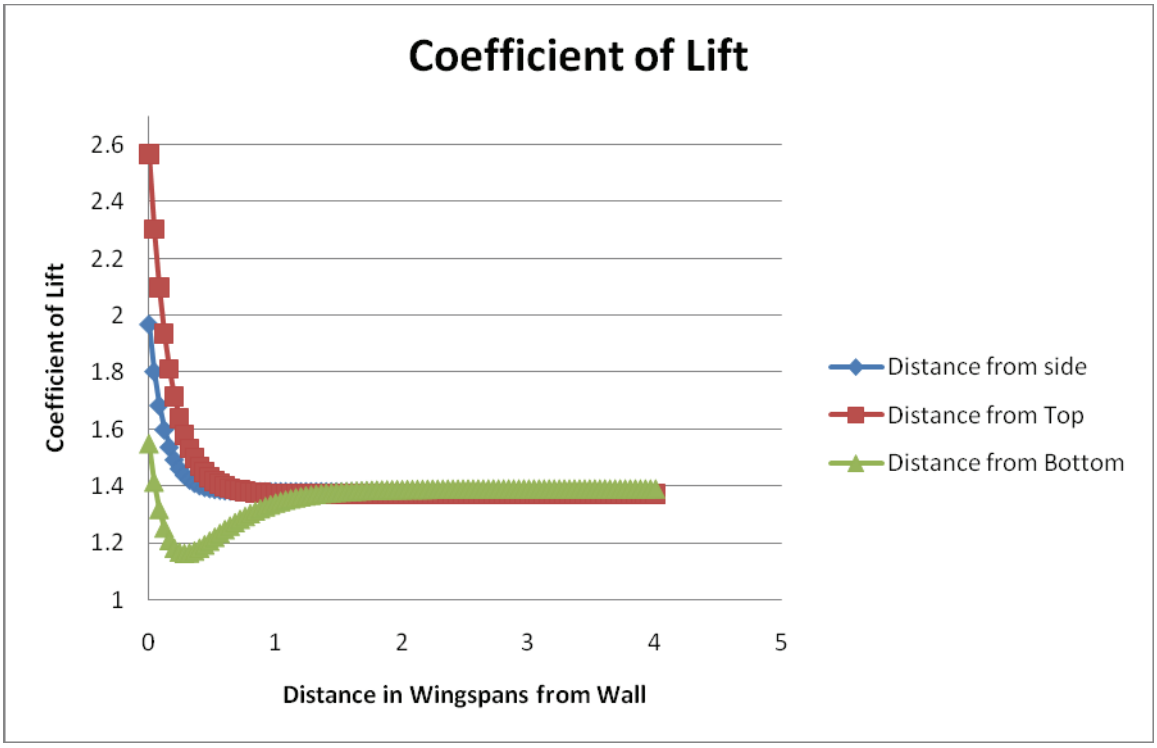

Figure 14. Effect of varying boundary distance on coefficient of lift.

In the future, this apparatus will be supplemented with a third degree of motion, commonly referred to as plunging (figure 15). As the wing beats back and forth, it dips down at the center of the flap, resulting in a gentle concave U-shaped profile. This supplements lift production by

capturing the vortex created on each wing beat, and therefore, more accurately reproduces true biological motion. To accomplish this plane of motion while maintaining flap and twist, a universal joint similar to that employed in truck driveshafts will be installed along the wing spar, and a hinging mechanism will provide a secure anchor while still allowing for plunge in the wing beat. With this third degree of motion, practically any wing motion achieved by an insect can be fully reproduced in the test apparatus including dragonflies, hoverflies, butterflies, bees, and many others that are reflective of potential vehicle size.

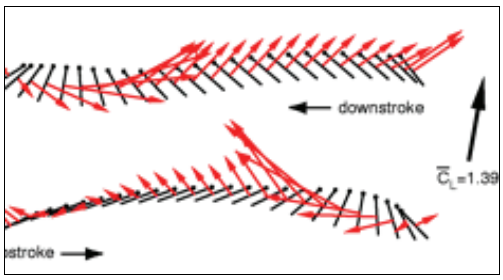

Figure 15. Time history of wing beat.

4. Summary and Conclusions

The primary finding of this study is that this testing tank is an effective device for force measurement of flapping wings. By altering variables such as geometric scaling and fluid viscosity, a wide range of Reynolds numbers is easily produced. This directly corresponds to a large range of flight velocities that can be accurately modeled during testing. Additionally, by altering the software-generated signal output, the pattern of the wing beat is highly customizable to almost any biological or man-made inspiration for which force analysis would be a useful test within the constraints of a flapping/pitching motion. By optimizing wing structure, shape, and flapping patterns with this testing equipment, the Army can improve the capabilities of existing UAVs, as well as design in desirable features into new and developing technologies. The end result is that the Soldier will benefit from increased surveillance capabilities, and improved situational awareness in uncertain and complex battlefield conditions.

5. References

1. Dickinson, M.; Lehmann, F.; Sane, S. *Science* **1999**, *284*, 1954-1959.
2. Gotz, K. G.; Wandel, U. *Biological Cybernetics* **1984**, *51*, 135.

INTENTIONALLY LEFT BLANK.

U.S. Army Research Laboratory

SUMMER RESEARCH TECHNICAL PAPER

Photogrammetry Technique for Deformation Measurement of Millimeter-Scale Wings

by Aaron Harrington and Christopher Kroninger

Contents

List of Figures **181**

Abstract **182**

Acknowledgment **183**

1. Introduction/Background **184**

2. Experiment/Calculations **185**

2.1 Calibration 187

2.2 Image Capture 189

3. Results and Discussion **189**

4. Summary and Conclusions **190**

5. References **191**

List of Figures

Figure 1. Close up of wings. 184
Figure 2. Camera mount with sample stage. 186
Figure 3. Photogrammetry technique. 187
Figure 4. LED “calibration block.” 188
Figure 5. Image run in TargetFinder() Matlab function. 189

Abstract

Measurement of objects using photographic images is a technique known as photogrammetry. This method uses known camera and lens parameters to map points identified in pixels on two or more image planes to points in a 3D object space. This technique was applied to measure the deformation of an insect-scale wing as it is actively flapped. Using specialized photogrammetry software photographs of the wings were analyzed, and predetermined titanium targets on the wings were programmatically located and measured in pixel space. Using the collinearity equations these points were transformed and measured in object space. The method used to accomplish this is outlined as well as basic photogrammetric theory and techniques.

Acknowledgment

The Photogrammetry Tool Kit, a collection of programs for solving photogrammetry problems, was written by Liu or Al Burner or NASA Langley Research.

1. Introduction/Background

Even before unmanned aerial vehicles (UAVs) were introduced, people have envisioned remotely controlled and autonomous insect-scale vehicles. These vehicles are commonly called micro-aerial vehicles (MAVs). There are many inherent problems with developing vehicles of this size falling under many disciplines including controls, power and energy, structures, aerodynamics, and aeroelastics. Each of these areas requires specialized equipment and research techniques unique for the scale on which they are being applied. In the area of aerodynamics, insect wings and flapping flight are rapidly becoming a popular area of study. Wood and Fearing used high speed cameras to perform shape measurements on insect wings using photogrammetry. The application of microelectromechanical systems (MEMS) fabrication techniques has allowed the fabrication of millimeter-scale wings, comparable to those of *Drosophila Melanogaster* (a common fruit fly), which have been manufactured containing three piezoelectric actuators at the base that allow the wings to flap. By measuring the displacement of the flap of these wings aerodynamic, inertial, and elastic forces in the wing can be calculated.

These wings, developed by the Sensors and Electronic Devices Directorate (SEDD), were actuated during testing by an offset sine wave with a peak-to-peak voltage range of 0–5 V. The piezoelectric actuators are unimorph benders, meaning they operate most effectively in one direction, so they were only tested for this positive voltage range only. Also, three sizes were tested referred to by their respective size to a baseline model as 1X, 1.5X, and 2X. At the 1X scale, the wings are approximately 1 mm in span (figure 1). Made on small integrated circuit (IC) packages, a custom Zero Insertion Force (ZIF) mounting platform was supplied for testing.

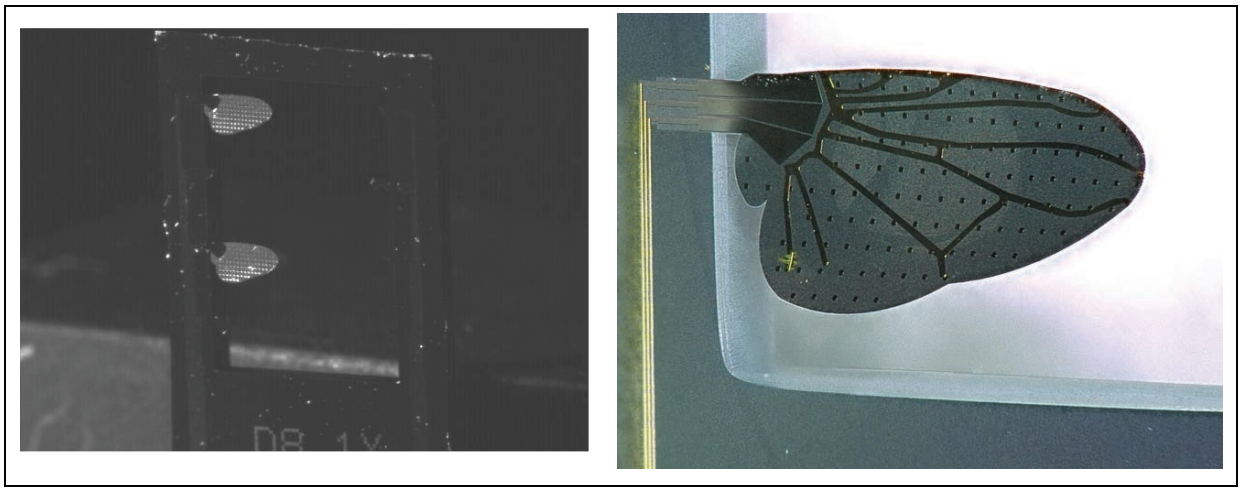

Figure 1. Close up of wings.

2. Experiment/Calculations

In order to take photographs of the wings, proper camera mounting and placement were imperative. Four cameras with telecentric lenses with focal lengths of about 300 mm all needed to be mounted in close proximity to each other but also have freedom to be moved in any position around the wing. Flexibity in camera mounting was required as these lenses only have a few millimeters of adjustment in the distance between the lens and the object. This is due to the telecentricity and a depth of field (DOF) of only a millimeter or two depending on the lighting. Further difficulty was added by the large dimensions of the lenses, which all had to be positioned about 5 cm from the wing. To accomplish this, a custom camera mount was designed and built. This camera mount used joints that provided 4° of freedom for each camera. Each camera had two of these joints that provided a total of 6° of freedom, allowing them to be mounted in any configuration (figure 2). Multiple mounting arms could be placed on a single shaft creating a tree style of mounting. This not only allowed multiple cameras to be mounted close together, but it is sufficiently rigid to minimize vibration introduced from the surrounding environment. To fix the wings in place but also allow them to be moved or rotated, they were also mounted to a mounting arm. Two more joints were used with a single arm and a mounting plate. This allowed the stage to have both rotational and translational ranges of motion as seen in figure 2.

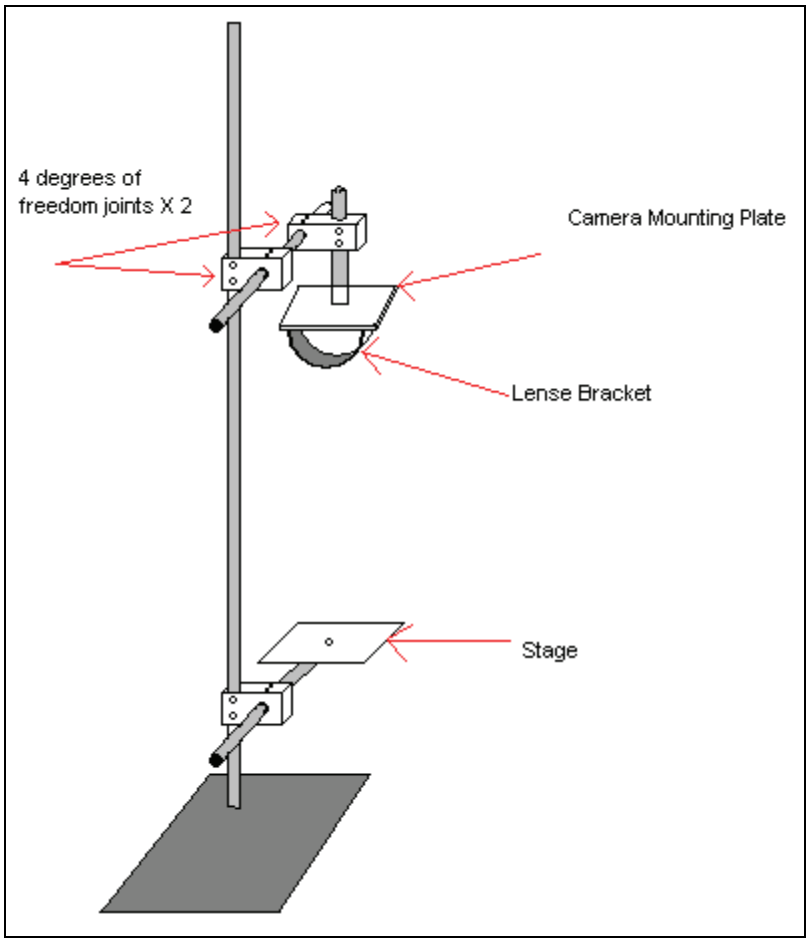

Figure 2. Camera mount with sample stage.

SEDD supplied a data sheet on the wings that included experimentally determined resonant frequencies for the three sizes of wings. These frequencies for the 1X and 1.5X sizes were between 500 and 800 Hz, which were much faster than the frame rate that the cameras could reach, max of 30 fps. Thus, a method needed to be developed that would allow the flapping motion to be captured by the cameras. By sending a through-the-lens (TTL) trigger from a timing device to control the strobe lights and the cameras at a rate of approximately 10–12 Hz. At these shutter speeds, fine adjustments of $\pm$01 Hz could be made to obtain phase locked photographs and slowed motion photographs. However, an accurate method of flapping the wings that allowed for quick frequency and voltage changes was also needed so that various resonant modes could be examined as well as higher voltage inputs to try and get larger flapping ranges. To do this, instrumentation software, along with data acquisition devices and controllers, were used to control the input signal to the wing actuators.

Custom subroutines and code were also written that allowed for steady or progressive frequencies and amplitudes to be tested. These scripts allowed both amplitudes and frequencies to be steadily incremented in a single test. Frequency increments as high as 10 Hz and as low as

.1 Hz allowed for the determination of the resonant frequency for each individual wing. The true resonant values were hard to obtain because wing flap magnitudes appeared the same over a small range of frequencies.

Measuring the position and movement of wings as they flap is very difficult to do with passive measuring equipment such as calipers, micrometers, rulers, and scales because of their dynamic motion as well as minute changes in wing positions, even under resonance. Active methods such as velocimetry or photogrammetry must then be used. Photogrammetry has been around for nearly a century but has traditionally been used in aerial photography for accurate measurement of actual distances in photographs. Burner et al. (*1*), have recently been applying the use of photogrammetry to wind tunnel testing while Wallace (*4*) applied high speed photogrammetry on insects. The basic premise of photogrammetry is that from known positions of two or more cameras, intersecting rays can be "drawn" from each image plane outward to points on the object. This intersection provides coordinates in the object space. In order to obtain coordinates from these intersecting rays, calibrations for each camera are crucial. Figure 3 demonstrates the basic photogrammetry technique.

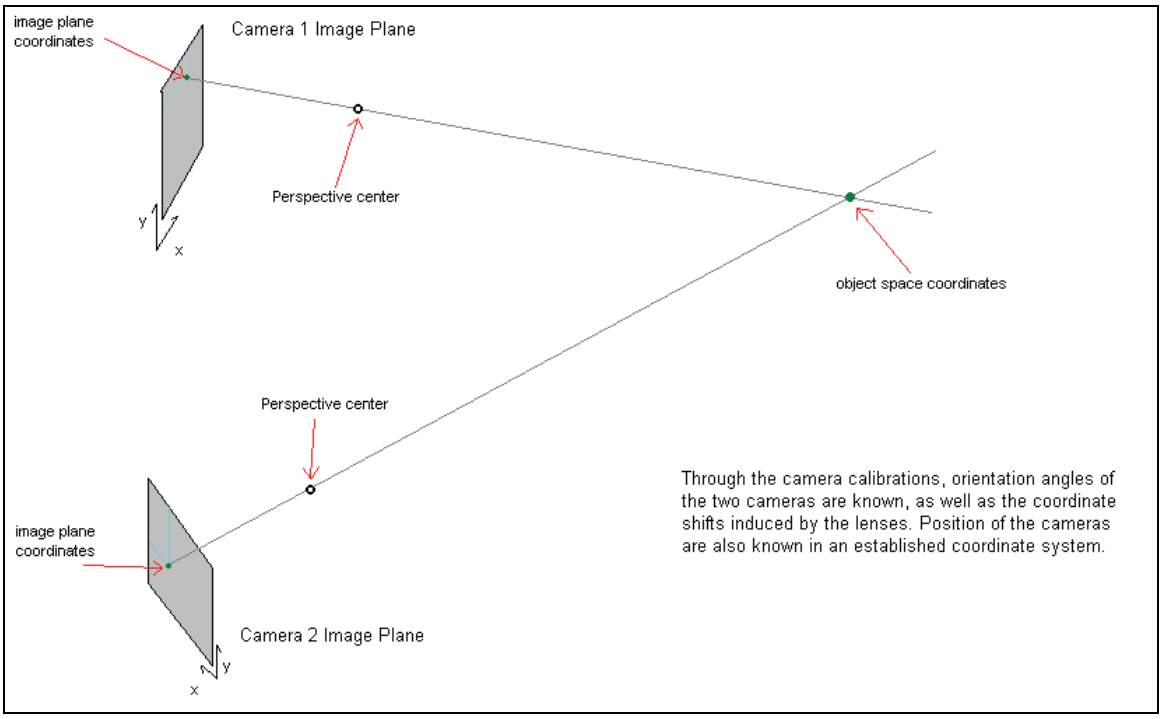

Figure 3. Photogrammetry technique.

2.1 Calibration

The prerequisite step in doing photogrammetric measurements is the calibration of the cameras. This procedure defines all the attributes for individual cameras needed for determining how the rays will be projected toward the object. Calibration defines the object space coordinates (X,Y,Z) relative to coordinates on the image plane (x,y) of the cameras. The lens position

(X_c,Y_c,Z_c) is also defined as a single point called the perspective center. A point on the object, the perspective center, and the image point all lie on a straight line for a camera with no lens distortions. Relationships for these points can be defined by collinearity equations (*1*).

$$x_n - x_p + dx = -c\frac{m_{11}(X_n - X_c) + m_{12}(Y_n - Y_p) + m_{13}(Z_n - Z_c)}{m_{31}(X_n - X_c) + m_{32}(Y_n - Y_p) + m_{33}(Z_n - Z_c)} \tag{1}$$

$$x_n - x_p + dx = -c\frac{m_{21}(X_n - X_c) + m_{22}(Y_n - Y_p) + m_{23}(Z_n - Z_c)}{m_{31}(X_n - X_c) + m_{32}(Y_n - Y_p) + m_{33}(Z_n - Z_c)} \tag{2}$$

The variables x_p and y_p represent the principal-point location and c the camera principal distance. The variables m_{ij} are used to represent elements of a rotation matrix M that are functions based on the Euler orientation angles for the camera (*1*). Also accounted for in these equations is dx and dy, which represent ray deviations due to lens distortions.

To accomplish proper calibration of the cameras, images must be taken of an object of known dimensions. This presented a challenge in creating a technique for imaging objects on a millimeter scale. A first attempt to create a calibration block using a Computer Numerically Controlled (CNC) mill were unsuccessful because of subtle variations in block size when measured with a micrometer. It was later suggested that a surface mount light-emitting diode (LED) be used because the data sheet, including dimensions, was readily available. By selecting the corners and other known points on the LED photograph (figure 3) calibrations for each camera were successfully completed using photogrammetry toolbox software. The variables that the calibration solved for include the Euler orientation angles of the cameras, lens distortion parameters, and positions of the cameras. Dimensions of the LED "calibration block" were also verified using a digitally controlled microscope.

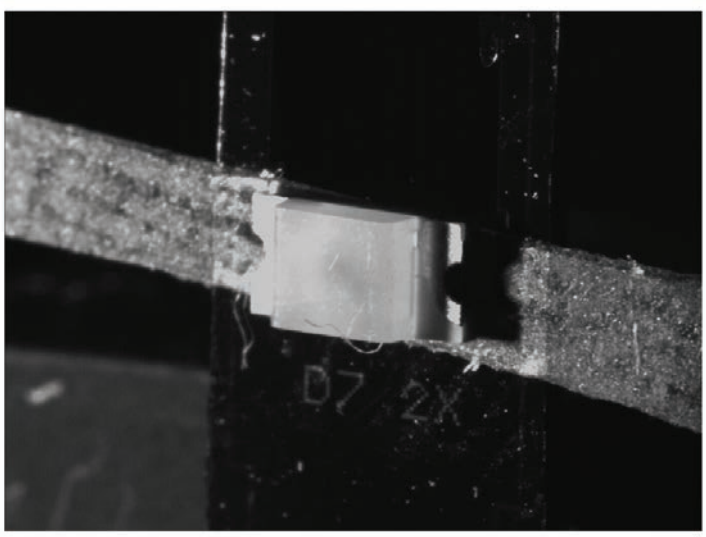

Figure 4. LED "calibration block."

2.2 Image Capture

The next step was to automatically find bright spots created by reflected light from the strobe light on the targets on wings. As part of the design and manufacture of the wings, titanium foil dots were arranged in a grid-like pattern. This foil reflected light back to the cameras and was used to identify the points of interest on the wings on which to do the photogrammetry. To accurately find the centroids of these bright spots custom scripted software was developed. When run, this spot finding function would read in a gray scale image in the form of a matrix. Higher value entries represented bright pixels and lower value entries represented dark pixels. A function called "TargetFinder()" was written to scan the matrix line by line searching for pixels as bright or brighter than a threshold value input by the user. It would then store the pixel location in an array. Using a centroid calculation function included in the Photogrammetry Toolkit, TargetFinder() would then take a field of bright pixels and find the centroid locations. The user would also input a maximum centroid deviation in pixels that would eliminate multiple centroids for each hot spot. These final values were the centroids of hot spot or target and could be output to a file and overlaid on the image for use by the photogrammetry software (figure 5).

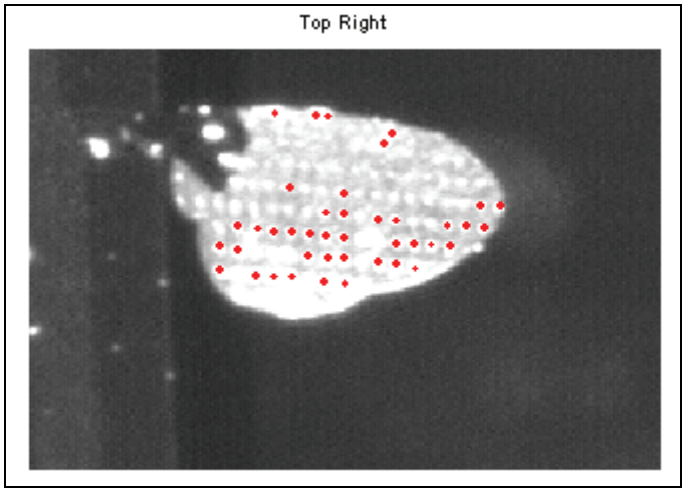

Figure 5. Image run in TargetFinder() Matlab function.

3. Results and Discussion

Results thus far are very promising and measurements are close to expected values. Initial photogrammetric analysis performed by my mentor estimates deflection angles of about 10° for a 1X scale wing actuated at 748 Hz. Observations of images in a movie format seem to validate an approximate 10° flap angle. One of the nicest features of the technique used for doing the photogrammetry is the tree style of camera mounting. Having all cameras on a single shaft saves a large amount of space and reduces vibration by using its mass to dampen oscillations. The

target finding software works well with both light and dark images because it automatically detecting the photograph's brightness as well as requiring input from the user.

4. Summary and Conclusions

The current technique that includes tree style camera mounting, computer controlled wing output, custom target finding software, and photogrammetry software will provide a good basis for future work. Using lenses with more magnification will allow for more accurate measurements of wing deflections and clearer photographs, and thus will increase the accuracy of the calibrations, target finding, and photogrammetry analysis. The use of LabView or similar software also allows for expandability and possibly the complete automation of the entire process for controlling the wings, triggering the strobe and cameras, and saving the images. Current work is being done to control the Imaging software using custom executables to reduce the amount of manual labor required in data acquisition. The wings also allow for increase capability because of the three actuators on them. To accurately mimic insect flapping, pitch also needs to be incorporated. This can be done by sending multiple phased sinusoids to each actuator. To date, the same signal has been sent to all three actuators, which should mainly drive a flapping motion. Current collaboration through the MAST program among multiple directorates as well as colleges and universities will help broaden the knowledge base for similar research and the push toward micro-systems and MAV research.

5. References

1. Burner, A. W.; Radeztsky, R. H.; Liu, Tianshu; Cattafesta III, L. N. Photogrammetry Applied to Wind-Tunnel Testing. *AIAA Journal* 6th ser. **2000**, *38*, 964–971.
2. Dewitt, Bon.; Wolf, Paul. *Elements of Photogrammetry with Applications in GIS, 3rd Edition.* McGraw Hill, Boston, MA. 2000
3. Kroninger, Christopher. Personal interview. 2008.
4. Wallace, I.; Lawson, N.; Harvey, A.; Jones, J.; Moore, A. High-Speed Photogrammetry System for Measuring. *Applied Optics* 17th ser. **2006**, *45*, 4165–4173.

INTENTIONALLY LEFT BLANK.

Weapons & Materials Research Directorate (WMRD)

INTENTIONALLY LEFT BLANK.

U.S. Army Research Laboratory

SUMMER RESEARCH TECHNICAL PAPER

Novel Thin Film Materials for Tunable Device Applications

by Claire Weiss

Contents

List of Figures **197**

Abstract **198**

Acknowledgment **199**

1. Introduction/Background **200**

2. Experiment/Calculations **201**

3. Results and Discussion **202**

4. Summary and Conclusions **206**

5. References **207**

List of Figures

Figure 1. Cross-sectional (a) and plan-view images (b) from the FESEM show a dense, well-crystallized microstructure. A clear delineation is also visible between the film and bottom electrode, indicating good electrical contact. 202

Figure 2. AFM micrographs showing (a) the plan-view of the 40nm thick film, with some amorphous sections circled, (b) the plan-view of the 280nm thick film, and (c) the 3D image showing the smoothness of the films, with an average roughness of about 1.92nm. 203

Figure 3. The Rutherford back-scattering data is shown ad a spectrum above. Here, the ratio of the barium (Ba) and strontium (Sr) peak heights gives the ratio of barium and strontium in the film.....205

Figure 4. Dielectric measurements (a) dielectric constant and loss tangent as a function of the frequency. Up to 1 MHz, little dispersion in either the dielectric constant or the loss is shown. (b) The tunability as a function of applied field shows a maximum tunability of almost 30%.....205

Figure 5. The leakage current density as a function of applied voltage for two representative film thicknesses. As the thickness of BST film increases, the leakage current density decreases. 206

Abstract

The morphology and dielectric properties of Barium Strontium Titanate ($Ba_{0.6}Sr_{0.4}TiO_3$ or BST) thin films were studied as a function of film thickness. The films were prepared by metalorganic solution deposition (MOSD), and the BST precursor solution was then spin-coated onto platinum silicon wafers. The thin films were then characterized using a field emission scanning electron microscope (FESEM), an atomic force microscope (AFM), Rutherford back-scattering (RBS), and dielectric and electrical measurements. The dielectric constant varied with film thickness and was largest for the thickest film (ε_r=503), with a nominal thickness of 400 nm. However, the loss tangent was also highest for this film at 0.045. Overall, the best combination of dielectric properties is found in the medium-thickness films, with a thickness ranging from about 160 nm to 240 nm. These films had a dielectric constant near 300, loss around 0.03, and tunability up to 30%. These findings show that careful thickness control of BST thin films may be a useful method to obtain the desired dielectric properties necessary for tunable devices.

Acknowledgment

The author grateful acknowledges the staff at ARL, especially those in the Weapons and Materials Research Directorate. The work at ARL was supported by the U.S. Army Research Office Grant No. W911NF-05-1-0528.

1. Introduction/Background

In recent years, Barium Strontium Titanate ($Ba_{0.6}Sr_{0.4}TiO_3$ or BST) has become a leading materials candidate for tunable device applications, such as phase shifter arrays for steerable antennas. Like many other candidates for tunable device applications, BST is a ferroelectric material, meaning that it displays a spontaneous polarization below a certain temperature (the Curie temperature or T_C) and that the dielectric response can be tuned with the application of an external electric field. BST has a substituted cubic perovskite structure, meaning that its structure can be described by the general formula, ABO_3. Here, barium and strontium compete to occupy the A site and titanium occupies the B site. BST is a variant on barium titanate ($BaTiO_3$), and the strontium effectively stabilizes the barium titanate by suppressing "undesirable phases," such as a hexagonal phase. BST has gained importance as a ferroelectric material partly because the Curie temperature can be adjusted by changing the relative amount of barium and strontium in the BST (*1*). Requirements for successful tunable devices include a moderate dielectric constant, high tunability of the dielectric constant, low loss tangent, and affordability and ease of fabrication. Although thin film BST has a moderate dielectric constant and good tunability, it still has a rather high loss for device applications. Many approaches have focused on simultaneously improving tunability and lowering loss, such as controlling the film stress (*2–6*), acceptor doping, (*7–8*) and identifying better electrode materials and film fabrication processes (*9*). To ensure the affordability and ease of fabrication, the metalorganic solution deposition (MOSD) technique has been employed. This technique is desirable for tunable device materials because it is fairly easy, inexpensive, and it allows for careful control of the stoichiometry and large-area deposition. The use of thin films over bulk materials has significantly cut down on the cost of producing these devices.

The use of thin films in tunable devices presents many new challenges. For example, strain plays a major role in determining the properties of thin films. Thin film strain is caused by differences in the coefficients of thermal expansion of the film and substrate and the degree of lattice mismatch between film and substrate. The thickness of the film also has a strong influence on the strain. Therefore, changing the thickness of the film can also change the dielectric properties. A thickness-dependent study of the dielectric properties of BST thin films is useful for determining the optimum thickness for the integration of BST thin films into tunable devices. This study can also give us an idea of the threshold values of thickness. For example, electrical measurements were not reliable on the thinnest samples $\leq$40nm. This shows us that our samples must possess a critical thickness to be successfully integrated into tunable device structures. In this paper, we systematically study how the thickness of BST thin films affects the dielectric properties such as dielectric constant, tunability, loss tangent, and the electrical properties such as the leakage current.

2. Experiment/Calculations

The films were fabricated by metalorganic solution deposition (MOSD) technique, using barium acetate, strontium acetate, and titanium isopropoxide as the precursors. Acetic acid and 2-methoxyethanol were used as the solvents. The precursor solution was concentration optimized (0.43 M) to obtain the desired stoichiometry of the film. Proper molarity is necessary to ensure that each spin-coated layer is thin enough to cover any defects left behind by pyrolysis of the previous layers. This causes fewer pinholes in the annealed film as well (*10*). In the optimized procedure, barium acetate was added to the acetic acid and stirred for one hour. Then the strontium acetate was added to the barium mixture and stirred for another hour. Finally, the titanium isopropoxide was added to the 2-methoxyethanol, and then this mixture was added to the barium-strontium mixture. The final mixture was stirred for one hour until the solution was clear. The viscosity of the solution was adjusted by adjusting the amount of 2-methoxyethanol. Correct stoichiometry was ensured by carefully measuring the amount of barium acetate, strontium acetate, and titanium isopropoxide dissolved in solvent. Prior to film deposition, the Pt-Si substrates were spin-cleaned using 2-methoxyethanol. Subsequently, the BST precursor solution was deposited onto the substrates using a spin coater (Headway Research, Inc.). Particulates were removed from the solution by filtering through 0.2 mm syringe filters. Again, we have optimized a spin procedure (spin speed and spin time) to create a high quality film with the desired properties. For each BST layer, the samples were spun at 15,000 rpm for 50 s. Deposition was repeated until the desired thickness was achieved. After the deposition of each layer, the sample was pyrolyzed at 350 °C on a hot plate for 10 min to remove the organic addenda and form an inorganic amorphous film. Finally, all of the films were annealed at 750 °C in flowing oxygen for one hour to ensure crystallinity.

The surface morphology of the films was assessed by atomic force microscopy (AFM) using a Digital Instruments Dimension 3000 in tapping mode. A Hitachi S4500 field emission scanning microscope (FESEM) was utilized to assess the cross-sectional and plan-view film microstructure. Rutherford backscattering spectrometry (RBS) using 2.0 MeV He+ was used to determine the stoichiometry of the deposited BST film. The electrical measurements were achieved in the metal–insulator–metal (MIM) capacitor configuration, with Pt as both the top and bottom electrodes. The dielectric constant was calculated from the capacitance measured at 100 kHz without bias voltage using the geometry of the device (*8*). The tunability was measured as a function of applied bias from 0 to 553 kV/cm. The measurements were performed as cycle sweeps (negative voltage to positive voltage back to negative voltage) to check for any possible hysteretic behavior. The leakage current was evaluated via current–voltage measurements at 237–474 kV/cm with a step delay time of 30 s using an HP 4140B semiconductor test system.

3. Results and Discussion

Cross-sectional and planar FESEM data are given in figure 1. From the micrographs, it is clear that the BST thin films show a dense, well-crystallized grain structure that is defect and pinhole-free. The cross-sectional FESEM image demonstrates that the microstructure of the BST film is granular and randomly oriented. This is expected from the MOSD method, while other film deposition methods, such as pulsed laser deposition (PLD) produce films with highly oriented grains (*2*). Although oriented grains have been shown to exhibit excellent tunability, they also tend to exhibit higher loss due to induced film strain (*10)*. In our films, we observe an abrupt interface and a clear delineation between the film and the Pt bottom electrode (BE). This is desired because a poor interface can increase leakage current and frequency dispersion (*11*). Plan-view FESEM (figure 1) results indicate an extremely fine grain structure. The average grain size for the 160 nm film, for example, is on the order of 20 nm. The film roughness of dielectric thin films is important because a smooth surface (at least ≤4nm) is crucial in order to make good electrical contact between the film and the top electrode. Without good electrical contact between the film and electrode, conductor loss can become a problem, and this in turn will increase the insertion loss for the device. Hence, a smooth film-electrode interface is desired for these films. The film roughness was measured from the height data taken by the AFM and are shown in figure 2. The average surface roughness for all of the films is about 1.92 nm, which is well below the 4 nm limit for successful integration in devices. Some of the individual films had a slightly higher or lower average roughness, the most significant being the thickest film having an average surface roughness of 2.52 nm. The larger roughness value in this film may be due to the fact that the film has exceeded its "critical thickness." At this point, the large thickness causes the stress in the film to increase, which may form a rougher surface.

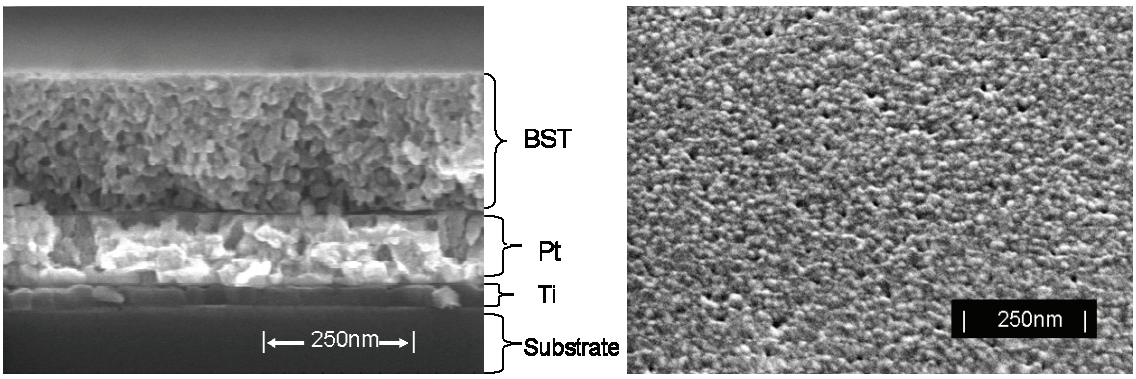

(a) **(b)**

Figure 1. Cross-sectional (a) and plan-view images (b) from the FESEM show a dense, well-crystallized microstructure. A clear delineation is also visible between the film and bottom electrode, indicating good electrical contact.

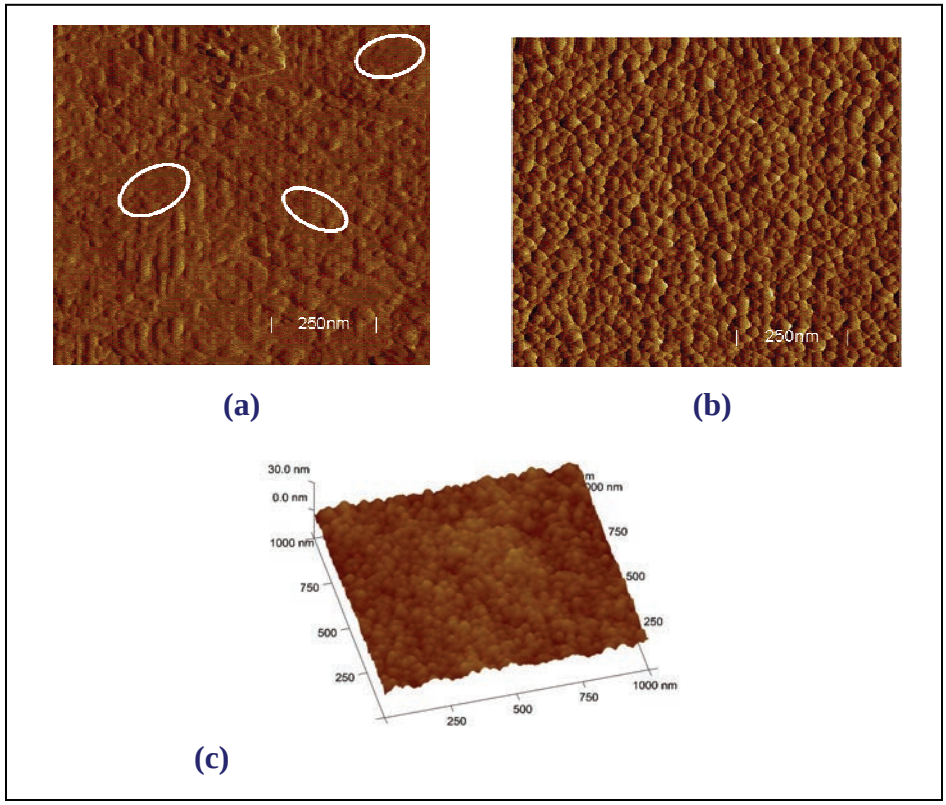

Figure 2. AFM micrographs showing (a) the plan-view of the 40nm thick film, with some amorphous sections circled, (b) the plan-view of the 280nm thick film, and (c) the 3D image showing the smoothness of the films, with an average roughness of about 1.92nm.

After examining the microstructure, Rutherford back scattering measurements (RBS) were employed in order to determine the stoichiometry of the BST film. The RBS spectrum is given in figure 3. From this figure, we simply calculate the ratio of the peak heights of the barium and strontium, and obtain the stoichiometric ratio of barium and strontium in the BST. The stoichiometry of the film was found to be $Ba_{0.57}Sr_{0.43}TiO_{3,}$ which is very close to our predicted $Ba_{0.6}Sr_{0.4}TiO_3$ film stoichiometry. Finally, dielectric and electrical measurements were performed on the samples. In order to perform dielectric and insulation measurements, the film must be configured in the metal-insulator-metal (MIM) device design. This configuration requires sputter deposition (through a shadow mask) of a Pt top electrode (TE) on the BST film surface. The film can now be tested in an approximation to the parallel plate configuration, with the platinum on the substrate acting as the bottom electrode and the sputtered platinum acting as the top electrode. It is important to note that the values obtained from this device construction represent a "worst case scenario." For example, electrodes fabricated via a shadow mask are prone to inexact geometries with inherent errors, which in turn degrade both the capacitance and loss measurements. For each sample, the capacitance and loss were measured as a function of both frequency and applied voltage. As stated earlier, meaningful dielectric measurements could

not be obtained for the thinnest samples (≤40nm) for two main reasons. The first reason is that the film thickness approaches the order of 1–2 relative grain sizes which is too small to obtain a reliable dielectric response. The second reason is that the thinnest samples contain areas of both amorphous and crystallized film, as seen in figure 2a. In contrast, in figure 2b, the thicker film (280 nm) exhibits a fully crystallized well developed microstructure. The thickness-dependent microstructure displayed in figure 2 may provide important information regarding the relationship of film thickness with respect to growth mechanisms. This topic requires further investigation, and it will be a main focus of our future research on these films. Figure 4a shows that the dielectric constant and loss were fairly constant up to a frequency of 1 MHz, indicating that there were no surface layer or electrode barrier effects in this region (*11*). The tunability was also found using the equation for relative tunability,

$$\eta = \Delta C/C_0$$

where ΔC is the change in the capacitance with electric field and C_0 is the capacitance at zero field. Capacitance values were then converted to the dielectric constants using the geometry of the parallel plate configuration. The tunability as a function of applied voltage (in kV/cm) is given in figure 4b. Overall, the films possessed good dielectric response with respect to those found in the literature for BST thin films. These properties include a dielectric constant around ≤400, a loss tangent around 0.029, and tunability up to about 30%. The dielectric properties changed as the films increased in thickness. Possible explanations for this observed thickness dependence include film stress (due to lattice mismatch and different coefficients of thermal expansion of the film and substrate) and electrode effects (*11*). The best combination of dielectric properties was found for the films of medium thickness (about 160 nm to 240 nm). For example, although the 120 nm and 400 nm thick films had the highest dielectric constants, they also had higher loss tangents than the moderate thickness films. Furthermore, the dielectric constant for the 400 nm film was found to be 503.19 at 100 kHz, which exceeds the acceptable value for impedance matching in these devices. In general, the dielectric constant needs to be lower than 500 for impedance matching purposes. Proper impedance matching is essential in creating a device with efficient power transfer.

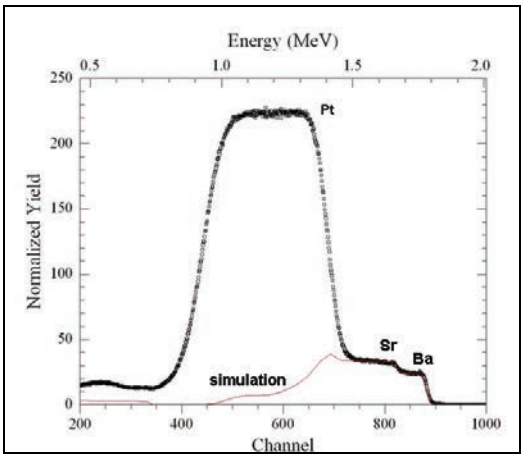

Figure 3. The Rutherford back-scattering data is shown ad a spectrum above. Here, the ratio of the barium (Ba) and strontium (Sr) peak heights gives the ratio of barium and strontium in the film.

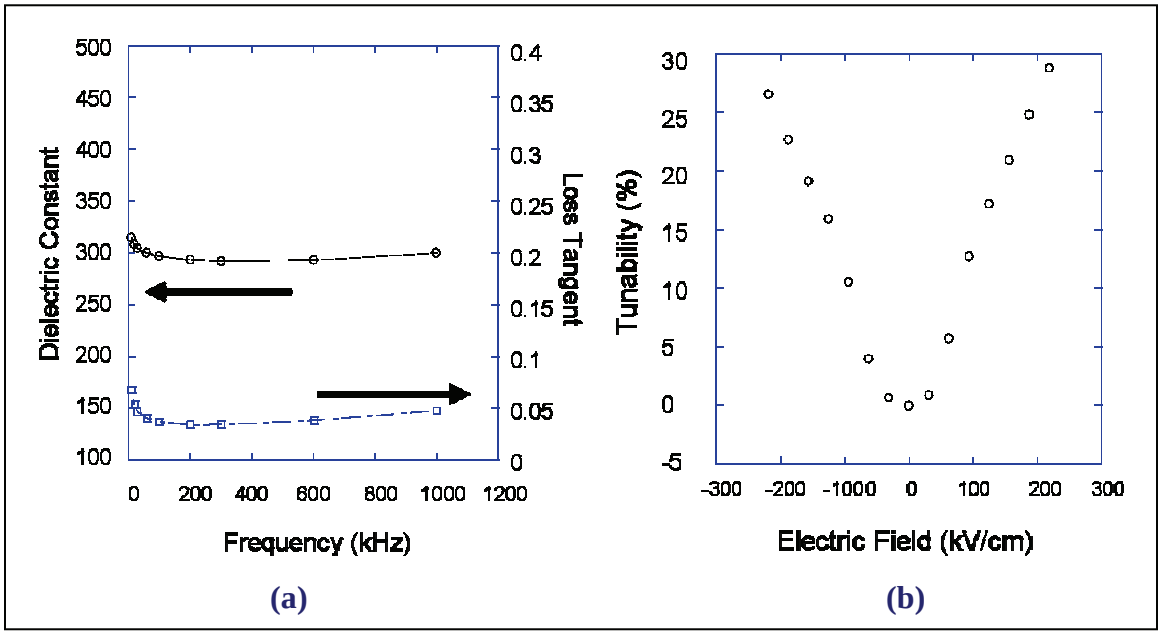

Figure 4. Dielectric measurements (a) dielectric constant and loss tangent as a function of the frequency. Up to 1 MHz, little dispersion in either the dielectric constant or the loss is shown. (b) The tunability as a function of applied field shows a maximum tunability of almost 30%.

After measuring the dielectric properties, the leakage current was measured. The leakage current density as a function of applied field is given in figure 5. It is clear that by increasing the film thickness, the leakage current density can be significantly lowered. The relationship between film thickness and leakage current is not yet entirely understood, but it is possible that film thickness engineering is one tool that can be used to lower the leakage current. Other attempts to lower the leakage current have included using conductive oxides as electrode materials (*12*) and using different temperatures (*13*) or gas ambients when annealing the films (*14*). Leakage

current is important to measure along with the dielectric measurements, because the leakage current gives us information about the reliability of the device. For example, since the values obtained for our leakage current are well below the breakdown point for this device, we conclude that our values of current density are low enough to promote long-term reliability and stability.

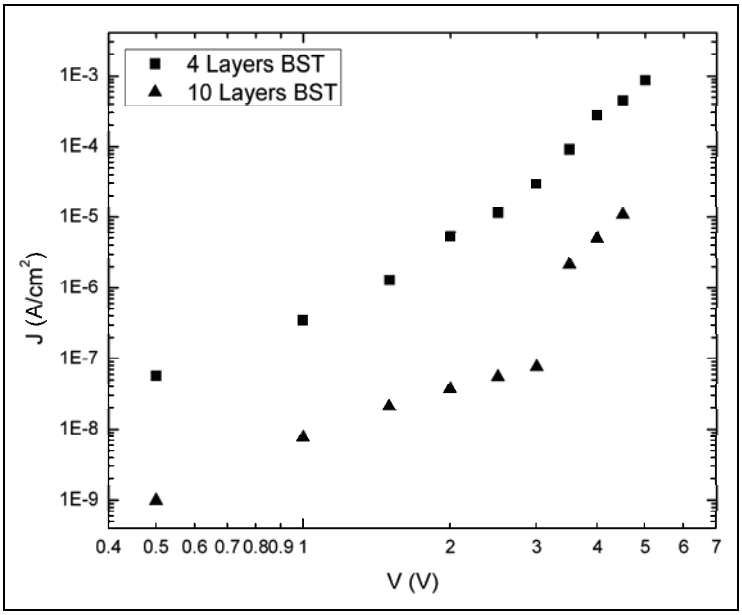

Figure 5. The leakage current density as a function of applied voltage for two representative film thicknesses. As the thickness of BST film increases, the leakage current density decreases.

4. Summary and Conclusions

The thickness-dependent dielectric properties of BST thin films were investigated. BST thin films were successfully deposited onto Pt-Si substrates; the films had a dense, well-crystallized microstructure with an average grain size of about 20 nm and an average roughness of 1.92 nm. The dielectric properties varied with film thickness. For device integration, a proper balance of properties is desired. Therefore, we must find the optimum combination of properties such as tunability and loss needed for the specific device design. The moderate thickness films (160–240 nm) show the best combination of moderate dielectric constant (about 300), low loss (about 0.029), good tunability (about 30%), and low leakage current (~10^{-8} A/cm^2). Although for tunable devices, a balance of moderate dielectric constant and low loss is desired, it is also useful to know at which thickness the highest dielectric constant and lowest loss are obtained. These property specific films can then be integrated into components to meet the demands of different device requirements. Since the morphology and dielectric properties rely heavily on the film thickness, precise thickness control may be an excellent method to “tune” the properties of the films to their desired values

5. References

1. Langhammer, H. T.; Muller, T.; Felgner, K. H.; Abicht, H. P. *Materials Letters* **2000**, *42*, 21–24.
2. Park, J. H.; Peterson, E. J.; Jia, Q. X.; Lee, J.; Zeng, X.; Si, S.; Xi, X. X. *Applied Physics Letters* **2001**, *78*, 533.
3. Shaw, T. M.; Suo, Z.; Huang, M.; Liniger, E.; Laibowitz, R. B.; Baniecki, J. D. *Applied Physics Letters* **1999**, *75*, 2129.
4. Taylor, T. R.; Hansen, P. J.; Acikel, B.; Pervez, N.; York, R.A.; Streiffer, S. K.; Speck, J. S. *Applied Physics Letters* **2002,** *80*, 1978.
5. Chang, W.; Gilmore, C. M.; Kim, W. J.; Pond, J. M.; Kirchoefer, S. W.; Qadri, S. B.; Chrisey, D. B.; Horwitz, J.S,.; *Journal of Applied Physics* **2000**, *87*, 3044.
6. Li, H.; Roytburd, A. L.; Alpay, S. P.; Tran, T. D.; Salamanca-Riba, L.; Ramesh, R. *Applied Physics Letters* **2001**, *78*, 2354.
7. Cole, M. W.; Ngo, E.; Hirsch, S.; Okatan, M. B.; Alpay, S. P. *Applied Physics Letters* **2008**, *92*, 072906.
8. Cole, M. W.; Joshi, P. C.; Ervin, M. H. *Journal of Applied Physics* **2001**, *89*, 6336.
9. Jeon, Y. A.; Shin, W. C.; Seo, T. S.; Yoon, S. G. *Journal of Materials Research* **2002**, *17*, 2831.
10. Cole, M. W.; Nothwang, W. D.; Hubbard, C.; Ngo, E.; Ervin, M. *Journal of Applied Physics* **2003**, *93***,** 9218–9225.
11. Cole, M. W.; Joshi, P. C. *Journal of Applied Physics* **1999**, *86*, 871–880.
12. Kil, D. S.; Park, J. B.; Yoon, D. S.; Song, C. R.; Cho, H. J.; Kim, Y.; Yu, Y. S.; Roh, J. S.; Yoon, H. K. *Japanese Journal of Applied Physics* **2001**, *40*, 3260–3265.
13. Hwang, C. S.; Park, S. O.; Cho, H. J.; Kang, C. S.; Kang, H. K.; Lee, S. I.; Lee M. Y. *Applied Physics Letters* **1995**, *67*, 2819–2821.
14. Jang, S. I.; Jang H. M. *Ceramics International* **2000**, *26*, 421–425.

INTENTIONALLY LEFT BLANK.

U.S. Army Research Laboratory

SUMMER RESEARCH TECHNICAL PAPER

Dynamic Fracture in Glass

by John Zumbrum

Contents

List of Figures **211**

List of Tables **211**

Abstract **212**

Acknowledgment **213**

1. Introduction/Background **214**

2. Experiment/Calculations **215**

2.1 Experimental Setup 215

2.2 Projectiles 217

2.3 Trigger Mechanisms 220

2.4 Triggering 221

2.5 Computational Setup 222

3. Results and Discussion **225**

3.1 Location of Branching 225

3.2 Orientation of Crack Branches 227

3.3 Crack Nucleation 228

3.4 Fragmentation 229

3.5 Validating the Model 230

4. Summary and Conclusions **230**

4.1 Summary 230

4.2 Future Work 231

4.3 Conclusions 231

5. References **232**

List of Figures

Figure 1. Plot of fracture energy (G) as a function of crack tip speed in polycarbonate (PC) and polymethylmethacrylate (PMMA). 214

Figure 2. Conventional gas gun testing apparatus. 215

Figure 3. Photo detector output to oscilloscope. 216

Figure 4. Square window for camera showing the white glue (misty region) that limits the camera's field of view. 217

Figure 5. Projectile Types. The projectiles from left to right are foam/small BB, foam/large BB, wood/small BB, and wood/tungsten. 218

Figure 6. Bending moment patterns in taped glass. 219

Figure 7. Aluminum tape make-screen. 221

Figure 8. Dimensions and modeling constraints for finite element code. 222

Figure 9. Mesh resolution at three different zoom levels. 223

Figure 10. Simulations of crack propagation at projectile velocities of (a) 2.0 m/s and (b) 4.5 m/s Stress levels are given in pascals. 224

Figure 11. Four finite element simulations of crack propagation at projectile velocities of (a) 2.0 m/s, (b) 2.6 m/s, (c) 3.5 m/s, and (d) 4.5 m/s. 225

Figure 12. Optical microscope picture of transition from mirror to mist to hackle. 226

Figure 13. SEM image of the notch tip. The smooth surface on the right is the actual crack surface. 227

Figure 14. Comparison of crack branching at (a) low speed experimental, (b) high speed experimental, (c) low speed simulation, and (d) high speed simulation. 228

Figure 15. SEM image of same fracture surface shown in figure 12, but at a different location. 229

Figure 16. Extent of fragmentation damage caused by direct impact of a Wood/Tungsten projectile at 48 m/s. 230

List of Tables

Table 1. Projectiles 217

Abstract

An experimental effort to understand dynamic crack propagation in soda-lime glass panels was conducted. Single edge, notched fracture specimens were impacted to generate mode I dominant cracking. In particular, the transition from smooth surface (mirror) crack growth to rough surface (hackle) crack branching was examined. A detailed discussion of the critical aspects of obtaining experimental data is included. Crack surface morphology and finite element simulation results are also presented and compared.

Acknowledgment

The author wishes to acknowledge the mentorship of Todd Bjerke.

1. Introduction/Background

When objects collide, significant energy must be transferred. As the kinetic energy of the striking object is increased beyond the fracture energy of the material, molecular bonds are broken, creating a fracture surface.

Dynamic crack propagation has been studied for many materials. As the crack tip speed is increased (accomplished by increasing the projectile velocity), the fracture energy associated with the cracking surface increases until it becomes a vertical asymptote. For the limited studies conducted, the asymptotic crack tip speed is approximately 60% of the Rayleigh wave speed (i.e., 60% of the speed of surface waves in a solid) (*1*). Figure 1 is a representative plot of fracture energy as a function of crack tip speed.

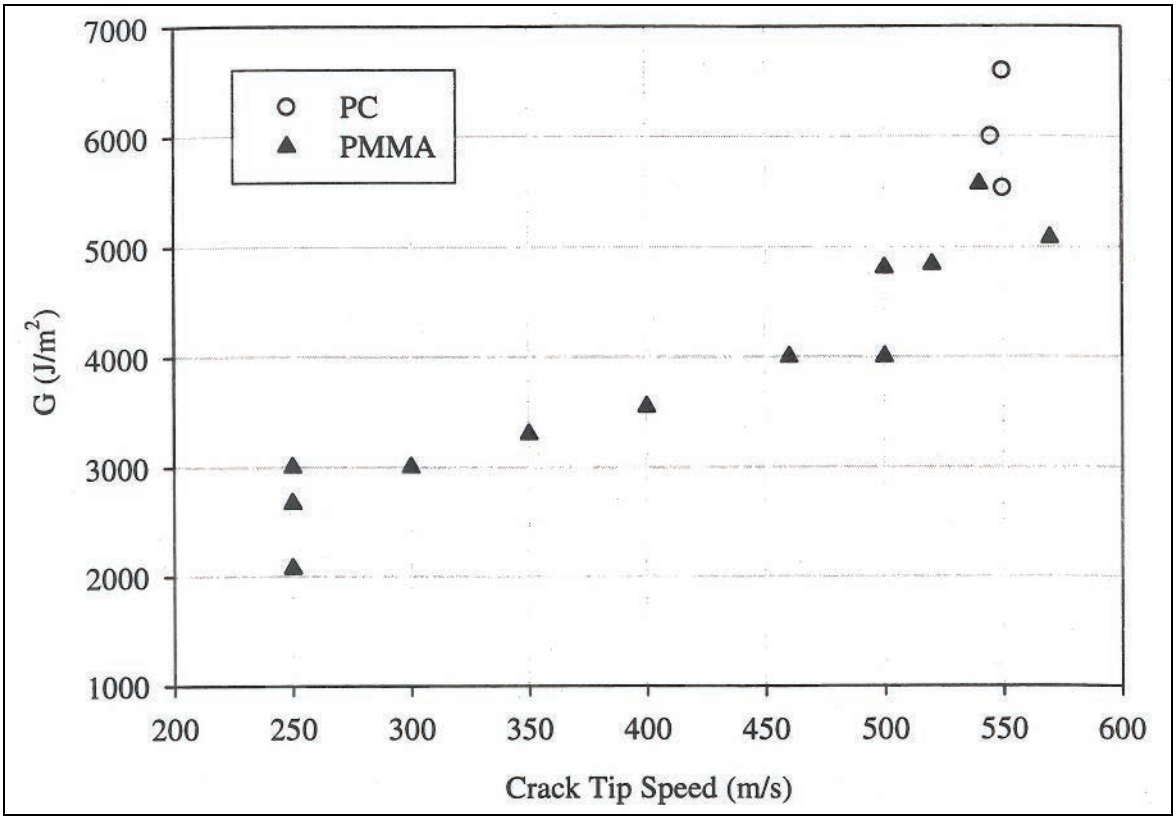

Figure 1. Plot of fracture energy (G) as a function of crack tip speed in polycarbonate (PC) and polymethylmethacrylate (PMMA).

When the fracture energy reaches this asymptote, it becomes energetically favorable to split into two cracks, otherwise known as bifurcation. One of the purposes of this research project was to determine at what crack tip speed this branching occurs for soda-lime glass, and validate a numerical model of the event.

2. Experiment/Calculations

2.1 Experimental Setup

A conventional gas gun with impact chamber at the muzzle, fired by opening a quick-release Norgren A1038C-A1 300 psig valve, was utilized during the experimental procedure. Once fired, the projectile traveled down the 2.44 m steel barrel (38.3 mm OD, 25 mm ID), passed through the velocity lasers, and struck the target in the impact chamber. Figure 2 is a digital picture of the setup.

Figure 2. Conventional gas gun testing apparatus.

The two velocity lasers were monitored by photo detectors which sent square pulses to an oscilloscope. By measuring the time difference between the same point on the two different curves, such as the corner of the square pulse shown in figure e, and dividing that time difference into the 6.35 cm distance between the two photo detectors, the projectile speed can be calculated.

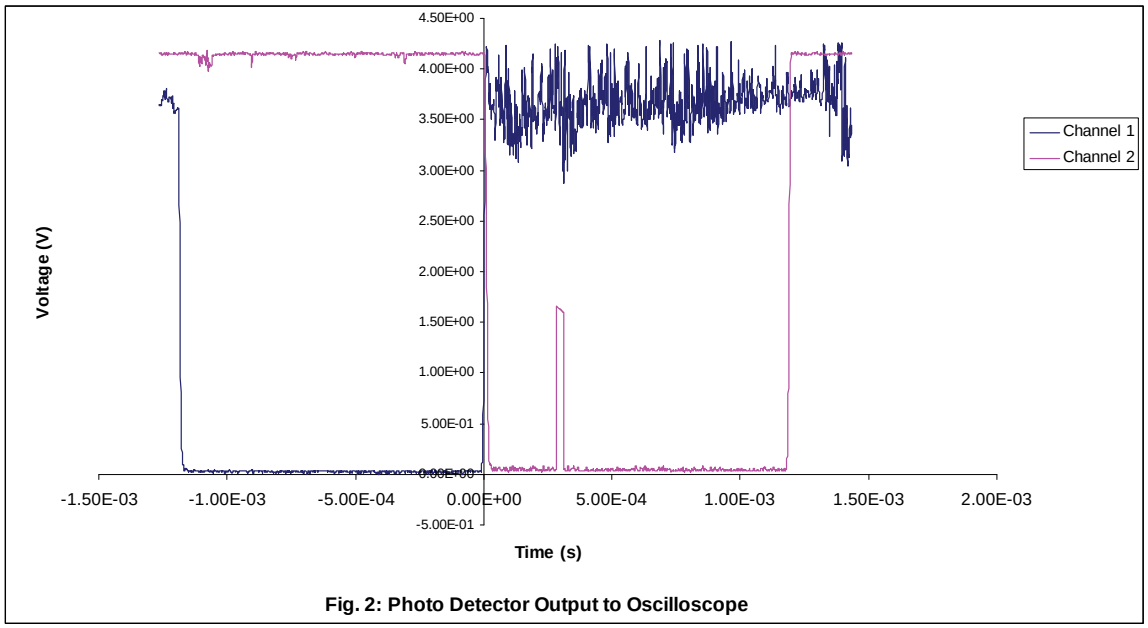

Figure 3. Photo detector output to oscilloscope.

The accuracy of this method was verified by multiplying the width of the square pulse (this corresponds to the time that the projectile was in front of the laser) by the calculated speed of the projectile. This yields the length of the projectile, which can be easily verified through application of a measurement tool such as calipers. The accuracy of this method for calculating the speed was determined to be ±5%. To obtain optical images of cracks a DRS Hadland Imacon 200 high-speed camera (200 million frames/second maximum) was used. For the 1 µs exposure times selected, high-intensity, auxiliary lighting was necessary to illuminate the test specimen. Two commercially available Photogenic brand PowerLight 2500DR lights were used. These lights had a ramp-up time of 150 µs, duration of 1300 µs, and could be triggered by very low voltages. Flash bulbs were used as an alternative to illuminate the specimen, because although they have a much longer ramp-up time (25 ms), they stay at peak intensity for 10 ms, making timing of the camera with the flash less difficult. The impact chamber (red box) sits on the I-beam support, and has inner dimensions of 23 cm wide by 44 cm long by 25 cm high. A two-piece window was made in the impact chamber for the camera. A large diameter hole was drilled into the chamber on one side, and a piece of polycarbonate was screwed onto the exterior of the chamber over the hole to resist projectile and test specimen debris from damaging the equipment. Although the best optical images would result from unobstructed space between the camera and the test specimen, practical considerations make this unachievable. The next best option is to cover the opening with glass (because of its low index of refraction and resistance to distorting optical images). There was a small hole in the polycarbonate for the camera viewing window, and this opening was covered with a piece of 10.16 cm square, 1.27 cm thick glass. The diameter of the camera lens was about 8 cm, however, so there was very little room for translating the camera. The regions where the glass was glued to the polycarbonate further

restricted the placement of the camera, as shown in figure 4. Because of this, the specimen had to be located such that it lay in front of the camera lens.

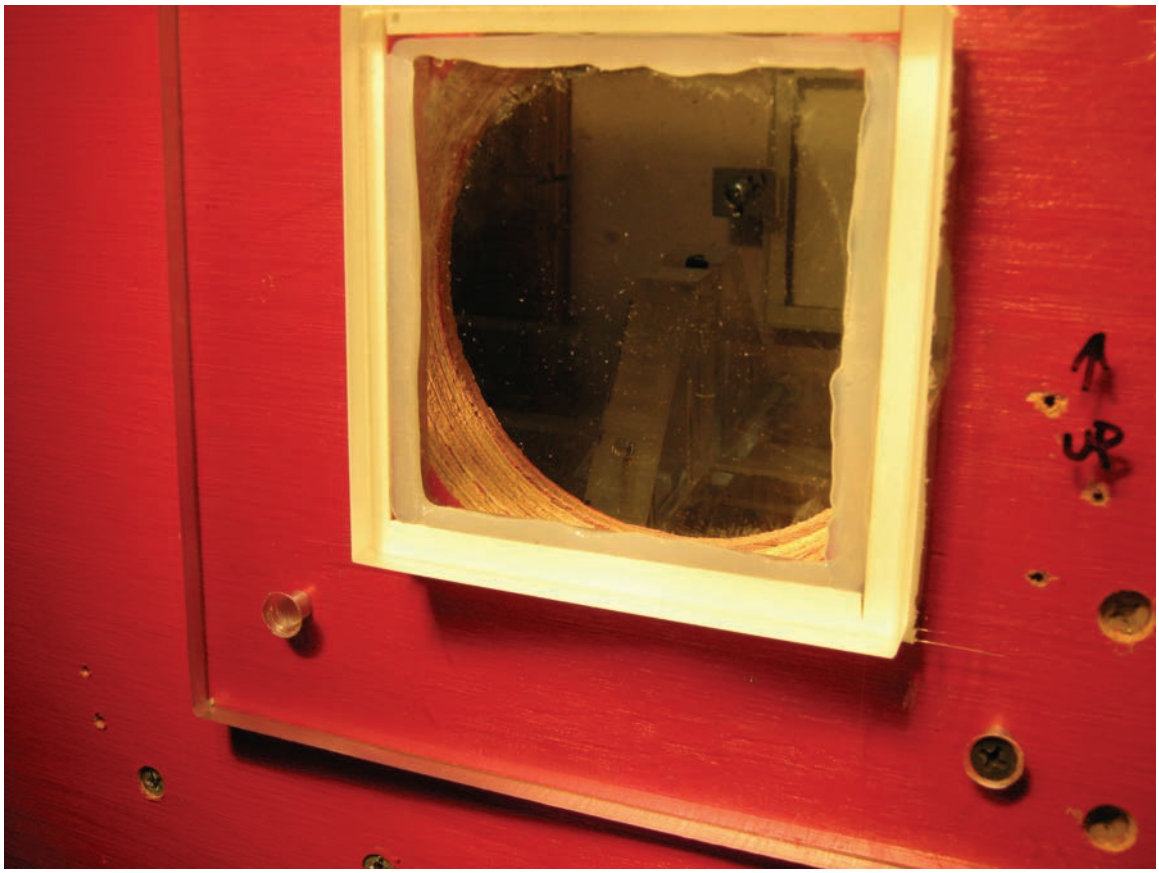

Figure 4. Square window for camera showing the white glue (misty region) that limits the camera's field of view.

2.2 Projectiles

In order to control the type and speed of crack propagation, several different projectile types and materials were selected. Table 1 summarizes the dimensions, materials, and properties of the different projectile types, and figure 5 is a digital photograph of the projectiles.

Table 1. Projectiles.

Sabot	Outer Diameter (mm)	Impacter	Impacter Diameter (mm)	Overall Length (mm)	Mass (g)
Wood	25	Tungsten	9.7	45.7	62
Wood	25	BB			
Foam	22–25	Large BB	9.5	46.9	4
Foam	22–25	Small BB	5.5	42.5	1
Foam	22–25	Aluminum Disk	23	38.5	

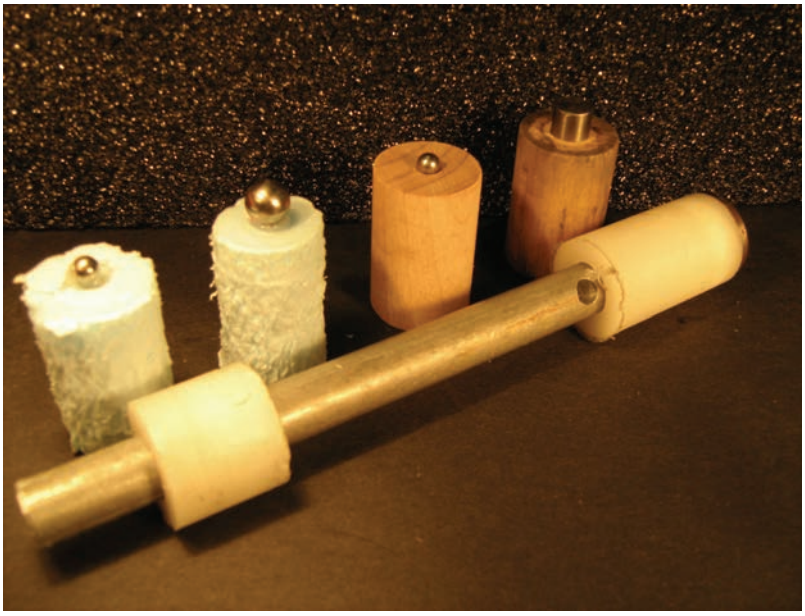

Figure 5. Projectile Types. The projectiles from left to right are foam/small BB, foam/large BB, wood/small BB, and wood/tungsten.

NOTE: In front is the bar that was struck by the wood/tungsten projectile during the most recent trials. Notice the hole in the rod close to the second plastic spacer; this hole allowed the laser to pass through, but once the rod started moving, the laser light was blocked.

First, a wood/tungsten projectile was selected as it had been used previously in impact tests. This projectile completely shattered the glass specimens on impact. To reduce the severity of fragmentation, the sides of each glass specimen were wrapped in clear packing tape. This approach revealed details of crack propagation, after the impact event, which had previously been lost. While this imparted a bending moment to the glass, resulting in the curved patterns shown in figure 6, it was possible to see that the crack had bifurcated essentially at the point of initiation.

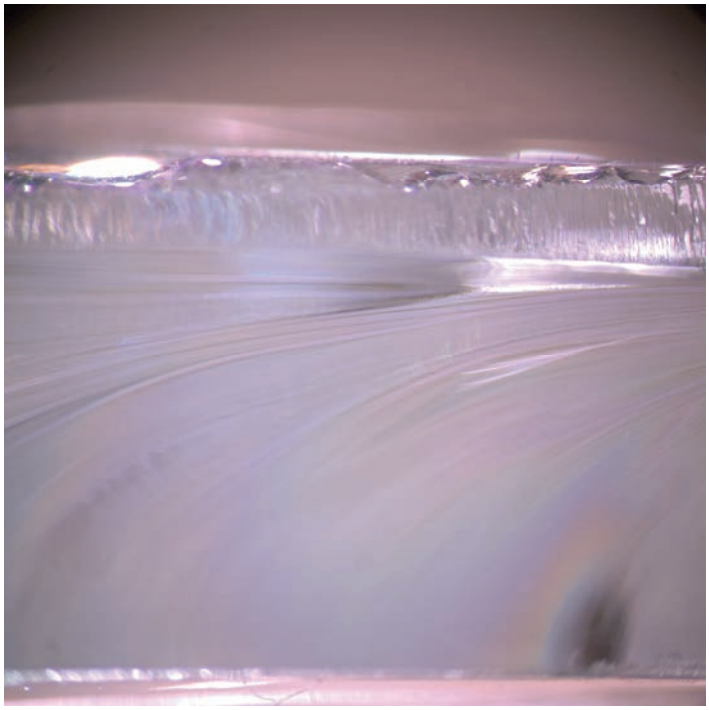

Figure 6. Bending moment patterns in taped glass.

To reduce the extent of specimen destruction due to the impact, the mass of the projectile was reduced by switching to a foam sabot and BB impacter. As shown in table 1, this decreased the mass by almost 100 times. Several different sizes of BB's, a drop of hot glue, and a thin plate of aluminum were used as impacters (glued to the front of the foam sabot). All of these impacters resulted in a significant reduction in surface damage to the test specimen compared to the wood/tungsten projectiles. They did not, however, allow a crack to go straight across, and they were too inconsistent in both trajectory and velocity.

Another procedure examined was to use a stripper plate which would allow the BB to proceed through, but would stop the foam sabot from continuing onward. When it worked, the crack patterns could be seen much more clearly (due to the decrease in impact zone shattering), but it still showed immediate bifurcation. Unfortunately this method was very inconsistent in both trajectory and speed of the BB after being stripped. After these problems became apparent, the approach was abandoned because consistency is paramount when triggering a high speed camera at such short exposure times.

In preparing to take high-speed photographs of the crack propagating, it was recommended by Dr. Todd Bjerke to more actively pursue straight-line cracks than a reduction in impact surface deformation (*2*). A few members of the Impact Physics Branch suggested using a split-Hopkinson bar approach in order to reduce the speed of the projectile impacting the specimen. The general operating principle is conservation of linear momentum, which can be easily shown to take the form of equation 1:

$$m_1 v_1 = m_2 v_2 \tag{1}$$

Simply put, when a fast, light object hits a heavy object at rest, the heavy object will move slowly. This is important because a low speed projectile will impart lower fracture energy to the glass specimen than a low mass projectile, in accordance with the kinetic energy relation:

$$E_{kinetic} = \tfrac{1}{2} m v^2 \tag{2}$$

Using this split-Hopkinson bar approach, straight-line cracks in glass test specimens were obtained. When the projectile impacts the rod, a momentum transfer takes place. The rod then accelerates up to the speed prescribed by equation 1. One must be careful to account for the acceleration region when using this method. For the wood/tungsten projectile and aluminum rod, the acceleration region was about 25 mm. Because of the constraints of camera positioning, it was necessary to operate within this acceleration region, which meant that precise placement of the specimen and rod every time was critical for repeatability and triggering. To this effect, a test stand was made for the specimen, and a hole was drilled through the aluminum rod so a laser beam break signal could trigger the camera.

2.3 Trigger Mechanisms

Several devices were used to trigger the flash and camera. First a diode and sensor setup was used. This was eventually discarded as a triggering mechanism because it had a 5 ms rise time which made timing incredibly difficult. Even though it was consistent, in order to have a reasonable delay, the trigger level would have to be set so low that noise in the signal would set it off. To replace the diode, a laser and photo detector setup was used. This mechanism never caused any problems with delay because the rise time was so quick (about 15 μs). For triggering the flash, this was more than adequate. When using the single-use flash bulbs, however, a single strand of stainless steel wire, stretched taut between two alligator clips taped to the outside of the barrel, was used. As the projectile traveled down the barrel, it broke the wire, resulting in a break-screen signal. This worked every time it was employed to trigger the flash bulbs. To exclusively trigger the camera, two different mechanisms were tried. First, a make-screen consisting of two pieces of aluminum tape separated by a thin piece of cardboard with a rectangular notch cut in it sent the signal. When the impacter made contact with the first piece of aluminum tape, it pushed it into the second piece, completing the circuit. After going through the make-screen box, (built at APG) which used circuits to eliminate noise in the signal, the box sent a signal to the camera. The second device used to trigger just the camera was a crack gage glued to the glass surface directly up range of the notch tip. As the glass cracked and opened up, it severed the crack gage, sending a break signal to the camera. It was found that the commercial lights would prematurely trigger the gage when they ramped up; the gages seemed unaffected by flash bulbs.

2.4 Triggering

Capturing images of the crack propagating hinges upon precise and accurate triggering of both the flash and the camera because the crack tip moves at approximately 5 mm/µs (*3*). The first and simplest method of triggering is to have one trigger source which goes to the camera, and let the camera software trigger the flash. This method ensures that the target is illuminated when the camera is capturing images. Using the camera software, settings were applied to provide a specified delay from when the camera received the signal until it captured the image, and 150 µs before the pictures were taken, the flash was triggered to ramp-up.

Using this method, three different trigger sources were tried. First, the trigger source was the second velocity laser (61 cm from muzzle). There was significant variability associated with this trigger source, because it depended upon knowing the velocity of the projectile and guessing a time delay for the camera. Because of the variability it was too difficult to actually capture the crack propagating so this trigger source was inadequate for any of the projectile types. Next, triggering off of a make-screen (shown in figure 7) glued to the front edge of the glass specimen was attempted.

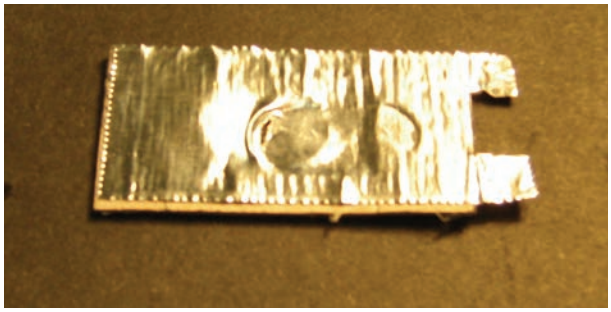

Figure 7. Aluminum tape make-screen.

After several trials, it appeared that the make-screen was affecting the path of the projectile, dissipating energy, or somehow compromising the integrity of the experiments. The last trigger source used for the combined camera/flash system was a laser and photo detector close to the barrel exit (11.5 cm). After spending considerable time and panels of glass, the appropriate time delay to yield pictures of the crack propagating was determined. Two trials with identical settings and configuration were run. In the first run, the glass had not cracked at all, and in the second run, the glass was already completely cracked. This verified what was suspected: there was too much variability in this experiment compared to the narrow time window to trigger off of merely the projectile/rod movement.

Next it was decided to trigger the flash separately from the camera so that the camera could be triggered much closer to the actual propagation event, thereby limiting the effects of variability. The most successful combination was to use the wire break-screen in the barrel for the flash bulbs, and a crack gage for the camera. This was still unsuccessful in capturing images of the crack propagating. According to Seth Halsey, some cameras buffer images constantly, which

make it possible to obtain frames before the time of the trigger signal. This option has yet to be investigated (*4*).

It has now been determined that a split-Hopkinson bar approach is effective for obtaining straight-line cracks in glass test specimens. Using flash bulbs to illuminate the test specimen is effective because it greatly simplifies the difficulties of timing. Camera triggering needs to be done by methods other than a diode/sensor, laser/sensor, crack gage, or aluminum tape make-screen.

2.5 Computational Setup

The entire fracture event was modeled using the Finite Element Method. The test specimen was modeled in two dimensions as a rectangle with a triangular notch. The two left corners were made rigid, and the projectile was modeled by forcing a 3.56 cm section of the mesh on the right side to move directly towards the notch tip at constant velocity. This is assumed to represent a projectile moving at a specified velocity in a three point bend configuration. Figure 8 shows these boundary conditions and the dimensions of the specimen.

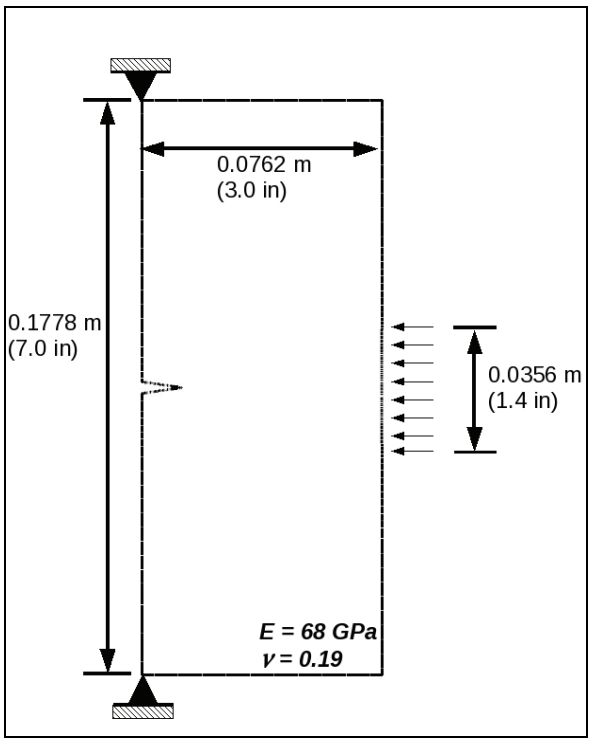

Figure 8. Dimensions and modeling constraints for finite element code.

To generate the geometry of the specimen, a mesh was created using the software program Cubit, as shown in figure 9.

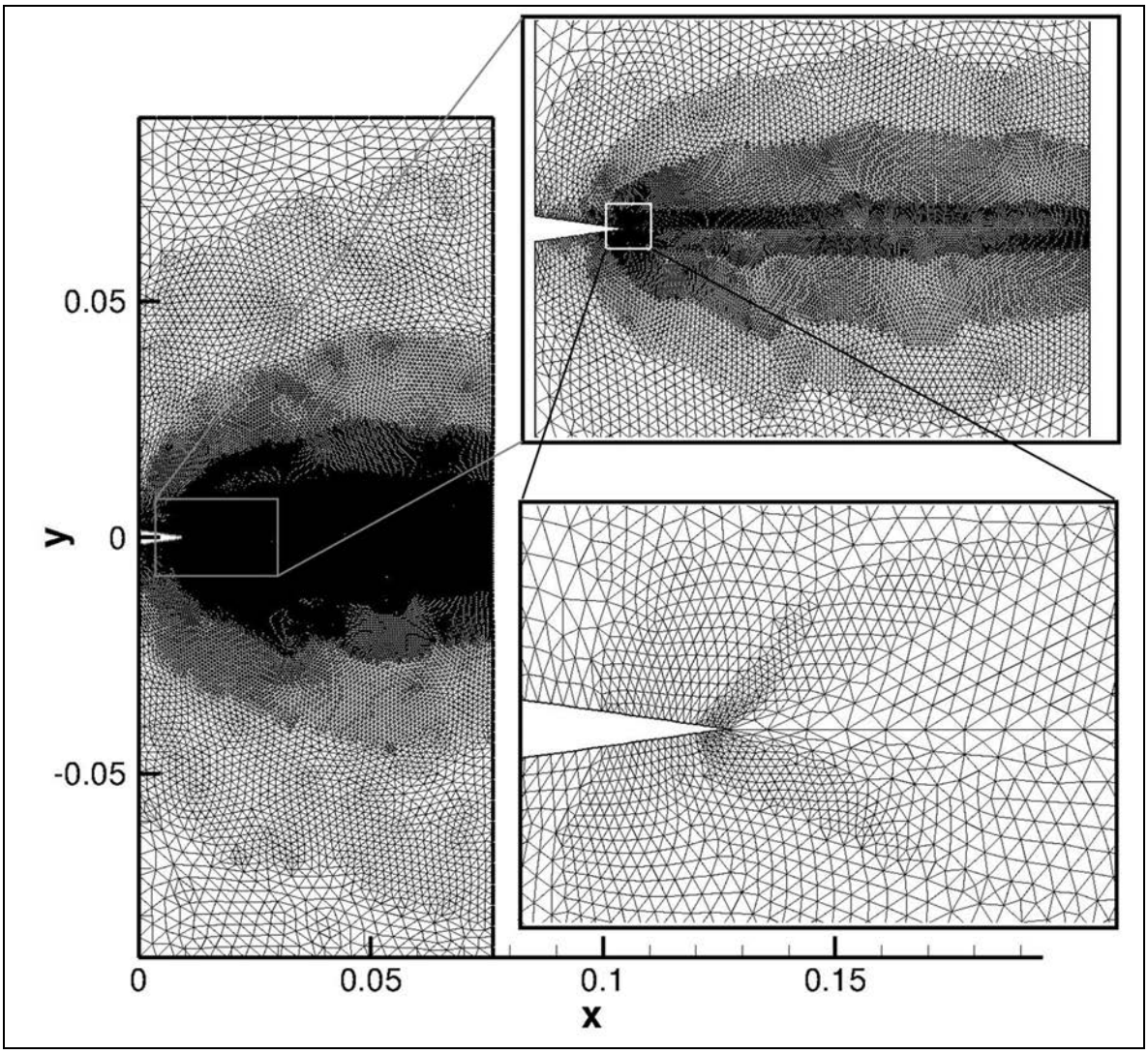

Figure 9. Mesh resolution at three different zoom levels.

Once the mesh was established, stress fields were generated using preexisting code. The code uses the Finite Element Method (approximates the solutions to partial differential equations), in the Lagrangian framework (nodes move with the material itself, similar to how grid lines painted on a rubber band would distort if it were stretched), to solve the governing equations at the boundaries of the 6 node, triangular elements. When the stress on a boundary exceeds the cohesive strength, a cohesive element is dynamically inserted between the two elements. This cohesive element has no volume, but has a thickness that can increase to accommodate cracking. As Dr. Reuben Kraft describes it, the phenomenon is similar to pulling apart two surfaces that have been glued together (*5*).

When creating a mesh, it is necessary to know the cohesive zone length of the material. According to Dr. Kraft, the element size should be about 10% of the cohesive zone length in order to have good resolution of the crack propagation (*5*). After obtaining property data from

MatWeb for soda-lime glass (real data was unavailable), the fracture energy was calculated according to equation 3

$$G_c = \frac{K_{IC}^2}{E}. \tag{3}$$

This fracture energy was used to calculate the cohesive zone length according to Rice's formula:

$$l_{cohesive} = \frac{9\pi}{32}\frac{E}{1-\upsilon^2}\frac{G_c}{\sigma_c^2} \tag{4}$$

where E is Young's Modulus (measure of elasticity), G_c is the fracture energy (amount of energy needed to create new surfaces), σ_c is the maximum cohesive stress (measure of failure point), and ν is Poisson's Ratio (measure of a material's tendency to contract in the dimensions perpendicular to an applied load) (*6*).

Four trials were run at simulated projectile velocities of 2.0 m/s, 2.6 m/s, 3.5 m/s, and 4.5 m/s respectively. Figure 10 shows snapshots of two simulations 33.6 µs into the impact.

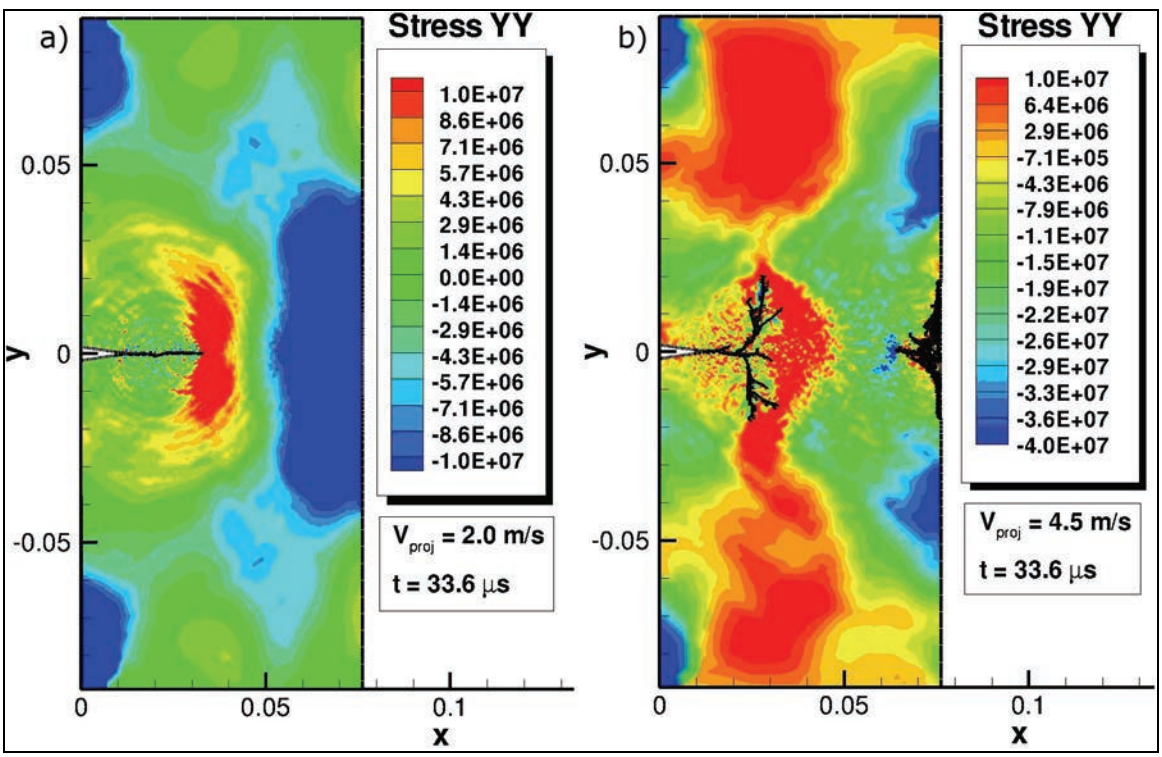

Figure 10. Simulations of crack propagation at projectile velocities of (a) 2.0 m/s and (b) 4.5 m/s stress levels are given in pascals.

These images were generated in Tecplot running on RedHat Linux. Each simulation took approximately one hour to run on a single processor; the run-time is a function of the mesh resolution.

3. Results and Discussion

3.1 Location of Branching

As the velocity of the projectile was increased (and thereby the kinetic energy, according to equation 2), the physical location at which bifurcation occurred began to approach the notch tip. This phenomenon is also seen in the computational simulation snapshots in figure 11.

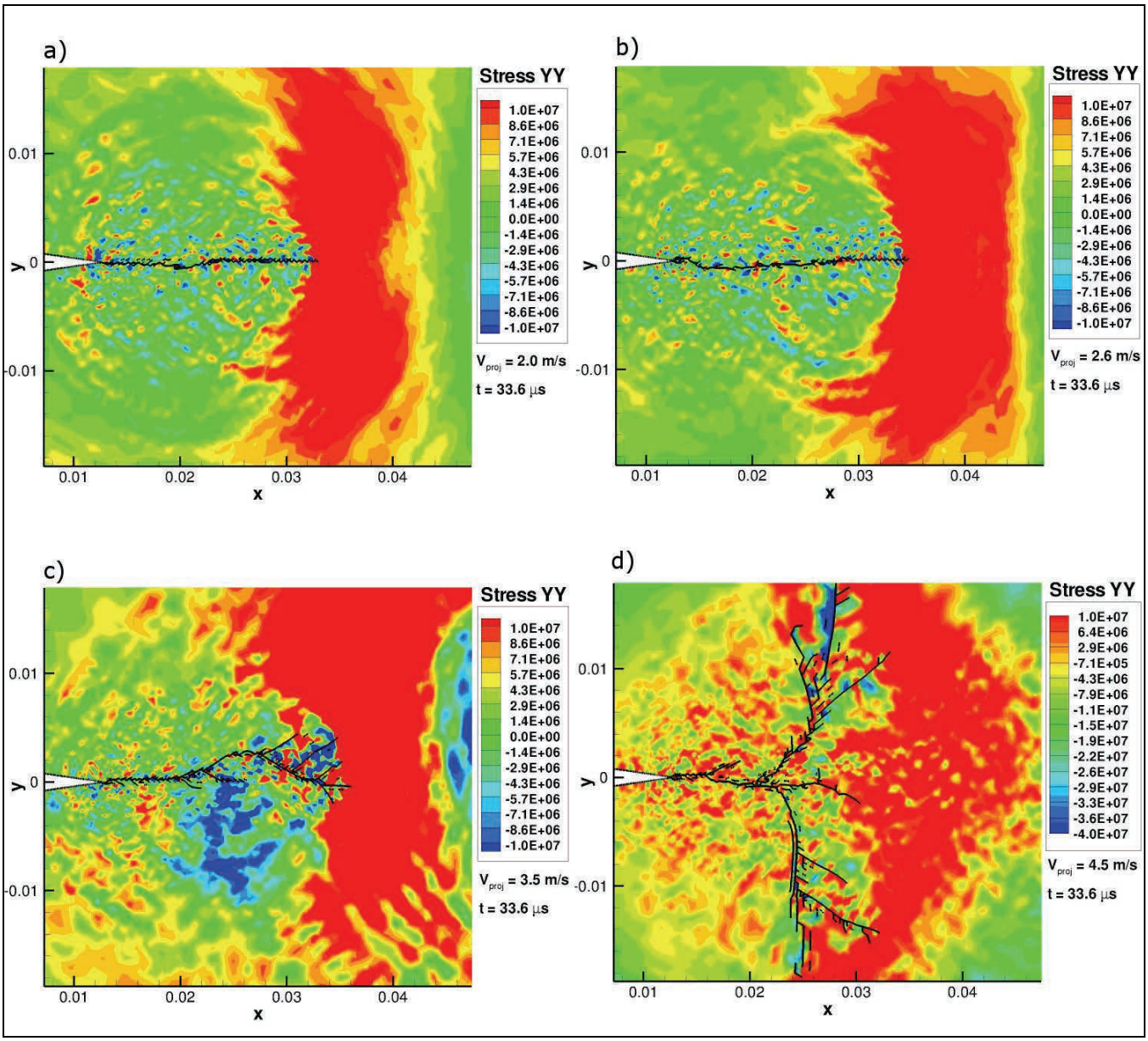

Figure 11. Four finite element simulations of crack propagation at projectile velocities of (a) 2.0 m/s, (b) 2.6 m/s, (c) 3.5 m/s, and (d) 4.5 m/s.

At higher speeds, considerable microcracking occurs, which are failed attempts to bifurcate. The broken glass samples exhibit a region of smooth “mirror” surface which becomes a rougher “mist” surface until finally the surface becomes a very rough “hackle” at the point of bifurcation. The mirror surface is indicative of straight-line cracking, the mistregion indicates microcracking, and the hackle surface results from a combination of branching and microcracking. This surface transition is shown in Figure 12.

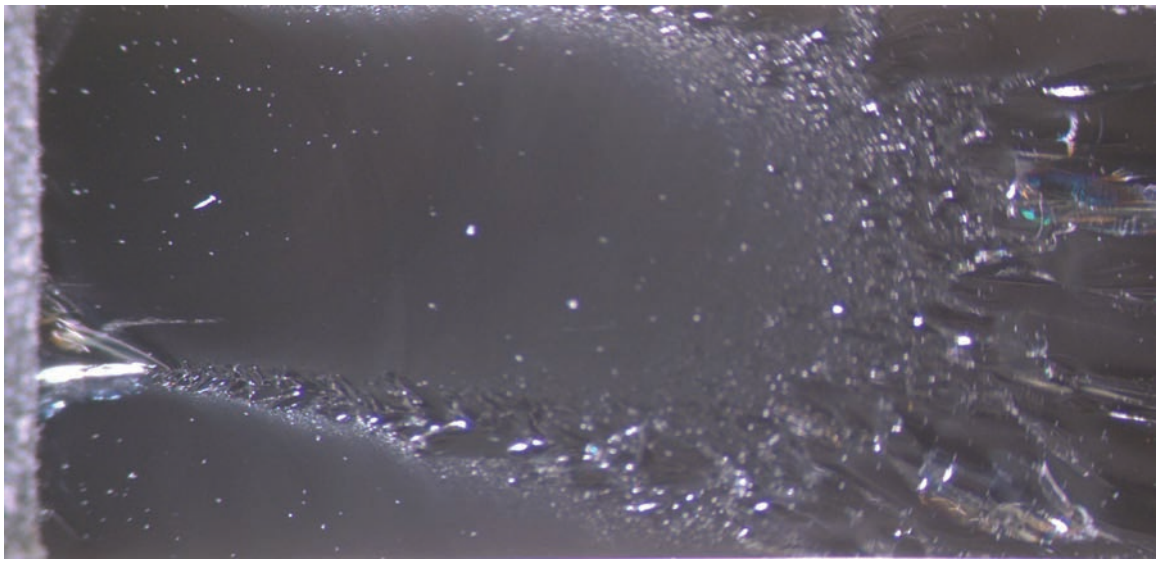

Figure 12. Optical microscope picture of transition from mirror to mist to hackle.

Using an Environmental Scanning Electron Microscope, I investigated the surface detail at a much higher resolution. Figure 13 shows the same fracture surface as in figure 12, at the notch tip.

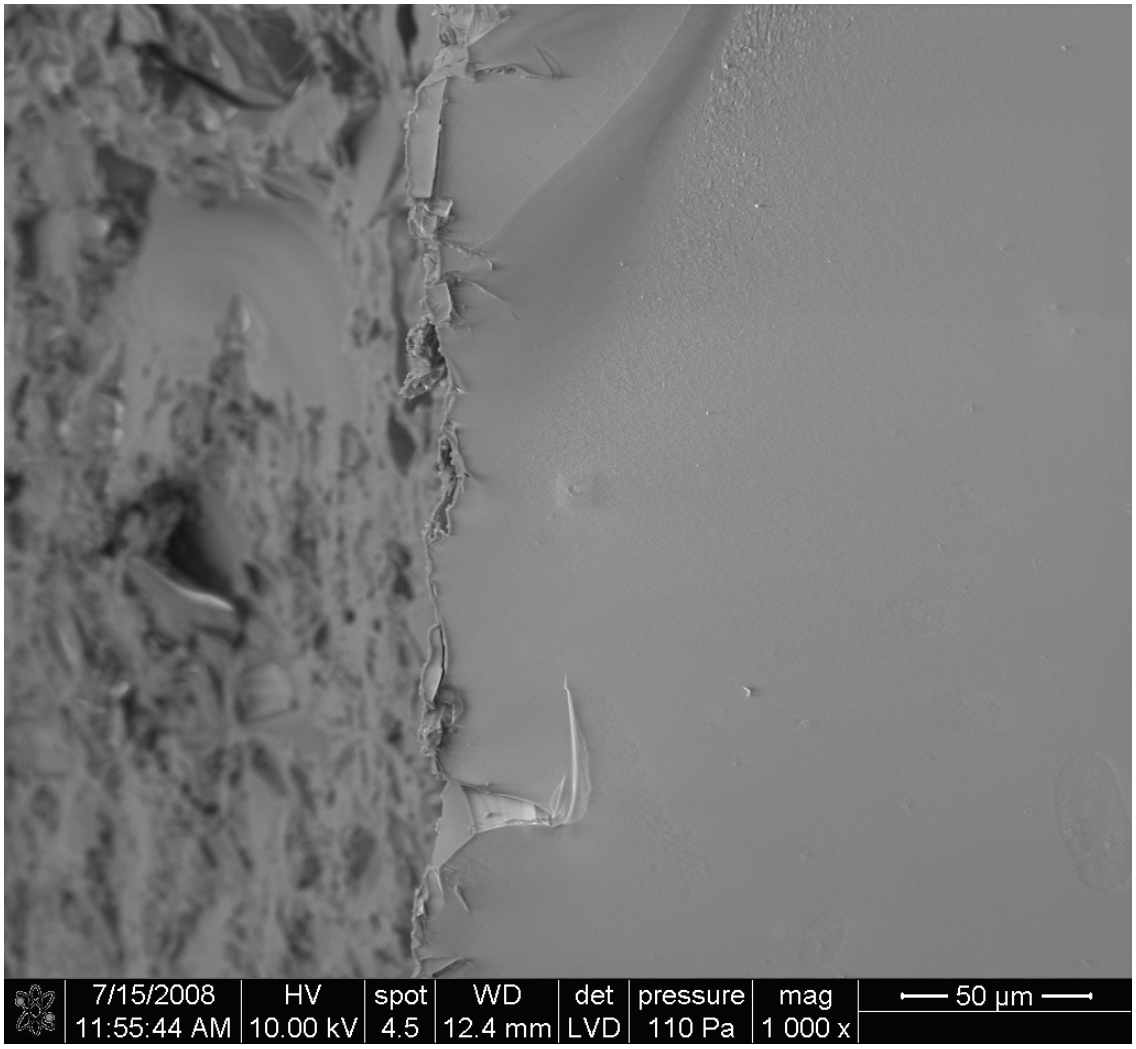

Figure 13. SEM image of the notch tip. The smooth surface on the right is the actual crack surface.

NOTE: Notice that the surface is relatively free from defects (i.e. "mirror"), but the notch, out of focus in the background, is very rough. Also, the water jet cutter is a fairly abrasive tool, as can be seen from the roughness of the notch tip.

Figure 12 shows a region of roughness surrounding the point of bifurcation which I believe is manifested in the computational simulations by the vast amount of microcracks that seem to flourish at that location.

3.2 Orientation of Crack Branches

The angle of crack branching is also notable. Figure 14 shows the angle of cracking approaching 90˚, as the projectile velocity is increased, for both the experimental and simulation results. Also notice that the point of bifurcation approaches the notch tip as the projectile velocity is increased.

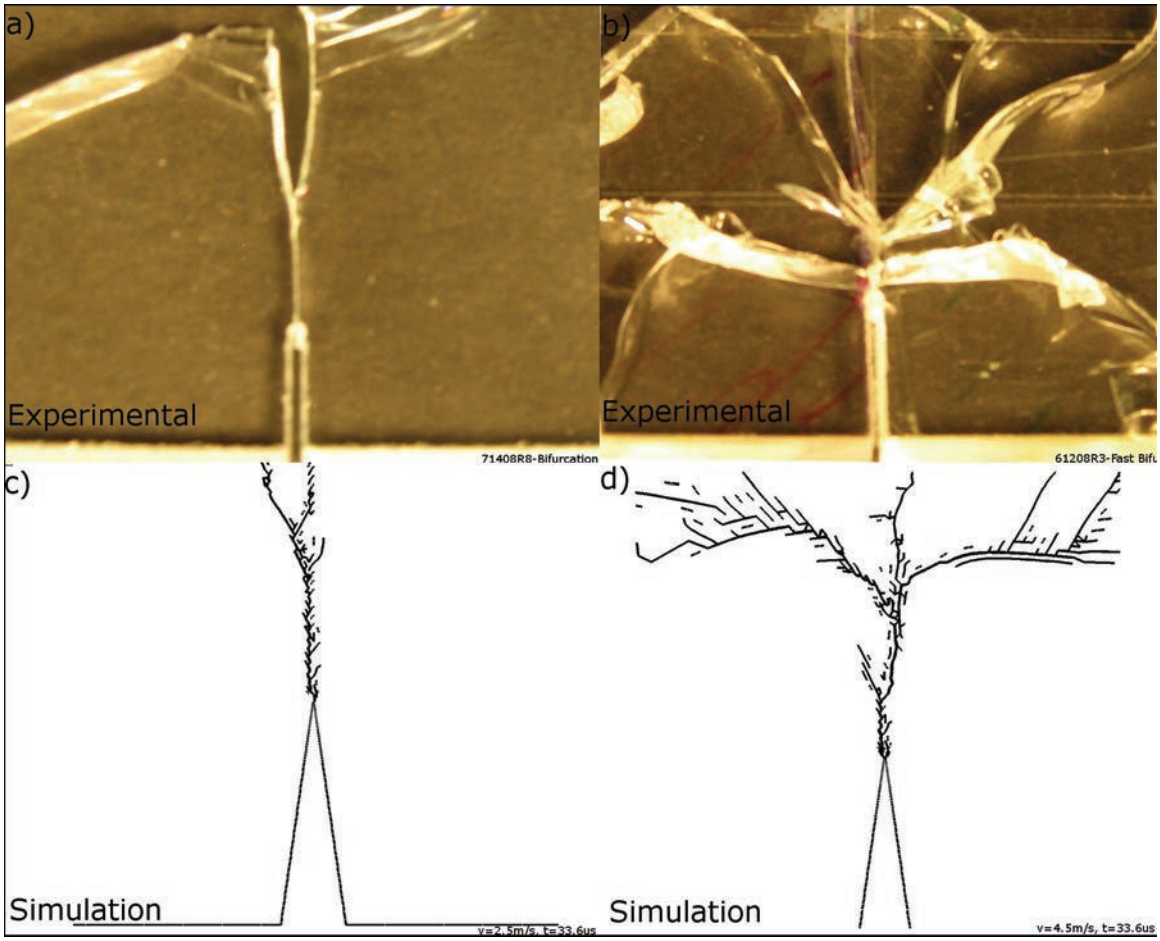

Figure 14. Comparison of crack branching at (a) low speed experimental, (b) high speed experimental, (c) low speed simulation, and (d) high speed simulation.

3.3 Crack Nucleation

When the projectile strikes the face of the target, a crack nucleates at the notch tip and runs towards the projectile. Depending on how much the notch tip has been refined, the crack could start anywhere on the notch tip. To control the location of crack initiation, the notch could be cut with a laser which is much less abrasive than the water jet cutter used in these experiments.

Figure 15 is an SEM image of the actual site of crack nucleation. Notice that the surface is "mirror-like" around regions where the notch tip is relatively smooth, but turns to mist where the notch tip is rough. This image also shows the entire region 75 µm to the right of the notch tip to be mist. Figure 13, however (different location on the same fracture surface), does not show these same characteristics. Instead, the entire surface is mirror.

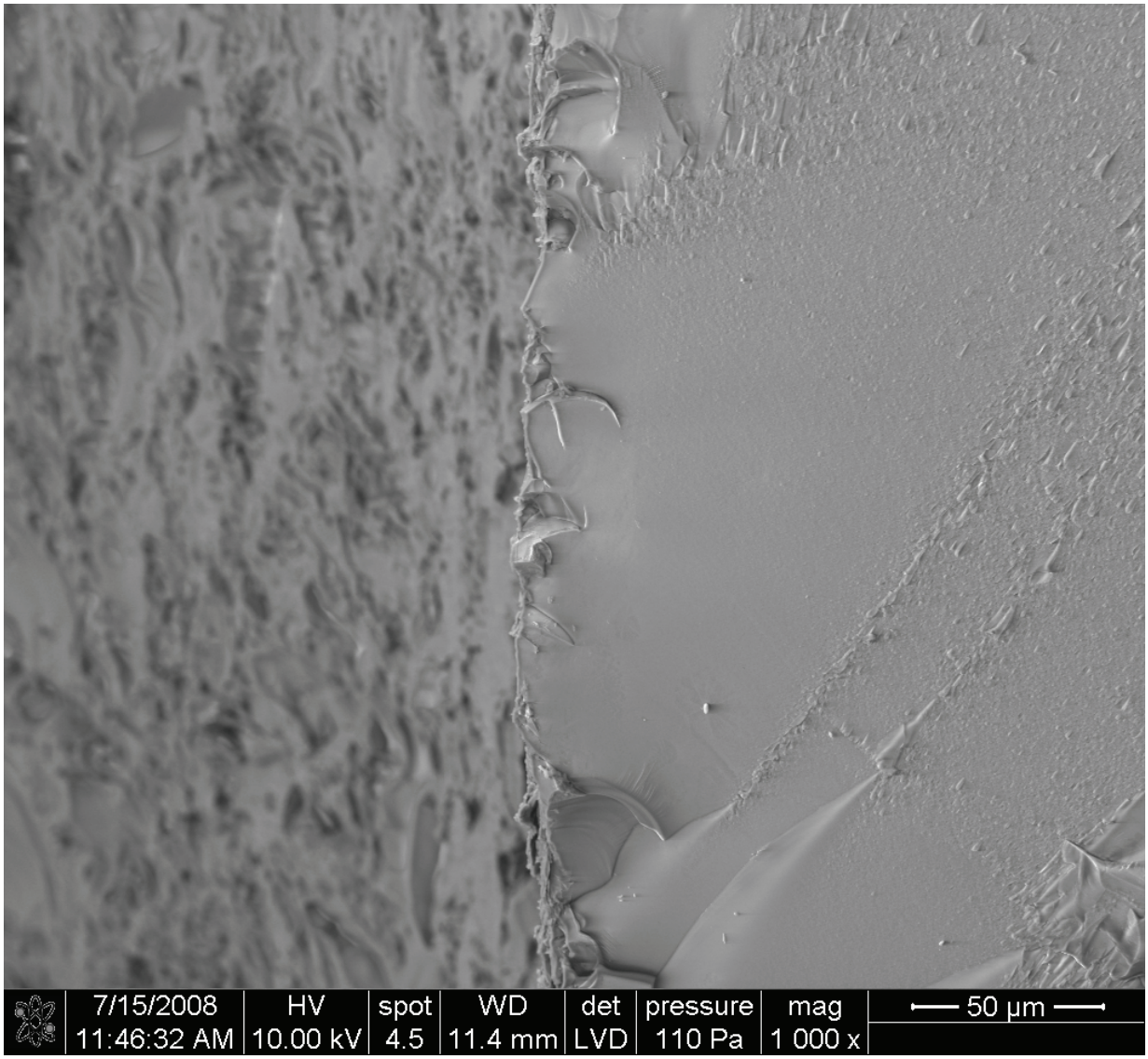

Figure 15. SEM image of same fracture surface shown in figure 12, but at a different location.

3.4 Fragmentation

At high projectile velocities, the impact zone is not only destroyed, but the entire specimen becomes fragmented. Computational simulations at these velocities were not run, but could easily be done in the future. Figure 16 shows the extent of fragmentation for a specimen that was coated in clear packing tape.

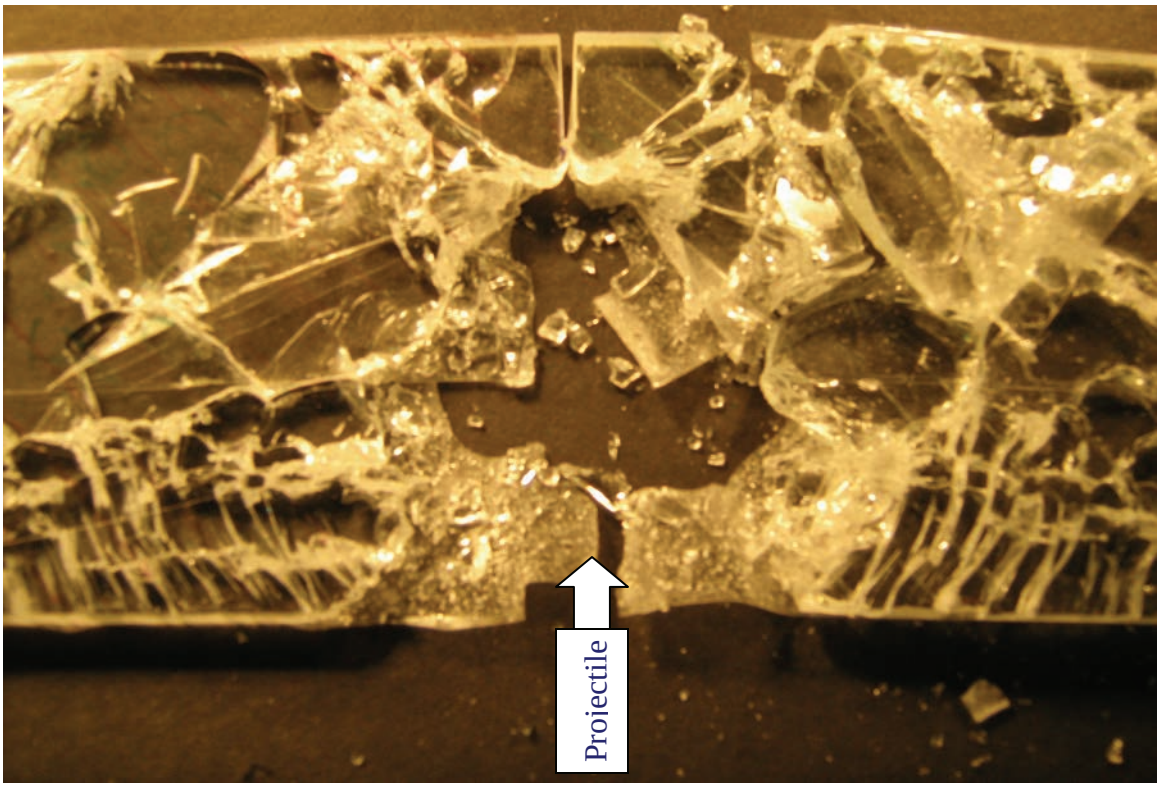

Figure 16. Extent of fragmentation damage caused by direct impact of a Wood/Tungsten projectile at 48 m/s.

3.5 Validating the Model

One of the potential issues with simply deforming the side of the mesh at a constant rate is that in reality, the projectile decelerates as it deforms, crushes, and cracks the glass. After comparing the images generated by the model to panels of actual glass that have been broken, it seems that this method of constant rate loading is sufficient to model the event. It will be interesting to see how the crack tip speeds compare when optical images of the crack propagation are obtained. Also, the crack tip speed at which bifurcation occurs will be compared for the computational model and the optical images.

4. Summary and Conclusions

4.1 Summary

The computational simulations are consistent with the experimental results. As projectile velocity is increased, the angle of branching steepens, the physical location of branching approaches the notch tip, and the frequency of microcracking increases. The validity of the computational model was further verified by examining the fracture surfaces with optical and scanning electron microscopes. Triggering flash bulbs with a steel wire break-screen has been shown to be effective in illuminating the test specimen during the propagation event.

4.2 Future Work

In the remaining third of this summer project, two specific objectives will be completed. First, optical images of crack propagation will be obtained using the high-speed camera. With the flash triggering satisfactory, projectile type selected, and placement of the specimen/projectile/rod precise, it is reasonable to expect that proper triggering of the camera will soon follow. Second, work with Dr. Kraft will continue until the intricacies of Finite Element modeling are more fully understood. By the end of the program, the author will be able to independently construct Finite Element meshes of basic shapes using the computer software package Cubit, apply initial/boundary conditions, and run the simulations.

4.3 Conclusions

As an introduction to fracture mechanics, this summer research project has been very thorough. The author has learned about the experimental and computational sides of this subject, and even performed basic fractography. In terms of educational merit, the author would classify this as more useful than any one semester at his alma mater.

5. References

1. Yoffe, E. H. The Moving Griffith Crack. *Philosophical Magazine* **1951**, *42*, 739–750. 1951.
2. Bjerke, T. Personal communication, ARL-TED, Aberdeen, MD, July 2008.
3. Love, B. Personal communication, ARL-TED, Aberdeen, MD, July 2008.
4. Halsey, S. Personal communication, ARL-WM-TA, Aberdeen, MD, July 2008.
5. Kraft, R. Personal communication, ARL-TED, Aberdeen, MD, July 2008.
6. Rice, J. R. The Mechanics of Earthquake Rupture. In *Proceedings of International School of Physics*, Enrico Fermi ed. In *Physics of the Earth's Interior*, Dziewonski, A.M.; Boschi, E., eds. North Holland, 1980.

ADMNSTR
DEFNS TECHL INFO CTR
ATTN DTIC OCP (ELECTRONIC COPY)
8725 JOHN J KINGMAN RD STE 0944
FT BELVOIR VA 22060-6218

US ARMY RSRCH LAB
ATTN AMSRD ARL CI OK TP TECHL LIB T LANDFRIED
BLDG 4600
ABERDEEN PROVING GROUND MD 21005-5066

DIRECTOR
US ARMY RSRCH LAB
ATTN AMSRD ARL RO EV W D BACH
PO BOX 12211
RESEARCH TRIANGLE PARK NC 27709

US ARMY RSRCH LAB
ATTN AMSRD ARL CI OK T TECHL PUB
ATTN AMSRD ARL CI OK TL TECHL LIB
ATTN AMSRD ARL D J M MILLER
ATTN IMNE ALC IMS MAIL & RECORDS MGMT